

**EXPERIMENTAL STUDY OF THE BEHAVIOUR AND STRENGTH OF
DEEP CONCRETE BEAMS REINFORCED WITH CFRP BARS**

**EXPERIMENTAL STUDY OF THE BEHAVIOUR AND STRENGTH OF
DEEP CONCRETE BEAMS REINFORCED WITH CFRP BARS**

By

MOHAMMADREZA ZEIDIDOUZANDEH, B.Sc.

A Thesis

Submitted to the School of Graduate Studies

In Partial Fulfillment of the Requirements

For the Degree

Master of Applied Science

McMaster University

Hamilton, Ontario

© Copyright by Mohammadreza Zeididouzandeh, October 2008

MASTER OF APPLIED SCIENCE
(Civil Engineering)

McMaster University
Hamilton, Ontario

TITLE: Experimental Study of the Behaviour and Strength of Deep Concrete
Beams Reinforced with CFRP Bars

AUTHOR. Mohammadreza Zeididouzandeh, B.Sc. (McMaster University)

SUPERVISOR. Dr A. Ghani Razaqpur

NUMBER OF PAGES xx, 262

ABSTRACT

An experimental program was conducted to investigate the strength and deformations of deep beams reinforced with Carbon Fibre Reinforced Polymer (CFRP) longitudinal and transverse reinforcement. Two groups of beams were tested, with each group comprising three beams. Two of the three beams in each group were reinforced with CFRP bars while the third beam was reinforced with conventional rebars and the latter beam was used as a control specimen.

Beams in group 1 had span-to-depth ratio of one, while those in group 2 had a span-to-depth ratio of two. Beams in both groups had height of 900 mm and width of 250 mm. All the beams were simply supported and were tested in four-point bending with the point loads applied at one-third of the span.

The test results revealed no significant difference between the behaviour of the FRP reinforced beams and the companion control beams. On the other hand due to lack of hooks at the ends of the CFRP bars, and the loss of bond between the CFRP fibres and the sand grains on the surface of the bar, the failure in the CFRP reinforced beams was caused by the loss of anchorage while in the steel reinforced beams, the failure was initiated by the yielding of the longitudinal steel, followed by the crushing of the horizontal compression strut, but the nodal zones did not fail in any of the beams. Consequently, it was concluded that CFRP reinforced deep beams could be designed using the current CSA method for

conventional steel reinforced concrete deep beams, provided the anchorage or bond strength of FRP bars could be properly determined. The existing nodal efficiency factors for the CCC nodal zones, as given in the CSA A23.3 standard, could be applied to CFRP reinforced beams while the corresponding factor for the CCT zone may be conservatively assumed to be 0.68. Finally, despite the linear elastic behaviour of CFRP reinforcement, deep beams reinforced with CFRP bars could be designed using strut and tie models.

ACKNOWLEDGEMENTS

I would like to express my profound gratitude to Dr. A. Ghani Razaqpur for his encouragement, guidance and technical support throughout the research program.

I would like to thank McMaster University, the Department of Civil Engineering and the Center for Effective Design of Structures for the financial support that made it possible for me to pursue graduate studies. I would like to extend special thanks to the Applied Dynamic Laboratory technical staff, in particular to Mr. David Perrett, for his assistance during my experimental work.

I would like to express my deepest appreciation and thanks to my parents and my sister for their endless love, support and encouragement.

TABLE OF CONTENTS

	Page
ABSTRACT	iii
ACKNOWLEDGEMENTS	v
LIST OF FIGURES	ix
LIST OF TABLES	xiv
LIST OF SYMBOLS	xv
CHAPTER 1: INTRODUCTION.....	1
1.1 General.....	1
1.2 Research Significance and Objectives.....	4
1.3 Scope of the Research.....	5
1.4 Methodology.....	6
CHAPTER 2: LITERATURE REVIEW	8
2.1 Introduction.....	8
2.2 Methods of Analysis of the Shear Strength of Deep Beams.....	8
2.2.1 Elastic analysis.....	9
2.2.2 Equilibrium method	13
2.2.3 Compression field theory.....	19
2.2.4 Strut-and-tie model	24
2.2.4.1 Historical development of strut-and-tie model	26
2.2.4.2 Components of strut-and-tie model	29
2.2.4.3 Current North American code provisions for strut-and-tie modeling	40
2.3 Force Transfer Mechanism in Deep Beams.....	49
2.3.1 Tied arch mechanism	51
2.3.2 Truss mechanism	52
2.3.3 Modes of failure.....	52
2.4 Brief Review of the Behaviour of FRP Bars	54
CHAPTER 3: EXPERIMENTAL PROGRAM.....	66
3.1 General.....	66
3.2 Material Properties.....	67
3.2.1 Concrete	68
3.2.2 Steel reinforcement	72
3.2.2.1 Reinforcing bar	72
3.2.2.2 Welded-wire fabric	76
3.2.3 CFRP reinforcement	76
3.2.3.1 Reinforcing bar	77

3.2.3.2	Reinforcing grid.....	79
3.3	Details of Test Specimens and Testing Procedure.....	80
3.3.1	Test specimens.....	81
3.3.2	Fabrication of the beams.....	91
3.3.2.1	Formwork preparation.....	92
3.3.2.2	Preparation of reinforcement cages.....	93
3.3.2.3	Casting of concrete.....	95
3.3.2.4	Curing of concrete.....	95
3.3.3	Instrumentation.....	96
3.3.3.1	Electrical resistance strain gauges.....	97
3.3.3.2	Linear displacement transducers.....	100
3.3.3.3	Draw wire sensors.....	101
3.3.3.4	Dial gauges.....	102
3.3.3.5	Load cell.....	103
3.3.4	Test set-up.....	103
3.3.5	Testing procedure.....	107

**CHAPTER 4: OBSERVATION AND DISCUSSION OF THE
EXPERIMENTAL RESULTS..... 109**

4.1	General.....	109
4.2	Evaluation of the Test Setup.....	109
4.2.1	General behaviour of beam S1-A.....	113
4.3	Beams with Span-to-Depth Ratio of 1.....	115
4.3.1	Observed behaviour of tested beams.....	116
4.3.2	Load-deflection response.....	124
4.3.3	Deflected shape.....	127
4.3.4	Strain in concrete.....	130
4.3.4.1	Mid-span strain profile.....	131
4.3.4.2	Strain along the compression struts.....	134
4.3.5	Strain in reinforcement.....	141
4.3.5.1	Strain in longitudinal reinforcement.....	142
4.3.5.2	Strain in transverse reinforcement.....	146
4.4	Beams with Span-to-Depth Ratio of 2.....	150
4.4.1	Observed behaviour of tested beams.....	151
4.4.2	Load-deflection response.....	159
4.4.3	Deflected shape.....	162
4.4.4	Strain in concrete.....	164
4.4.4.1	Mid-span strain profile.....	165
4.4.4.2	Strain along the compression struts.....	167
4.4.5	Strain in reinforcement.....	174
4.4.5.1	Strain in longitudinal reinforcement.....	175

4.4.5.2	Strain in transverse reinforcement	177
CHAPTER 5:	ANALYSIS OF RESULTS.....	181
5.1	General.....	181
5.2	Failure Mechanism.....	181
5.3	Efficiency Factors of Concrete Strength.....	185
5.3.1	Effective compressive strength of the strut.....	185
5.3.2	Effective compressive strength of the nodal zones.....	191
CHAPTER 6:	SUMMARY, CONCLUSIONS, AND	
	RECOMMENDATIONS.....	198
6.1	Summary	198
6.2	Conclusion	200
6.3	Recommendations for future work	203
REFERENCES.....		205
APPENDIX A: SAMPLE CALCULATION		210
APPENDIX B: ADDITIONAL EXPERIMENTAL DATA.....		246
APPENDIX C: MATERIAL TESTING.....		260

LIST OF FIGURES

	Page
Figure 2.1: Lever arm variation for simply supported shallow and deep beams (adapted from Leonhardt et al. (1966)).....	10
Figure 2.2: Deep beam with $l_e < h$ (adopted from Schlaich et al. (1991)).....	13
Figure 2.3: Equilibrium conditions from 45° truss model (adopted from Collins and Mitchell (1991)).....	14
Figure 2.4: Equilibrium conditions from variable-angle truss model (adopted from Collins and Mitchell (1991))	16
Figure 2.5: Compatibility conditions for cracked web element (adopted from Vecchio and Collins (1986)).....	20
Figure 2.6: Stress vs. strain relationships (adopted from Vecchio and Collins (1986))	21
Figure 2.7: Components of a typical strut-and-tie model for deep beams.....	25
Figure 2.8: Strut-and-tie model (adopted from Schlaich et al. (1991))	27
Figure 2.9: Strength of the beams failing in shear for different a/d ratio (adopted from Collins and Mitchell (1991), tested by Kani (1979)).....	29
Figure 2.10: Geometric representation of various compression struts in deep beam	30
Figure 2.11: Typical types of nodal zones in strut and tie models for deep beams	38
Figure 2.12: Strut-and-tie models used for deep beams	50
Figure 3.1: Uniaxial compression testing of the concrete cylinders.....	71
Figure 3.2: Stress-strain relationship of concrete in compression (28 days after casting).....	71
Figure 3.3: Splitting test of the concrete cylinders	72
Figure 3.4: Tensile test of the steel bars	74
Figure 3.5: Stress-strain relationship for No.10 steel bar	74
Figure 3.6: Stress-strain relationship for No.15 steel bar	75
Figure 3.7: Determination of yield strength by the offset method.....	75

Figure 3.8: Typical stress-strain profile of the Isorod CFRP bars (adapted from Benmokrane et al. (2002))	78
Figure 3.9: Typical surface texture of sand-coated CFRP Isorod.....	78
Figure 3.10: Typical stress-strain profile of the NEFMAC CFRP reinforcement (adapted from Benmokrane et al. (2002)).....	80
Figure 3.11: NEFMAC CFRP section cut off from the original reinforcement grid.....	80
Figure 3.12: Typical test specimen geometry and dimensions.....	83
Figure 3.13: STM for the beams with span-to-depth ratio of 1	86
Figure 3.14: STM for the beams with span-to-depth ratio of 2	87
Figure 3.15: Reinforcement and the geometry of S1 beams.....	88
Figure 3.16: Reinforcement and geometry of F1 beams.....	89
Figure 3.17: Reinforcement and geometry of S2 beam	90
Figure 3.18: Reinforcement and geometry of F2 beams.....	91
Figure 3.19: Formwork used to cast the concrete.....	92
Figure 3.20: Beam S1 A/B reinforcement cage.....	94
Figure 3.21: Beams F1 A/B reinforcement cage	94
Figure 3.22: Typical test specimens during storage period	96
Figure 3.23: Typical strain gauge positions for all the beams except Beam S2 ...	99
Figure 3.24: Strain gauge locations for Beam S2	99
Figure 3.25: Position of linear displacement transducers and draw wire sensors.....	101
Figure 3.26: Dial gauges used to measure the slippage of main reinforcement .	103
Figure 3.28: Photograph of the test set-up	107
Figure 3.29: Photograph of the data acquisition system.....	108
Figure 4.1: The adjusted test setup	111
Figure 4.2: Failure of the S1-A beam	112
Figure 4.3: Schematic view of the crack patterns of S1-A beam at failure	114
Figure 4.4: Load-deflection relationship of the S1-A beam	114
Figure 4.5: Cracking development in the F1-A beam.....	117

Figure 4.6: Cracking development in the F1-B beam.....	118
Figure 4.7: Cracking development in the S1-B beam.....	119
Figure 4.8: Schematic view of the crack patterns for the beams with span-to-depth ratio of 1	121
Figure 4.9: Anchorage failure of the CFRP reinforced beams with $l_e/h=1$	123
Figure 4.10: Complete load-deflection curves for the beams with $l_e/h=1$	125
Figure 4.11: Load vs. mid-span deflection curves for the beams with $l_e/h=1$	126
Figure 4.12: Deformed shape of the beams with $l_e/h=1$	128
Figure 4.13: Rosette electrical strain gauge numbering for the tested beams	130
Figure 4.14: Strain distribution along the depth of the beams with span-to-depth ratio of 1	132
Figure 4.15: Average compression strain in the struts of the beams with span-to-depth ratio of 1	135
Figure 4.16: Compression strain comparison in the west strut for beams with span-to-depth ratio of 1	137
Figure 4.17: Compression strain comparison in the east strut for beams with span-to-depth ratio of 1	138
Figure 4.18: Strain measurements normal to the axis of the diagonal struts in the beams with span-to-depth ratio of 1	140
Figure 4.19: Strain gauge numbering and position in all the beams except beam S2.....	141
Figure 4.20: Strain distribution along the longitudinal reinforcement of the beams with span-to-depth ratio of 1	143
Figure 4.21: Load-strain relationships in the stirrups of F1-A beam.....	147
Figure 4.22: Load-strain relationships in the stirrups of F1-B beam.....	148
Figure 4.23: Load-strain relationships in the stirrups of S1-B beam.....	149
Figure 4.24: Cracking development in the F2-A beam.....	153
Figure 4.25: Cracking development in the F2-B beam.....	154
Figure 4.26: Cracking development in the S2 beam.....	155
Figure 4.27: Schematic view of the crack pattern for the beams with $l/d=2$	156
Figure 4.28: Anchorage failure of the CFRP reinforced beams with $l_e/h=2$	158

Figure 4.29: Complete load-deflection curves for the beams with $l_e/h=2$	160
Figure 4.30: Load vs. mid-span deflection curves for the beams with $l_e/h=2$	161
Figure 4.31: Deformed shape of the beams with $l_e/h=2$	163
Figure 4.32: Strain distribution along the depth of the beams with span-to-depth ratio of 2.....	166
Figure 4.33: Average compression strain in the struts of the beams with span-to-depth ratio of 2.....	168
Figure 4.34: Compression strain comparison in the web strut for beams with span-to-depth ratio of 2.....	169
Figure 4.35: Compression strain comparison in the east strut for beams with span-to-depth ratio of 2.....	170
Figure 4.36: Strain measurements normal to the axis of the diagonal struts in the beams with span-to-depth ratio of 2.....	173
Figure 4.37: Strain gauge numbering and position in the stirrups of S2 beam...	174
Figure 4.38: Strain distribution along the longitudinal reinforcement of the beams with span-to-depth ratio of 2	176
Figure 4.39: Load-strain relationships in the stirrups of F2-A beam.....	178
Figure 4.40: Load-strain relationships in the stirrups of F2-B beam.....	179
Figure 4.41: Load-strain relationships in the stirrups of S2 beam.....	180
Figure 5.1: Equilibrium of nodal zones in the tested deep beams	192
Figure B.1: Deformed shape of the beams with $l_e/h=1$	247
Figure B.2: Strain distribution along the depth of the beams with $l_e/h=1$	248
Figure B.3: Strain distribution along the longitudinal bar of the beams with $l_e/h=1$	250
Figure B.4: Strain measurements from the rosette gauges in the F1-A beam	251
Figure B.5: Strain measurements from the rosette gauges in the F1-B beam.....	252
Figure B.6: Strain measurements from the rosette gauges in the S1-B beam.....	253
Figure B.7: Deformed shape of the beams with $l_e/h=2$	254
Figure B.8: Strain distribution along the depth of the beams with $l_e/h=2$	255
Figure B.9: Strain distribution along the longitudinal bar of the beams with $l_e/h=2$	256

Figure B.10: Strain measurements from the rosette gauges in the F2-A beam .. 257

Figure B.11: Strain measurements from the rosette gauges in the F2-B beam... 258

Figure B.12: Strain measurements from the rosette gauges used in the S2 beam
..... 259

Figure C.1: Stress-strain relationship of the concrete for F1 beams (151 days
after casting) 262

Figure C.2: Stress-strain relationship of the concrete for S2 beams (165 days
after casting) 262

Figure C.3: Stress-strain relationship of the concrete for S2 beams (176 days
after casting) 263

Figure C.4: Stress-strain relationship of the concrete for S1-B beam (182 days
after casting) 263

LIST OF TABLES

	Page
Table 2.1 Effective stress limits in concrete struts	33
Table 2.2. Effective stress limits of nodal zones	39
Table 3 1 Average compressive cylinder strength of concrete for various specimens.....	70
Table 3.2. Compressive cylinder strength and splitting tensile strength of concrete at 28 days	70
Table 3.5 Longitudinal and transverse reinforcement ratio and rigidities for the test beams.....	85
Table 3.6: Number of electrical resistance strain gauges in each specimen.....	99
Table 4.1 Test results for the beams with span-to-depth ratio of 1	115
Table 4.2. Test results for the beams with span-to-depth ratio of 2	150
Table 5.1 Measured and calculated structural capacities.....	182
Table 5.2. Predicted versus actual failure mechanisms for the tested beams	184
Table 5.4: Calculated effective stress levels at the nodal zones	194
Table 5.5 Calculated effective stress level for concrete node vs. proposed values	196
Table B.1 Compressive cylinder strength of concrete, for specimens F1-A/B (151 days after casting)	260
Table B.2. Compressive cylinder strength of concrete, for specimen S2 (163 days after casting)	260
Table B.3 Compressive cylinder strength of concrete, for specimens F2-A/B (176 days after casting)	260
Table B.4: Compressive cylinder strength of concrete, for specimen S1-B (182 days after casting)	261
Table B.5 Tensile properties of No.10 steel reinforcing bar	261
Table B.6: Tensile properties of No.15 steel reinforcing bar	261

LIST OF SYMBOLS

All symbols and terms presented in equations within this thesis are summarized below. Typical units are included in parentheses.

- a Depth of rectangular compression block (mm)
- a Length of the shear-span (mm)
- A_{cs} Cross sectional area of strut (mm^2)
- A'_s Area of compression reinforcement (mm^2)
- A_s Area of tension reinforcement (mm^2)
- A_{si} Total area of reinforcement in the i -th layer of the grid crossing the diagonal strut (mm^2)
- A_{ss} Area of compression steel reinforcement in struts (mm^2)
- A_l Area of longitudinal reinforcement (mm^2)
- A_{nz} Area of the face of nodal zone subjected to loading (mm^2)
- A_v Area of shear reinforcement (mm^2)
- A_w Area of web reinforcement (mm^2)
- b Width of deep beam (mm)
- C_1 Compression force in top horizontal strut (kN)
- C_2 Compression force in diagonal struts (kN)
- d Distance from extreme compression fibre to centroid of longitudinal tie (mm)

d_b	Diameter of the reinforcement rebar (mm)
D	Compressive force in the diagonal strut (kN)
E_{FRP}	Modulus of elasticity of CFRP reinforcement (MPa)
E_s	Modulus of elasticity of main steel reinforcement (MPa)
E_w	Modulus of elasticity of steel web reinforcement (MPa)
f_c	Concrete cylinder compressive strength (MPa)
f_{cu}	Effective compressive strength of concrete (MPa) $=\nu f_c$
f_{fu}	Ultimate tensile strength of FRP reinforcement (MPa)
f_s	Tensile stress of steel reinforcement before yielding (MPa) $=E_s \varepsilon_s$
f'_s	Tensile stress in compression reinforcement (mm ²)
f_v	Average tensile stress in stirrups caused by shear force V (MPa)
f_y	Yield strength of steel reinforcement (MPa)
f_2	Compressive stress in diagonal struts (MPa)
f_{2max}	Compressive strength of diagonal struts (MPa)
F_n	Nominal strength of the STM components (kN)
F_{nn}	Nominal force in nodal zones (kN)
F_{ns}	Nominal force in struts (kN)
F_{nt}	Nominal force in tension tie (kN)
F_u	Force in the strut-and-tie model (STM) components (kN)

- h Height of deep beam (mm)
- h_a Depth of longitudinal tension tie (mm)
- jd Distance from the centroid of the rectangular compression block to the centroid of the longitudinal tie (mm)
- k_1 Bar location modification factor
=1 for minimum cover below the longitudinal bars (CSA S806-02, Clause 9.3.4)
- k_2 Concrete density modification factor
=1 for normal-density concrete (CSA S806-02, Clause 9.3.4)
- k_3 Bar size modification factor
=0.8 for 9.5mm diameter Isorod reinforcement bar (CSA S806-02, Clause 9.3.4)
- k_4 Bar fibre modification factor
=1 for CFRP reinforcement bar (CSA S806-02, Clause 9.3.4)
- k_5 Bar surface profile modification factor
=1 for sand surface texture (CSA S806-02, Clause 9.3.4)
- l Length of deep beam (mm)
- l_d Development length of straight reinforcement bar (mm)
- l_e Span of deep beam (mm)
- l_o Length of the loading plate (mm)
- l_r Length of the reaction plate (mm)

M_{uexp}	Observed ultimate moment (kN.m)
N_u	Ultimate compressive force in the struts (kN)
N_{ut}	Ultimate tensile force in the tie (kN)
N_v	Tension in flexural reinforcement caused by shear force V (kN)
O	Overhang distance of deep beam (mm)
r	Radius of the reinforcing bar (mm)
R	Reaction force (kN)
s	Center-to-center spacing of transverse reinforcement (mm)
s_i	Spacing of the reinforcement in the i -th layer of the grid crossing the diagonal strut (mm)
T	Tensile force in the main longitudinal tie (kN)
v	Strength efficiency factor for concrete in nodal zones and struts =0.85 for struts (CSA A23.3-04, Clause 11.4.2.3) = $0.85\phi_c$ for CCC node, $0.75\phi_c$ for CCT node (CSA A23.3, Clause 11.4.4.1) = $\alpha_1 \beta_s$ for struts (ACI 318-08, Section A.3.2) = $\alpha_1 \beta_n$ for nodal zones (ACI 318-08, Section A.3.2)
V	Applied shear force (kN)
V_{ACI}	Ultimate shear strength, determined by ACI 318-08 standard (kN)
V_{crexp}	Observed shear cracking load (kN)
V_{CSA}	Ultimate shear strength, determined by CSA A23.3-04 (kN)
V_{uexp}	Observed ultimate shear capacity of the deep beams (kN)

z	Internal moment lever arm (mm)
α_i	Angle of the i -th layer of reinforcement with diagonal strut (deg.)
α_l	Load duration effect factor =0.85 (ACI 318-08, Section A.3.2 and A.5.2)
β_n	Type of nodal zone =1 for CCC nodal zone (ACI 318-08, Section A.5.2.1) =0.8 for CCT nodal zone (ACI 318-08, Section A.5.2.2)
β_s	Strut geometry factor =1 for prismatic strut (ACI 318-08, Section A.3.2.1) =0.75 for bottle-shaped struts (ACI 318-08, Section A.3.2.2)
γ_{xy}	Shear strain of concrete
ϵ'_c	Concrete strain at the peak compressive strength =0.002 (CSA A23.3-04, Equation 11-22)
ϵ_s	Tensile strain of steel reinforcement before yield point
ϵ_x	Concrete longitudinal strain in the direction of the bottom tie
ϵ_y	Concrete vertical strain
ϵ_1	Principal tensile strain in cracked concrete (CSA A23.3-04, Equation 11-23)
ϵ_2	Principal compressive strain =0.002 (CSA A23.3-04, Section N11.4.2.3)
θ	Angle of inclination of diagonal struts to the longitudinal tie (deg.)

- θ_s Smallest angle between the tie and the strut (deg.)
- λ Concrete density factor
 =1 for normal weight concrete (ACI 318-08, Clause 8.6.1)
- ρ Ratio of total area of longitudinal reinforcement to gross concrete section
 (%)
- $\sigma_{le/4}$ Tensile stress in the CFRP Isorod reinforcement at the distance $l_e/4$ away
 from the center of supports (MPa)
 = $E_{FRP} \varepsilon_{le/4}$
- σ_{sp} Tensile stress in the CFRP Isorod reinforcement at the center of supports
 (MPa)
 = $E_{FRP} \varepsilon_{sp}$
- τ Average bond stress of the CFRP Isorod reinforcement (MPa)
- ϕ Strength reduction factor
 =0.7 for axial compression
 =0.9 for axial tension
 =0.75 for shear (ACI 318-08, Clause 9.3.2.6)
- ϕ_c Concrete resistance factor
 =0.65 (CSA A23.3-04, Clause 8.4.2)
- ϕ_s Reinforcement steel resistance factor
 =0.85 (CSA A23.3-04, Clause 8.4.3 (a))

CHAPTER 1: INTRODUCTION

1.1 General

The corrosion of steel reinforcement is one of the principal causes of the deterioration of reinforced concrete (RC) structures which impacts their serviceability and strength. Offshore, coastal, underground, and other structures exposed to marine environment and deicing salts are subject to corrosion attack and require extensive and expensive maintenance. The performance of concrete structures exposed to aggressive environments could be improved by utilizing high strength corrosion resistant reinforcement. Other techniques have already been developed to inhibit corrosion such as epoxy coating of reinforcing bars and application of cathodic protection. The selection of an appropriate technique is mainly based on the cost, ease of application, and the efficiency of the solution.

A relatively new development in civil engineering has been the use of fibre-reinforced polymers (FRP) as reinforcement in concrete. The principal reason for the use of FRP as a substitute for conventional steel reinforcement is the corrosion immunity of FRP due to its resistance to acid and alkalis. FRP's high tensile strength and light weight compared to steel reinforcement offers additional advantages in construction. Thus, it would be reasonable to investigate further the structural applications of FRP in RC structures.

FRP is made of high strength non-metallic fibre such as glass, carbon and aramid fibers embedded in a polymer matrix and produced in a wide variety of shapes with different characteristics. The applications of Carbon Fibre Reinforced Polymer (CFRP) reinforcing bars and grids in previous studies on slender beams have led to promising results and have proven effective.

Although deep and shallow beams both originate from the same family of structural elements, they resist applied loads differently and thus each has its own design requirements. In comparison with RC slender beam, RC deep beam shear strength is significantly greater because of the manner in which shear is resisted. Furthermore, in slender beams bending may be the predominant resistance mechanism while in deep beams shear is the main resisting mechanism. The shear resistance mechanism in deep beams is not the same as in shallow beams. Deep beams are expected to fail in a relatively brittle and non ductile manner due to their relatively small span-to-depth ratio and their failure being initiated by crushing of the concrete.

Conventional steel reinforced concrete has been used for over one hundred years, and many types of reinforced concrete elements have been investigated to understand their behaviour and this includes deep beams. The results of these investigations have demonstrated the effectiveness of internal steel reinforcement in increasing the strength and ductility of reinforced concrete members. Information concerning FRP reinforced concrete members, particularly regarding

deep beams reinforced with FRP, is scarce. Thus if FRP is to be used as an alternative reinforcement, the behaviour of FRP reinforced concrete members and structures must be investigated.

RC deep beam is a subject of considerable interest in structural engineering practice as indicated by de Paiva and Siess (1965) and Leonhardt and Walther (1966). RC deep beams are mainly used as load distributing structural elements such as transfer girders, foundation walls, pile caps in tall buildings and offshore structures. A deep beam is a beam element having a depth comparable to its span length. The small span-to-depth ratio in deep beams causes improvement in their shear capacity rather than their flexural capacity. This is mainly due to the fact that the shear deformation in RC deep beams is usually greater than the flexural deformation and therefore shear makes a more significant contribution to the overall resistance of the member. Only limited studies have been carried out to examine the strength of concrete deep beams reinforced with FRP reinforcement. The available studies on the structural behaviour of FRP reinforced deep beams have been concerned with their shear strength enhancement through application of FRP composite laminates as externally bonded reinforcement.

To the writer's knowledge, no research has yet been reported concerning the shear and flexural behaviour of deep beams internally reinforced with FRP material. Due to the influence of the reinforcement on the failure mode and strength of deep beams, it is difficult to develop design rules for FRP reinforced

deep beams solely based on theoretical considerations. The current strut-and-tie models for steel reinforced deep beams in the Canadian and American concrete design codes, although different, are both practical and safe. Similar design methods need to be developed for FRP reinforced concrete deep beams. Neither the current CSA standard S806-02 (2002) nor the ACI 440 (2001) committee guidelines have any recommendations with respect to the design/analysis of FRP reinforced deep beams. Therefore, a comprehensive testing program is required in order to fully understand the shear and flexural behaviour of FRP reinforced deep beams and to eventually develop the necessary code provisions for design.

1.2 Research Significance and Objectives

The use of FRP as an alternative solution to the corrosion problem of RC structures has made it a suitable topic for further investigation. The objective of this research is to experimentally evaluate the strength and the overall performance of deep beams internally reinforced with FRP longitudinal and transverse reinforcement. Although code provisions and design guidelines are available for concrete members reinforced with FRP bars and grids, none of these deal with the design of deep beams. Due to the semi-empirical basis of most of the design methods for conventional RC deep beams, it is not possible to directly apply them to FRP reinforced concrete deep beams. Thus, additional research is needed in order to examine the applicability of the available design methods to

FRP reinforced deep beams. In the light of the above discussion, the main objectives of this investigation are:

- 1 To consider the effect of FRP longitudinal and transverse reinforcement on the shear and flexural behaviour and strength of deep beams.
2. To examine the applicability of the current design methods for conventional RC deep beams to the design of FRP reinforced deep beams.
- 3 To investigate the effect of certain parameters, including the straight anchorage of the FRP longitudinal reinforcement, on deep beams strength.
4. To provide recommendations for the design of FRP reinforced deep beams.

1.3 Scope of the Research

The presented study was designed to examine the influence of two types of FRP reinforcement on two categories of deep beams made of medium strength concrete. The CFRP reinforcement used in this study consisted of CFRP bars; know commercially as Isorod, and CFRP grids; known as NEFMAC. The two categories of deep beams selected for this study had span-to-depth ratio of one and two.

1.4 Methodology

In order to achieve the objective of this research an experimental program was adopted. Seven large-scale deep beams were tested, including three conventional RC deep beams, and four CFRP reinforced deep beams. The beams were subjected to four-point bending and based on the result of the test, the influence of the CFRP reinforcement on the shear and flexural strength of the tested beams was investigated.

The beams were designed based on the strut-and-tie models described in the Appendix A of the ACI 318 (2008) code. Since FRP can not be bent, once the polymer sets, an important issue would be the anchorage of the longitudinal reinforcement and its effect on the ability of the FRP to transfer the necessary tension in deep beams. Thus, the FRP longitudinal reinforcements was provided with a minimum anchorage length in order to investigate the effect of this parameter on the flexural and shear capacity of such members.

To ensure the proper use of FRP in structural applications, the Canadian standards Association (CSA) has developed a standard for the design of FRP reinforced structures called CAN/CSA S806-02 (2002). Since this standard is the first of its kind in the world, and due to lack of adequate research results, the shear and flexural design of FRP reinforced deep beams are not covered by the standard. Thus it is anticipated that the findings of this research would assist in

arriving at reasonable recommendations with respect to the design of FRP reinforced deep beams, which may prove useful to the standard writers.

CHAPTER 2: LITERATURE REVIEW

2.1 Introduction

In order to efficiently design RC deep beams to resist the applied loads, a thorough understanding of their structural behaviour is required. This chapter provides a general discussion on the current design methodology for RC deep beam structures, as well as a review of the results of previous studies carried out by various researchers on this topic. This chapter also includes background information on the current applications of CFRP as internal reinforcement in concrete members.

2.2 Methods of Analysis of the Shear Strength of Deep Beams

The shear resistance mechanisms of deep flexural members have been the subject of considerable interest since the beginning of the twentieth century. The early investigations on deep concrete beams were mainly focused on their elastic behaviour and could not provide adequate information about the complete response of such members. The major breakthrough in the understanding of the complete response of steel reinforced deep beams occurred in the 1960's when the first set of ultimate load tests were carried out by de Paiva and Siess (1965) and Leonhardt and Walther (1966). These tests were carried out on numerous simply supported deep beams, and they showed that the shallow beam theory does not

apply to deep beams due to the differences among the distribution of their internal stresses and their load resisting mechanisms. For many years after that, the design of such members was based on good practice and empirical rules.

This topic was further investigated by Schlaich and his co-workers, including Weischede, Schäfer and Jennewein from 1982 until 1991 (MacGregor 1997). Schlaich broadly divided the stress fields within structural members into two regions; namely B-region, which follows beam (flexural) theory based on Bernoulli's hypothesis, and disturbed or D-region which does not follow this hypothesis. He then adopted the simple truss model analogy introduced by Ritter (1899) and Mörsch (1912), in order to explain the internal flow of forces in D-region. Based on this approach, the behaviour of deep beams was explained by the D-region stress fields.

2.2.1 Elastic analysis

Elastic analysis allows for accurate prediction of the flow of stresses in D-region before cracking and also can indicate where and when the initial cracking of concrete will occur. Although this technique is not capable of explaining the behaviour of cracked sections, it could provide good guidance for the necessary amount and the location of the reinforcement.

Leonhardt et al. (1966) tested the first set of deep beams subjected to flexural and shear loading. The beams were designed based on the shallow beam

theory with various span-to-depth ratios. The strain profile along the depth of the beam was captured during the test, which showed nonlinearity of stress distribution. Based on their studies, the internal lever arm of the simply supported uniformly loaded beams was approximated based on the theory of elasticity as indicated in Figure 2.1.

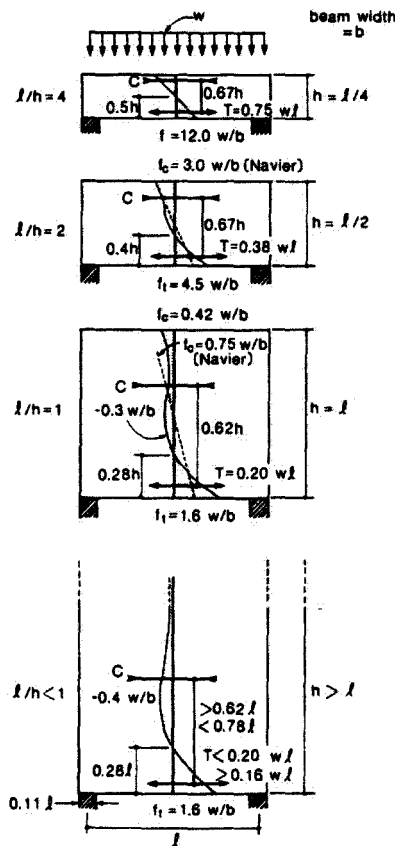


Figure 2.1: Lever arm variation for simply supported shallow and deep beams (adapted from Leonhardt et al. (1966))

They observed that as the span-to-depth ratio decreased, the principal stresses deviated more and more from those predicted based on plane-section

remains plane theory and the strain or stress profile across the depth of the member was no longer linear.

The European Concrete Committee (1964) further adjusted their proposed flexural lever arm formulas so they can be applied to other practical load cases, as listed below.

$$z = 0.2 (l_e + 2h) \quad \text{where} \quad 1 \leq l_e / h \leq 2 \quad (2.1)$$

or

$$z = 0.6 l_e \quad \text{where} \quad l_e / h < 1 \quad (2.2)$$

where z is the internal moment lever arm, l_e is the span of the beam and h is the height of the beam.

To obtain the elastic solution for deep beam structures, one should treat them as a two-dimensional plane stress problem and two-dimensional stress analysis methods must be performed to obtain a realistic stress distributions. The recommended techniques for finding the elastic solution of deep beams, as noted by Kong (1990), include the classical analytical methods, the finite difference and finite element methods. He suggests that the finite element method is a much more adaptable tool compared with the other techniques. The major advantage of the finite element method is the ability to model non-homogeneous and non-linear composite structures such as reinforced concrete deep beams, as the different

properties of the constituent materials can be separately represented by this method.

Finite element analysis was adopted by Robins and Kong (1973) to predict the ultimate load and crack pattern of deep beams and was found to be effective when applied to flanged deep beams. Schlaich et al. (1991) used finite element analysis to obtain the pattern of stress distribution for the deep beams tested by Leonhardt et al. (1966). Figure 2.2a shows one of the deep beams subjected to uniform loading that was tested by Leonhardt et al. (1966), while Figure 2.2c shows its reinforcement arrangement. Figure 2.2b illustrates the pattern of internal stresses trajectories computed by finite element analysis as reported by Schlaich et al. (1991).

Identifying the distribution of principal stresses within the disturbed region is very beneficial for the design of deep beams as it assists in determining the required amount of main tensile reinforcement and its proper position. The amount of main tensile reinforcement could be estimated based on the magnitude of principal tensile stresses near the bottom of the beam and ideally it would be positioned according to the pattern of the tensile stress trajectories. The reinforcement arrangement in Figure 2.2c is based on this kind of consideration.

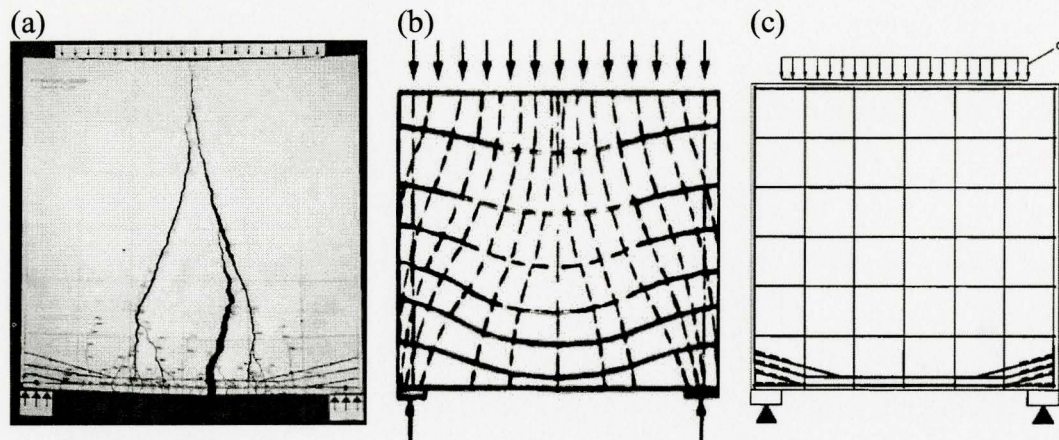


Figure 2.2. Deep beam with $l_e < h$. (a) Crack pattern of the tested beam (b) Elastic Stress trajectories, (c) Reinforcement profile (adopted from Schlaich et al. (1991))

2.2.2 Equilibrium method

The equilibrium method was first adopted by Ritter (1899) as he applied the 45° truss model to idealize the flow of forces in cracked reinforced concrete beams. The elements of the truss model represent the flow of internal forces in the beam, as illustrated in Figure 2.3. The diagonal elements of the truss represent the compressive stress flow in the concrete while the vertical elements follow the tension forces resisted by hangers or stirrups. The bottom and top chords of the truss are aligned with the longitudinal tension reinforcement and the flexural compression zone, respectively. Morsch (1902) explained the 45° truss model in more details by illustrating the strut components of the truss as a field of diagonal compression resisting the shear (see Figure 2.3b). He stated that at the early stages of crack formation the shear cracks propagate at an angle of 45° , while later they become flatter as the load increases. He also noted that the estimated amount of

stirrups based on the flatter crack could result in an unsafe design of the member. Consequently, for practical purposes it was suggested that after cracking, the diagonal compression stresses be assumed to remain at an angle of 45° with respect to the longitudinal axis of the member

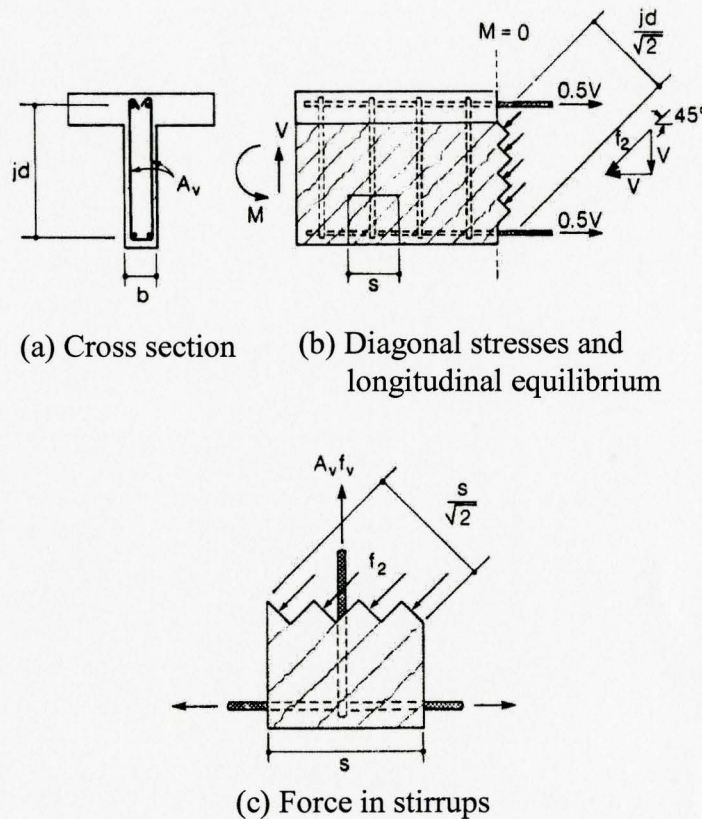


Figure 2.3 Equilibrium conditions from 45° truss model (adopted from Collins and Mitchell (1991))

The equilibrium conditions based on this truss analogy are illustrated in Figure 2.3. The magnitude of principal compressive stresses f_2 can be computed based on the free body diagram shown in Figure 2.3b; assuming that the shear

stresses are uniformly distributed over the thickness and the beam width is denoted by b , as shown in Figure 2.3a.

$$f_2 = \frac{2V}{bjd} \quad (2.3)$$

where jd is the distance between the centers of the top and bottom chord and V is the shear force acting on the section.

Furthermore, the tensile force in the longitudinal reinforcement N_v , caused by the shear, is the force required to balance the horizontal component of the diagonal compressive force. Assuming the diagonal compressive forces to be acting at an angle of 45° with respect to the beam axis,

$$N_v = V \quad (2.4)$$

Furthermore, the tensile force in the stirrup $A_v f_v$ can be calculated by equating it to the vertical component of the diagonal compressive force as follows (see Figure 2.3c).

$$\frac{A_v f_v}{s} = \frac{V}{jd} \quad (2.5)$$

where A_v and f_v are the total cross sectional area and the average tensile stress in the stirrup, respectively, and s is the spacing of the stirrups.

Mörsch's truss model was subsequently refined to the variable-angle truss model to provide more realistic estimation for design purposes (Collins and Mitchell 1991). This truss model provided more accurate estimation by

recognizing the fact that the inclination of the diagonal compression stresses is often less than 45°

The equilibrium conditions based on the variable-angle truss analogy can be established by reference to Figure 2.4.

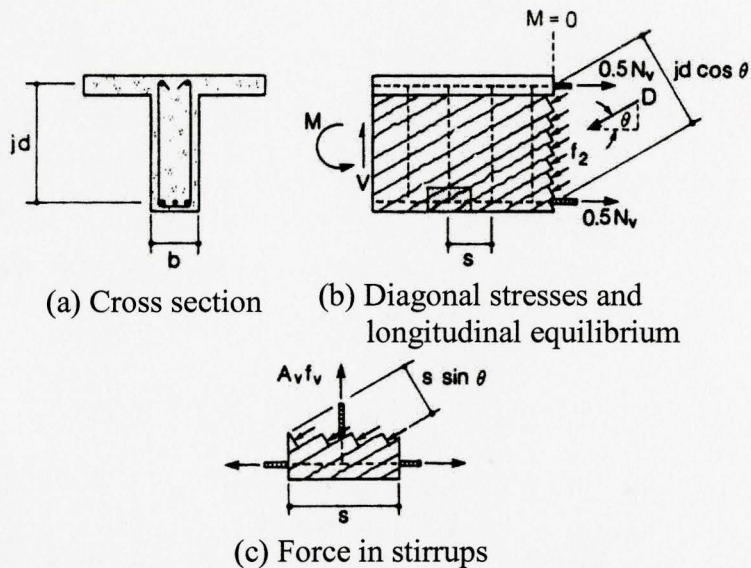


Figure 2.4: Equilibrium conditions from variable-angle truss model (adopted from Collins and Mitchell (1991))

The magnitude of principal compressive stresses f_2 can be computed based on the free body diagram shown in Figure 2.4b. Equilibrium suggests that the resultant of the diagonal compression stresses, D , must be equal to $V/\sin\theta$, but D is also equal to $f_2 b j d \cos\theta$, therefore, the following relationship could be found.

$$V = D \sin\theta = (f_2 b j d \cos\theta) \sin\theta$$

or

$$f_2 = \frac{V}{b j d} (\tan\theta + \cot\theta) \tag{2.6}$$

note that $\tan\theta + \cot\theta = 1/\sin\theta\cos\theta$.

The horizontal component of the diagonal compression force in the concrete, $V \cot\theta$, will be counteracted by the tensile force in the longitudinal reinforcement N_v (see Figure 2.4b).

$$N_v = V \cot\theta \quad (2.7)$$

Furthermore, the force in the stirrup caused by the diagonal compression in the concrete can be found from the equilibrium requirements as illustrated in the free body diagram shown in Figure 2.4c.

$$A_v f_v = (f_2 b s \sin\theta) \sin\theta$$

Substituting for f_2 from Equation (2.6) gives:

$$\frac{A_v f_v}{s} = \frac{V}{jd} \tan\theta \quad (2.8)$$

The above equilibrium equations are not sufficient to find the stresses in the beam subjected to shear since there are four unknowns (i.e., f_2 , N_v , f_v and θ) and three equilibrium equations, Equations (2.6) through (2.8). In order to find the inclination angle θ and the amount of shear V at failure, the theory of plasticity could be adopted by assuming the magnitude of the compressive stress f_2 in the concrete at failure and then solving for V and θ from Equations (2.6) and (2.8). Alternatively by assuming that at failure the stirrup and the longitudinal reinforcement reach yielding, it would be possible to determine the V and θ through solving Equations (2.7) and (2.8). The application of the theory of

plasticity as a practical tool in solving the equilibrium equations was first introduced by Nielsen (1984).

For predicting the strength of a concrete beam subjected to shear using the variable-angle truss model, it would be required to use an effective concrete compressive strength less than the one obtained from a cylinder compression test. For this purpose a value of $0.6 f'_c$ was suggested by Marti (1985), while Eurocode EC2, part 1 (1991) specifies the maximum strength of the diagonal struts, f_{2max} as:

$$f_{2max} = f'_c \left(0.7 - 0.9 \frac{f'_c}{200} \right) \quad (2.9)$$

where f'_c is expressed in MPa.

Due to the practicality of this approach, the variable-angle truss model was adopted into the CEB-FIP Code (1978), and it recommended that the designer choose the inclination of the diagonal compressive force between 31° and 59° .

Although the variable-angle model seems to be a more realistic approach when compared to the 45° truss model, both the 45° and the variable-angle truss models neglect the tensile stresses in the cracked concrete and assume that no stresses are transferred across the cracks. Consequently both models yield conservative results compared to the experimental results, as pointed out by ASCE-ACI Committee 445 (1998).

2.2.3 Compression field theory

The concept of diagonal compression field theory was introduced by Mitchell and Collins (1974) while analyzing the behaviour of beams subjected to torsion. Collins (1978) extended the basis of this theory so that it could be applied to beams subjected to shear. This theory is intended mainly for the shear design of shallow beams and cannot be applied directly to deep beams; however, certain aspects of it can be used to predict the shear resistance of deep beams, as discussed below.

The compression field theory is based on the assumption that the principal strain direction in the concrete coincides with the corresponding principal stress direction. In order to determine the shear strength and the load-deformation response of a member subjected to shear, the compatibility, equilibrium and constitutive relationships need be satisfied.

Compatibility in reinforced concrete requires that the steel reinforcement be fully bonded to the concrete. Thus, any change in concrete strain will be accompanied by an equal change in steel strain. Mitchell and Collins (1974) derived a set of compatibility equations based on the assumption that concrete carries no tension after cracking and that shear is carried by a field of inclined diagonal compression oriented at an angle θ to the axis of the member. In order to determine the angle of inclination θ for the diagonal compression, as shown in

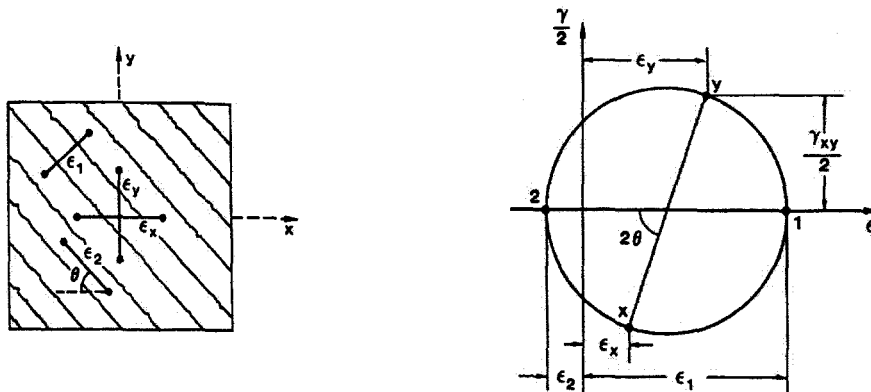
Figure 2.5a, the following expressions were derived from geometry of the Mohr's circle for average strains (see Figure 2.5b):

$$\gamma_{xy} = \frac{2(\epsilon_x + \epsilon_2)}{\tan\theta} \tag{2.10}$$

$$\epsilon_1 + \epsilon_2 = \epsilon_x + \epsilon_y \tag{2.11}$$

$$\tan^2\theta = \frac{\epsilon_x + \epsilon_2}{\epsilon_y + \epsilon_2} \tag{2.12}$$

where ϵ_x , ϵ_y , and γ_{xy} represent the longitudinal, transverse and shear strains in the web, respectively. The ϵ_1 and ϵ_2 represents the principal tensile and compressive strains, respectively.



(a) Average strains in cracked element (b) Mohr's circle of average strains
 Figure 2.5: Compatibility conditions for cracked web element (adopted from Vecchio and Collins (1986))

Note that the equilibrium equations used in the compression field theory are the same as those used in the variable-angle truss model (refer to Equations (2.6) through (2.8)).

To relate average stresses to average strains, the constitutive relationships are required which involves the stress-strain relationships of concrete under compression and of the reinforcement under tension.

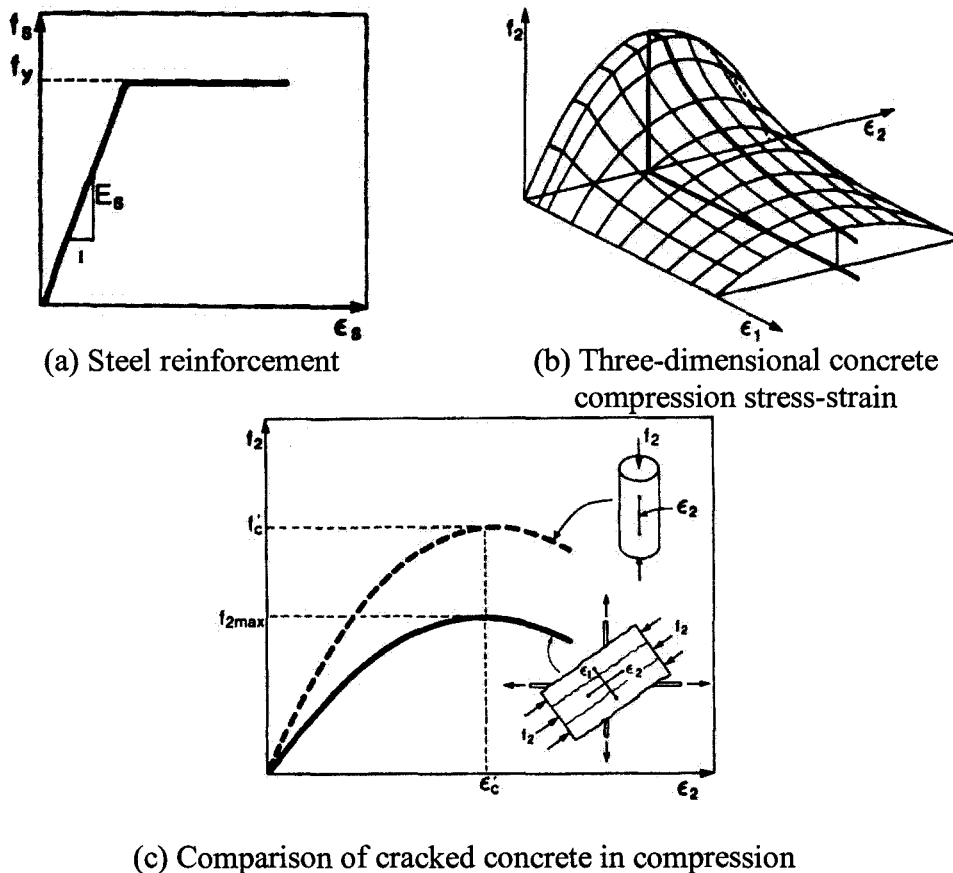


Figure 2.6: Stress vs. strain relationships (adopted from Vecchio and Collins (1986))

In case of steel reinforcement the usual elasto-plastic stress-strain relationship is used as shown in Figure 2.6a. Consequently, before yielding the stress in the reinforcement, f_s , could be linearly related to the strain in the reinforcement, ϵ_s , as shown below:

$$f_s = E_s \cdot \varepsilon_s \leq f_y \quad (2.13)$$

where E_s is the elastic modulus of the reinforcement and f_y is its yield stress.

In the case of cracked concrete in the web of the beam subjected to shear, it should be recognized that the strain conditions differ from those existing in the standard concrete cylinder test. As stated by Collins and Mitchell (1991) the concrete in a cylinder test is subjected to limited tensile strains due to the influence of Poisson's effect. In contrast, the cracked web element is subjected to substantial tensile strain and the interference of the existing cracks in the flow of diagonal compressive stresses leads to a weaker and softer concrete.

This effect was taken into account by Vecchio and Collins (1986) in formulating the stress-strain relationship of a cracked web element. They discovered that the principal compressive stress in the cracked concrete, f_2 , is not only influenced by the principal compressive strain, ε_2 , but also by the coexisting principal tensile strain, ε_1 (see Figure 2.6b). They suggested the following stress-strain relationship

$$f_2 = f_{2max} \cdot \left[2 \left(\frac{\varepsilon_2}{\varepsilon'_c} \right) + \left(\frac{\varepsilon_2}{\varepsilon'_c} \right)^2 \right] \quad (2.14)$$

where

$$\frac{f_{2max}}{f'_c} = \frac{1}{0.8 + 0.34 \varepsilon_1 / \varepsilon'_c} \leq 1 \quad (2.15)$$

Note that f_{2max} and ε'_c refer to the strength and corresponding strain of diagonally cracked concrete (usually taken as 0.002), respectively, and f'_c represents the concrete cylinder compressive strength, as illustrated in Figure 2.6c.

Although this technique provides a good prediction of the behaviour of members subjected to shear, it neglects the contribution of tensile stresses in the cracked concrete which leads to lower predicted strength and higher deformations in comparison with the corresponding values observed in tests. In order to refine the compression field theory, Vecchio and Collins (1986) further modified it. They noted that the magnitude of tensile stresses in the diagonally cracked concrete is zero at the crack location and reaches maximum at the midpoint between the cracks, while the tensile stresses in the reinforcement reach maximum at the locations crossed by the cracks. The refined model was named modified compression field theory (MCFT) since it was formulated based on the same assumptions as the compression field theory.

Neither the CSA Standard A23.3-04 nor the ACI 318 makes use of the concepts involved in the MCFT to arrive at their recommendations for the design of deep beams. It is, however, important to bear in mind that deep beams resist shear by compression and tension bands, which are often referred to as strut and ties. The strength of the diagonal concrete strut is influenced by the tensile strain imposed on it by the tension reinforcement crossing it.

2.2.4 Strut-and-tie model

The theory of flexure (beam) theory, and the associated shear design approach, which accounts for the shear contribution of both concrete and steel applies only to B-regions and cannot be directly applied to disturbed regions in deep beams. However, as pointed out earlier, compression field theory can be used to assess the strength of the shear resisting components in deep beams.

The modeling of the disturbed or D-regions can be achieved through visualization of the flow of principal stresses in concrete elements which form a series of hypothetical trusses, better known as struts and ties. Furthermore, the behaviour of these trusses is modeled by so-called strut-and-tie model (STM). These trusses consist of concrete diagonal compression struts and tension ties joined together at joints referred to as nodes, as shown in Figure 2.7. The beneficial aspect of using STM in representing the key load resisting elements in a disturbed region is that it portrays the flow of stresses in the structural element. In turn, this information can be used to carefully detail and reinforce the crucial regions of the truss model.

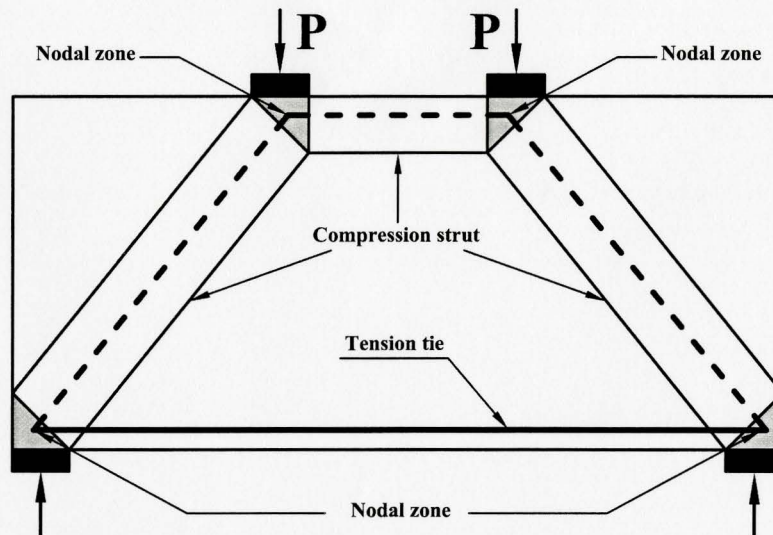


Figure 2.7 Components of a typical strut-and-tie model for deep beams

Strictly speaking, the strut and tie models fall within the confines of the upper bound theorem of the theory of plasticity. In the upper bound method, a failure pattern or mechanism is assumed and external loads and internal resisting forces are related to each other by either equating the work of the external loads to the internal energy of the structure at failure, or by considering the equilibrium of the various parts of the mechanism. The load thus obtained is an upper bound and thus several possible mechanisms must be assumed to obtain the actual strength of the member.

Although, implementing such a model would be valuable in designing deep beams, its beneficial effect could be limited based on the geometry and type of the STM selected. Note that the type of the strut refers to the type of failure mechanism. Schliach et al. (1991) state that the most efficient and realistic STM

would be the one that can carry the internal stresses with the least internal energy. He suggests that since the reinforced ties are more deformable than the concrete struts, the ideal model is the one which minimizes the amount of reinforcement and utilizes the shortest ties.

2.2.4.1 Historical development of strut-and-tie model

The use of STM can be traced back to the early 1980's as Rogowsky and MacGregor (1983) used the early plastic truss models to explain the behaviour of non-flexural structural members, such as deep beams. Since the establishment of plastic truss models by Nielsen (1971), various techniques have been suggested for designing the geometric layout as well as dimensions of the STM components [Schlaich et al. (1987), Collins and Mitchell (1991) and MacGregor (1997)] which would allow one to efficiently predict the ultimate strength of the D-regions in deep beams.

Marti (1985) and Schlaich et al. (1987) offered various approaches to model the discontinuity regions in complex structural elements. Schlaich et al. (1991) adopted the STM to evaluate the behaviour of deep beam specimens tested by Leonhardt et al. (1966). They identified the principal elastic stress trajectories and their directions for uncracked D-region using linear finite element analysis and then modeled the D-region by tracing the flow of the stress trajectories through the structure using load path method. They managed to model the D-

region at the onset of yielding of the main tension tie using the theory of elasticity, as illustrated in Figure 2.8a. In order to provide better estimate of ultimate load capacity of deep beams, the simplified model was further modified to simulate the real behavior of the structure at failure, as illustrated in Figure 2.8b.

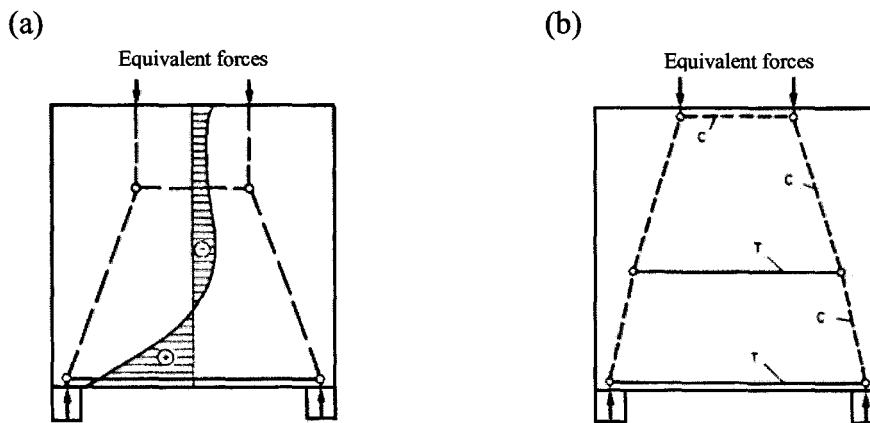


Figure 2.8: Strut-and-tie model: (a) Simplified model orientated for the theory of elasticity, (b) Refined model adjusted to the failure mechanism (adopted from Schlaich et al. (1991))

It is important to recognize that the STM shown in Figure 2.8 corresponds to the deep beam specimen shown in Figure 2.2. Comparing the failure state of the beam with the refined STM, it is apparent that the optimum STM is the one closer to the real behaviour of the cracked structure at failure; however, Schlaich et al. (1991) recommended not to depart too much from the elastic STM.

In order to correctly design and analyze the structures that are influenced by the behaviour of D-regions, one must first outline the vicinity of disturbed

regions so that the implementation of the traditional flexural theory could be avoided. The St. Venant's principle suggest that the effect of isolated D-region diminishes about one member depth from the point of disturbance directly below the concentrated load. Based on the experimental work of Kani (1979) on a number of simply supported beams, Collins and Mitchell (1991) noted that the D-region behaviour dominates the strength of deep beams with shear span-to-depth ratio less than 2.5 (Figure 2.9). As it can be seen from the figure, the effect of D-region is more and more noticeable as the shear span-to-depth ratio (a/d) approaches 1. It was also concluded that for a/d less than 2.5 the behaviour of the beam was more accurately predicted using STM, while for the beams with a/d values more than 2.5 the sectional design model prevailed, which is based on plane section theory. The ACI Committee 318 (2002) outlined the length of disturbance region as the effective depth (d) for isolated D-region and up to $2d$ for overlapping D-regions.

A lot of research has been carried out in the past to effectively design and detail the individual components of the STM. The description and the course of development for each of the STM components are briefly described in the following section.

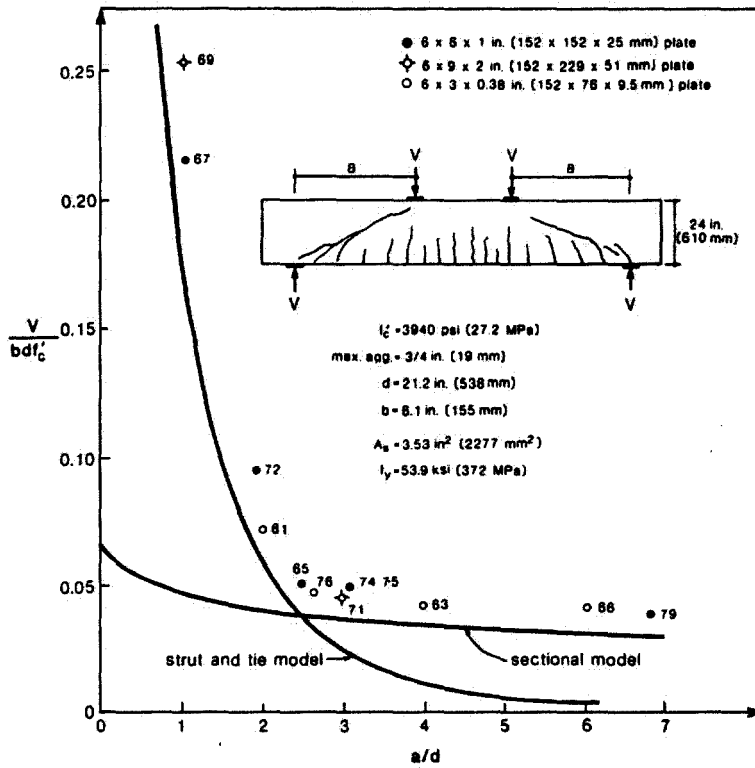
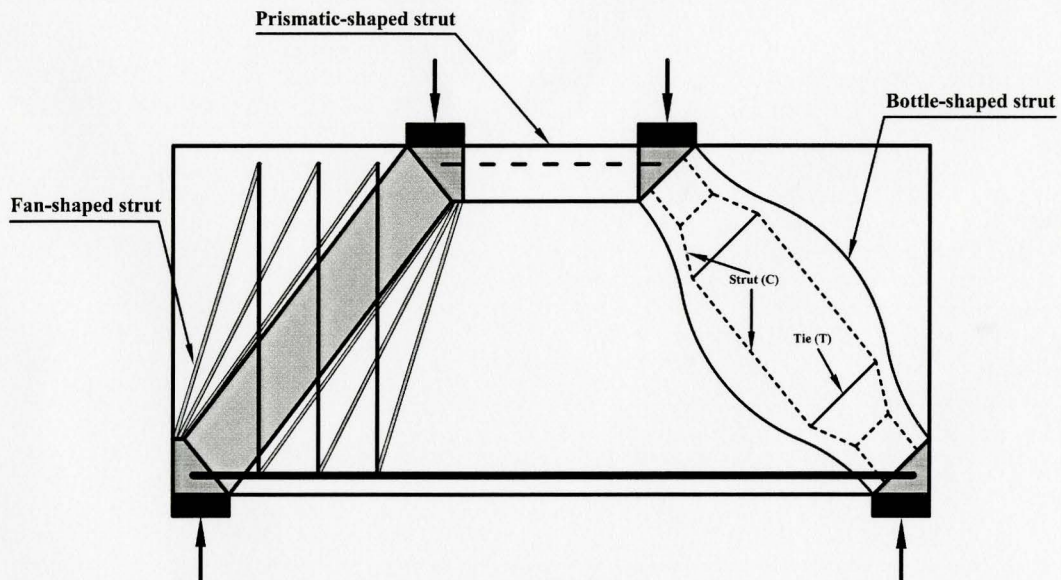


Figure 2.9: Strength of the beams failing in shear for different a/d ratio (adopted from Collins and Mitchell (1991), tested by Kani (1979))

2.2.4.2 Components of strut-and-tie model

Compression struts

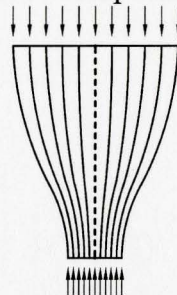
For the two-point loaded deep beams, as in Figure 2.10, there are two types of compression struts, namely the horizontal compression block which forms within the constant moment region and the inclined strut elements that develop in the web of the concrete section between the inclined shear cracks.



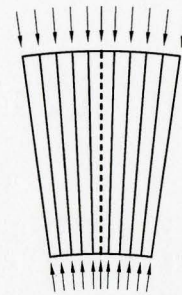
(a) Layout of compression struts



(b) Prismatic-shaped strut



(c) Bottle-shaped strut



(d) Fan-shaped strut

Figure 2.10: Geometric representation of various compression struts in deep beam

The geometry of the compression struts for a simply supported deep beam can be classified as prismatic, bottle-shaped or fan-shaped. The confinement of compression stresses within the constant moment region causes the top compressive stress block to have a prismatic geometry with a uniform cross section along its length, as can be seen in the Figure 2.10b. The width of the inclined compression strut on the other hand becomes wider at the mid-length due

to the dispersion of the principal compression stresses as they travel away from the concentrated load point (see Figure 2.10c). The dispersed compression stresses form an angle to the axis of the strut and produce tension forces, as it could be seen in the bottle-shaped struts. A bottle-shaped strut results in the formation of diagonal cracks which tend to weaken the strut, and this phenomenon can be modeled by assuming a collection of small struts and ties as suggested by Schlaich et al. (1987) (see Figure 2.10a). As the length of the shear span decreases, the amount of dispersion diminishes thus less tension force is induced within the shear span. The fan-shaped strut is an idealization of such stress field with negligible curvature (see Figure 2.10d). This type of strut applies to deep beams with stirrups as vertical tension members, as indicated by Rogowsky and MacGregor (1986) (see Figure 2.10a).

The layout and boundaries of the compression struts were studied by Schlaich and Weischede (1982) and based on their findings they indicated that the orientation of the compression diagonals could vary within $\pm 15^\circ$ of the slope of the elastic compressive stress trajectories. In order to simplify the design procedure, however, the compressive struts are usually treated as straight truss members following the centerline of the compressive diagonals and are usually reinforced with orthogonal web reinforcement to control cracking along the strut.

The crushing of the struts could occur when the compressive stresses applied to the ends of the struts reach the effective compressive strength of the

strut, $f_{cu} = \nu f'_c$ where ν is referred to as the efficiency factor. The failure of struts leads to brittle shear failure of the member and should be avoided by applying a suitable efficiency factor in the design. Rogowsky et al. (1983) suggested the efficiency factor of 0.85 to be used for analyzing fan-shaped compression struts. Marti (1985) suggested that the cross sectional area and thus the strength of the struts are highly dependent on the details of their ends and the width of the loading plates. He recommended that the compressive stress in the strut be limited to $0.6f'_c$, while Ramirez and Breen (1991) recommended a limit of $2.5\sqrt{f'_c}$ (MPa), and Bergmeister et al. (1991) proposed the following equation to compute the stress limit:

$$f_{cu} = \left(0.5 + \frac{1.25}{\sqrt{f'_c}} \right) f'_c \quad \text{for} \quad 20 \leq f'_c \leq 80 \text{ MPa} \quad (2.16)$$

Schlaich et al. (1987), Alshegeir and Ramirez (1990) and MacGregor (1997) introduced various compressive stress limits which account for the stress conditions, the concrete confinement by reinforcements and the orientation of cracks surrounding the strut. Table 2.1 summarizes the effective compression stress limits proposed by these researchers. It should be noted that a portion of this table was adopted from the ASCE-ACI Committee 445 report on the shear design of concrete members (ACI-445 1998). The notation ν_2 in the table

represents the stress limit proposed by Bergmeister et al. (1991) (refer to Equation (2.16)).

Table 2.1 Effective stress limits in concrete struts

Proposed by	Effective stress limits	Concrete strut condition
Schlaich et al. (1987)	$0.8 f'_c$	Undisturbed and uniaxial state of compressive stress that may exist for prismatic struts
	$0.68 f'_c$	Tensile strain perpendicular to the axis of the strut may cause cracking parallel to the direction of compression stresses
	$0.51 f'_c$	Tensile strains causing skew cracks at skew angles to the strut's axis
Alshegeir and Ramirez (1990)	$0.85 f'_c$	Moderately confined diagonal struts going directly from point load to support with shear span to depth ratio less than 2
	$0.75 f'_c$	Struts forming arch mechanism
	$0.95 f'_c$	Undisturbed and highly stressed compression struts
MacGregor (1997)	$v_2 f'_c$	Uncracked uniaxially stressed struts or fields
	$v_2 (0.8) f'_c$	Struts cracked longitudinally in bulging compression fields with transverse reinforcement
	$v_2 (0.65) f'_c$	Struts cracked longitudinally in bulging compression fields without transverse reinforcement
	$v_2 (0.6) f'_c$	Struts in cracked zone with transverse tension from transverse reinforcement

An alternative approach for determining the compression stress limits was proposed by Vecchio and Collins (1986) which accounted for the strain compatibility of the struts and the strain softening effect of diagonally cracked concrete. Based on their procedure, the compressive strength, f_{2max} , must first be calculated and then incorporated in the following expression in order to find the required force capacity of the compressive strut, N_u .

$$N_u \leq \phi A_{cs} f_{2max} \tag{2.17}$$

where

$$f_{2max} = \frac{f'_c}{0.8 + 170\varepsilon_1} \leq 0.85f'_c \quad (2.18)$$

and

$$\varepsilon_1 = \varepsilon_x + (\varepsilon_x + 0.002) \cot^2 \theta_s \quad (2.19)$$

In the expressions above, the notation ϕ represents the strength reduction factor for axial compression, taken as 0.7 (ACI-445 1998); A_{cs} is the effective cross sectional area of the strut; ε_1 represent the principal tensile strain, which incorporates the strain conditions of the concrete and the reinforcement in the vicinity of the strut; ε_x is the tensile strain of the tie-reinforcement and is usually taken as the yield strain of the longitudinal steel rebar; the value 0.002 is the presumed principal compressive strain in the strut at failure and the θ_s represents the smallest angle between the longitudinal tie and the compressive strut.

If the strut is reinforced, the beneficial effect of the reinforcement is incorporated by adding a steel resisting component to Equation (2.17),

$$N_u \leq \phi \left(A_{cs} f_{2max} + A_{ss} f_y \right) \quad (2.20)$$

where A_{ss} and f_y , respectfully, represent the area and yield strength of the reinforcement used to enhance the performance of the strut with the cross-sectional area of A_{cs} .

It is noteworthy that the compressive stress limit provided by Vecchio and Collins (1986) is included in the Canadian Standard CSA–A232.3 (2004) and it is

claimed to provide a more realistic means for calculating the compressive limits in the struts in comparison with the other mentioned approaches.

The strength and performance of the strut is also influenced by the anchorage details and distribution of the tension ties. The effect of the arrangement of tension tie and the width of the bearing plate on the geometry of the compression strut will be shown later in this section.

Tension tie

Based on the strut-and-tie model selected, there could be more than just a single longitudinal tension tie element at the bottom of the structure (refer to Section 2.3). The horizontal tension tie element represents the longitudinal reinforcement along the bottom of the beam which anchors the arches and maintains equilibrium at the nodal zones. The yielding of longitudinal reinforcement causes a ductile behavior for the deep beams and could lead to flexural failure.

The tension force within the shear span that is produced by the dispersed compression stresses would have to be carried by evenly distributed transverse reinforcement. In the truss mechanism this is represented by a vertical tie element positioned at the center of the shear span (refer to Section 2.3.2). The presence of transverse reinforcement delays the extension of the inclined cracks, caused by

shear, and allows the beam to not only sustain the design load but also to respond in a ductile manner.

Once the force in the tension tie, N_{ut} , is determined from the statics of the selected STM, the required amount of reinforcement could be determined, as shown below

$$N_{ut} \leq \phi (A_s f_y) \quad (2.21)$$

where ϕ represent the strength reduction factor for axial tension taken as 0.9 (ACI-445 1998).

In the deep beam members the anchorage of the tension tie is of major concern. The relatively deep geometry of these members makes them susceptible to experiencing large in-plane forces. This would in turn severely stress the individual truss elements and thus special attention must be paid in selecting adequate anchorage for the tie elements to ensure the stability of the truss. It is important to design an anchorage that is capable of developing the required stress in the reinforcement at the inner face of the extended nodal zone to prevent premature failure due to loss of anchorage (see Figure 2.11).

The arrangement of longitudinal reinforcement must be selected in a way to avoid the crushing of nodal zones positioned above the bearings. This could be achieved by evenly distributing the longitudinal reinforcing bars over a height that could maintain the tie stresses below the nodal zone stress limit. In the other

words, the longitudinal reinforcement must be evenly distributed over an area of concrete equal to the tension tie force divided by the nodal stress limit.

Nodal zone

The intersection of the truss elements (i.e., compression strut and tension tie) is called node and is enclosed within a region called nodal zone. The tie and strut forces balance each other in these regions and thus generate a multi-axial state of stress at the nodal zones. The design of nodal zone is of particular importance and has to be carefully detailed in order to balance all the oncoming forces of struts and ties without crushing the nodal concrete. The compressive strength of the nodal zone is influenced by the level of confinement provided by the reaction forces and the transverse reinforcements as well as the tensile straining from intersecting tension ties.

The characteristics of the nodal zones can be categorized into three groups, based on their different straining and confinement conditions (See Figure 2.11). Nodal zones bounded by two compression struts and one tension tie are designated as CCT, nodal zones bounded by a compression strut on one side and tension ties on the other sides are called CTT, and nodal zones bounded by compression struts on all sides are termed CCC, as illustrated in Figure 2.11a, b and c, respectively.

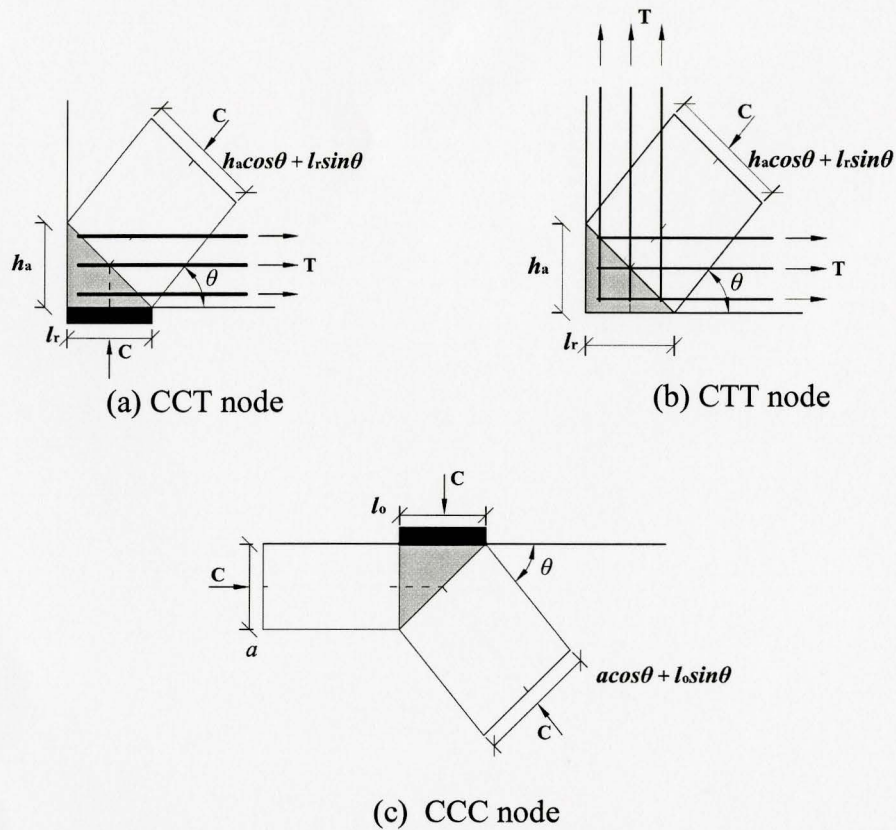


Figure 2.11 Typical types of nodal zones in strut and tie models for deep beams

The crushing of a nodal zone could cause premature bearing failure which is brittle and has to be avoided by making sure that the nodal zone is large enough to maintain the stresses below permissible limits. This could be achieved by selecting an adequate size for the bearing plates and also by distributing the bottom reinforcement over a larger area.

Collins and Mitchell (1986) have specified stress limits for the nodal zones in terms of the strength reduction factor, ϕ , and the same limits are included in the Canadian Standard CSA-A23.3 According to these investigators, the stress

limit for CCC, CCT and CTT nodal zone are $0.85\phi f'_c$, $0.75\phi f'_c$, $0.6\phi f'_c$, respectively Marti (1985) suggested that the nodal zones be treated as a hydrostatic region with a maximum capacity of $0.6f'_c$. Jirsa et al. (1991) recommended a limit of $0.8f'_c$ for the CCT and CTT nodal zones.

Schlaich et al. (1987), Bergmeister et al. (1991) and MacGregor (1997) each proposed values for the effective stress limits of various nodal zones. Table 2.2 summarizes the effective stress limits proposed by these investigators. Note that a portion of this table was adopted from the ASCE-ACI Committee 445 report on the shear design of concrete members (ACI-445 1998).

Table 2.2. Effective stress limits of nodal zones

Proposed by	Effective stress limits	Concrete strut condition
Schlaich et al. (1987)	$0.85 f'_c$	Nodes where only compression struts meet
	$0.68 f'_c$	Nodes where reinforcement is anchored in/or crossing the node
Bergmeister et al. (1991)	$0.8 f'_c$ for $f'_c \leq 30$ MPa $(0.9 - 0.25 f'_c / 70) f'_c$ for $30 < f'_c \leq 70$ MPa	Unconfined nodes without bearing plates
	$0.65 f'_c$ for $f'_c \geq 70$ MPa	
	$v_2 f'_c (A/A_b)^{0.5}$ $+ \alpha (A_{core} / A_b) f_{lat} (1 - s/d)^2 \leq 2.5 f'_c$	Confined nodes
	$v_2 f'_c (A/A_b)^{0.5}$	Unconfined nodes with bearing plates
	$2.5 f'_c$	Triaxially confined nodes
MacGregor (1997)	$v_2 f'_c$	Nodes bounded by compressive struts and bearing areas
	$v_2 (0.85) f'_c$	Nodes anchoring one tension tie
	$v_2 (0.75) f'_c$	Nodes anchoring one tension tie in more than one direction

In Table 2.2 the symbols A , A_b , A_s , A_{core} are the area of confined concrete, bearing plate, one leg of confining reinforcement, and confined strut, respectively; $f_{lat} = (2f_y A_s / ds)$ is the lateral pressure; s represents the pitch or spacing of confining reinforcement; d is the diameter of confined core; $\alpha = 4$ for spiral confinement, 2 for square closed hoop confinement anchored with longitudinal reinforcement and 1 for square closed hoop confinement without longitudinal reinforcement anchorage.

2.2.4.3 Current North American code provisions for strut-and-tie modeling

As it can be noted from the previous discussion there have been many studies over the past few decades to accurately predict the performance of deep beams subjected to in-plane loading. However, due to the complex influence of D-regions on the performance of these structural elements, there has not emerged a unified design model that could accurately predict their ultimate behaviour.

The major factors that influence the design of STM for deep beams consist of the strength, layout and the anchorage of the struts and ties, shape and strength of the compression struts, arrangement and strength of the nodal zones. Therefore, adequate detailing of these components is required in order to generate a sound STM design.

The North American design codes recommend the use of STM for designing disturbed regions such as deep beams. However, each design standard takes a different approach in detailing the STM components, as described below.

The American Concrete Institute (ACI) introduced STM provisions in the year 2002. Reineck (2002) argues that the foundation of the STM provisions in the American code is mainly based on the information and provisions of European design codes. Appendix A of the ACI 318-08 contains the provisions for the use of STM.

All references to the ACI code in the text below pertain to the latest edition of this code (ACI 318-08), where a deep beam is defined as a beam having a clear span-to-overall depth ratio not exceeding four or shear span to depth ratio not exceeding two, and being loaded from one face and supported on the opposite face. The design procedure of the STM is based on the philosophy that the permissible strength in each component (i.e., struts, ties, and nodal zones) has to be limited to the product of the nominal strength in the component and the strength reduction factor. The following condition could be found in Section A.2.6.

$$F_u \leq \phi F_n \quad (2.22)$$

where F_u represents the force in each component, caused by the applied load; F_n denotes the nominal strength of each component; and ϕ is the strength reduction

factor taken as 0.75 for shear (ACI 318, 2008). The nominal capacity is calculated based on the effective strength of each component.

With reference to the Appendix A of the ACI code, the normal compressive strength of an unreinforced strut, F_{ns} , can be calculated based on Equation (A-2) of Section A.3.1 as follows:

$$F_{ns} = f_{cu} A_{cs} \quad (2.23)$$

where A_{cs} is the cross-sectional area of compressive strut and f_{cu} is the effective compressive strength of the concrete in the strut, which can be determined in accordance with Equation (A-3) of Section A.3.2 as:

$$f_{cu} = 0.85 \beta_s f'_c \quad (2.24)$$

where f'_c is the concrete compressive strength and β_s is the strut efficiency factor based on the type of the strut. For the rectangular stress block within the constant moment region (prismatic-shaped strut) the efficiency factor is taken as 1. For the inclined compression struts (usually treated as bottle-shaped strut) the efficiency factor depends on the presence of reinforcement within the strut. In the bottle-shaped strut as the compression spreads out from the support tension forces develop (see Figure 2.10), which lead to inclined crack formation once they exceed the tensile strength of concrete. Without any reinforcement, the strut may split and cause brittle failure. The efficiency factor is taken as 0.6λ if the strut is not crossed by layer of reinforcement, where the factor λ accounts for the concrete

density and is equal to 1 for normal-weight concrete. If the strut meets the minimum reinforcement criterion (Equation (A-4) in Section A.3.3) as shown below, the efficiency factor can be taken as 0.75.

$$0.003 \leq \sum \frac{A_{si}}{bs_i} \sin \alpha_i \quad (2.25)$$

where A_{si} and s_i represent the area and the spacing of reinforcing bars in the i -th layer crossing the strut; α_i is the angle between the axis of the strut and the reinforcement bar in the i -th layer; and b is the width of the strut normal to the plane of the reinforcement bars (web thickness).

Based on Section A.3.5, compression reinforcement could be used to enhance the performance of the strut. Compression reinforcement should be positioned parallel to the axis of the strut and properly anchored near the nodal zones. Equation (A-5) of Section A.3.5 specifies the strength of the longitudinally reinforced strut as:

$$F_{ns} = f_{cu} A_{cs} + A'_s f'_s \quad (2.26)$$

where f'_s is the stress in the compression reinforcement (can be taken as f_y for grades 280 and 420); and A'_s represent the area of the compression reinforcement.

Appendix A permits the use of bottle-shaped struts without the minimum web reinforcement when adequate shear reinforcement is used in accordance with Clause 11.7.4 and 11.7.5. It is noteworthy that without having adequate transverse reinforcement (along the shear-span of the deep beam) the diagonal tension cracks

can grow along the axis of the strut un-impeded. Furthermore, due to formation of splitting diagonal cracks, the bottle-shaped strut loses its ability to maintain equilibrium and could lead to catastrophic failure at elevated loads.

The normal strength of a tie, F_{nt} , can be calculated based on Equation (A-6) of Section A.4.1 as follows:

$$F_{nt} = A_s f_y \quad (2.27)$$

The symbol A_s represents the area of reinforcement in the tension tie. It is stated in Section A.4.3.2 that the tie force should be developed where the centroid of the longitudinal reinforcement leaves the extended nodal zone, and should be anchored in accordance with Section 12.13 of the code.

The normal compressive strength of the nodal zone, F_{nm} , can be found based on Equation (A-7) of Section A.5.1, as follows:

$$F_{nm} = f_{cu} A_{nz} \quad (2.28)$$

where A_{nz} is the area of the face of the nodal zone subjected to loading and f_{cu} is the effective compressive strength of the concrete in the nodal zone and can be determined using Equation (A-8) of Section A.5.2 as follows:

$$f_{cu} = 0.85 \beta_n f'_c \quad (2.29)$$

where β_n is a nodal efficiency factor and is dependent on the elements that intersect to form the node. The nodal efficiency factor is taken as 1 for CCC node, 0.8 for CCT node and 0.6 for CTT node. The width of each face of the nodal zone

should be selected in a way that it does not restrict the strength in other components of the STM. It is evident that at the intersection of the strut and nodal zone, whichever component has the lower efficiency factor, β , would control the design at that interface.

Appendix A also provides a restriction on the minimum angle between the axes of any strut and any tie entering a common node. A minimum angle of 25° is specified to eliminate the reduction in the capacity of the strut as it approaches the orientation of the tie.

The Canadian standard CSA A23.3, like the ACI code, places limits on the allowable stresses in each component of the STM. This standard was the first design code to employ STM in 1984, based on the early investigation of Vecchio and Collins (1982) on reinforced concrete panels subjected to in-plane shear. The deep beam design provisions have remained practically intact over the last two cycles of the standard over the past two decades.

Based on Clause 10.7.1 of the CSA A23.3, deep flexural members are identified as flexural members that have a clear span less than twice the overall depth. Furthermore it has been outlined by the provision to account for the non-linear strain distribution and lateral buckling of such members, while providing adequate anchorage for the longitudinal reinforcement at the nodal zones. This provision permits the use of the STM as the suitable procedure for the design of

deep flexural members. In the latest version of the standard, CSA A23.3-04, Section 11.4 contains the provisions for the use of STM.

Clause 11.4.2.1 suggests that the width of the unreinforced compression strut has to be large enough to ensure that the ultimate compressive force in the strut does not exceed $\phi_c f_{cu} A_{cs}$. The symbol ϕ_c is the resisting factor of concrete (taken as 0.65); A_{cs} is the cross sectional area of the strut; and f_{cu} is the effective compressive strength of the diagonally cracked concrete which can be calculated following Equation (11-22) of the CSA code as follows:

$$f_{cu} = \frac{f'_c}{0.8 + 170\varepsilon_1} \leq 0.85f'_c \quad (2.30)$$

where ε_1 represents the principal tensile strain in cracked concrete and can be found using the Equation (11-23) of the CSA code as:

$$\varepsilon_1 = \varepsilon_x + (\varepsilon_x + 0.002)\cot^2\theta_s \quad (2.31)$$

The θ_s is the smallest angle between the tension tie having the tensile strain of ε_x and the adjoining compressive strut.

Clause 11.4.2.4 provides guideline for using compression reinforcement to enhance the compression capacity of the diagonal strut. It is suggested to place compression reinforcements parallel to the strut and apply adequate reinforcement to develop its yield strength in compression. Furthermore, it is recommended to use adequate amount of transverse reinforcement in order to enclose the compression reinforcement in the struts. Based on this clause, the force in the

compression strut must be limited to $\phi_c f_{cu} A_{cs} + \phi_s f_y A_{ss}$, where ϕ_s is the resisting factor of the reinforcement (taken as 0.85) and A_{ss} is the area of the compression reinforcement in the strut.

From the expressions above it is evident that the CSA approach for the permissible stresses in the strut is based on the Compression Field Theory (refer to section 2.2.3) rather than the reinforcement ratios used in the ACI code. The CSA code bases the strut strength efficiency on the average strain of the concrete at the location of a tie as opposed to the amount of reinforcement that crosses the inclined crack. The CSA code provides no limit on the angle θ_s in comparison to the ACI code.

Clause 11.4.3.1 suggests that reinforcement area in the tension tie should be large enough to ensure that the tension force in the tie does not exceed $\phi_s f_y A_s$, where A_s represents the area of reinforcement in the tension tie. It is stated in Clause 11.4.3.2 that the longitudinal reinforcement should be anchored in a way that it allows the reinforcement to resist the tie force at the point where the centroid of the longitudinal reinforcement crosses the inner edge of the inclined strut in accordance with Clause 12.

Clause 11.4.4.1 specifies the compressive stress limits for the different types of nodal zones. It is indicated that unless special confinement is provided,

the compressive stress in the node should not exceed $0.85\phi_c f'_c$ for CCC nodes; $0.75\phi_c f'_c$ for CCT nodes, and $0.65\phi_c f'_c$ for the CTT nodes.

It was noted that both the CSA and ACI codes incorporate the nonhydrostatic nodal configurations, which is based on the size of the bearing, inclination of the strut framing into the node and the location of the tie element. By comparing the provisions of the two codes, it is evident that in the CSA A23.3-04 nodal efficiency factors are directly multiplied by f'_c rather than $0.85 f'_c$ as specified in ACI 318-08.

In the Canadian code the use of bottle-shaped strut without minimum horizontal and vertical shear reinforcement is prohibited. Clause 11.4.5 specifies the minimum amount of orthogonal web reinforcement to be placed near each face of the deep beam member. It is indicated that the ratio of the reinforcement area to the gross concrete area should not be less than 0.002 in each direction, and the spacing of the reinforcement bars should not exceed 300mm.

It is worth mentioning that the AASHTO LRFD (1998) and CSA A23.3 present nearly identical provisions for detailing the STM components. The only noticeable difference is that the AASHTO LRFD requires slightly more crack control reinforcement than the CSA provisions. Based on the AASHTO LRFD, the required reinforcement ratio should be at least 0.003 in each direction.

In the Canadian standard the minimum requirement of web reinforcement, unlike ACI 318-08, does not affect strut efficiency factors and is required when STM provisions are used.

Section 11.7 of the ACI 318-08 permits the use of transverse reinforcement perpendicular to the flexural tension reinforcement, and therefore assumes the formation of truss mechanism (refer to Section 2.3.2 in this thesis). In contrast, as stated by Collins and Mitchell (1991) the CSA standard restricts the use of stirrups and assumes a single direct strut between the load point and the support reaction (refer to the Section 2.3.1 in this thesis).

2.3 Force Transfer Mechanism in Deep Beams

Many researches have attempted in the past to describe the load resisting behaviour of deep beams subjected to shear. Aoyama (1993) ascribed the load resisting mechanisms of deep beams to the arch and truss mechanisms (see Figure 2.12). Brown and Bayrak (2008) suggested that any mechanism could be used as long as the selected model satisfies equilibrium and the appropriate constitutive relationships. Therefore, when applying STM for the design of deep beams, the selection of an adequate truss model is highly subjective and is based on the expectations of the designer from the member. Brown and Bayrak (2008) managed to determine the main load carrying mechanism in deep beams, with a/d less than 2, through analyses based on strain energy. They indicated that the main

parameters that could alter the shear resistance mechanism between the two models are the transverse reinforcement ratio and the shear span-to-depth ratio. They also suggested that when transverse reinforcement is present in a deep beam, a more comprehensive truss mechanism must be adopted, such as the ones with vertical tie elements (Figure 2.12b)

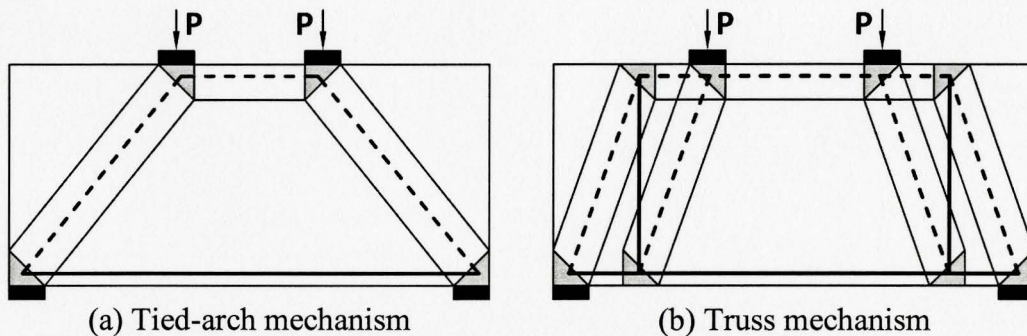


Figure 2.12. Strut-and-tie models used for deep beams

The influence of the amount, distribution and anchorage of reinforcement on the behaviour of deep beam was studied by Rogowsky and MacGregor (1986) as they tested a series of simply supported and continuous deep beams with different reinforcement detailing. Based on their research, it was concluded that beams without stirrups approached tied-arch action at failure, which was brittle and occurred regardless of the amount of horizontal web reinforcements present. In contrast, beams with large amount of stirrups failed in a ductile and controlled manner

Collins and Mitchell (1991) argued that the slenderness ratio of a deep beam can significantly affect its strength and alter its load transfer characteristics,

as shown in Figure 2.9. Based on the experimental study carried out on a series of longitudinally reinforced concrete beams by Kani (1979), it is evident that the shear strength of simply supported deep beams loaded with two point loads changes with their a/d value. It was observed that for the beams with a/d less than 2.5 the load was resisted through formation of tied-arch mechanism and that the resistance reduced rapidly as a/d increased.

In order to select an adequate design model for deep beams, one would have to clearly identify the load transfer mechanism and understand the significance of the reinforcement in strengthening the components of that mechanism. The common shear resistance mechanisms used to explain the behaviour of deep beams subjected to in-plane loading, as well as the modes of failure of deep beams, are described in the following sections.

2.3.1 Tied arch mechanism

This mechanism applies to deep beams with shear span-to-depth ratio of one or smaller. For such beams the load transfer mechanism is via formation of two diagonal struts extended from the position of applied loads to the supports and a horizontal tie which anchors the diagonal struts as shown in Figure 2.12 (a).

2.3.2 Truss mechanism

This type of mechanism, also known as vertical truss mechanism, represents the shear resistance of deep beams with shear span-to-depth ratio of two or greater. This mechanism consists of the same elements as arch mechanism with the addition of vertical tie elements, as can be seen in Figure 2.12 (b). The vertical elements represent the tension tie within the shear-span of the beam which is essentially a band of vertical stirrups. The top chord represents the centroid of compression stress, and the bottom chord corresponds to the centroid of the longitudinal reinforcement.

2.3.3 Modes of failure

The common modes of failure for simply supported deep beams subjected to two-point loading could be classified as flexural, shear, bearing and anchorage failure.

Flexural failure could occur due to formation of wide diagonal cracks which originate from the soffit around the mid-span and propagate to almost the full effective height of the beam with increasing load. Often this would lead to inelastic yielding and final fracture of the longitudinal reinforcement and produces a high energy release at failure. However, as it has been observed in laboratory tests, in rare circumstances the propagation of critical flexural crack could lead to crushing of compression block within the constant moment region of

the beam. Moreover, this type of behaviour will occur when the flexural capacity is attained. The flexural failure is preferable to other types of failure since it permits a ductile response and allows the structure to reach its ultimate flexural capacity.

Shear failure is usually due to widening of a series of diagonal cracks and crushing of the concrete between them and is highly dependent upon the a/d ratio, the amount and distribution of transverse reinforcement within the shear-span and the f'_c of concrete. The critical diagonal shear cracks usually originate from the inner face of the supports and propagate diagonally towards the inner edge of the loading plates. Shear failure may be recognized by three brittle modes of failure as identified by Kong (1990). The first mode of shear failure is referred to as diagonal-splitting and could be found when the critical inclined cracks split the beam over its full depth, without crushing the concrete in the web. The second mode of shear failure is referred to as diagonal-compression and is due to crushing of the concrete in the strut between the parallel diagonal cracks which usually form at elevated loads. The third mode of shear failure is observed when the diagonal crack penetrates the compressive zone directly under the concentrated load and causes the crushing of the nodal zone.

The presence of high compressive stresses in the zones over the supports and under the concentrated loads could cause local concrete crushing at elevated loads. This type of failure is called bearing failure which is a brittle premature

type of failure and tends to significantly diminish the ultimate capacity of the section. Bearing failure is likely to occur in beams with low compressive strength and high a/d ratio.

Anchorage failure is also a premature failure and has to be prevented by adequately detailing the tie reinforcement and making sure that the reinforcement can develop the tie force at the critical sections.

2.4 Brief Review of the Behaviour of FRP Bars

The use of FRP reinforcement as a promising solution to the corrosion problem of the traditional steel reinforcement has provided the need to examine its behaviour as primary reinforcement in structural elements. The FRP reinforcements are nonmagnetic and therefore eliminate problems caused by electromagnetic interference of steel. On the other hand, for FRP reinforcement bending in the field is not allowed, and it can not be welded to other reinforcing elements. The nonductile behavior of FRP reinforcement restricts its application in situations where ductility and inelastic energy dissipation are essential. FRP reinforcing bars have significantly higher ultimate strength but lower elastic modulus than steel rebars. The properties of a FRP bar are highly dependent on the type of fibres and their volume fractions, therefore, its strength and elastic modulus cannot be related to the properties of its constituent fibres only.

Generally speaking, however, for rebars of the same size, existing FRP bars have higher strength and lower elastic modulus than a similar size steel bar.

Many countries such as Canada, United States, Japan and some European countries have already employed FRP reinforcement in the construction of new bridge decks and superstructures exposed to deicing salts and aggressive environmental conditions due to their high tensile strength and noncorrosive characteristics.

The differences between the material characteristics of FRP and steel reinforcement necessitate a change in the design philosophy of concrete structures involving FRP reinforcement. The effect of FRP flexural and shear reinforcement on the load carrying capacity of slender reinforced concrete members has been investigated by many researchers in the past couple of decades and the results of their work have been implemented in the design provisions, standards and guidelines dealing with concrete members reinforced with FRP composites (ACI 440.1R, 2001). However, to the writer's knowledge, no research has been reported on the behaviour of FRP reinforced deep beams, and this topic is not dealt with neither in the CSA standard S806 nor the ACI Committee 440 guidelines.

The FRP products are composite materials consisting of reinforcing fibres embedded in a polymeric resin matrix. The commonly used reinforcing fibre materials are carbon, glass and aramid which are used to fabricate composite

laminates and rods termed CFRP, GFRP and AFRP, respectively. The fibers are characterized as linearly elastic and brittle materials and recognized as the main load resisting component of the composite material with strength usually higher than the resin matrix. The efficiency of the fibres depends on their cross sectional shape, length and chemical composition. The performance of the composite material depends on the type, orientation and volumetric ratio of fibres, type of resin and the manufacturing process (ACI 440.1R, 2001).

The FRP products have anisotropic characteristics with high tensile strength in the direction of reinforcing fibres and relatively small resistance in direction normal to the orientation of fibres. FRP reinforcement is usually fabricated in the form of bars, grids, sheets, fabrics and cables. For the purpose of this research, it was decided to study the performance of CFRP reinforcing bars and grids as the main longitudinal and transverse reinforcements on the load resisting behaviour of deep beams. The selection of the CFRP over other FRP composite materials was based on their superior fatigue characteristics along with their high ultimate strength, good durability and high elastic modulus.

The carbon fibres are an aggregate of imperfect fine graphite crystals and are obtained by heating organic precursor materials containing carbon, such as coal pitch, polyacrylonitrile (PAN) and rayon in an inert environment (Machida, 1993). The characteristics of carbon fibres are based on the composition and orientation of the graphite crystals. The CFRP reinforcing bars consist of

primarily longitudinal unidirectional fibers bounded by a rigid polymer resin material and their shear resistance and dowel action as well as their bond performance are affected by the anisotropic nature of the FRP bars. The CFRP bars are generally produced in the forms of square and round cross sections and the bonding mechanism is usually provided by means of sand coating, exterior wound fibres and separately formed surface deformations. The CFRP reinforcement does not exhibit yielding and its stress-strain relationship is linearly elastic until failure (refer to Figure 3.8, Section 3.2.3). Consequently, in the structure reinforced with FRP, limited load redistribution and non-linearity can be expected. Generally speaking, all FRP materials have very high strength to stiffness ratio compared to steel reinforcement, consequently in ordinary reinforced concrete their full strength cannot be utilized in the design. This provides an extra margin of safety, which could partially compensate for their lack of ductility.

In Canada there are quite a few demonstration projects where CFRP reinforcement has been used, such as in Calgary (Crowchild Trail Bridge), Headingley, Manitoba (Taylor Bridge), Sherbrooke (Joffre Bridge), as identified by Tennyson et al. (2001). In the Crowchild Trail Bridge, CFRP grid reinforcement (NEFMAC) was used to reinforce the side barriers and was found to be effective in resisting the structural loads. In Taylor Bridge, four girders were prestressed with CFRP cables and CFRP stirrups were used as shear

reinforcements. Taylor Bridge is the first demonstration of the use of CFRP stirrup as shear reinforcement in bridge girders. In the Joffre Bridge the NEFMAC product was used to reinforce the concrete deck slab and CFRP bars were used as reinforcement for the concrete sidewalk and traffic barriers.

CFRP reinforcement bars and grids have a much smaller density in comparison with steel reinforcement, and usually weigh one-sixth to one-fourth of steel; depending on the size of the reinforcement. The reduced weight provides ease of transportation and handling and speed in construction without loss in performance.

In the production of CFRP NEFMAC reinforcement the carbon fibres are impregnated with an appropriate resin system, such as polyester, vinylester or epoxy (Karbhari 1998). The presence of nodes at the intersections of orthogonal ribs in NEFMAC grids provides very good anchorage and mechanical interlock in the concrete, which allow for effective stress transfer without loss of bond. NEFMAC grids are available with various grid spacings and cross sectional areas. The details of the NEFMAC reinforcement used in this study can be found in Section 3.2.3.2.

The low strength of resin matrix has limited influence on the strength of the composite material, while the type and volume ratio of the fibre has the predominant effect on the ultimate tensile capacity of the reinforcement. The fibre

content in CFRP NEFMAC grid and CFRP Isorod reinforcing bar used in the current study is about 40% and 65%, respectively (Karbhari 1998).

CFRP bar can be found with different tensile strength and surface deformation. The CFRP bars are anisotropic and are often manufactured using pultrusion, braiding and weaving techniques. For the purpose of this study, it was decided to use CFRP Isorod reinforcing bar with the sand coated surface texture and high tensile strength, as described in Section 3.2.3.1. The Isorod reinforcement is fabricated as circular rod and is pultruded using unidirectional continuous carbon fibers. The sand grains are adhered to the surface of the reinforcing bars by applying layers of rigid and soft epoxy solutions and thermoplastic resins (Machida 1993). The Isorod reinforcement has a coefficient of thermal expansion of $-2.5 \times 10^{-6}/^{\circ}\text{C}$ in longitudinal direction and $38 \times 10^{-6}/^{\circ}\text{C}$ in transverse direction (Pultrall Inc. 2007). The negative coefficient indicates that the material contracts in high temperature and expands in low temperature.

Based on the studies carried out by Maruyama et al. (1989) on the bond performance of the sand coated CFRP reinforcement, it was discovered that the sand surface texture provides good bond with the surrounding concrete when the stress in the bar is small at the initial stage of the loading. However, as the load is increased and the bar reaches its ultimate limit, the interface between the sand grains and the bar detaches suddenly and cause interlaminar shear failure. For this type of failure although there exists a good bond between the sand particles and

the surrounding concrete, it is still characterized as an anchorage failure and could be avoided by providing additional development length or by enhancing the strength of the epoxy used to bond the sand to the carbon fibres. By preventing anchorage failure, it would be possible to make use of the total strength in the reinforcement.

Due to lack of standard specifications for the fabrication of FRP bars, a wide variety of surface texture and deformation are currently being used to improve their bond characteristics with the surrounding concrete. Benmokran et al. (2002) studied the bond behavior of CFRP Isorod bars by performing a series of pullout bond test on 9.5 mm diameter sand coated bar with their ends embedded in a concrete block with specified embedment length. The concrete that was used for this experiment was a normal strength concrete, with compressive strength of 34 MPa. Based on their experimental results the bar tensile failure occurred for the samples with development length equal or greater than 200 mm, or $(20d_b)$. Hence, they concluded that for a normal strength concrete the minimum development length of $20d_b$, or 190 mm, was sufficient to prevent the pullout failure for the 9.5 mm sand coated CFRP Isorod.

The minimum development length of $20d_b$ could be easily compared with the specifications of the ACI guidelines and the CSA standards, for the same reinforcement and concrete conditions. Clause 11.1 of the ACI 440.1R (2001)

employs a more conservative approach for finding the straight development length (l_d) of FRP bars, as shown below:

$$l_d = \frac{d_b f_{fu}}{18.5} \quad (2.32)$$

where d_b is the bar diameter and f_{fu} is the ultimate strength in the bar. As can be seen from Equation (2.32), the development length approach in the ACI code depends solely on the diameter and strength of the reinforcement. By employing Equation (2.32) and assuming the ultimate tensile strength of 1536 MPa for the CFRP bars, as indicated by Benmokran et al. (2002), the development length would be equal to 788 mm which is equivalent to about $83d_b$.

Clause 9.3.3 of the CSA S806 (2002) provides a more refined expression for finding the straight development length as shown below:

$$l_d = 0.5k_1k_2k_3k_4k_5f_{fu}d_b/\sqrt{f'_c} \quad (2.33)$$

The k symbols in the expression above represent the modification factors and they are defined in Clause 9.3.4 of the CSA S806 standard. In Equation (2.33) the notation k_1 represents the bar location factor; k_2 is the concrete density factor; k_3 is the bar size factor; k_4 is the bar fibre factor and k_5 is the bar surface profile.

Based on Clause 9.3.4 of the CSA S806 the modification factors for the 9.5 mm diameter Isorod and 34 MPa strength concrete are as follows:

$$k_1 = 1$$

$$k_2 = 1$$

$k_3 = 0.8$	for	$A_b = 71 \text{ mm}^2 < 300 \text{ mm}^2$
$k_4 = 1$	for	CFRP reinforcing bar
$k_5 = 1$	for	Sand surface texture

Substituting the variables above in to the Equation (2.33) leads to a development length of 1001 mm which is equivalent to about $105d_b$. Based on the calculation above it seems that the CSA code employs a more conservative approach in finding the development length in comparison with the ACI guidelines. The development length requirement based on the CSA code is 5.25 times greater than that presented by Benmokran et al. (2002), and 1.25 times greater than the development length requirements of the ACI code. It should be noted that the pullout test results cannot be used directly to determine the development of rebars in members under flexure. This is because the strain gradient in flexural members tends to decrease the bond strength of rebars in comparison to their bond strength in pullout tests.

The issue of bond and anchorage of reinforcement is one of the main concerns in the design of deep beams because for the tie force to be fully developed, adequate anchorage must be provided for the main longitudinal reinforcement. In the case of FRP reinforcement the anchorage strength cannot be increased by providing end hooks, for bending of FRP can diminish its strength by up to 60% (CSA, 2002).

It should be pointed out that due to lack of shear design provision for FRP reinforced concrete deep beams, it was decided to design the CFRP reinforced beams based on the STM approach used for the conventional steel reinforcement. Hence all the deep beam specimens in this study were designed based on the same STM approach, considering the different development length and anchorage requirements. This made it possible to check the applicability of STM provisions for deep beams reinforced with FRP bars.

As stated in Section (2.2.4.3), the STM in the CSA code accounts for the reduced compressive strength of diagonally cracked concrete by considering the strain field in the diagonal struts. However, this condition can not be applied directly to FRP reinforced concrete, since the current provisions of the CSA A23.3 were derived using experimental data from tests on conventional steel reinforced concrete. Therefore, the current provisions are intimately linked to the yielding of reinforcement, a phenomenon which does not exist in FRP. Hence further research is required to explore the differences between the behaviour of steel reinforced and FRP reinforced concrete deep beams.

On the other hand, the STM provisions in the ACI 318 (2008) code specify compressive stress limits for the struts and the nodal zones and thus provide an alternative approach to the compatibility conditions used in the CSA standard. Moreover, the CSA standard only accounts for the arch action in deep beams and delays failure of struts by requiring minimum web reinforcement,

which may not be sufficient to prevent the diagonal-splitting shear failure in the beam. The ACI code, on the other hand, recognizes both truss and arch action in deep beams, therefore the designer is able to choose between the two approaches and construct the STM based on the model that can adequately explain the behaviour of the deep beams under consideration. As described in Section (2.2.4.3), when the STM is designed based on the truss mechanism, the presence of the vertical tie elements allows the designer to determine the amount of transverse reinforcement necessary to prevent diagonal-splitting of struts. This would in turn result in a more ductile response and shift the failure towards flexural failure, which results in high tensile stresses in the longitudinal bars and the need for their proper anchorage. Since this study is mainly concerned with the anchorage of CFRP bars in deep beams, efforts will be made to prevent premature failure of the other resisting elements such as the diagonal struts and the nodal zones. Applying the truss mechanism in designing the STM for the beam samples used in this study was found to be more appropriate for studying the performance of the CFRP bars attaining their ultimate strength in deep beams. Based on the discussion above it was decided to design the reinforced concrete deep beams in accordance with the STM provisions specified in the ACI 318 (2008).

In summary, the key points of concern in the current study are the identification of the proper method of design for CFRP reinforced deep beams and the performance of CFRP reinforcing bars as the main tie reinforcement, with

particular emphasis on their anchorage and the effect of their relatively large strain on the compressive strength of the diagonal concrete struts.

CHAPTER 3: EXPERIMENTAL PROGRAM

3.1 General

The main objectives of this research program are to investigate the influence of CFRP longitudinal reinforcement on the overall behaviour and the ultimate shear strength of reinforced concrete deep beams as well as to validate and/or improve the applicability of current design approaches for deep flexural members longitudinally reinforced with steel to beams reinforced with CFRP reinforcing bars. To fulfill the objectives of this research, an experimental program was conducted by testing seven reinforced concrete deep beams. The beams were designed and constructed in accordance with ACI 318 (2008), applying the strut-and-tie model introduced in this code.

The experimental program included two groups of simply supported deep beams, which were monotonically loaded up to failure under four-point bending. The first group comprised four large-scale reinforced deep beams having an effective span-to-depth ratio of one. The second group consisted of three large-scale reinforced deep beams with an effective span-to-depth ratio of two. In each group one specimen was reinforced with steel bars (control beam) and the remaining two identical specimens were reinforced using CFRP bars. The length of the beams varied, depending on the type of anchorage of the main longitudinal

reinforcement. The beams were constructed using normal-strength concrete. The test parameters were the reinforcement material and the span-to-depth ratio.

This chapter gives details about the test specimens, their fabrication, instrumentation, test setup, and the test procedure. The behavior and characteristics of the materials used to fabricate the deep beam specimens are described in detail in subsequent sections in this chapter.

3.2 Material Properties

The experimental program, involved the use of three materials. Concrete, reinforcing steel bars and welded-wire mesh, and carbon fibre reinforced polymers (CFRP) rebars and grids. Auxiliary tests were performed to determine the uniaxial strength and deformations of the concrete and of the steel reinforcement. The CFRP was not tested due to lack of proper testing equipment and the time-consuming procedures associated with the tensile test of NEFMAC grid and Isorod CFRP bars. To test FRP bars and grids, it is necessary to encapsulate the ends of the test coupons in epoxy-filled tubes which would be gripped by the chucks of the testing machine. This often requires elaborate preparations. It is important to note that in the design of the current test specimens it is envisaged that their failure will not be initiated by the rupture of the reinforcement.

3.2.1 Concrete

One batch of concrete was ordered from a ready mix plant (Lafarge Inc., Ontario, Canada). The concrete mix properties included type 10 cement, sand, maximum aggregate size of 10 mm and target concrete compression strength of 30 MPa. Upon arrival of the concrete truck a slump test was performed, and a 110 mm slump was measured. Twenty-three control concrete cylinders (150mm x 300mm) were cast and prepared for compression and splitting-tension tests. From these tests, the average compressive strength, f'_c , and modulus of rupture of concrete, f_r , were determined.

At the time of testing of each group of specimens, three cylinders were concurrently tested to find the compressive strength of concrete at that time. During the testing, the compression force was applied in small increments of 5 kips and the displacement between the designated Demec points was recorded using the Demec mechanical strain gauge. The maximum applied load was recorded and the maximum concrete compressive strength was calculated by dividing the force by the nominal cross-sectional area of the cylinder. The average of the three compressive strengths from the three repeat specimens included consideration of variation in material properties and random errors in the testing procedure. The detailed test results for these cylinders are given in Table C.1 to Table C.4 in Appendix C.

In addition, using displacement control, the stress-strain relationship of concrete in compression was obtained for each test cylinder. Figure 3.1 presents the setup used to test the cylinders under uniaxial compression and the condition of the cylinders before and after failure load was reached. It is important to point out that the testing machine was not able to apply the load in a manner that would allow it to capture the descending portion of the stress-strain curve despite the fact that displacement control was specified. On the other hand, the lack of capturing the descending branch will not cause any difficulty with respect to the analysis of the results. Figure 3.2 shows typical stress-strain curves of the three cylinders tested to measure the 28 day compressive strength of the concrete.

The average measured concrete compressive strength at the time of testing of the various specimens is given in Table 3.1. Note that beams with longitudinal steel reinforcement are designated as S1 or S2 while those with FRP reinforcement are denoted as F1 and F2. One can notice the strength gain with age by comparing the average compressive strength of F1 specimen and F2 specimens which were tested on average 25 days apart.

Splitting-tension test was conducted on five cylinders, 28 days after casting, using the universal testing machine in compression mode. Figure 3.3 shows the test setup used to perform the splitting tests, while the results are summarized in Table 3.2.

Note that the actual 28 day average compressive strength of 32.8 MPa is slightly higher than the specified strength of 30 MPa and the average splitting tensile strength of 3.30 MPa is approximately one-tenth of the average compressive strength, which is within the expected range.

Table 3 1 Average compressive cylinder strength of concrete for various specimens

Sample	Test type	Days after casting (Days)	Average strength (MPa)
S1-A	Compression test	121	32.80
F1-A/B	Compression test	151	33.71
S2	Compression test	163	34.37
F2-A/B	Compression test	176	34.95
S1-B	Compression test	182	35.38

Table 3.2. Compressive cylinder strength and splitting tensile strength of concrete at 28 days

Cylinder Number	Test type	Test Results (MPa)	Average strength (MPa)
Cylinder 1	Splitting test	3.4	3.3
Cylinder 2	Splitting test	2.85	
Cylinder 3	Splitting test	3.72	
Cylinder 4	Splitting test	2.9	
Cylinder 5	Splitting test	3.67	
Cylinder 6	Compression test	33.14	32.77
Cylinder 7	Compression test	31.78	
Cylinder 8	Compression test	33.38	

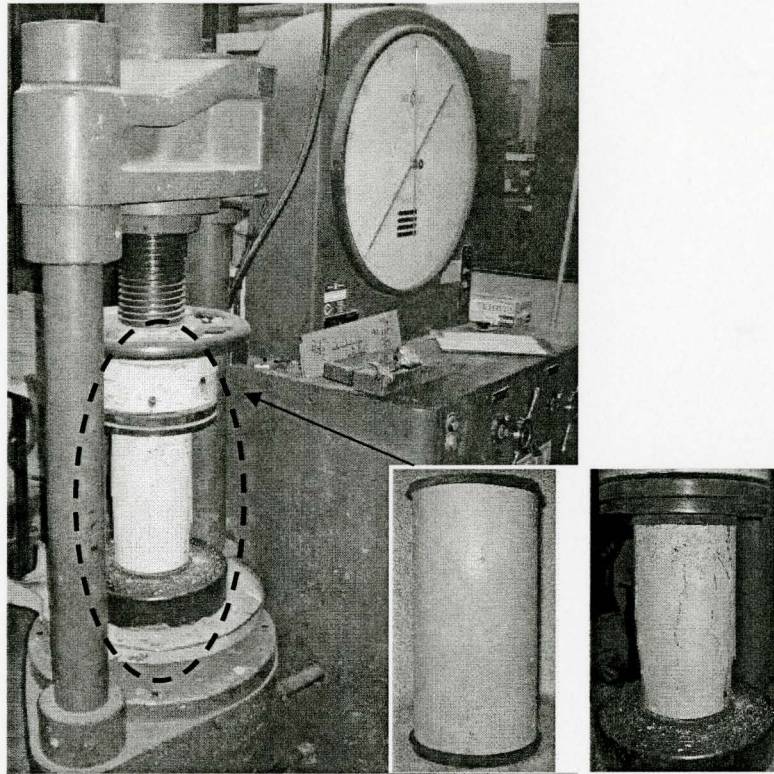


Figure 3 1 Uniaxial compression testing of the concrete cylinders

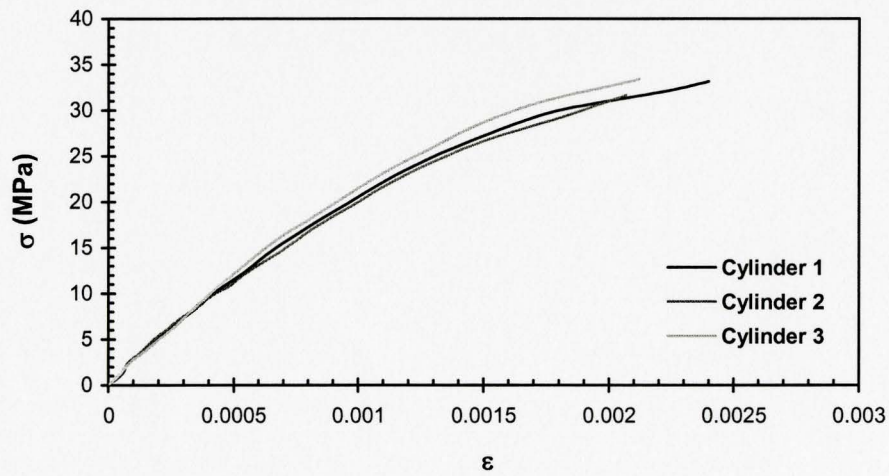


Figure 3.2. Stress-strain relationship of concrete in compression (28 days after casting)

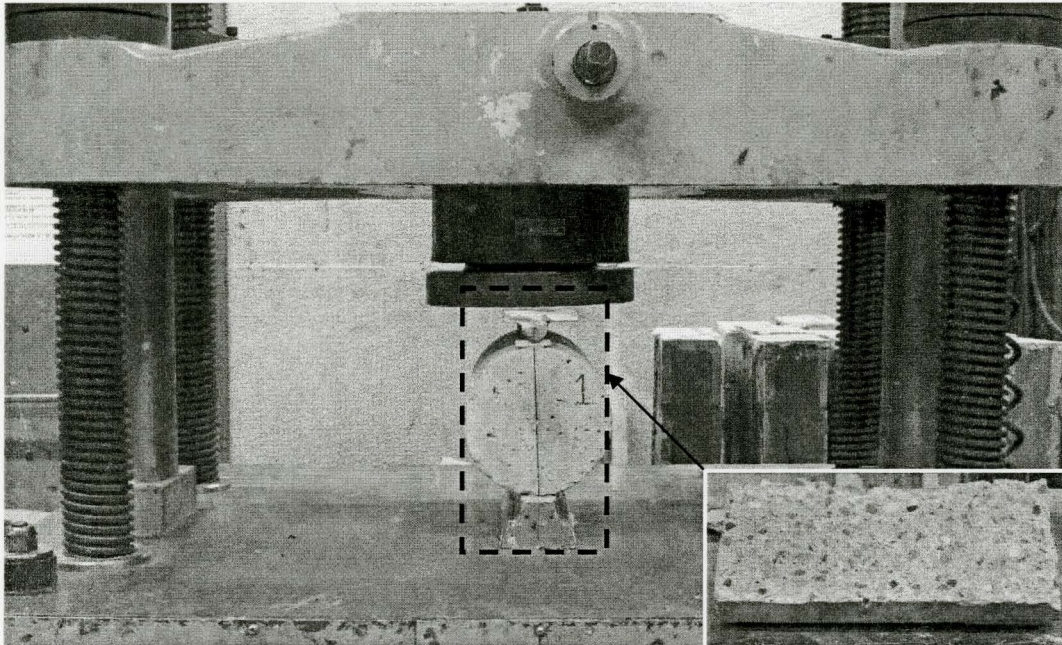


Figure 3.3 Splitting test of the concrete cylinders

3.2.2 Steel reinforcement

Deformed steel bars No. 10M and No. 15M were used as longitudinal and shear reinforcement, respectively, in the control beams while welded-wire mesh was used as skin reinforcement in all the test beams. The steel reinforcement used in constructing the beams was provided by Harris Rebar Inc., Ontario, Canada.

3.2.2.1 Reinforcing bar

The reinforcing steel used was Grade 400R hot-rolled deformed rebars. Coupons were ordered at the time of purchase and were tested to determine the steel yield stress and modulus of elasticity. The coupons were tested in tension using the universal testing machine in tension mode and the elongation in the

rebar was measured using an extensometer as shown in Figure 3.4. Six coupons were tested, three No.10 steel bars ($d_b = 11.3$ mm) and three No.15 bars ($d_b = 16$ mm), where d_b is the bar diameter. The test results for the No.10 and the No.15 bars are presented in Table A.5 and Table A.6, respectively, in Appendix A. The results were then compared with the manufacturer's specifications.

The stress-strain curves for the three No.10 and No.15 steel coupons are shown in the Figure 3.5 and 3.6, respectively. It can be seen from these figures that these bars do not have a defined yield point. Consequently, one may either use the 0.2% strain offset method, as in Figure 3.7, or the stress corresponding to the initiation of nonlinearity. Using the former method, the average yield stresses of the No.10 and No.15 bars, respectively, are 475 MPa and 464 MPa, and their corresponding elastic moduli are 196 GPa and 205 GPa. The preceding stress-strain curves are unexpected, despite the fact that the bars are made of medium strength low carbon steel, they lack a clear yield plateau.

Note that the tensile strength was calculated based on the nominal cross sectional area of 100 mm^2 for No.10 and 200 mm^2 for No.15 bar.

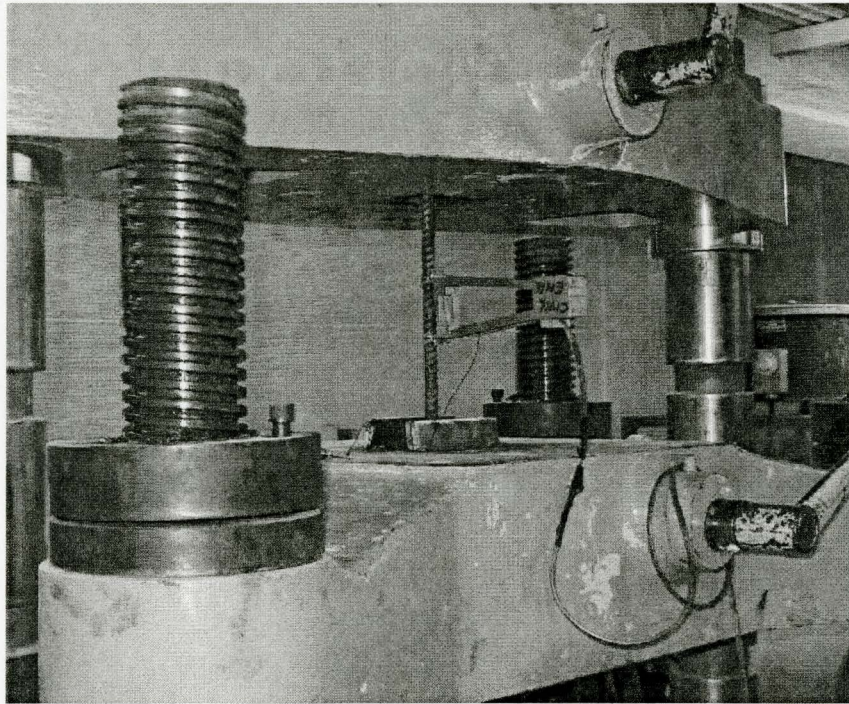


Figure 3.4: Tensile test of the steel bars

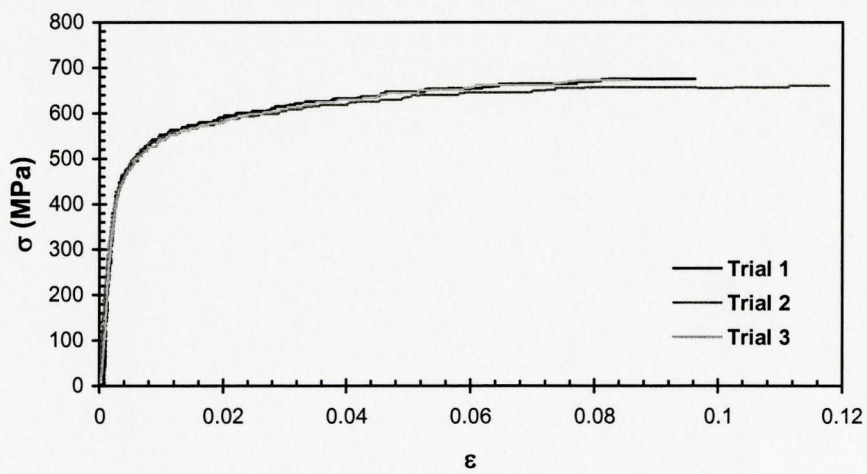


Figure 3.5 Stress-strain relationship for No.10 steel bar

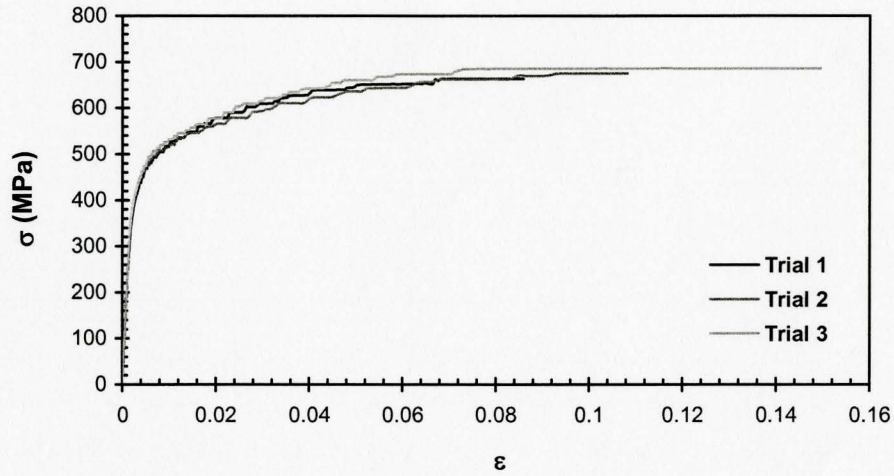


Figure 3.6: Stress-strain relationship for No.15 steel bar

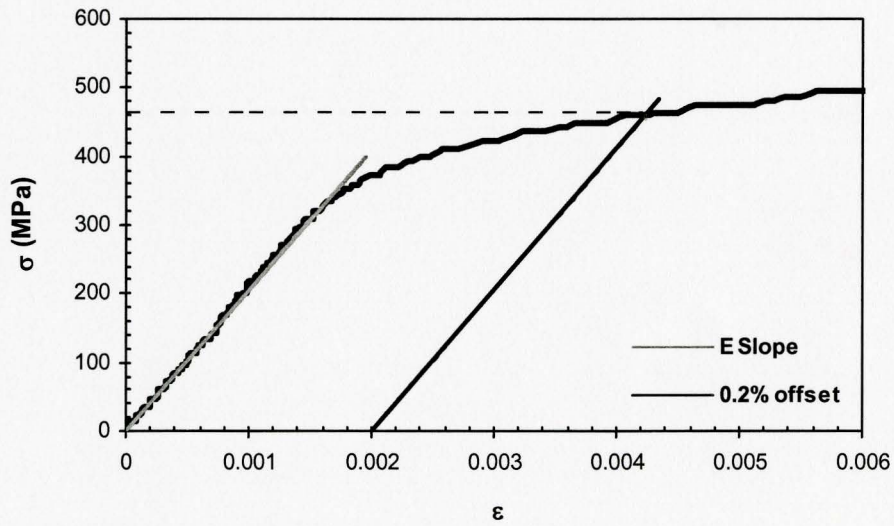


Figure 3.7: Determination of yield strength by the offset method

3.2.2.2 Welded-wire fabric

The welded-wire fabric was used as crack control or skin reinforcement for all the specimens. This reinforcement was placed near each of the two vertical faces of each beam and is intended to control the width of the cracks and to ensure a minimum level of ductility. The size of the steel mesh was selected based on the minimum requirements in accordance with the American standard ACI 318 (2008). The particular mesh used is designated as 102x102 MW25.8xMW25.8. Uniaxial tensile test was not performed on the mesh reinforcement due to the fact that it is a nominal reinforcement and is not supposed to significantly contribute to the strength of the beam specimens. However, the manufacturer's mill-test report indicates that the nominal yield strength of the welded-wire is 450 MPa and its elastic modulus is 200 GPa.

3.2.3 CFRP reinforcement

Due to time constraints and lack of proper grips for the universal testing machine, the tensile test was not performed on the CFRP reinforcement. Thus, manufacturer's recommended values were used to carryout the design. It is worth mentioning that for the purpose of this study, it is not expected that the CFRP reinforcement will rupture in tension due to their high ultimate tensile capacity.

3.2.3.1 Reinforcing bar

CFRP bars, known as Isorod, were used as the main reinforcement in the FRP reinforced deep beams. These bars are manufactured by Pultrall Inc., Quebec, Canada. According to the manufacturer, the bars are made of continuous longitudinal carbon-fibres embedded in a thermosetting vinylester resin using a pultrusion process. They have approximately 73% fibre content by volume and are sand-coated on the surface to improve their bond with concrete.

CFRP is a linear elastic material and its stress-strain behaviour is linear up to failure as it can be seen in Figure 3.8. The nominal diameter of the No.10 Isorod bar used in the current test beams is 9.5 mm. Figure 3.9 shows a typical Isorod and its surface texture.

The tensile property of the CFRP Isorod was adopted from the results of the tensile tests performed at the University of Sherbrooke by Benmokran et al. (2002). Their tests were conducted on 20 CFRP Isorod bar specimens with the same properties as the ones used in the present study. It is worth mentioning that the bars which were used to perform the tensile test were also manufactured by Pultrall Inc. Based on their findings, the tensile strength of CFRP Isorod bars is 1536 ± 61 MPa with the corresponding modulus of elasticity of 128 ± 5 GPa and an ultimate strain value of 1.2% (Benmokrane 2002). The manufacturer's recommended value for modulus of elasticity is 120 GPa and its ultimate tensile

strength is 1596 MPa (Pultrall Inc. 2008). These values were assumed to be correct and were used in the design of FRP reinforced deep beams.

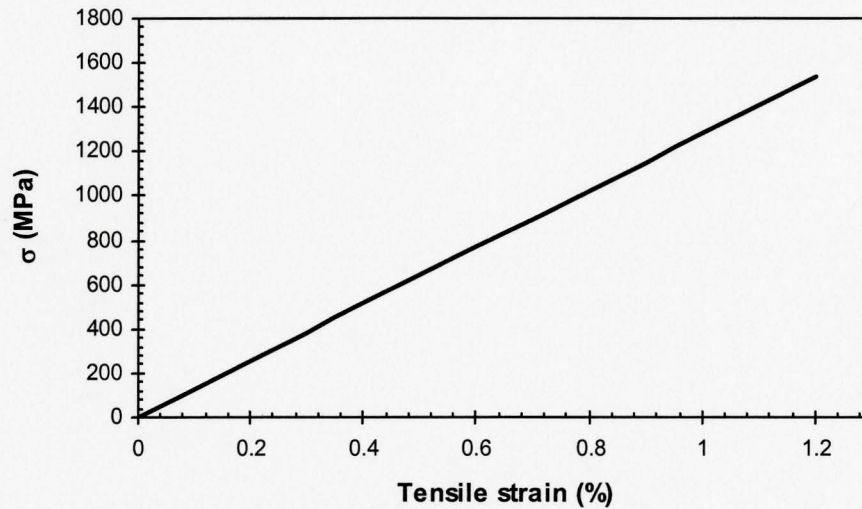


Figure 3.8. Typical stress-strain profile of the Isorod CFRP bars (adapted from Benmokrane et al. (2002))

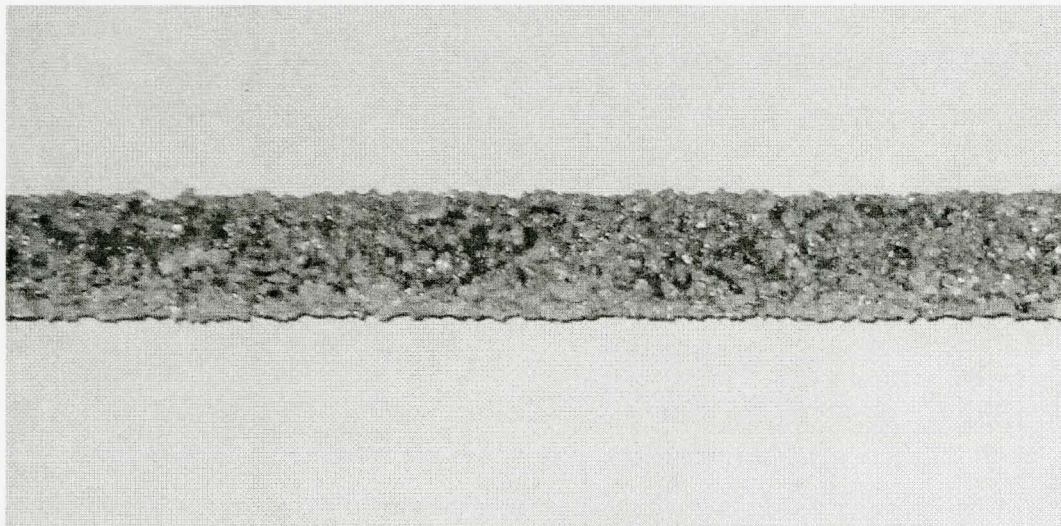


Figure 3.9. Typical surface texture of sand-coated CFRP Isorod

3.2.3.2 Reinforcing grid

NEFMAC CFRP reinforcing grids were used as shear reinforcement for the FRP reinforced deep beams. The grids were produced by AUTOCON Composites Inc., Ontario, Canada. The manufacturer's recommended value for modulus of elasticity is 98 GPa and its ultimate tensile strength is 1180 MPa (Autocon Inc. 1997). The NEFMAC grid used in this study is designated by the manufacturer as C16, with rib cross sectional area of 100mm^2 , and grid rib spacing of 100 mm in each of the two orthogonal directions. The grids are made of continuous pitch-based carbon fibers with tensile strength of 4800 MPa embedded in a vinylester resin. The bounded carbon laminates form an irregular cross-sectional shape which is not perfectly square (Karbhari 1998). The top and bottom surface of the grid ribs have a slightly deformed profile for improving their bond to concrete. Figure 3 10 shows that the NEFMAC CFRP reinforcement behaves linear elastic up to failure. Figure 3 11 shows a NEFMAC CFRP reinforcement that was trimmed off from the original grid using a normal carbide blade.

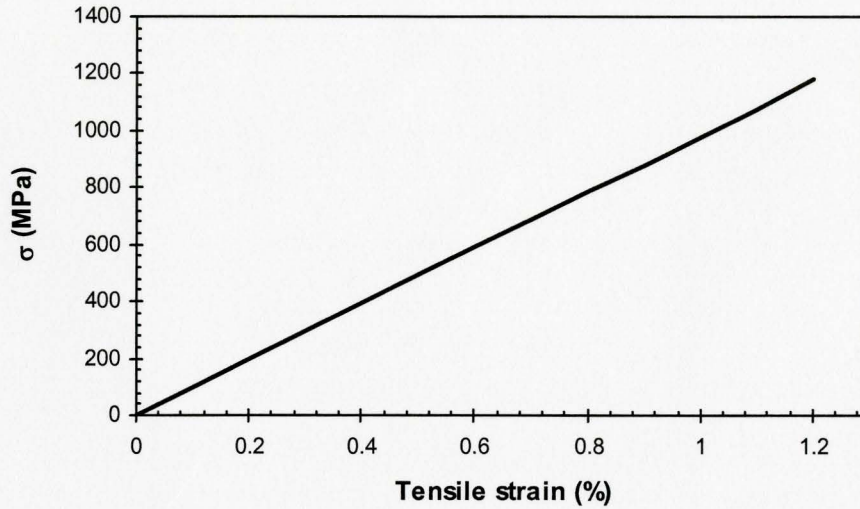


Figure 3.10: Typical stress-strain profile of the NEFMAC CFRP reinforcement (adapted from Benmokrane et al. (2002))

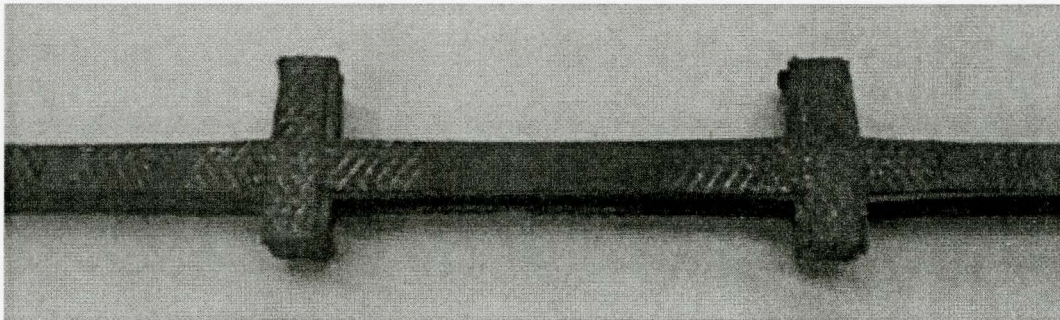


Figure 3.11 NEFMAC CFRP section cut off from the original reinforcement grid

3.3 Details of Test Specimens and Testing Procedure

To examine and better understand the behaviour of CFRP reinforced deep beams subjected to flexure and shear, an experimental program was carried out on concrete deep beams reinforced longitudinally and transversely with CFRP reinforcing elements. Companion beams reinforced with conventional steel

reinforcement were tested for comparing the behaviour of CFRP reinforced deep beams with that of the steel reinforced beams. A full description of the test specimens, test set-up, instrumentation and loading is provided in the following sections.

3.3.1 Test specimens

A total of seven beams were tested, three control beams reinforced with steel (S1-A/B and S2) and four CFRP reinforced beams (F1-A/B and F2-A/B). In addition to the type of reinforcement, the other test variable was the beam's span-to-depth ratio, which was either one or two. The beams with span-to-depth ratio of one and two are designated as group 1 and 2, respectively. For simplicity the steel reinforced beams are designated as S1 and S2 while the FRP reinforced beams are denoted as F1 and F2. In the case of the FRP reinforced beams and the small steel reinforced beam (S1), repeat specimens were fabricated, which are designated as A or B. For instance, F1-A and F1-B are repeat specimens with span-to-depth ratio of 1 and reinforced with CFRP.

All the specimens were made of normal strength concrete and they had the same rectangular cross-section (250 mm wide and 900 mm deep), while their span length, center-to-center of the supports, was either 900 mm or 1800 mm as indicated in Table 3.3. The bottom tension reinforcement was located at a constant 57 mm from the bottom surface of each beam. This resulted in an

effective depth, d , of 843 mm for all the beams, except for S2, where the centroid of the longitudinal reinforcement was at 818 mm. The effect of end anchorage of the longitudinal bars on the behaviour of deep beams was studied, using a 90-degree hook in the control specimens and a straight bar anchorage for the FRP reinforced beams. Straight anchorage was used in the case of FRP reinforced beams due to the fact that bending of FRP reduces its strength.

As described earlier in Section 3.2.2.2, a mesh of orthogonal web reinforcement was placed near each face in order to control the width of the cracks and the overall deflection and to ensure ductile failure. To prevent the vertical ribs of the mesh from transferring tension in the regions where stirrups are located, the vertical ribs in those regions were removed.

More explanation about the assemblage of the reinforcement cage could be found in Section 3.3.2.2. Figure 3.12 illustrates the overall shape and dimensions of the test specimens while complete data are given in Table 3.3 and 3.4. Table 3.5 gives the strength, rigidity and reinforcement ratio of the longitudinal and transverse reinforcements in the deep beam specimens. Figure 3.13 and 3.14 illustrate the resultant STM for each beam. Detailed design calculations are also provided in Appendix A.

Figures 3.15 to 3.18 schematically illustrate the position of the main reinforcement, forming the reinforcement cage. For the F1 and F2 series of beams NEFMAC CFRP grid was used as shear reinforcement. Figures 3.16 and 3.18

schematically show the typical shape and position of the CFRP shear reinforcement, while Figure 3.21 shows a photograph of NEFMAC CFRP tied to the reinforcement forming the reinforcement cage. To the writer’s knowledge, this is the first time this type of the FRP reinforcement has been used as shear reinforcement in deep beams. In all the tested beams, two No. 10 steel bars were used as hangers to facilitate the construction of the reinforcement cage.

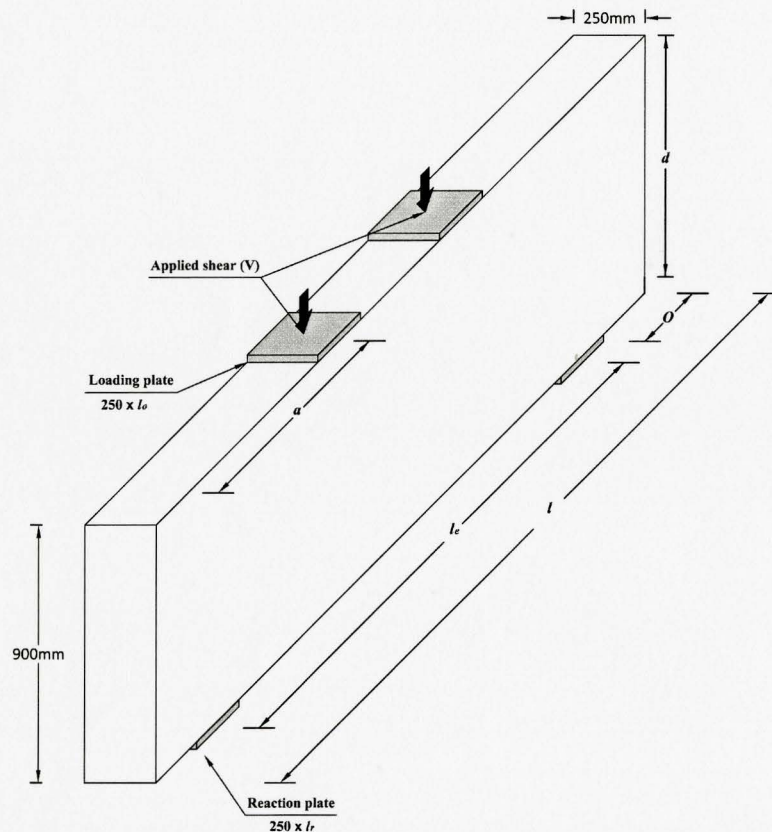


Figure 3 12. Typical test specimen geometry and dimensions

Table 3.3 Test specimen geometry

Group	Specimen	Span-to-depth ratio l_e/d	Shear span-to-depth ratio a/d	Span l_e (mm)	Shear span a (mm)	Length l (mm)	Anchorage type	Loading plate length l_o (mm)	Reaction plate length l_r (mm)	Overhang distance O (mm)
1	S1-A/B	1	0.33	900	300	1110	90-degree hook	100	150	30
	F1-A/B	1	0.33	900	300	1454	Straight bar	100	150	202
2	S2	2	0.66	1800	600	2010	90-degree hook	210	210	0
	F2-A/B	2	0.66	1800	600	2370	Straight bar	210	210	180

Table 3.4: Test specimen Reinforcement

Group	Specimen	f_c		Main Longitudinal reinforcement		Shear reinforcement		Confining transverse reinforcement
		Target (MPa)	Actual (MPa)	Material	Bars	Material	Stirrups	
1	S1-A/B	30	34.08	Steel	3 No.10	Steel	2 No.15 @ 60 mm	3 No.10 @ 45 mm
	F1-A/B	30	33.71	CFRP Isorod	2	CFRP NEFMAC	2 C16 @ 60 mm	N/E
2	S2	30	34.37	Steel	6 No.10	Steel	4 No.10 @ 120 mm	3 No.10 @ 45 mm
	F2-A/B	30	34.95	CFRP Isorod	3	CFRP NEFMAC	2 C16 @ 130 mm	N/E

Table 3.5 Longitudinal and transverse reinforcement ratio and rigidities for the test beams

Specimen	Shear reinforcement			Main longitudinal reinforcement			Rigidity of web reinforcement $E_w \frac{A_w}{bd_w}$ (MPa)
	Rigidity/unit length $\frac{E_R A_v}{s}$ (kN/m)	Reinforcement/unit length $\frac{A_v f_R}{s}$ (kN/mm)	$\left(\frac{E_R A_v}{s}\right) f_R$ (kN ² /mm ³)	Reinforcement ratio $\rho = A_l/bd$ (%)	Rigidity $E_R \rho$ (MPa)	Maximum force/unit area $f_R \rho$ (MPa)	
S1-A/B	2,733.33	6.19	1,268.27	0.14	279	66.22	54.77
F1-A/B	654	7.87	771.72	0.07	86.24	107.52	54.77
S2	1,306.67	3.17	620.67	0.29	575.06	137.17	54.77
F2-A/B	301.85	3.63	356.18	0.1	129.4	153.6	54.77

Note:

E_R = Elastic modulus of the reinforcement (i.e. No.10 and N0.15 steel reinforcement bars, NEFMAC C16 and 9.5 mm Isorod bars)

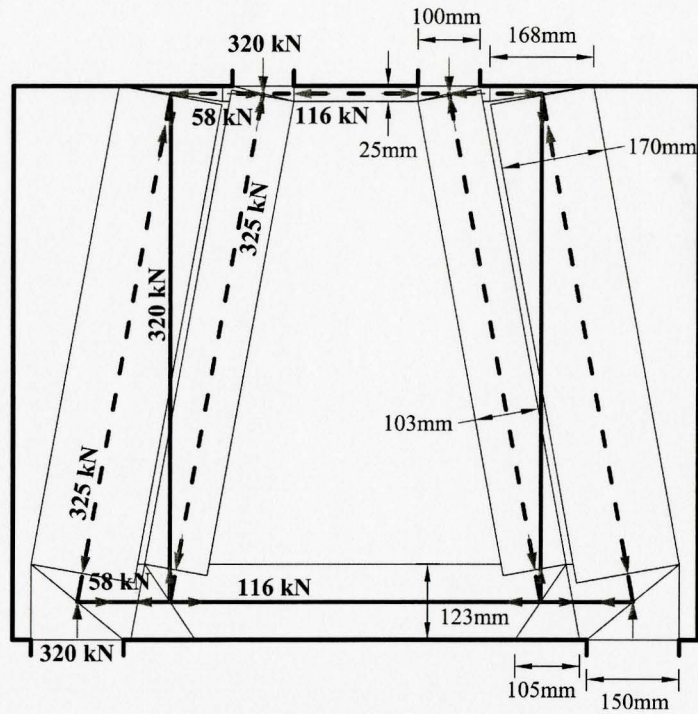
E_w = Elastic modulus of the web reinforcement ($\phi = 5.74$ mm steel Grids)

A_v = Area of the shear reinforcement

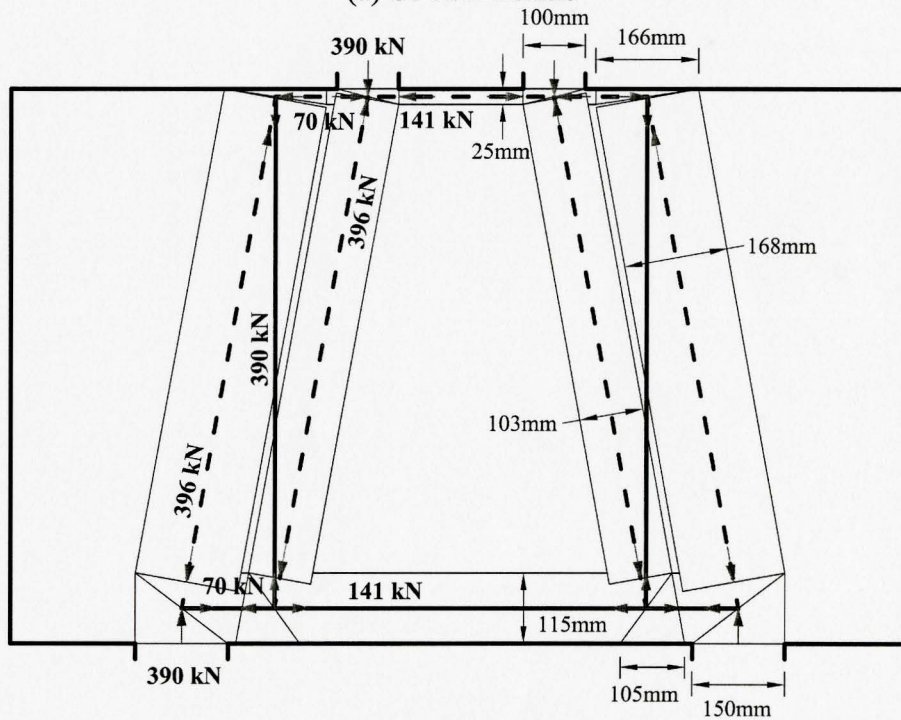
A_l = Area of the longitudinal reinforcement

A_w = Area of the web reinforcement (26 mm²)

f_R = Tensile strength of the reinforcement

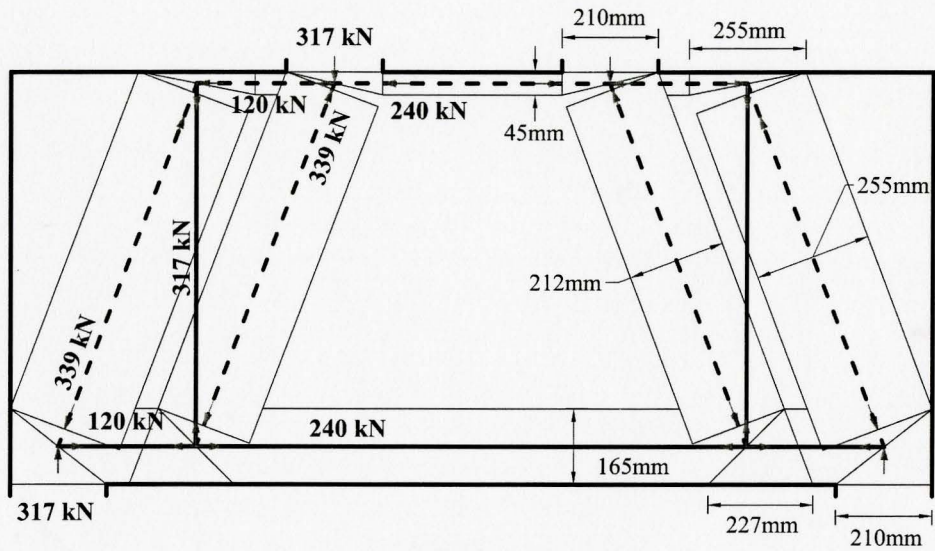


(a) S1 A/B beams

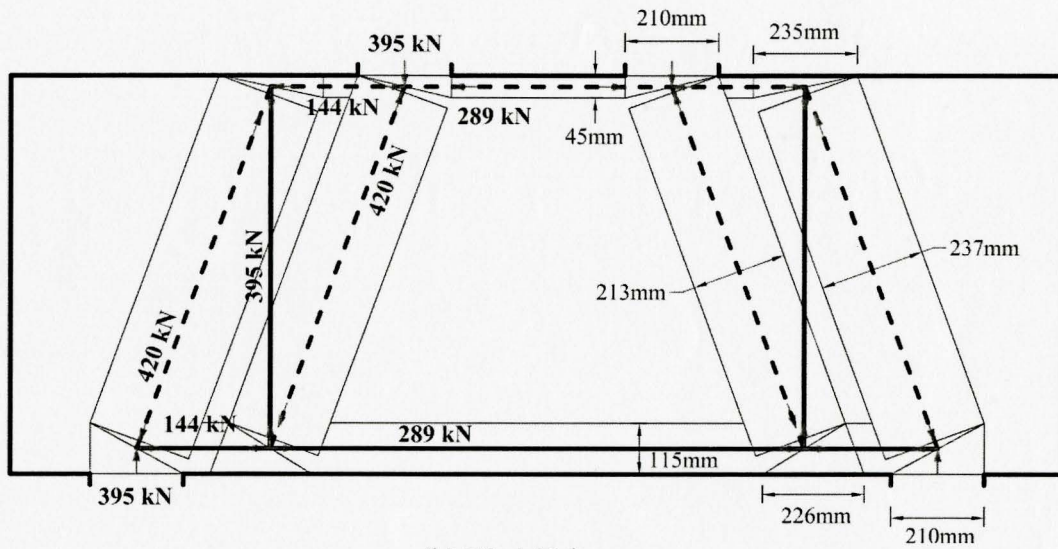


(b) F1 A/B beams

Figure 3 13 STM for the beams with span-to-depth ratio of 1

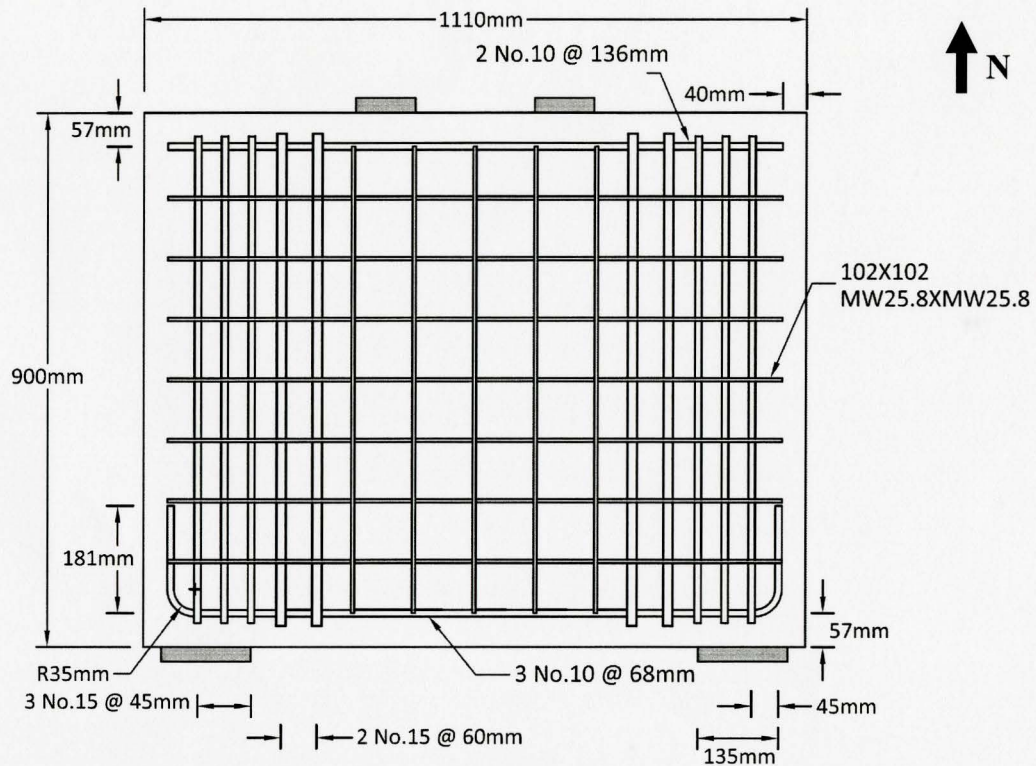


(a) S2 beam

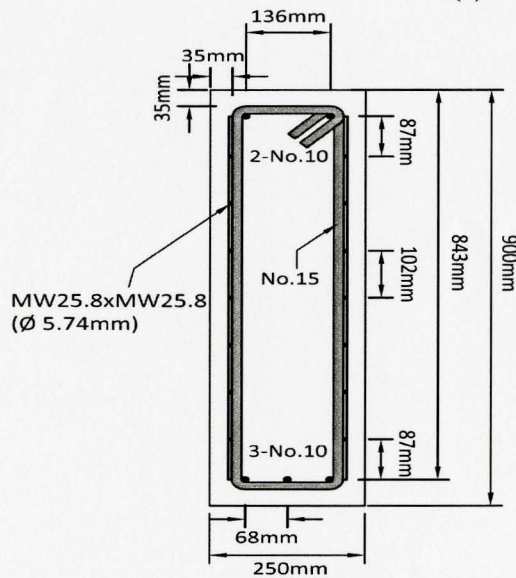


(b) F2 A/B beams

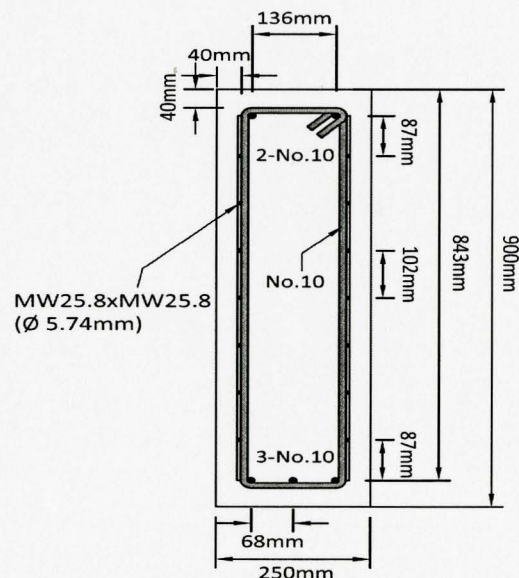
Figure 3 14: STM for the beams with span-to-depth ratio of 2



(a) Side view

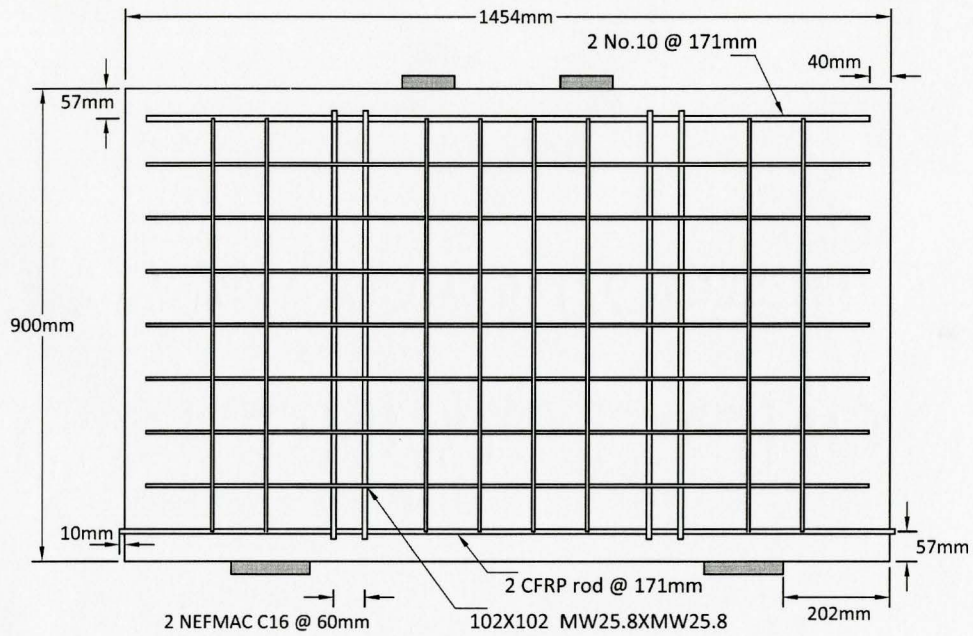


(b) Cross-sectional view across the shear span

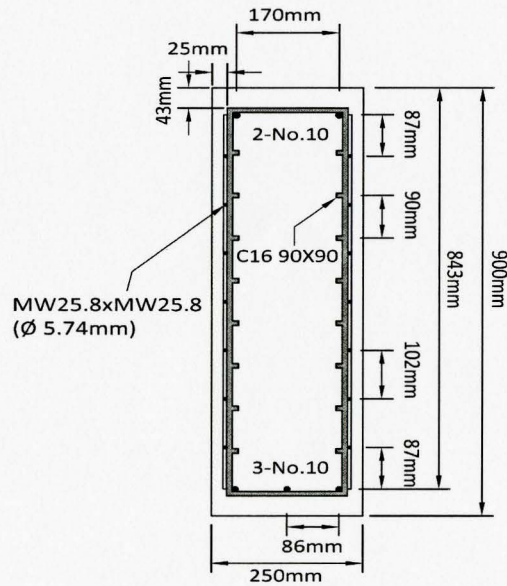


(c) Cross-sectional view at the supports

Figure 3 15 Reinforcement and the geometry of S1 beams

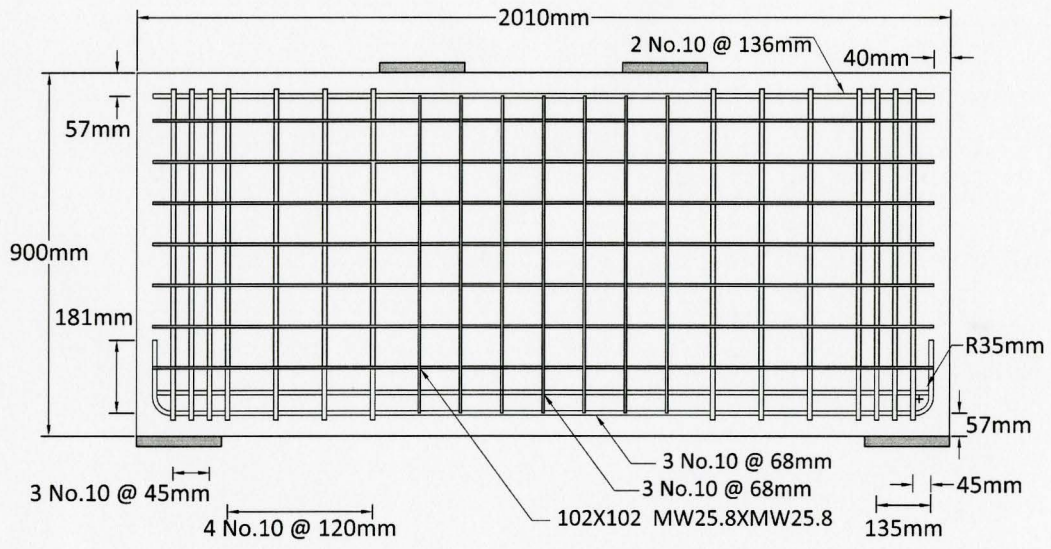


(a) Side view

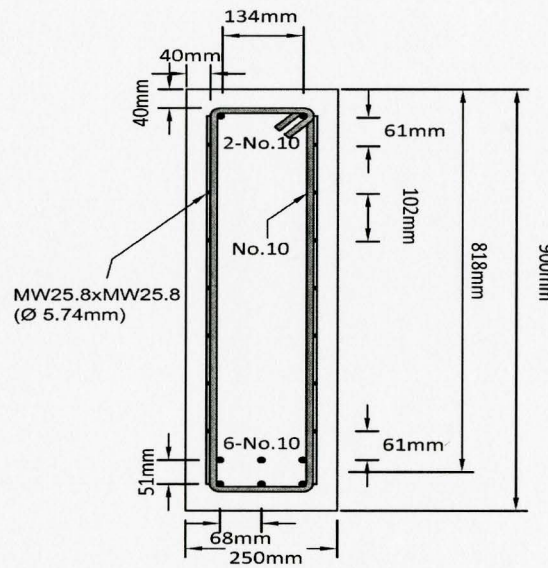


(b) Cross-sectional view

Figure 3 16: Reinforcement and geometry of F1 beams

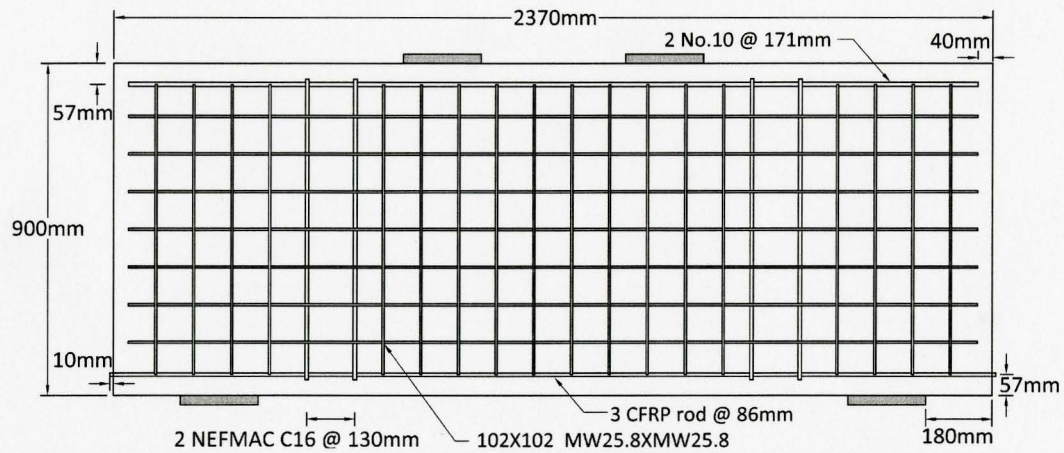


(a) Side view

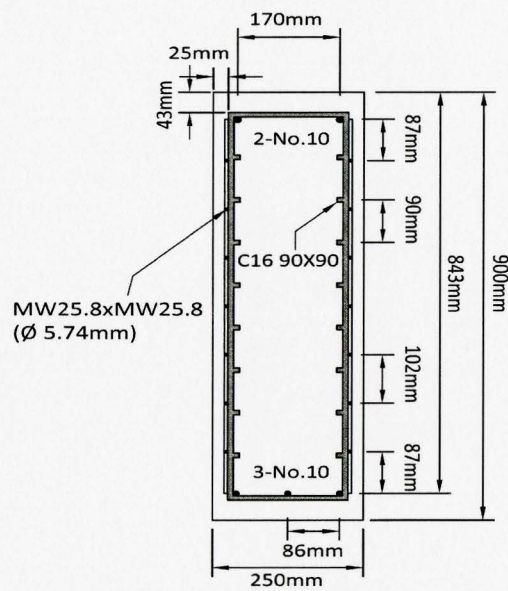


(b) Cross-sectional view

Figure 3 17 Reinforcement and geometry of S2 beam



(a) Side view



(b) Cross-sectional view

Figure 3 18 Reinforcement and geometry of F2 beams

3.3.2 Fabrication of the beams

The test specimens were fabricated in the Applied Dynamic Laboratory at McMaster University. The following section outlines the construction procedures.

3.3.2.1 Formwork preparation

The beams were cast in six wooden formworks. The formworks were designed to accommodate a single beam except one that was designed for casting S1 beams. The formwork of S1 specimens was designed in a way that could hold two specimens so that they could be cast next to each other at the same time. The formwork was made of plywood sheets that were finished on one face. The sheets were reinforced by 2"x2" stringers, as can be seen in Figure 3 19 To facilitate the removal of the test specimens from the formwork after casting, their inner surfaces were brushed with a lubricating oil. The forms were laid on level floor and the beams were cast in the vertical position. Figure 3 19 shows a photograph of all the formwork used to cast the concrete beams.

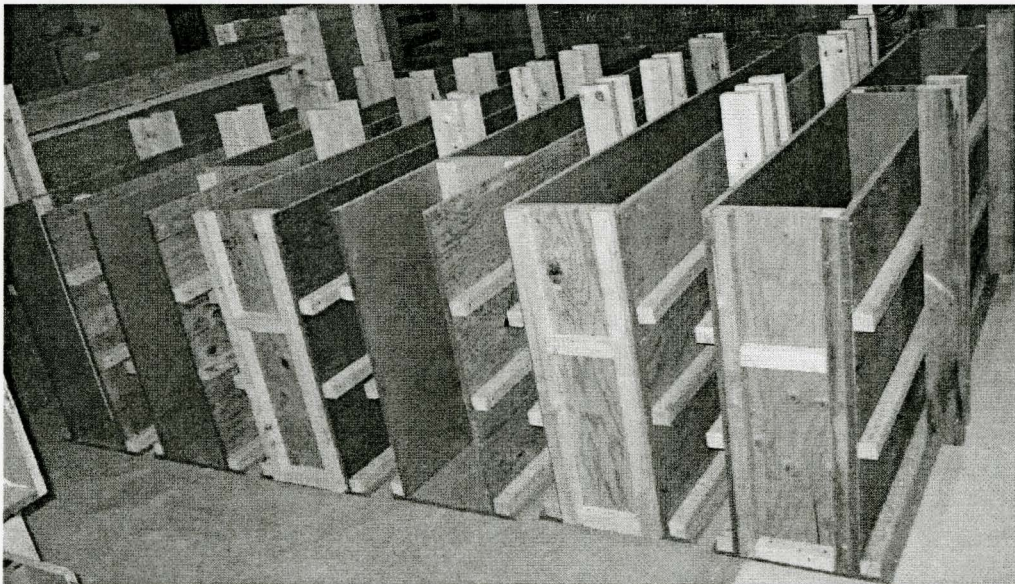


Figure 3 19: Formwork used to cast the concrete

3.3.2.2 Preparation of reinforcement cages

The location of stirrups was marked initially on the top and bottom reinforcement. The stirrups were then held in place as the longitudinal reinforcement passed through the stirrups and was tied at the designated location. Same procedure was applied to the top reinforcements. Subsequently to prevent shifting of the reinforcement cage during casting process and to maintain the correct side concrete cover on both faces, the welded wire mesh was firmly tied to the stirrups on both faces. Tie wires were used to connect the reinforcement elements in the reinforcement cage. In the final stage, the reinforcement cage was placed on small plastic chairs to maintain the proven cover. Lifting hooks were also added to facilitate the transportation of the beams. The reinforcement cage was then lifted up by the overhead crane and placed into the formwork and strain gauge wires were attached to the reinforcement and passed through the forms. Figure 3.20 and 3.21 show photographs of typical reinforcement cages for the control specimen and the CFRP reinforced specimen, respectively.

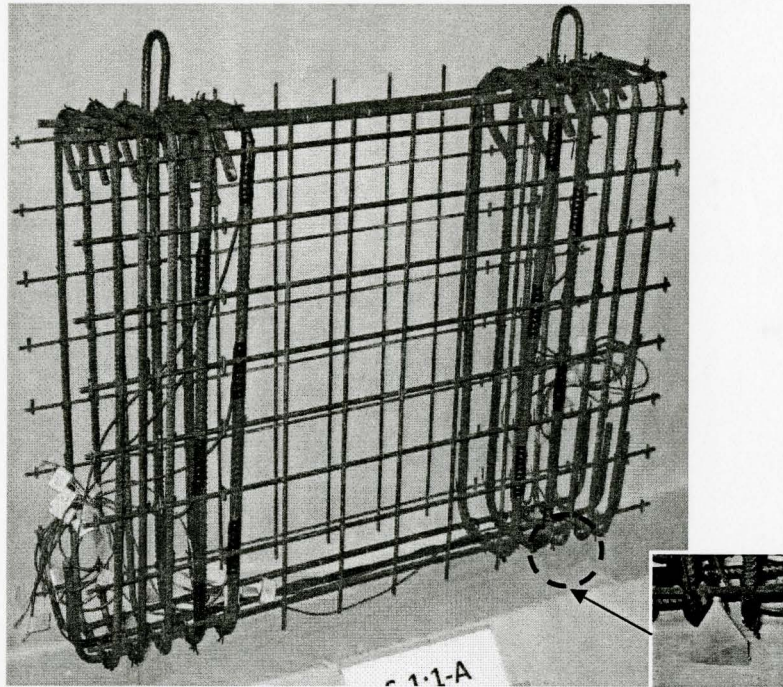


Figure 3.20: Beam S1 A/B reinforcement cage

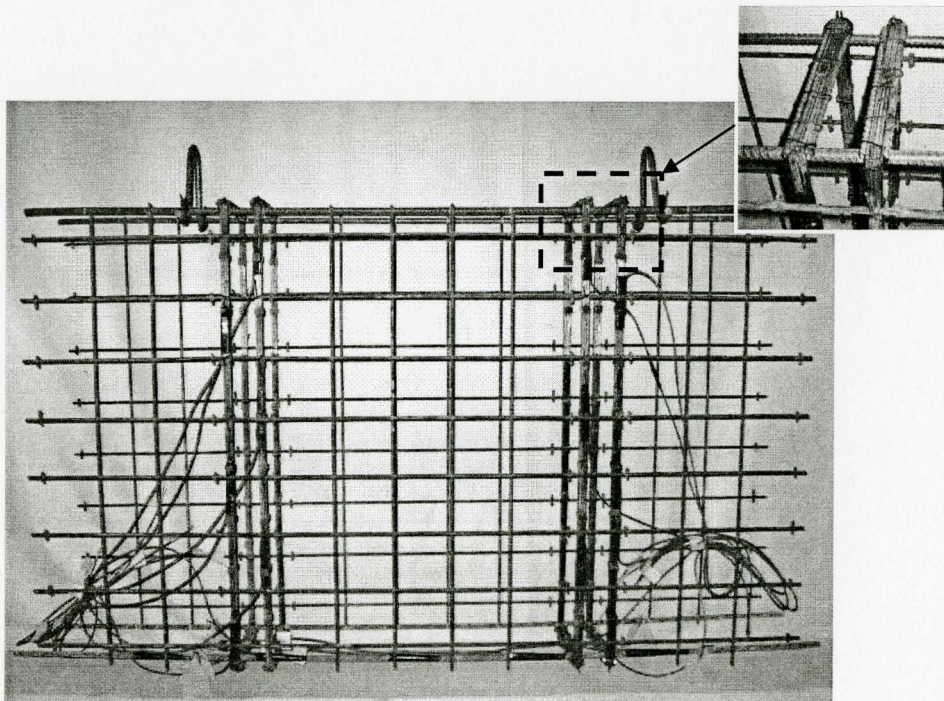


Figure 3.21 Beams F1 A/B reinforcement cage

3.3.2.3 Casting of concrete

The concrete was delivered from the ready mix plant in a mixing truck. A slump test was carried out before casting to measure the workability of the concrete batch. The concrete was carried from the truck to the forms using cement chutes, and was placed in the forms in two lifts, using two electrical internal poker vibrators to compact each lift. All the beams were cast in one batch to ensure the same concrete properties. Twenty-three standard cylinders were cast at the same time as the beams for compression and splitting tensile tests. Immediately after casting, the beams and control cylinders were covered with plastic sheets to avoid moisture loss.

3.3.2.4 Curing of concrete

The concrete beams and cylinders were pounded with water and covered with the plastic sheet, the night of casting and the morning after casting. Twenty-four hours after casting, the cylinders and the formworks were striped and then the beams and the concrete cylinders were covered with wet burlap sheets. The burlap was kept moist at all times during the curing period, which lasted 14 days. The specimens were then moved to the designated storage area and left exposed to the laboratory ambient condition until the day of testing. Figure 3.22 shows a photograph of the storage area and the test specimens during and after the wet curing phase. Before testing, each beam was painted with a coat of whitewash and

a dark color grid was drawn on one of its vertical faces to facilitate the observation of cracks formation and propagation under increased loading.

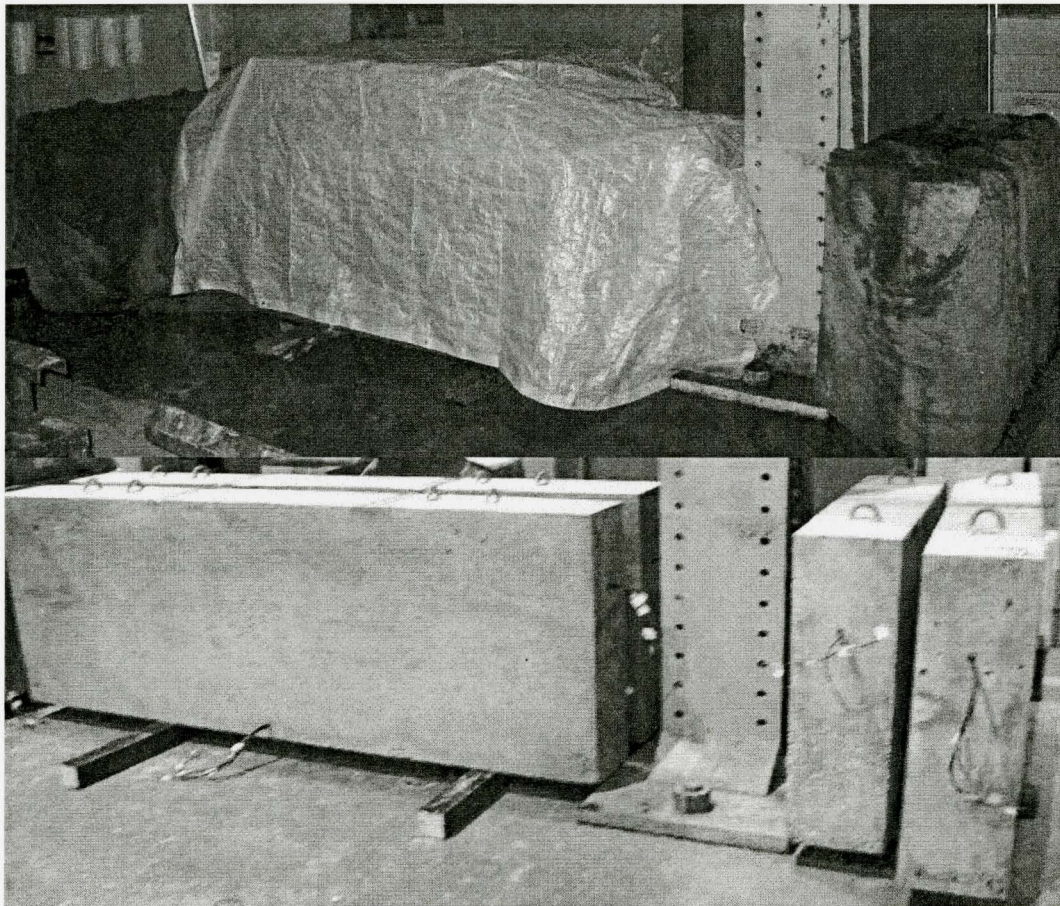


Figure 3.22. Typical test specimens during storage period

3.3.3 Instrumentation

To monitor the behaviour of the tested beams, the strain in the reinforcement and on the concrete surface, and the beams displacements were measured using different instrumentations. Instrumentation of the beams included electrical resistance strain gauges for strain measurement, linear displacement

sensors for deflection measurement along the span, draw wire sensors for measuring the average strain along the compression struts and a load cell for measuring the applied load. The instrumentation was calibrated in two stages, at the beginning and half-way through the experimental program.

3.3.3.1 Electrical resistance strain gauges

Two types of electrical strain gauge were used in this experiment, namely single-element universal gauge and three-element 45° rosette gauge. Both gauges were manufactured by SHOWA Measuring Instrumentations Co., Ltd., Tokyo, Japan with a resistance of 120 ohms and a gauge length of 5 mm. The strains in the steel and CFRP reinforcement and on the surface of concrete at mid-span were monitored by the use of single-element gauges of type N11-FA-5-120-11. The strains along the compression struts were monitored using rosettes of type N31-FA-5-120-11.

The reinforcement surface was first smoothed at the designated gauge location and then cleaned and thoroughly degreased with ethanol solution. In order to prepare the concrete for the strain gauges, the two-component Sikador gel was applied at the location of the strain gauge and then smoothed to the level of concrete surface. The strain gauges and their associated terminals were then attached to the prepared surface using M-Bond 200 adhesive. After the gauge lead and the gauge wires were soldered to the terminal, a thin layer of protective

coating was applied on the gauges to prevent damage of the foil metal grid in the strain gauge during subsequent handling and testing. The internal strain gauges, connected to the reinforcement, were also covered by a waterproof coating and sealed by electric wiring insulating tape to protect them from moisture damage or damages that could occur during casting.

The strain gauges were tested and checked thoroughly during and after installation. Precautions were taken to protect gauges from premature damage during the assembly of the reinforcement cages and during casting. Table 3.6 shows the total number of strain gauges used to monitor the strain in the longitudinal and the transverse reinforcement and on the surface of concrete. It can be noticed that the same number of strain gauges was used in all the other specimens except S2. The beam S2 contains more shear reinforcement in comparison with the other beams and therefore an extra four strain gauges were installed on the latter reinforcement.

The strain gauges along the longitudinal reinforcement were positioned in such a way as to measure the strains at the mid-span, at the center line of the supporting plates and midway between those points. The positions of the strain gauges on the stirrups were selected based on the expected diagonal crack pattern in deep beams. Figure 3.23 illustrates the typical strain gauge arrangement for all the other test beams, except Beam S2, with the arrangement for the latter beam given in Figure 3.24.

Table 3.6: Number of electrical resistance strain gauges in each specimen

Specimen	Main tension reinforcement	Shear reinforcement	Surface of concrete
S1	5	12	23
F1-A/B	5	12	23
S2	5	16	23
F2-A/B	5	12	23

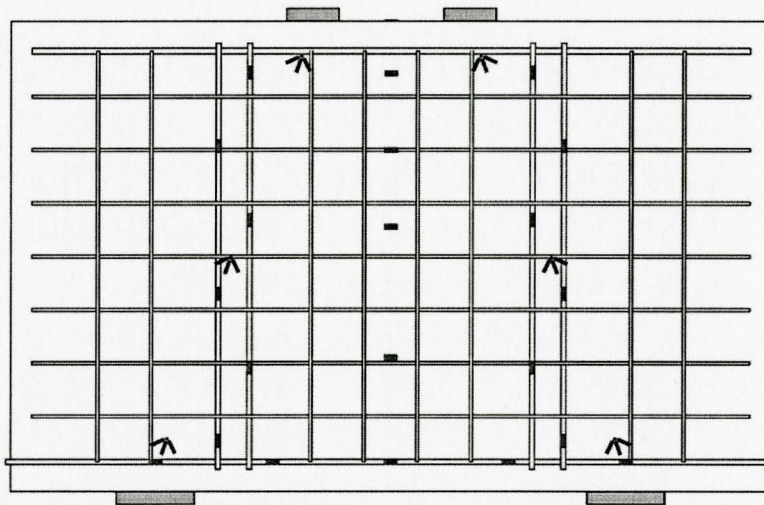


Figure 3.23 Typical strain gauge positions for all the beams except Beam S2

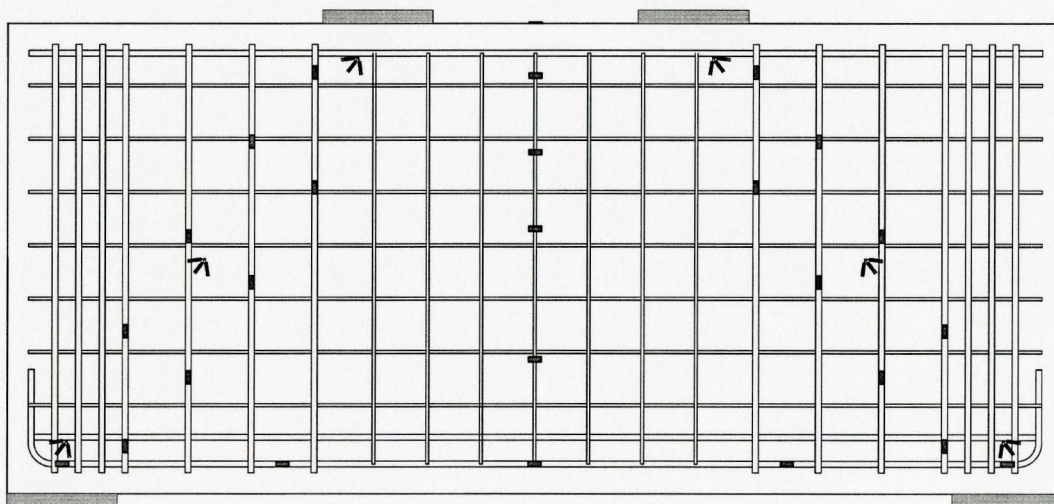


Figure 3.24: Strain gauge locations for Beam S2

3.3.3.2 Linear displacement transducers

The deflection of the beams was measured using six linear displacement transducers. Pairs of transducers were placed at quarter points and mid-span of each beam. The two transducers at each location were placed under the beam, opposite to each other, to the left and right of the cross-section. These transducers were manufactured by Penny and Giles Controls Ltd., Dorset, UK from a SLS190 series with a stroke length of 25 mm.

Magnetic base kit was used in order to hold the transducers in their positions. For each pair two magnetic bases were placed on a relatively thick (1.5 inch) metal plate long enough to support both gauge holders. To avoid damaging the sensors during testing of the specimens, it was decided not to place them directly underneath the beam. Rigid angles were mounted at the bottom of the beam to facilitate the deflection measurement at a slight distance from the specimen. The tip of the displacement transducer was rested against the bottom of the angles while its body was fixed to the central post of the magnetic base. The position of the magnets was adjusted to assure at least 10 mm gap between the tip of the transducer and the vertical face of the beam. Figure 3.25 shows the typical position and installation of the displacement transducers and the draw wire sensors.

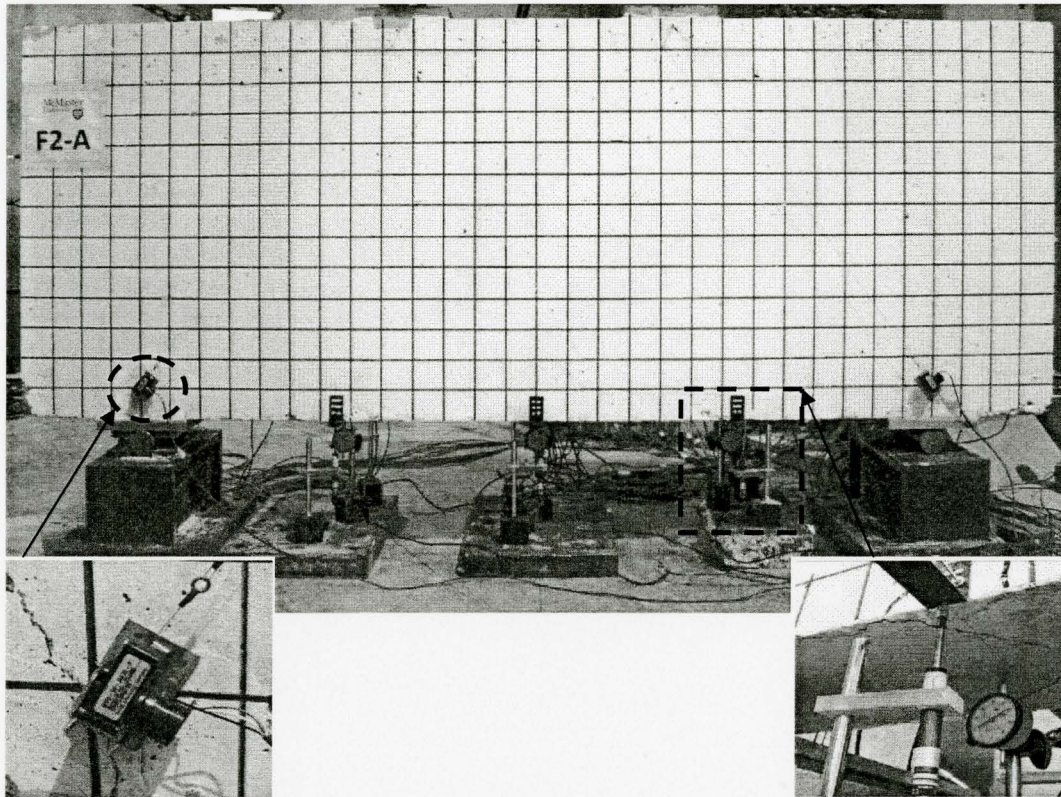


Figure 3.25 Position of linear displacement transducers and draw wire sensors

3.3.3.3 Draw wire sensors

Two wire sensors were used for each test specimen. The sensors were mounted on the concrete at the same level as the longitudinal reinforcement and orientated diagonally in the same direction as the expected diagonal compression struts on the east and west sides. A 2.0 mm stainless steel threaded rod was mounted at the center of each presumed compression strut, near the top of the beam. Stainless steel trolling fishing wire was used as non stretchable extension cable to link the draw wire sensors to the fixed rods at the top of the struts. The gauge length between the points of contact of the draw wire sensors and the

mounted rods at the top of the struts was measured before each test and was used to compute the average strain variation along each compression strut. Figure 3.25 shows the position of the draw wire sensors for a typical test specimen.

3.3.3.4 Dial gauges

Mechanical dial gauges in this study were mainly used as a back up measuring system. The readings of the dial gauges were recorded every time the loading was halted. Short stroke 25 mm dial gauges were used in this study. The recorded data from the dial gauges was then compared with the average readings from the linear displacement transducers to check the transducers readings.

Magnetic base kits were again used in order to hold the dial gauges in place. The gauges were located along the centerline of the bottom surface at the same locations along the span as the displacement transducers. This way it was possible to relate the readings from the three dial gauges with the average readings from the pair of displacement transducers.

Similar dial gauges were used to measure the slippage of the CFRP longitudinal reinforcement. In order to measure the relative movement of the longitudinal reinforcement with respect to the concrete, dial gauges were placed at the ends of the beam with the gauge shaft pressing against the end of the reinforcing bar. Figure 3.26 shows a photograph of the latter dial gauges used to measure the slippage of the longitudinal reinforcement.

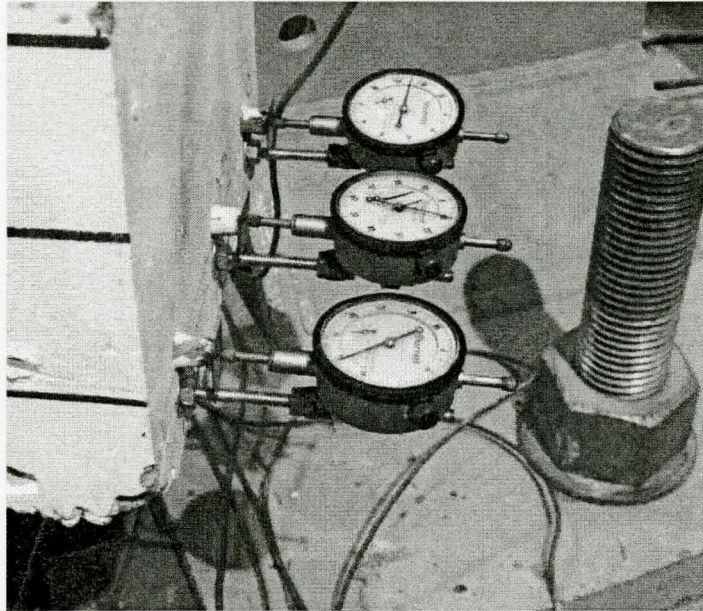


Figure 3.26: Dial gauges used to measure the slippage of main reinforcement

3.3.3.5 Load cell

A single load cell was placed at mid-span of the spreader beam under the cylinder to measure the total applied load. A convex plate was fixed to the top surface of the cell in order to spread the load over the cross section of the load cell. The load cell measurement was monitored in real time in order to relate the behaviour of the tested beams with the level of loading.

3.3.4 Test set-up

All the beams were simply supported and tested in four-point bending. Figure 3.27 shows the test set-up used to carry out the testing. The test frame consisted of two wide flange columns connected by two steel girders. The

columns were tightened to the strong floor of the laboratory by the use of four post-tensioned steel bolts.

A 200 ton jack was used to apply the load. The double acting jack is manufactured by Simplex, Illinois, USA and has a 6 inch stroke length. The jack was supported by the steel frame and the load was transferred from the jack to the full width of the tested beams via a one meter long wide flange spreader beam. Both the spreader beam and the two cross girders were stiffened at the critical section along their spans to minimize any deformation due to application of high loads. Three wide steel plates were screwed to the back of the cylinder and tightened to the cross girders using 4 bolted threaded rods. To avoid torsional buckling of the frame due to high reaction forces from the specimen during the test, the width of the plates were chosen to cover the width of the flanges of the girders.

Loading plates were used to transfer the load to the specimen. These plates permit the spread of the load over wider area of concrete and prevent premature crushing of the nodal zones. To ensure uniform contact between the loading or supporting plates and the surface of the specimen, a thin layer of hydro-stone was applied. The loading plates were 250×100 mm each, for the S1 and F1 beams and 250×210 mm for the S2 and F2 beams. The 250 mm length of the plate was oriented parallel to the width of the cross-section of the beams and therefore fully covered the entire width.

Two purpose-built bearing boxes were used to support the test beams which were resting on the rigid floor of the laboratory. A roller support was achieved by placing a steel cylinder between the reaction plate and a purpose-built bearing box. For the pin support, the lateral movement of the steel cylinder was restricted by means of two welded steel pieces on the bearing box. The spreader beam was also simply-supported following the same procedure. The steel cylinders used for the reactions were identical in size and length; long enough to cover the full width of each beam.

More details of the test setup can be seen in the Figure 3.27 and 3.28. As it can be seen in Figure 3.28 four steel angles were positioned at the top of the beam, two on each face, and tightened to the flanges of the columns to guard against lateral movement of the beams during the test.

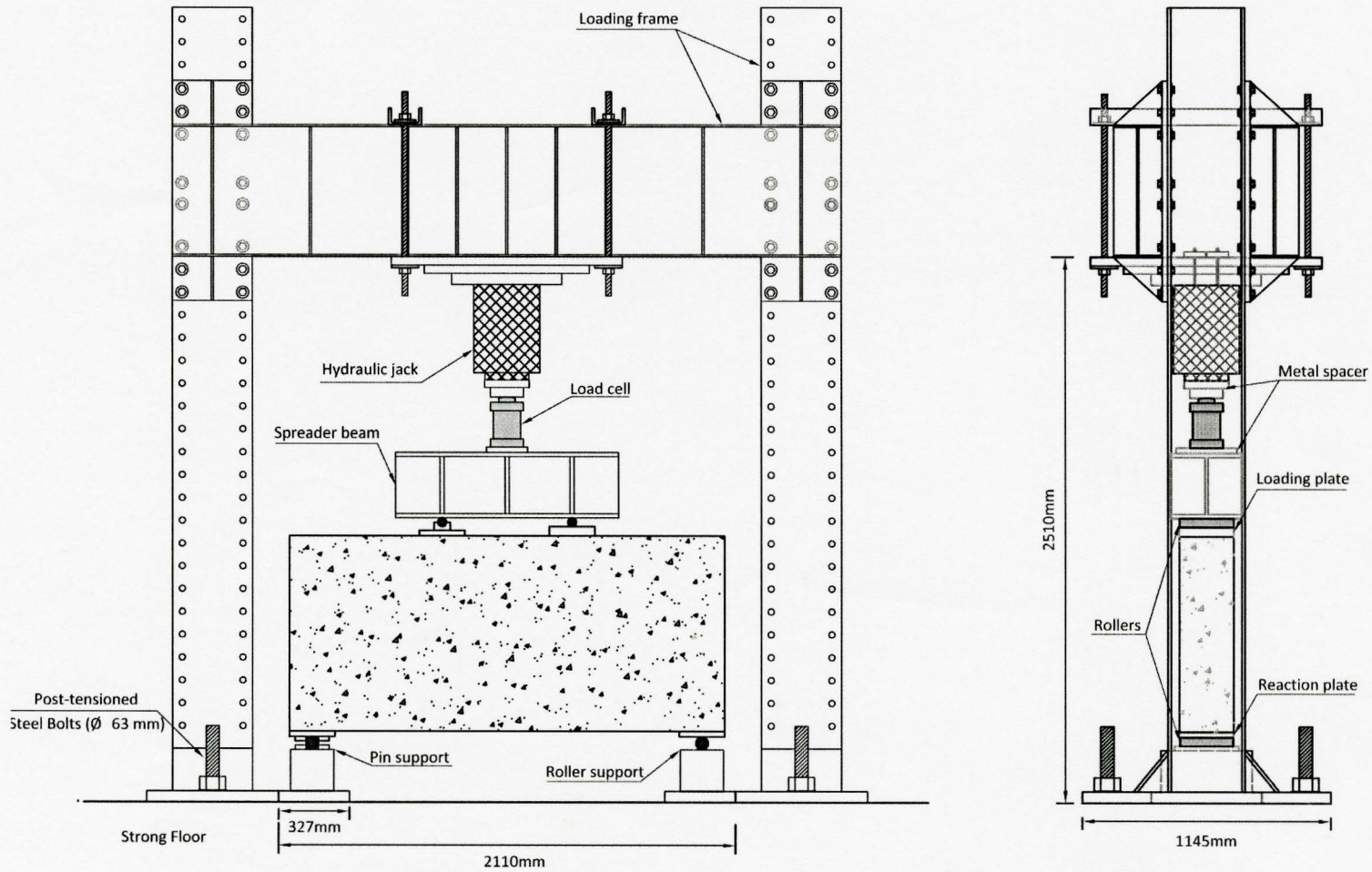


Figure 3.27: Test set-up elevation and side views.

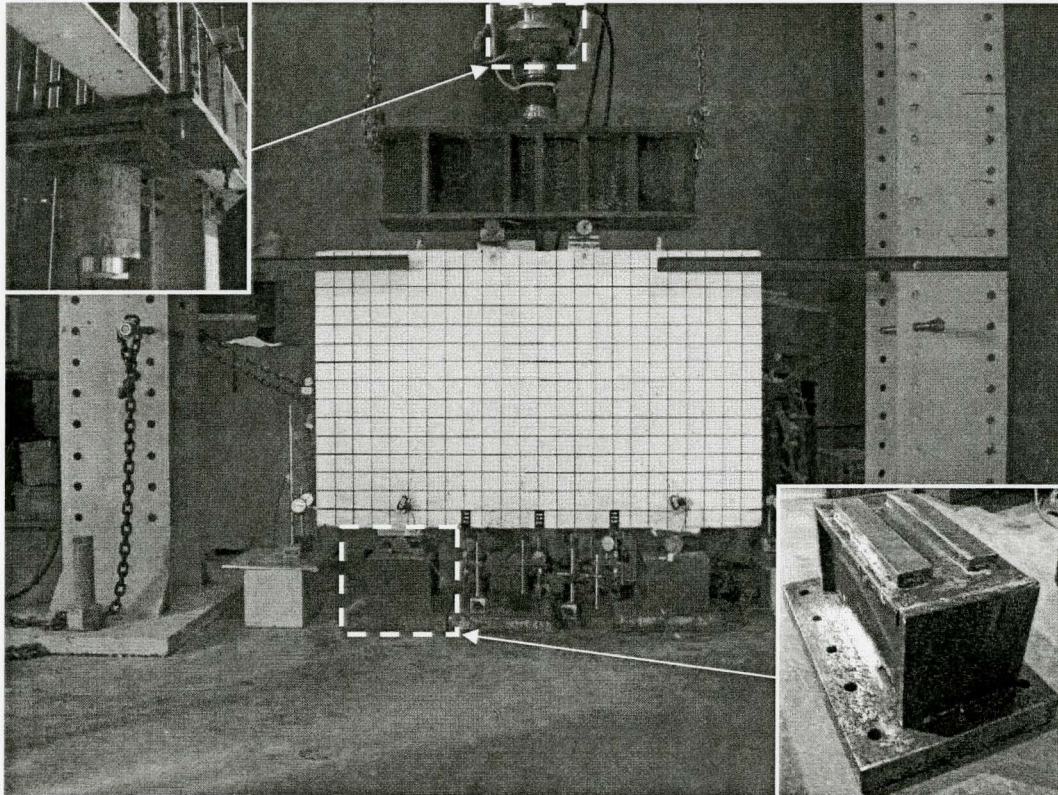


Figure 3.28. Photograph of the test set-up

3.3.5 Testing procedure

The load was applied to the beams manually using a hydraulic hand pump. The hand pump was produced by Enerpac Ltd., Ontario, Canada with a 10,000 psi operating pressure. The pressure was applied at a consistent rate and the loading was paused at the selected loading stages to allow for reading the dial gauges, tracing of the cracks and photography of the beam as cracks propagated under increased loading. The loading was applied in increments of 100 kN for the stage prior to cracking, followed by 50 kN increments in the interval between the

formation of the first crack and the maximum loading capacity, and then reduced to increments of 25 kN at the stage before failure.

The load was monotonically applied up to failure while the behaviour of the beam was monitor and recorded using a data acquisition system. All the instrumentation was connected to the data acquisition system and was calibrated and the readings were set to zero before commencing the test. Figure 3.29 shows a photograph of the data acquisition system and the wiring of the load cell, the strain gauges and the displacement transducers.

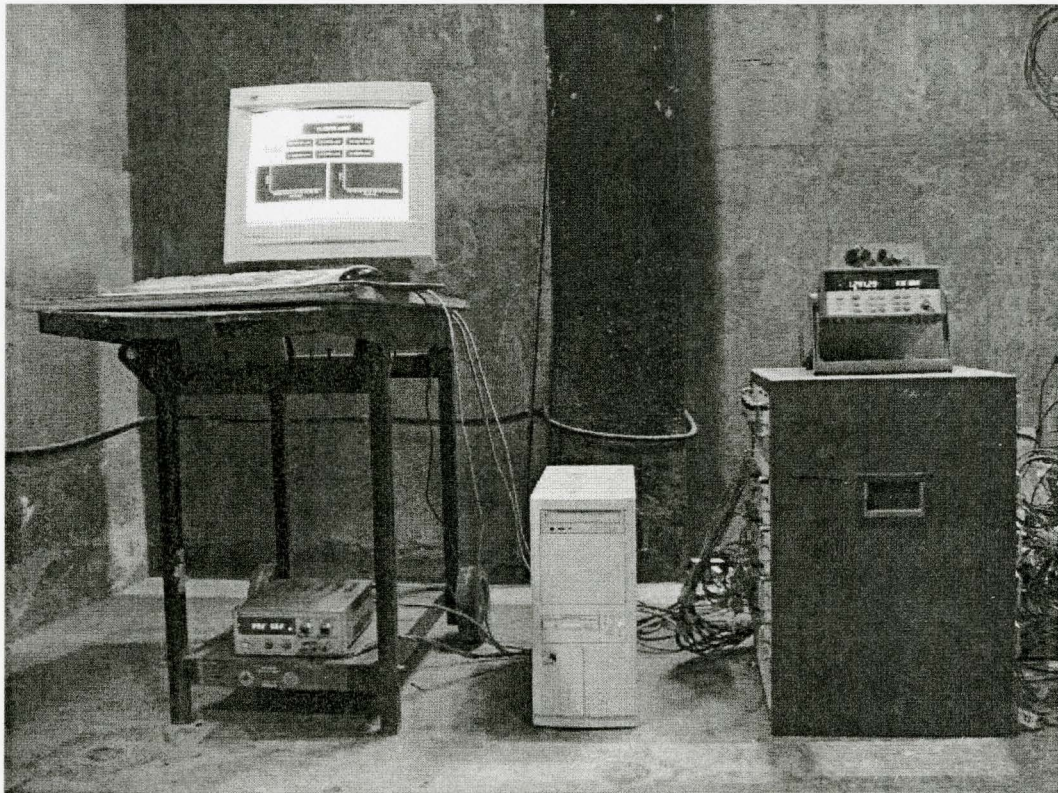


Figure 3.29: Photograph of the data acquisition system

CHAPTER 4: OBSERVATION AND DISCUSSION OF THE EXPERIMENTAL RESULTS

4.1 General

This chapter presents the more important data gathered during the testing of the six beams. The experimental program was designed to evaluate the shear and flexural behavior of the beams by focusing on the effect of their longitudinal reinforcement type and their span-to-depth ratio.

The presented observations in this chapter are mainly in terms of the mid-span deflection, propagation of the cracks and the failure mode of the tested beams. The experimental data is used to identify the cracking load and to monitor the deformations, load-deflection response and the strain distribution in the reinforcements and on the surface of the concrete. In order to examine the adequacy of the test setup and the loading jack capacity, a trial specimen S1-A was built, and tested before the main six specimens. Although the load-deflection response of the specimen S1-A is provided in this chapter, this specimen is not part of the main experimental program.

4.2 Evaluation of the Test Setup

The stability and the rigidity of the loading frame was examined by testing the trial specimen S1-A. The trial beam was fabricated at the same time as the other beams and had the same material properties and reinforcement ratio as S1-B

beam. The choice of the trial specimen was mainly based on highest failure load expected from the test beams. The beam had to be tested four times until failure was reached. The principal reason for the uncertainty associated with the ultimate load capacity of these beams is the rather conservative and highly empirical nature of the current design provisions of both CSA and ACI codes. Of course, for the FRP reinforced deep beams, there are no design guidelines available. The first attempt was made at 121 days after casting, followed by the second, third and the fourth attempts on the 135, 138 and 139 days after casting, respectively

In the first attempt the original hydraulic jack reached its loading limit (1200 kN) before failure of the S1-A beam. It was then decided to replace the original jack with a higher capacity cylinder (1800 kN). The test frame was strengthened in order to accommodate the higher load. To avoid torsional buckling of the girders as a result of applying a higher load, it was decided to add 4 stiffeners to each of the two girders supporting the jack and to further strengthen the connection between the girders and the columns of the loading frame, as shown in Figure 4.1

In the second trial the beam once again survived the test before the capacity of the new jack was reached. In order to maintain the same loading and avoid further adjustment to the test frame and the jack, it was decided to reduce the width of the loading plates. The width of the supporting plates was kept unchanged to avoid moving the already cracked beam. Thus, only the width of the

top loading plates was reduced which caused reduction in the width of the compression struts and consequently the load carrying capacity of the beam. The width of the loading plate was reduced, from the original size of 150 mm to 120 mm.

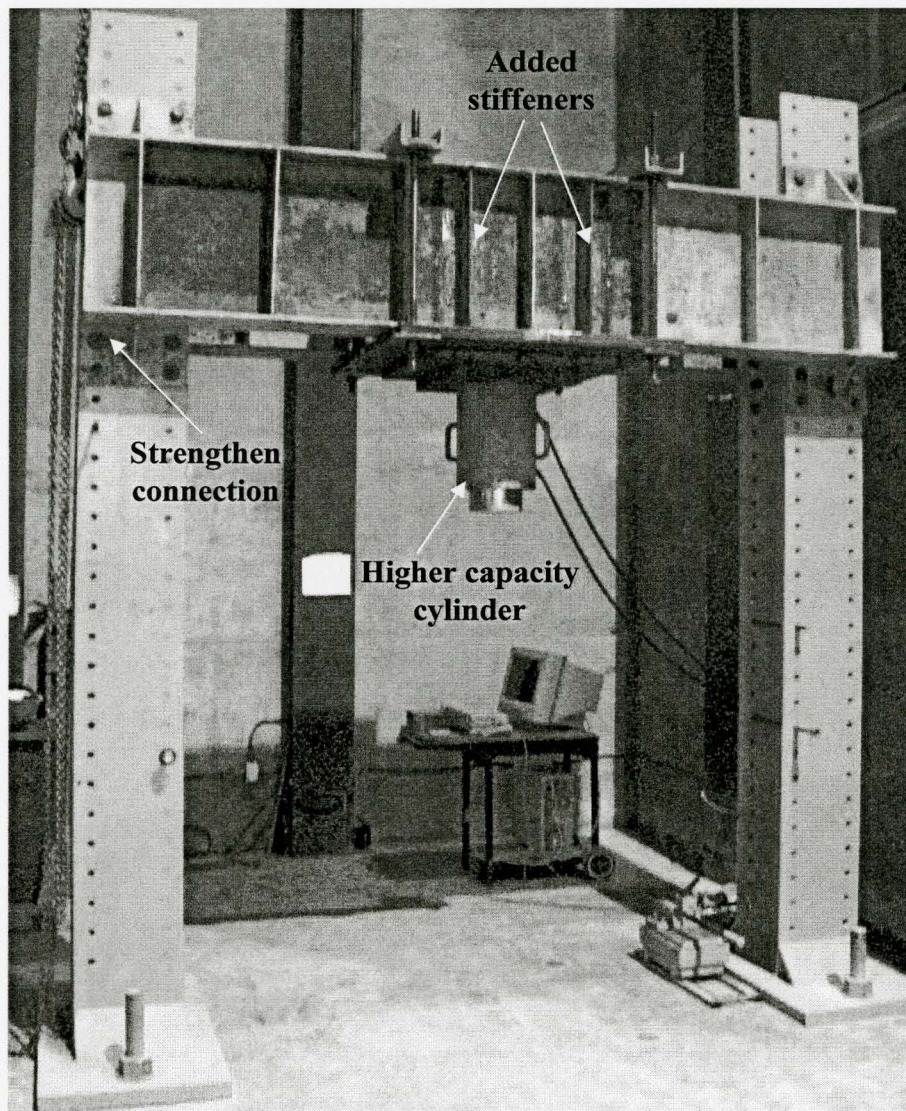


Figure 4.1 The adjusted test setup

However, this reduction did not lead to the failure of the trial beam and eventually the jack capacity was exhausted. The width of the loading plates was further reduced to 100 mm for the last attempt, which eventually led to the failure of the beam due to diagonal splitting of the east strut, as shown in Figure 4.2.

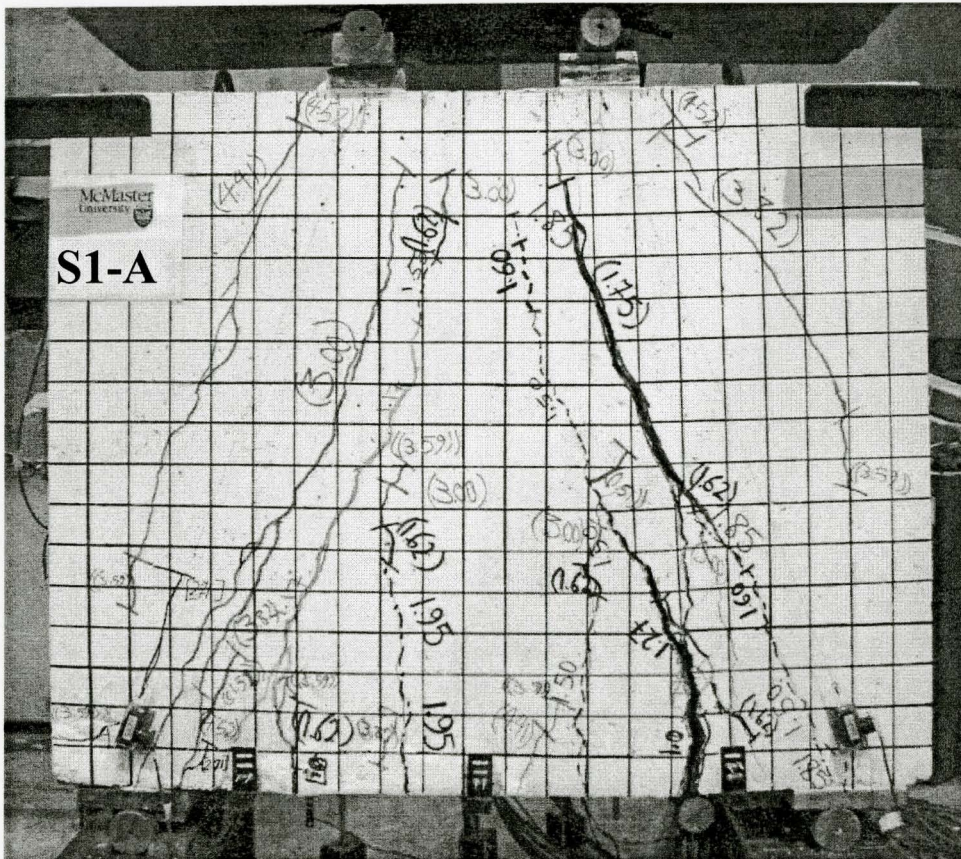


Figure 4.2. Failure of the S1-A beam

Based on the testing of the trial specimen, to ensure failure of the companion CFRP reinforced beams, it was decided to use the same size loading plates (250 mm \times 100 mm) for all the beams with span-to-depth ratio of 1. The use of same size loading plates allowed for proper comparison of the behaviour

between all the beams tested in this group. Refer to Figure 3.12 and Table 3.3 for more information about the size of the loading plates used for the various test specimens.

Using the 1800 kN jack and the loading plates and supporting plates specified in Table 3.3, the remaining six beams all reached failure at load levels below the capacity of the jack. The strengthened loading frame also proved adequate for testing all the beams.

4.2.1 General behaviour of beam S1-A

The beam experienced diagonal splitting shear failure through formation of the critical diagonal crack which propagated from the east support towards the inner edge of the east loading plate, forming the classical compression strut. Figure 4.3 schematically shows the position of the cracks with respect to the location of the longitudinal and transverse reinforcements in the S1-A beam.

The mid-span deflection of the beam was monitored under increasing load and its load-deflection curve was determined as can be seen in Figure 4.4. As shown in the latter figure, the beam was loaded and unloaded several times until it reached failure. Notice the relatively large plastic deformation after the second and third loading-unloading excursions.

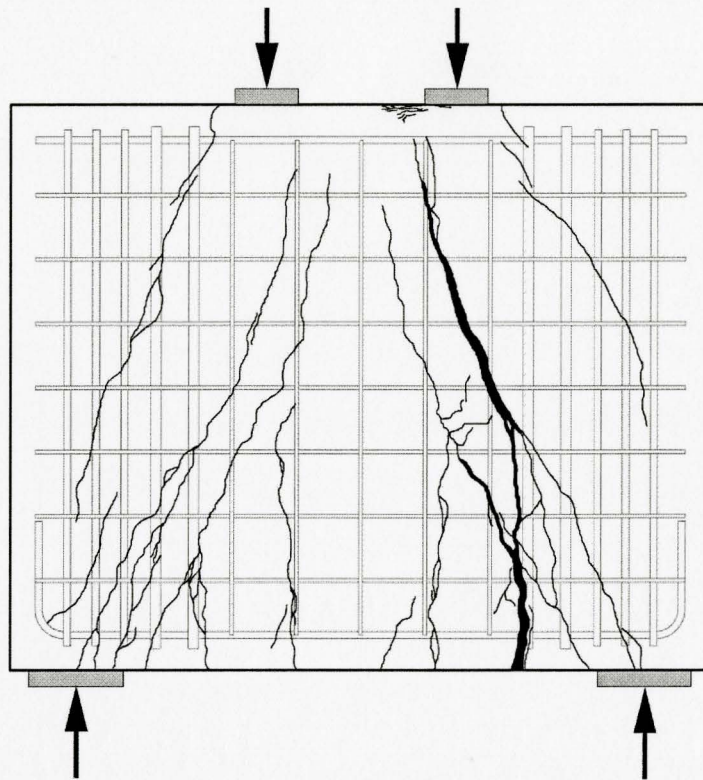


Figure 4.3 Schematic view of the crack patterns of S1-A beam at failure

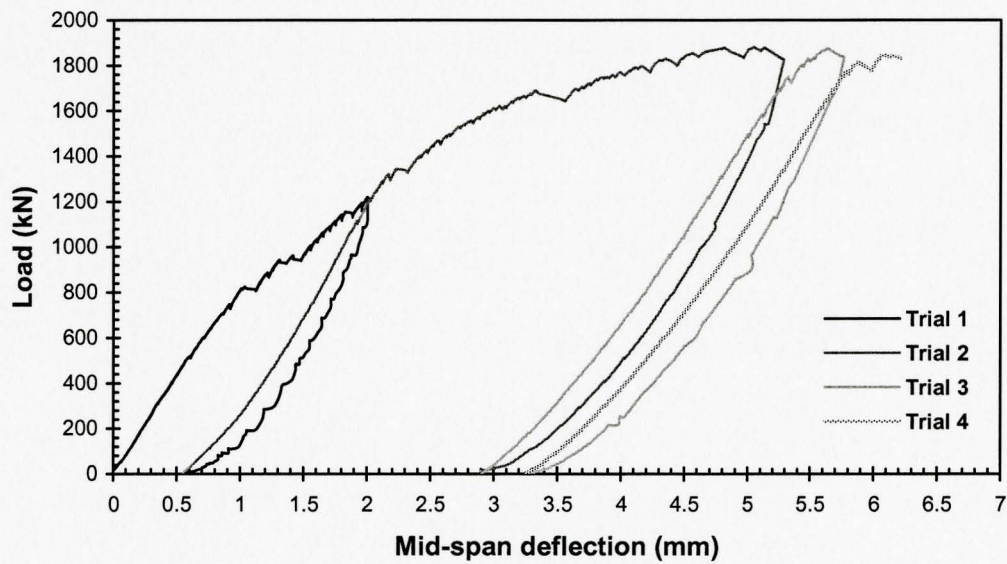


Figure 4.4: Load-deflection relationship of the S1-A beam

4.3 Beams with Span-to-Depth Ratio of 1

Three of the main tested beams had span-to-depth ratio of 1. These beams were loaded monotonically up to failure and their behaviour was studied. Here the experimental results for specimens F1-A, F1-B and S1-B are presented together with some observations made during the test.

Beams F1-A, F1-B and S1-B were tested at the age of 144, 151 and 182 days after casting, respectively. The compressive strength of the concrete was determined at these ages by testing standard cylinders and the test results are provided in Appendix C, Tables and Figures C.1 and C.4.

The following sections present the experimental results for the beams with span-to-depth ratio of 1, with some important data given in Table 4.1. Additional record of the beams behaviour could be found in Appendix B, Figures B.1 to B.6.

Table 4.1 Test results for the beams with span-to-depth ratio of 1

Beam	Ultimate load (kN)	Ultimate shear V_{uexp} (kN)	Flexural cracking load (kN)	Shear cracking load V_{crexp} (kN)	Mid-span deflection (mm)		Failure mode
					After flexural cracking	at the ultimate load	
F1-A	1600	800	415	N/E	1.00	3.4	A
F1-B	1551	775.5	482	N/E	1.20	3.3	A
S1-B	1560	780	350	430	0.87	3.1	F

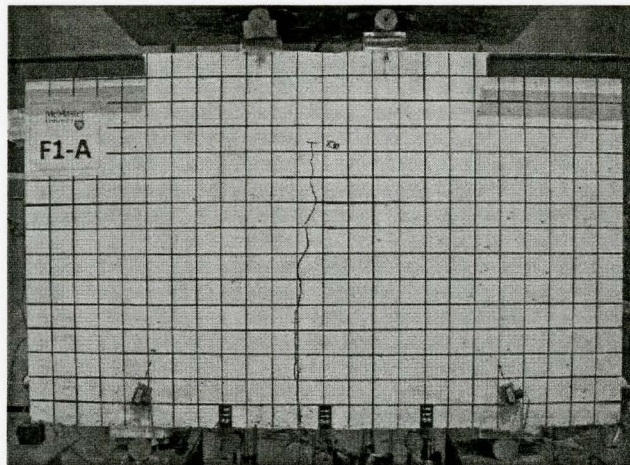
Note:

F = Flexural failure
 A = Anchorage failure
 Shear span=300 mm

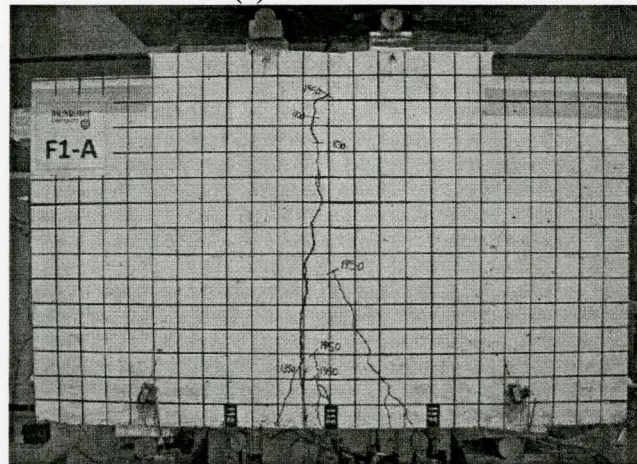
4.3.1 Observed behaviour of tested beams

Figures 4.5, 4.6 and 4.7 show photographs of the F1-A, F1-B and S1-B, respectively, at three different stages of loading (i.e. after the formation of the first flexural crack, after formation of the first inclined crack and at failure).

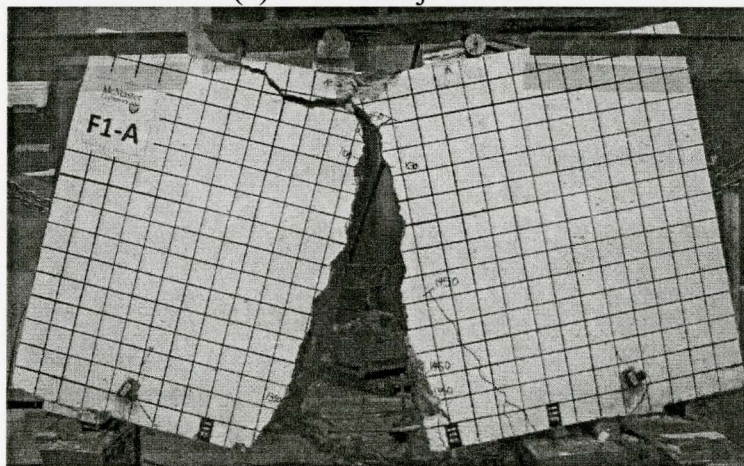
Specimens F1-A and F1-B experienced first crack at the shear force of 415 kN and 482 kN, respectively. These loads correspond to approximately 52% and 62% of the respective maximum shear sustained by the beams. For these beams the first cracks were deemed to be flexural crack, as they formed within the region of pure bending between the two concentrated loads. Upon formation, the initial flexural crack in both beams propagated three-quarter up the height of the beam, resulting in a considerable energy release and a loud noise. As the load increased further, the existing cracks propagated further towards the top surface of the beam. The second major cracks in the F1-A and F1-B beams were detected at shear force of 725 kN and 682.5 kN, respectively, which correspond to 90% and 88% of the ultimate shear capacity of the respective beam. The second major crack was also considered as a flexural crack for both specimens. It initiated directly below the east concentrated load and propagated towards the critical crack that eventually caused failure of the beam.



(a) Initial crack

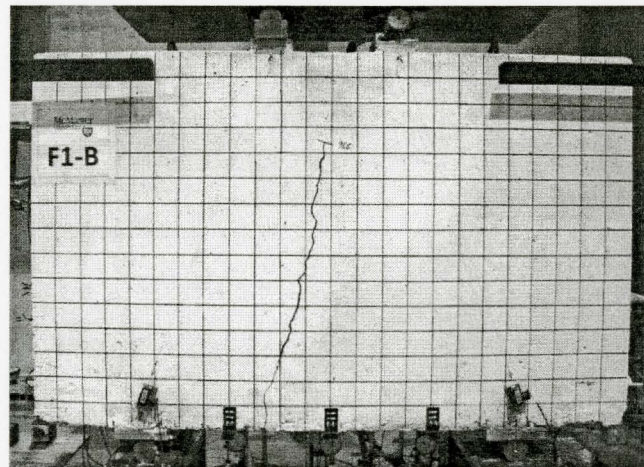


(b) Second major crack

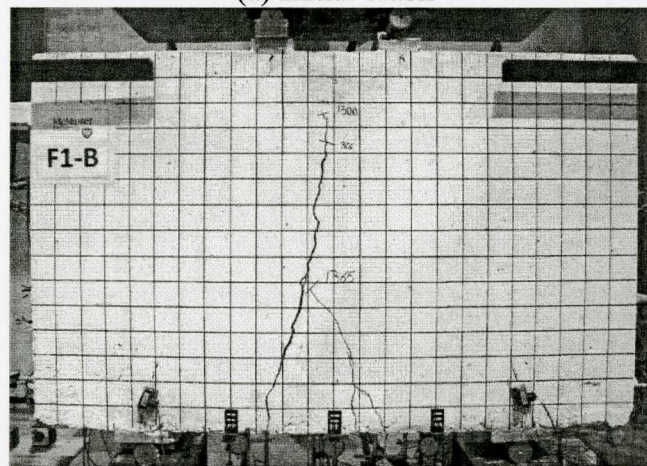


(c) After failure

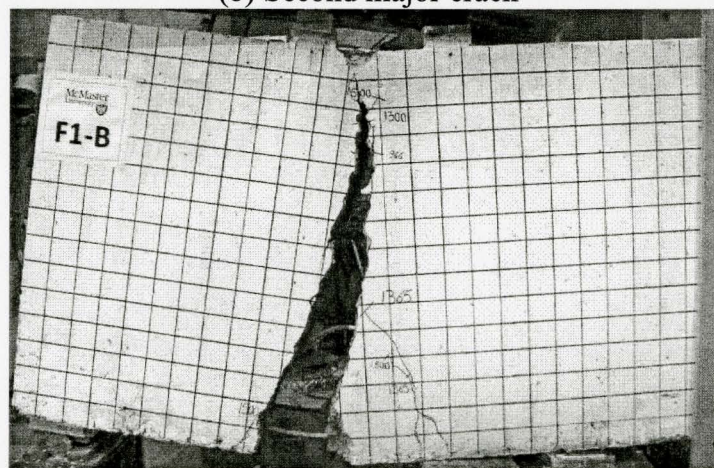
Figure 4.5 Cracking development in the F1-A beam



(a) Initial crack

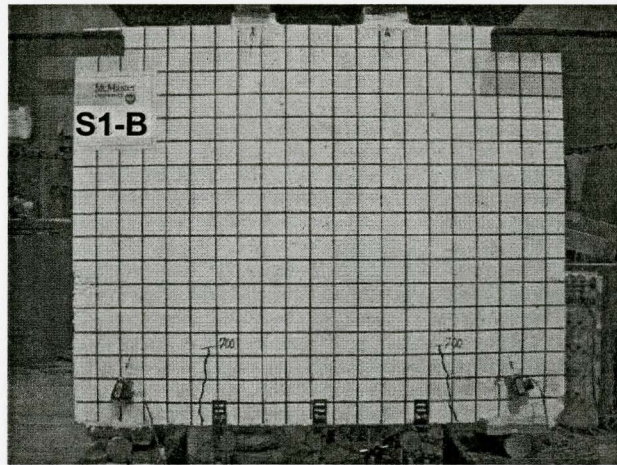


(b) Second major crack

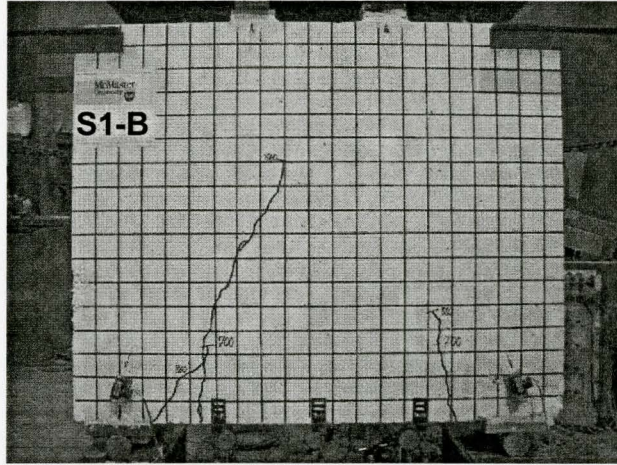


(c) After failure

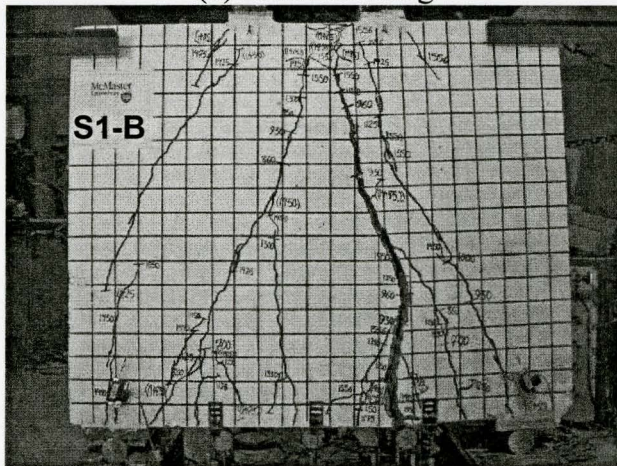
Figure 4.6: Cracking development in the F1-B beam



(a) Initial crack



(b) Shear cracking



(c) Onset of Failure

Figure 4.7: Cracking development in the S1-B beam

For the S1-B specimen, two cracks appeared simultaneously at the shear force of 350 kN, which is 45% of the ultimate shear capacity of the beam. These cracks initiated at the middle of the shear span on the east and the west side of the beam. The two initial cracks were marked as flexural cracks due to their vertical orientation. However, as load increased, the cracks changed direction and propagated diagonally towards the mid-span of the beam. The first shear crack appeared at the shear force of 430 kN or 55% of the ultimate shear capacity of the beam. The relatively large first shear crack initiated at the inner edge of the west reaction plate and immediately propagated diagonally up to two-third of the height of the beam.

It can be noticed that the cracking loads of the beams reinforced with CFRP are higher than that of the control steel reinforced specimen. This finding may be due to higher concrete shrinkage restraining stresses caused by steel reinforcement, which has higher rigidity than the CFRP reinforcement (refer to Table 3.5, Section 3.3.1).

Figure 4.8 schematically illustrates the crack pattern just before failure of the beams with span-to-depth ratio of 1. This figure also shows the reinforcement layout, which is useful to know when studying the strain variation in the reinforcements as the specimen approaches failure.

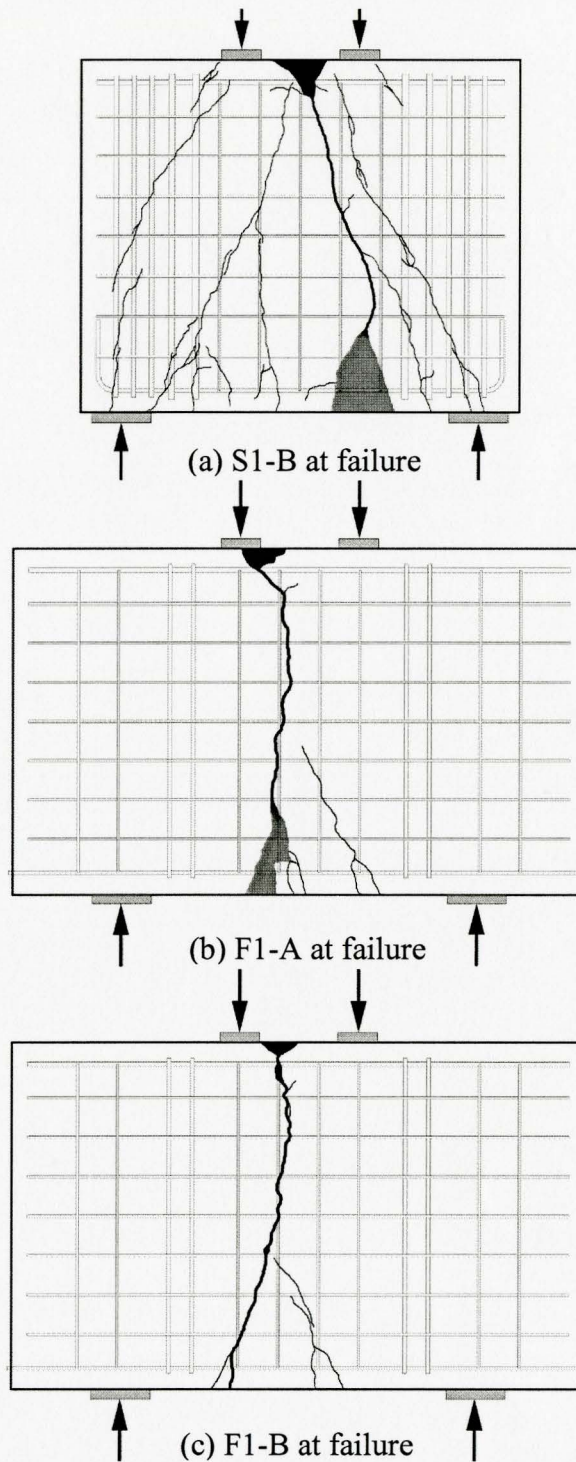
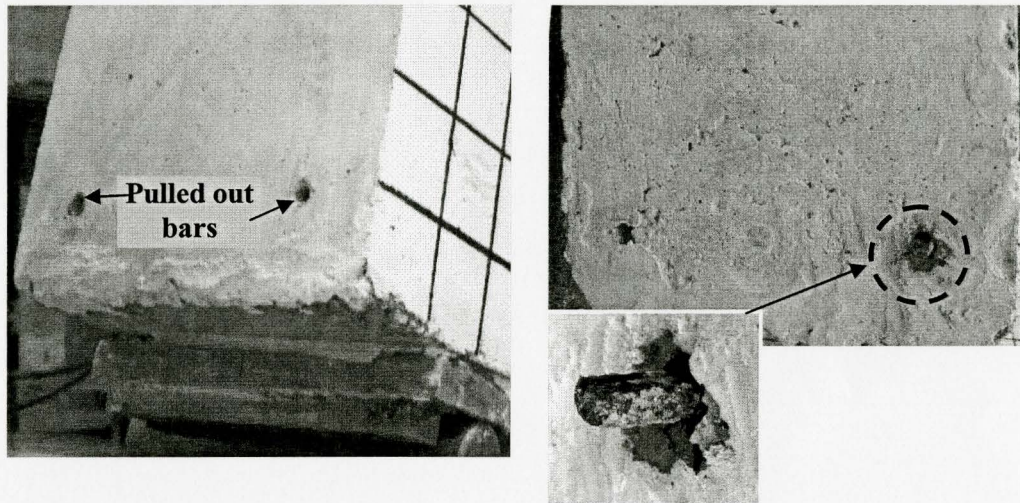


Figure 4.8. Schematic view of the crack patterns for the beams with span-to-depth ratio of 1

In Figure 4.8, the spalling of concrete is marked in gray near the bottom surface of the beam, while the crushing of concrete is shown in black, near the top surface. The failure crack for each beam is also marked in bold. There was no evidence of failure either in the diagonal struts or at any of the nodal zones for any of the tested beams in this group.

The crack patterns and the failure modes in the two CFRP reinforced beams were similar. As indicated in Table 4.1, both F1 beams failed due to anchorage failure of the CFRP longitudinal bars at the west end of the beam. The initial flexural crack, which occurred in the region of pure bending propagated vertically upward and continued to reduce the cross-sectional area of the horizontal strut as the load increased. The initiation of the bar slippage accelerated the vertical crack propagation and ultimately caused crushing of the concrete along the edge of the loading plate. Thus, the failure was initiated by anchorage loss. However, the anchorage loss was not due to bond failure at the concrete-CFRP bar interface, rather it was due to interlaminar shear failure of the Isorod bars. During the test, it could clearly be noticed that the sand coated surface of the bar separated from its core. Strictly speaking this is a type of failure of the reinforcing bar rather than the traditional loss of anchorage caused by loss of bond between the concrete and the bar. This failure occurred in all the CFRP longitudinal reinforcing bars as shown in Figure 4.9. Note that in the case of the F1-B beam, one of the longitudinal bars was sheared into two halves (see Figure

4.9b). Unfortunately, the end dial gauges were not able to measure any gradual slippage during the test and were found ineffective.



(a) F1-A reinforcement slippage

(b) F1-B reinforcement slippage

Figure 4.9. Anchorage failure of the CFRP reinforced beams with $l_d/h=1$

The failure of the control beam is schematically shown in the Figure 4.8a. The critical flexural crack to the east of the mid-span joined the existing inclined crack in the east shear span and caused flexural failure, manifested by the crushing of the compression zone near the top surface of the beam at maximum load of 1556 kN. After the ultimate capacity was reached, the full response of the control beam was captured by loading the beam up to the point of rupture of the longitudinal reinforcement.

Considering the number of cracks forming in the CFRP reinforced beams versus the companion steel reinforced beam in this group of beams, it is evident

that the CFRP reinforced beams behaved more rigidly and showed a more brittle response by experiencing fewer and wider cracks.

4.3.2 Load-deflection response

The load-deflection responses of the beams were captured by two displacement transducers installed on either side of the beam at the mid-span. Since the load versus mid-span deflection curve of a beam is a good indicator of its overall response to increased loading, the presentation of the experimental results is commenced by discussing the recorded load deflection curves as given in Figure 4.10. Notice that after reaching the ultimate load, beam S1-B undergoes much greater deformation before failure than the FRP reinforced beams and exhibits a long plateau. On the other hand, because of the linear elastic behaviour of CFRP reinforcement, the companion CFRP reinforced beams did not exhibit any plateau or descending branch in their load-deformation curves.

Figure 4.10 exhibits an initial response typical of reinforced concrete beam with a clear change in stiffness caused by cracking. Table 4.1 summarizes the values of the applied shear and internal forces corresponding to important points on these curves.

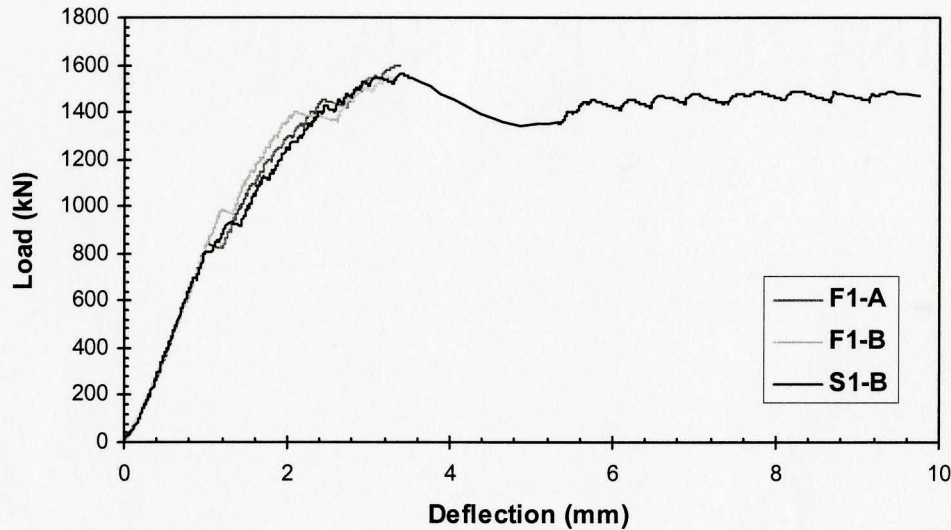


Figure 4.10: Complete load-deflection curves for the beams with $l_e/h=1$

The cracking load of beam S1-B appears to be lower than those of F1-A and F1-B, with the F1-B having the largest cracking load, which is almost 27% greater than that of S1-B. However, this difference cannot be ascribed to the presence of FRP only because the cracking load is sensitive to the tensile strength of concrete, which can be quite variable. On the other hand, the steel reinforcement has higher rigidity than the FRP reinforcement, which encourages early shrinkage cracking of concrete. The CFRP in this case also has negative coefficient of thermal expansion, which could impede or accelerate early cracking of concrete, depending on the thermal fluctuations experienced by the beam, particularly during the early hydration process of the cement which is accompanied by high temperature. Therefore, at this juncture, any comments with

regards to the beneficial effects of CFRP reinforcement on the cracking load of deep beams will be difficult to justify

After cracking, the steel reinforced beam exhibits the least stiffness. This is unexpected because the rigidity of the main longitudinal reinforcement in this beam is significantly higher than that of the companion FRP reinforced beams (refer to Table 3.5, Section 3.3 1). One explanation may be the presence of micro-cracks due to shrinkage and thermal deformations.

Figure 4.11 shows the load-deformation profile of the tested beams up to the maximum loads of the beams, and indicates that all the three beams essentially exhibit the same characteristics in the post-cracking regime up to the ultimate load. As indicated in Table 4.1, they have essentially the same failure load, with a maximum difference of less than 3% among them.

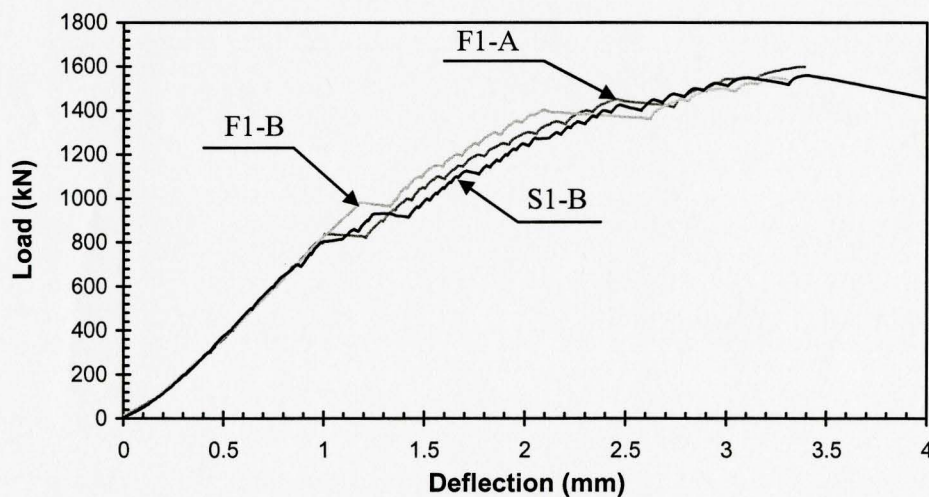


Figure 4.11 Load vs. mid-span deflection curves for the beams with $l_0/h=1$

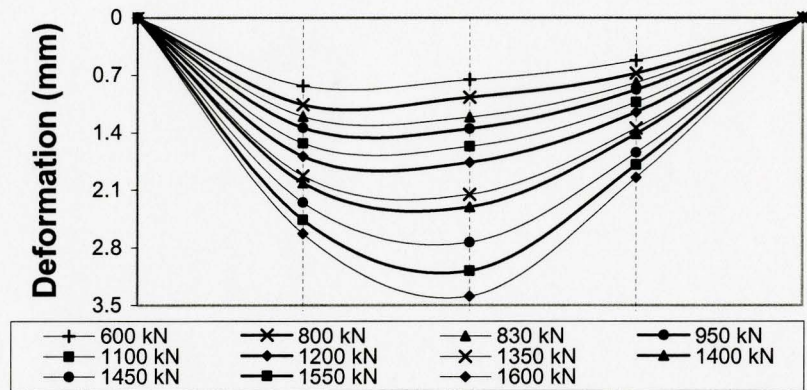
Figure 4.11 indicates that the CFRP deep beams experienced nonlinearity before reaching the maximum load. This nonlinearity is due to the combination of cracking and inelasticity of concrete and due to possibly partial bond loss.

Considering the results in Table 4.1, and load-deflection curves in Figure 4.10 and 4.11, it can be concluded that there is not a major difference between the behaviour of the CFRP reinforced beams and the steel reinforced beams up to the maximum load, but thereafter, the CFRP reinforced beams failed in a brittle manner while the steel reinforced beam exhibited noticeable ductility and post-peak load deformation with significant loss of strength. This type of behaviour is expected because CFRP is a linear elastic material while steel is an elasto-plastic material.

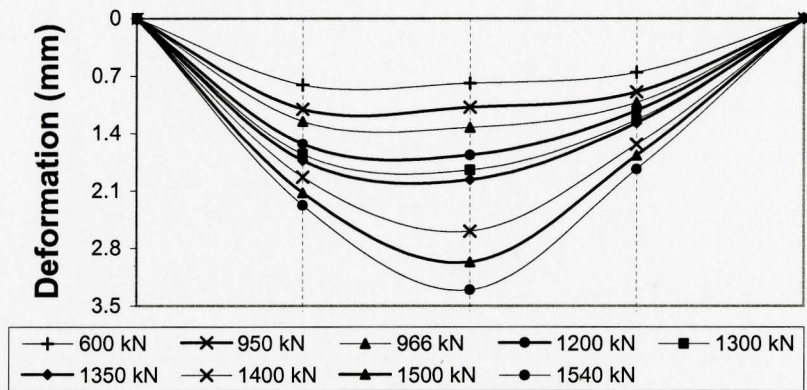
4.3.3 Deflected shape

Vertical deflection of each beam was monitored at three locations along its span (see Figure 3.25). At every point a pair of transducers was placed and the average value was used to plot the deformed shape of the tested beam. Figures 4.12a, b and c show the deformed shape of F1-A, F1-B and S1-B, respectively.

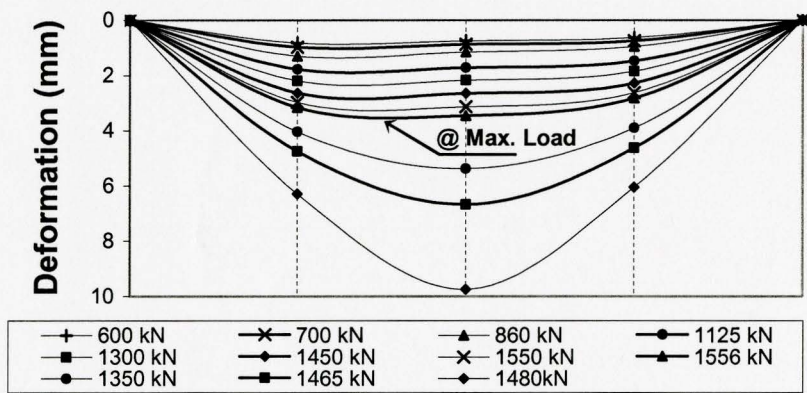
The selected loads in these figures correspond to the loads that represent a noticeable shift in the behavior of the beam. Note that in plotting the deformation profiles it was assumed that the reaction supports were completely rigid and did not deform during the test.



(a) Span deformation of F1-A beam



(b) Span deformation of F1-B beam



(c) Span deformation of S1-B beam

Figure 4.12. Deformed shape of the beams with $l_e/h=1$

The noticeable increase in the deflection of beam S1-B between 1556 kN and 1480 kN is due to the considerable widening of the critical crack and the crushing of concrete in the top compression zone between the applied loads. This event occurred after the peak load within the descending branch of the load-deflection curve. For the F1 beams the crushing of the compression zone occurred simultaneously with the interlaminar shear failure of the Isorod reinforcing bars, thus, there was no major increase in the width of the critical crack as the beams reached failure.

The deflected shapes show that prior to cracking, the deep beams do not exhibit the typical shape of the elastic curve of a beam under flexure. It can be observed in Figure 4.12 that all three points along the span of the beams exhibit practically equal deflection. This implies that flexural deformations may have been smaller than shear deformations therefore the middle half of the beam experienced essentially rigid body motion.

After cracking and at higher loads, the flexural stiffness of the beams decreased and the beams exhibited a deflected shape that is in agreement with the expected shape of a beam under flexure. Notice that none of the beams in this group lost much stiffness between the first cracking and the maximum load. The steel reinforced beam lost its stiffness quite dramatically after reaching its ultimate shear capacity. Thus, the steel reinforced beam experienced more deflection than the FRP reinforced beams near failure.

4.3.4 Strain in concrete

Six electrical strain gauges were used to monitor the strain distribution along the depth of each beam. Draw wire sensors were used to monitor the average strain along the axis of the diagonal struts. The local compressive and tensile strains in the concrete were measured at three points along the strut, in the middle and near the ends, using strain gauge rosettes. Figure 4.13 shows the strain gauge numbering system that was used in the analysis of the rosettes readings. More details about the instrumentation used to measure the concrete strains are given in Section 3.3.3 1 and presented in Figure 3.23

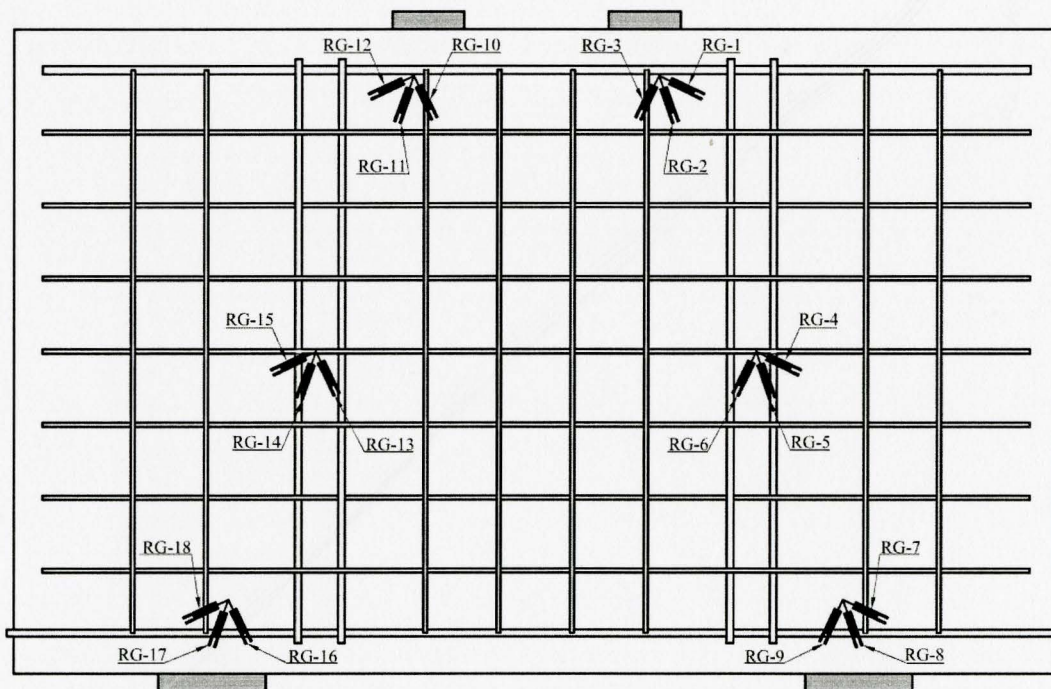
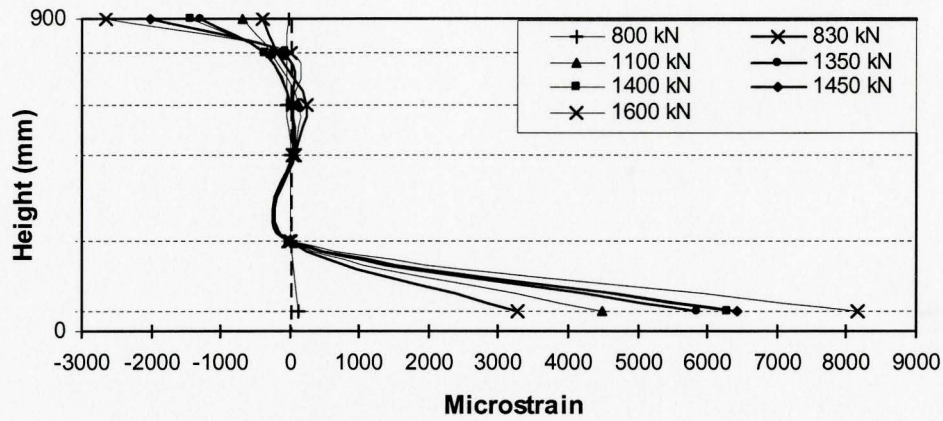


Figure 4.13 Rosette electrical strain gauge numbering for the tested beams

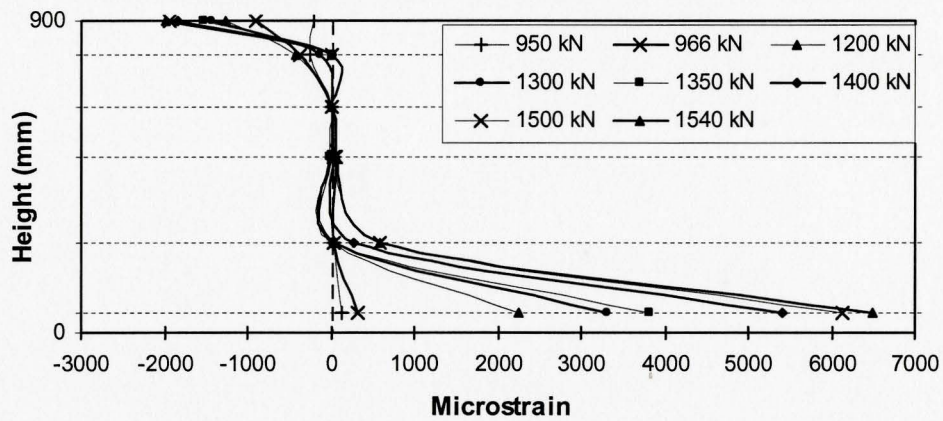
4.3.4.1 Mid-span strain profile

Figures 4.14a, b and c show the strain distribution along the depth of the specimens at the mid-span sections of beams F1-A, F1-B and S1-B, respectively. These figures clearly indicate a non-linear strain distribution along the depth of tested deep beams and show that the well known plane section remains plane theory of shallow beams does not apply to deep beams.

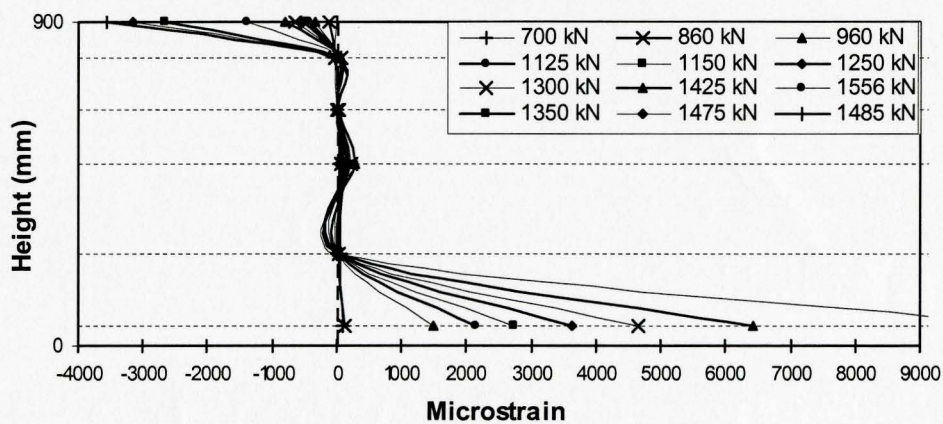
It is important to notice that the middle section of these beams experienced very little strains compared to the top and the bottom chords. Consequently, the beams act like an I-beam, with their top and bottom chords serving as flanges. Furthermore, after the initial cracking, there appears to be insignificant shift in the position of the neutral points along the height of tested beams. In other words, the neutral points along the height of the beam essentially remain stationary. Comparing the strain profiles for F1-A and F1-B beams with that for the S1-B beam, one can observe that they are very similar. This implies that the type of longitudinal reinforcement does not affect the strain profile of deep beams.



(a) Strain along the depth of the F1-A



(b) Strain along the depth of F1-B



(c) Strain along the depth of the S1-B

Figure 4.14: Strain distribution along the depth of the beams with span-to-depth ratio of 1

Since the main longitudinal reinforcement in beam S1-B yielded, it is possible to calculate the internal moment arm at ultimate load, by dividing the ultimate moment observed from the test $M_{uexp} = V_{uexp} \cdot a = 234 \text{ kN.m}$ by the maximum tie force $T = A_s f_u = 201 \text{ kN}$. Consequently, the internal moment arm is calculated as $z = M_{uexp} / T = 1.16 \text{ m}$, which is too large a value for the moment arm as it is larger than the actual height of the beam. There are two factors which may have contributed to this anomaly. First, the force in lower ribs of the welded-wire fabric must also be considered. Secondly, it may be more appropriate to calculate the external moment by using the clear shear span between the adjacent faces of the support plate and the loading plate. Using the clear span instead of the effective span is more reasonable because it is highly unlikely that any curvature could develop along the stiff loading plates. These adjustments result in a moment arm value equivalent to $0.67h$, which is slightly greater than the internal moment arm value of $0.6h$ as suggested by the European Concrete Committee (1964).

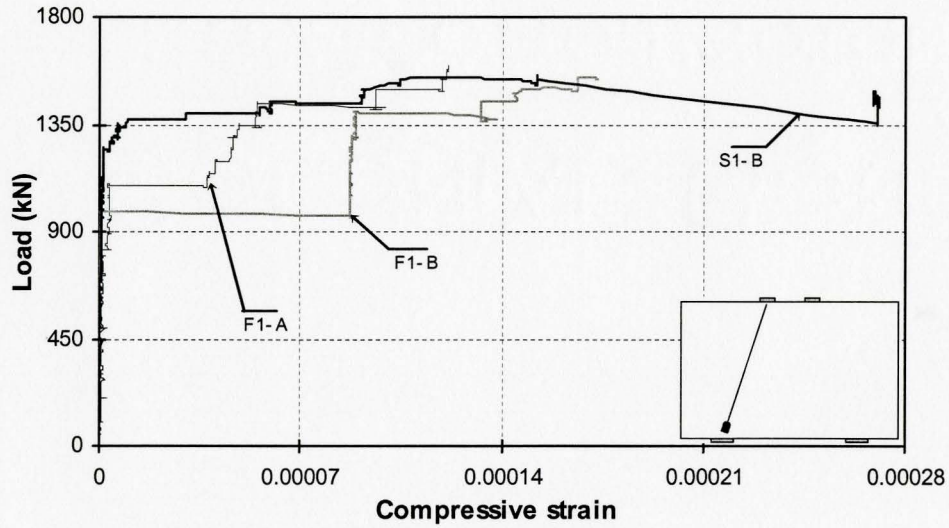
It is important to note that some strain gauges malfunctioned due to flexural cracks passing through them before the failure load was reached. More details about the mid-span strain distribution are provided in Appendix B, Figure B.2.

4.3.4.2 Strain along the compression struts

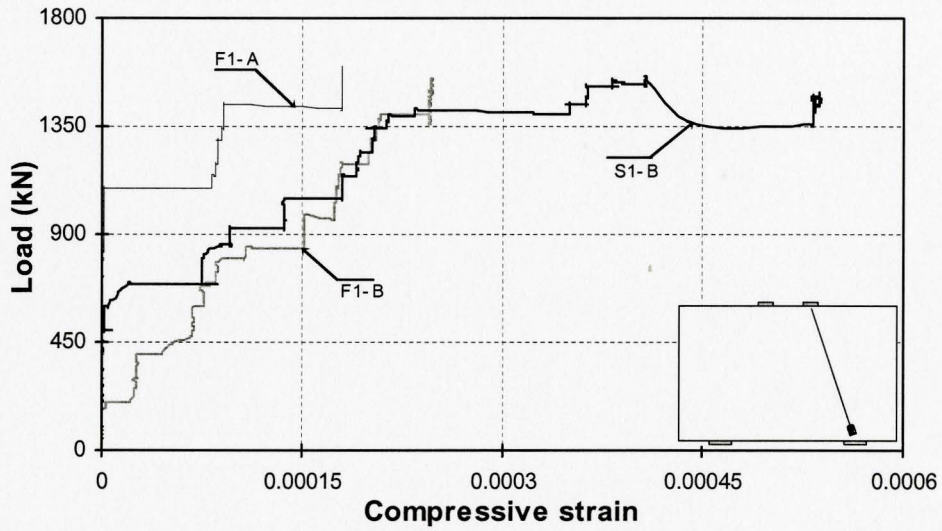
Figures 4.15a and b show the profile of the average strains along the axis of the diagonal struts for the tested beams with span-to-depth ratio of one.

The formation of inclined cracks caused a reduction in the effective width of the diagonal struts, which led to an increase in the diagonal compressive stresses and strains. Figure 4.15 shows the sudden increase in strain caused by the formation of diagonal cracks. Note that after the formation of the diagonal cracks, the average diagonal strains in the strut is not significantly affected by the type of reinforcement, and that the maximum value of the average strains did not exceed 0.0006, which is well below the failure strain of concrete.

For both CFRP reinforced deep beams the maximum average compressive strain at failure was observed in the east strut, and it ranged from 180 to 247 micro-strain, which is 8% to 10% of the maximum concrete compressive strain measured in the standard cylinder test on the day of the testing. The maximum average compressive strain in the control specimen S1-B was also recorded along the east strut as 532 micro-strain, which is 24% of the maximum compressive strain measured from the standard cylinder test. The fact that the average compressive strain along the struts was always well below the maximum compressive strain measured from the cylinder test, corroborates the absence of shear-compression failure along the struts.



(a) West diagonal strut



(b) East diagonal strut

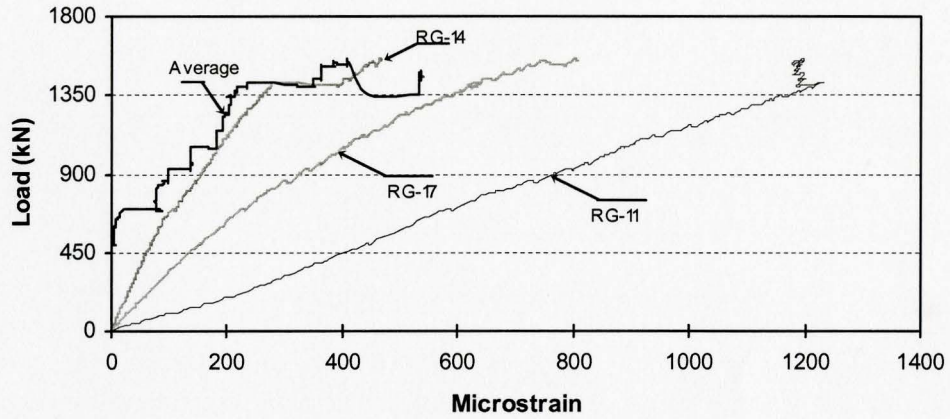
Figure 4.15 Average compression strain in the struts of the beams with span-to-depth ratio of 1

Figures 4.16 and Figure 4.17 show the variation of the average compressive strain captured by the draw-wire sensors and the three local

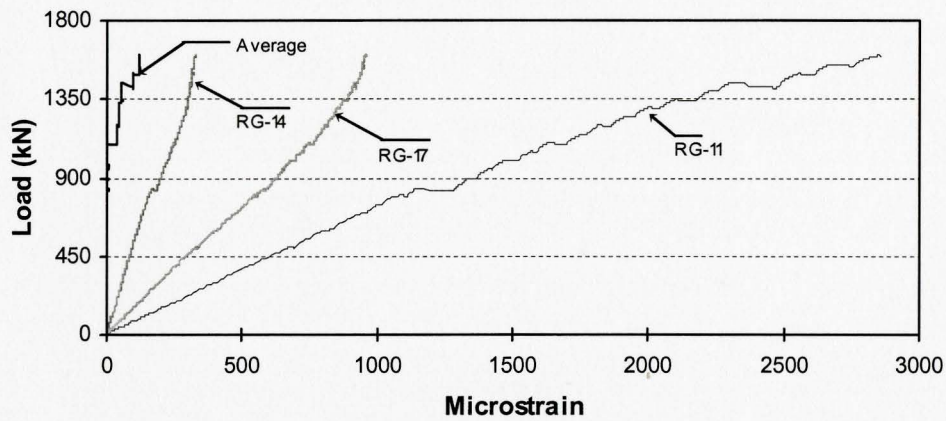
compressive strains measured by the strain gauge rosettes along the west and the east diagonal struts, respectively. It is evident that the average compressive strain in most cases underestimates the diagonal strain near the ends of the struts, but is closer to the local strain near the mid-length of the strut. Furthermore, this makes the assumption of a uniformly stressed diagonal strut connecting the CCC and CCT nodes questionable.

The strain plot in Figure 4.16 and 4.17 also show that the highest compressive strain values were recorded by gauges RG-11 and RG-2, which were located at the top ends of the west and east diagonal struts, respectively, as shown in Figure 4.13. Thus, from the compressive stress perspective, the most stressed points on the diagonal struts are located near the CCC nodal zones.

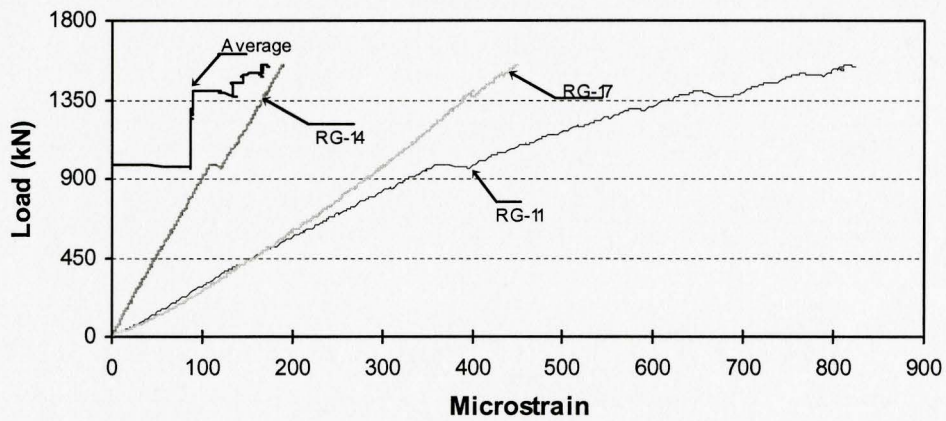
The plot of the local compressive strain readings can be used to determine the type of compression strut formed and to identify the critical areas along the axis of the struts most susceptible to shear-compression failure. From Figures 4.16 and 4.17 it can be noted that the middle strain gauges (RG-14 and RG-5) detected the least compressive strains throughout the test, which signifies the formation of bottle-shaped diagonal struts. Furthermore, the readings of the top strain gauges (RG-11 and RG-2) show the highest compressive strain throughout the test, indicating the higher probability of shear-compression failure in the struts near the CCC nodal zones.



(a) S1-B beam

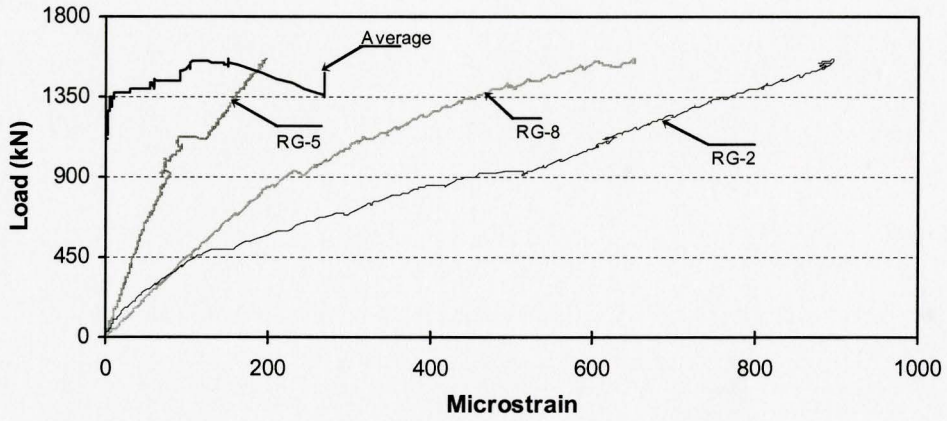


(b) F1-A beam

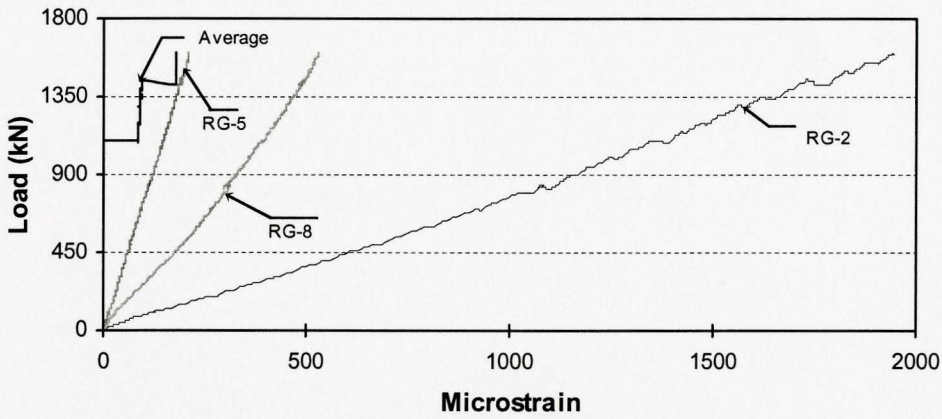


(c) F1-B beam

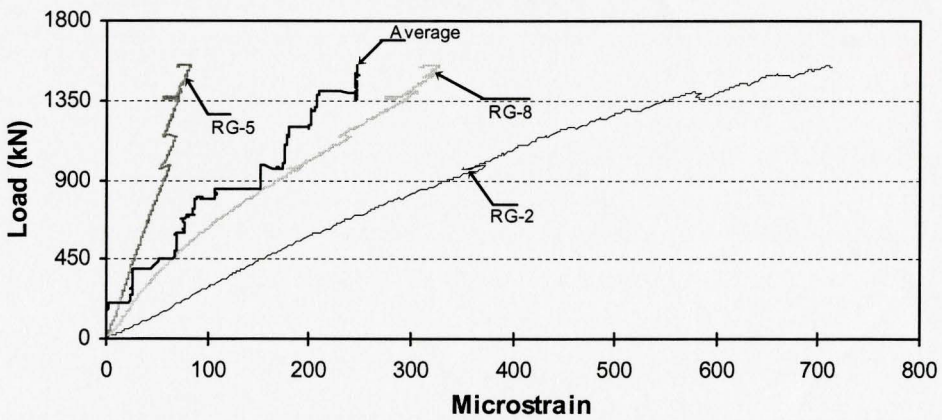
Figure 4.16: Compression strain comparison in the west strut for beams with span-to-depth ratio of 1



(a) S1-B beam



(b) F1-A beam



(c) F1-B beam

Figure 4.17 Compression strain comparison in the east strut for beams with span-to-depth ratio of 1

The three components of the rosette strain gauges were used to calculate the principal compressive and tensile strain in the diagonal struts. The maximum principal compressive strains for the specimens F1-A and F1-B were 2856 and 1391 micro-strain, while for the S1-B beam it was 2043 micro-strain. These strain values indicate the presence of relatively high local stresses in specimens F1-A and S1-B. However, relating the local strain in concrete to its average stress is difficult because local strains in concrete can exhibit relatively large fluctuations. On the other hand, the maximum principal compressive strain for all the deep beams with span-to-depth ratio of 1 was detected at the top of the west diagonal strut. The maximum measured principal tensile strain for specimen S1-B, F1-A and F1-B was 583, 515 and 826 micro-strain, respectively. These tensile strain values are all greater than the computed cracking strain of about 127 micro-strain for the 33 MPa concrete used in this study. The preceding cracking strain is based on the modulus of rupture of concrete as defined in the CSA standard A23.3.

Figure 4.18 shows the plot of the local strains normal to the axis of the east and the west diagonal struts. These strains do not show a consistent trend in all the beams, or consistency between the east and west struts in the same beam. It appears that generally at the top end of the strut, the strain normal to the axis of the strut is compressive, near the middle it is small but tensile and at the bottom it may be tensile or compressive.

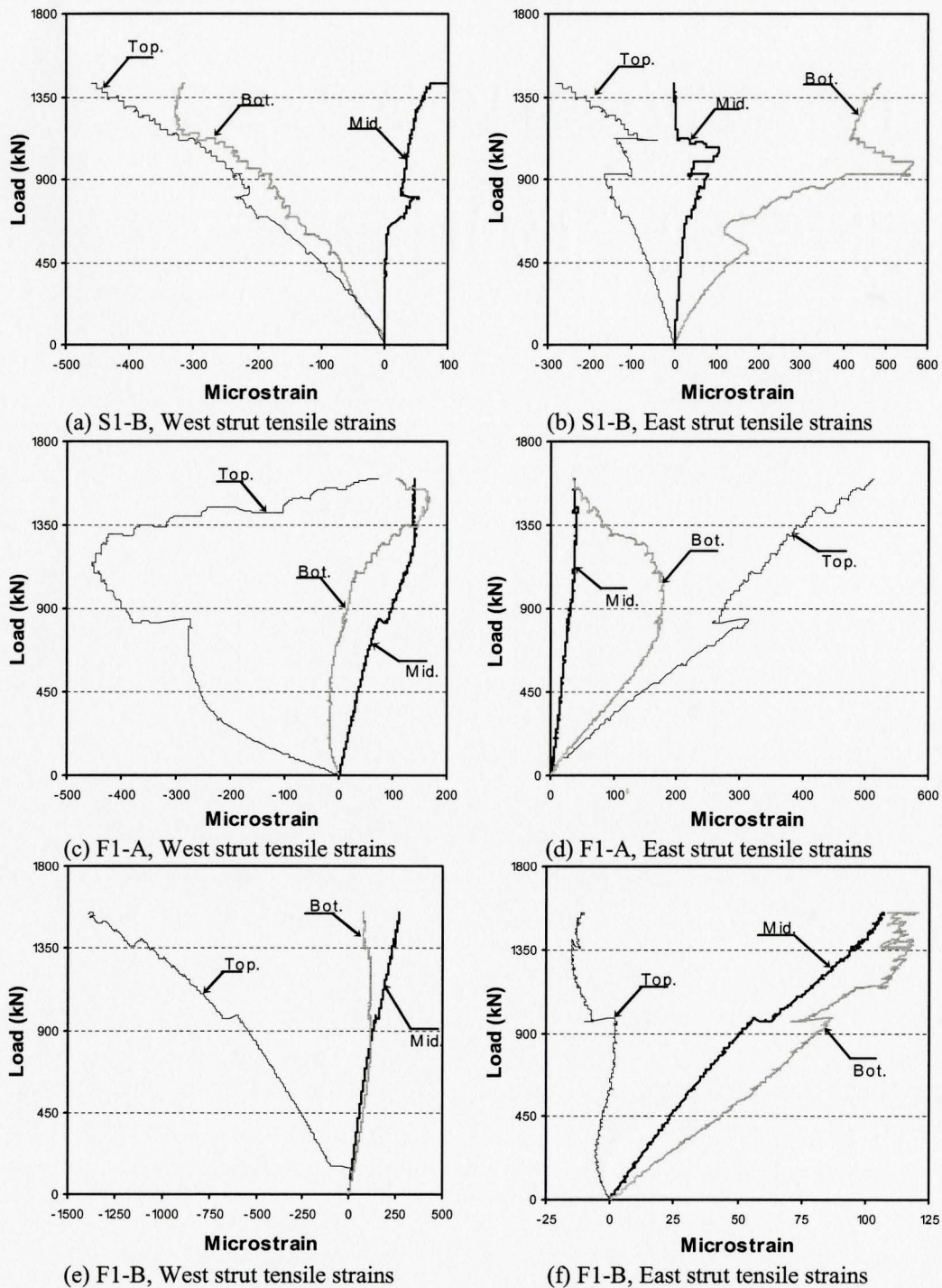


Figure 4.18. Strain measurements normal to the axis of the diagonal struts in the beams with span-to-depth ratio of 1

4.3.5 Strain in reinforcement

A total of 17 strain gauges were used to monitor the strain in the reinforcement, with 12 gauges attached to four stirrups and 5 affixed to the longitudinal reinforcement. To facilitate the comparison, the strain gauges locations were the same in the three beams tested in this group. The positions and the numbering of the strain gauges attached to the stirrups are illustrated in Figure 4.19

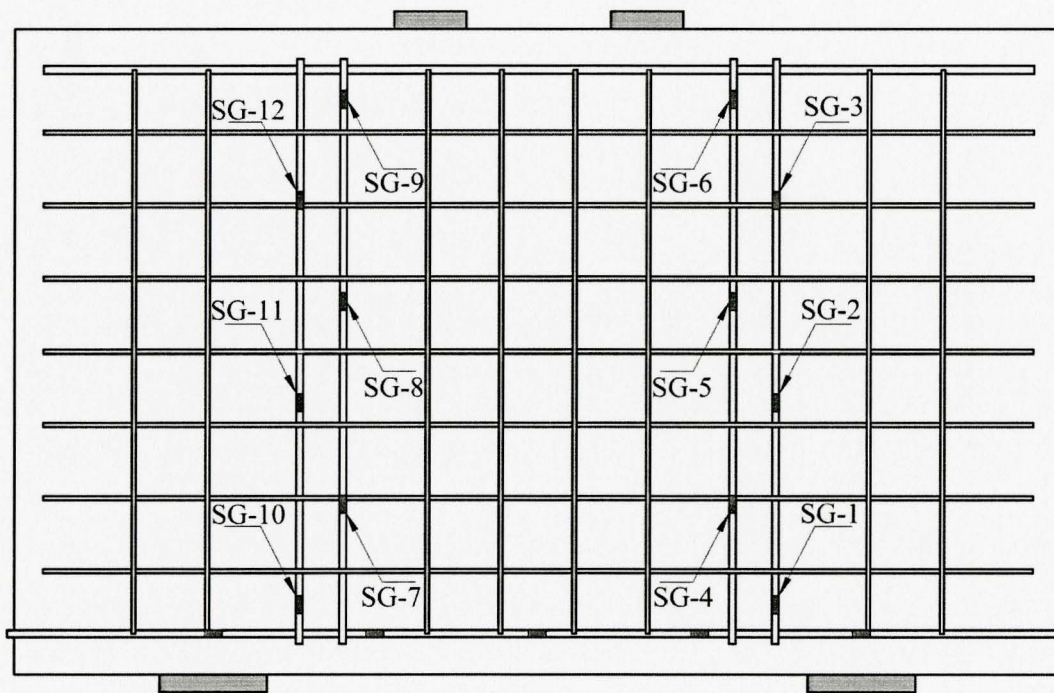


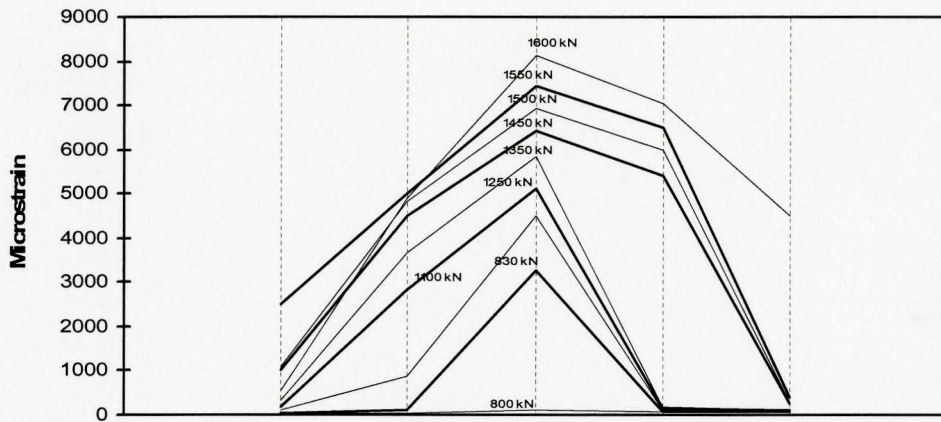
Figure 4.19: Strain gauge numbering and position in all the beams except beam S2

4.3.5.1 Strain in longitudinal reinforcement

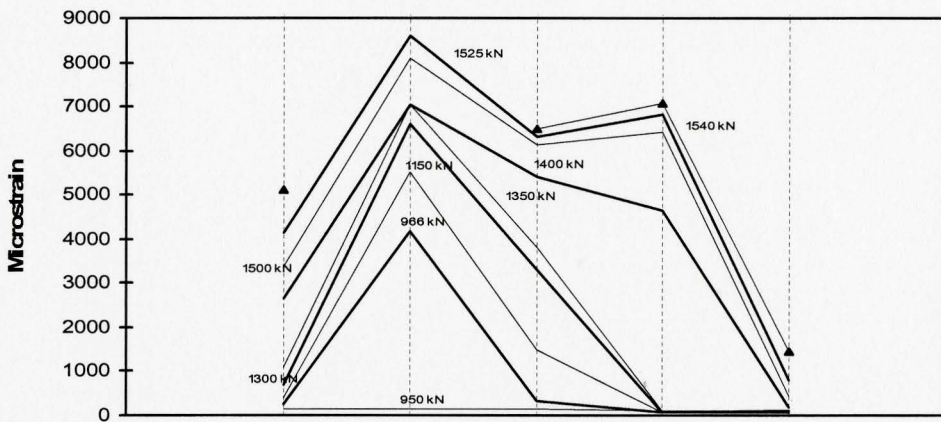
Figures 4.20a, b and c show the strain variation along the length of the longitudinal reinforcements for specimens F1-A, F1-B and S1-B, respectively.

It was observed that prior to the formation of cracks the strain distribution in the longitudinal reinforcement roughly followed the profile of the bending moment indicating that the reinforcement was mainly resisting flexure since the uncracked concrete could resist the shear without the assistance of the reinforcement. As it can be seen from the figure the strain distributions for the three specimens are similar, with the maximum strain near the mid-span of the beam and a gradual decrease of strains towards the supports. Note, however, that for the S1-B beam the strain in the steel bars near the support increased substantially as the maximum applied load was reached. This may be attributed to partial loss of bond, thus mobilizing arch action in the beam, or to the effect of shear on the tensile stresses in the longitudinal steel, or a combination of the two actions.

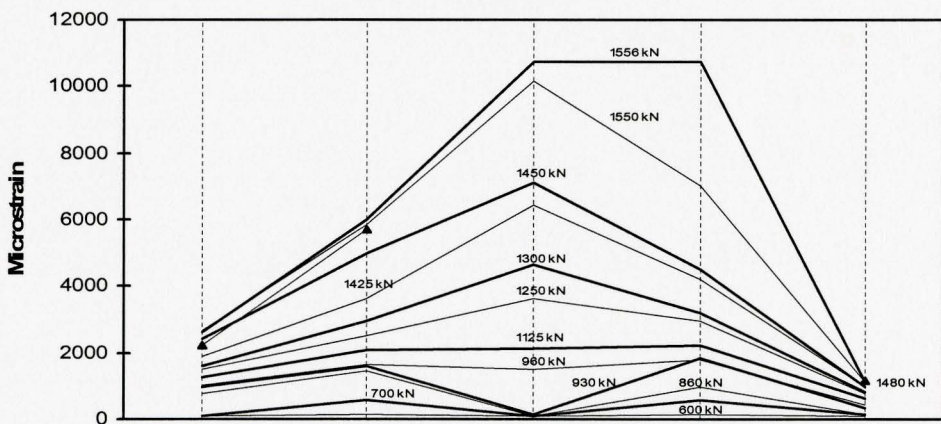
The lack of symmetry in the longitudinal strain distributions shown in Figure 4.20 can be attributed to the formation of unsymmetrical cracks relative to the location of the strain gauges on the longitudinal bar.



(a) F1-A beam



(b) F1-B beam



(c) S1-B beam

Figure 4.20: Strain distribution along the longitudinal reinforcement of the beams with span-to-depth ratio of 1

As the flexural cracks appeared, within the constant moment region, the strains in the reinforcement near the mid-span of the beam increased rapidly, while the strain remains negligible near the supports. With the formation of the inclined cracks the strains near the supports started to increase and became more noticeable as the beam approached failure.

The maximum measured tensile strain in the Isorod bars at failure ranged between 8150 and 8600 micro-strain, which are below the ultimate value of 12000 micro-strain reported by Benmokran et al. (2002), for this type of CFRP bar. The maximum measured tensile strain in the steel longitudinal reinforcement at failure was 10730 micro-strain, which is almost 12% of the measured rupture strain of No.10 reinforcement, and nearly five times the yield strain of a typical grade 400 steel reinforcement.

The maximum tensile stress in the CFRP longitudinal bar reached 1043 MPa and 1100 MPa, for the specimens F1-A and F1-B, respectively, while the maximum tensile stress near the supports was only half of the maximum stress in the span. The slope of the strain profile shown in Figure 4.20 is indicative of the level of bond stress resisted by the bar. If a uniform bond stress τ is assumed between the centerline of the support and the point load, then it can be calculated using the following equation:

$$\tau = \frac{(\sigma_{l_e/4} - \sigma_{sp})r}{2(l_e/4)} \quad (4.1)$$

where σ_s and $\sigma_{l_e/4}$ are, respectively, the stresses at ultimate load in the main longitudinal rebar at the center of the supports and at the $l_e/4$ distance away (within the shear-span), r is the radius of the bar and l_e is the span length of the beam.

Since CFRP is linear elastic, the stresses and strains can be related by Hooke's law, thus τ can be expressed in terms of the measured strains in the aforementioned locations

$$\tau = \frac{E_{FRP}r}{2(l_e/4)} (\varepsilon_{l_e/4} - \varepsilon_{sp}) \quad (4.2)$$

where E_{FRP} is the elastic modulus of CFRP Isorod reinforcement (taken as 128 GPa), ε_{sp} and $\varepsilon_{l_e/4}$ are the maximum measured strains in the longitudinal rebar at the center of the supports and $l_e/4$ distance away, respectively.

Using the strain values shown in Figure 4.20a and b, the average bond stress, τ , is approximately equal to 2.1 MPa for F1-A and 3.7 MPa for F1-B beam. The calculated τ values correspond to the strain values measured on the west side of the beam, as the anchorage failure occurred on that side for both F1 beams. Furthermore, the calculated average bond stresses are considerably smaller than the bond stress measured by Benmokran et al. (2002), as he found an average bond strength of 16.6 MPa for the same CFRP Isorod bar.

4.3.5.2 Strain in transverse reinforcement

As indicated in Figure 4.19, strain gauges were affixed to one leg of the stirrups, and they were numbered as shown in the figure. The strain readings in the stirrups were found to be sensitive to the location of the gauge relative to the diagonal cracks. It may be recalled that beams F1-A and F1-B had CFRP NEFMAC stirrups while beam S1-B had steel stirrups.

Figures 4.21, 4.22 and 4.23 show the strain distribution in the stirrups of the specimens F1-A, F1-B and S1-B, respectively. Figures 4.21 and 4.22 indicate that the stirrups in the FRP reinforced beams remained in compression throughout the testing, which suggests the lack of need for transverse reinforcements in beams F1-A and F1-B. This behaviour is engendered by the mode of failure of these beams and the fact that that they did not develop shear cracks. Consequently, the shear reinforcement was not mobilized.

In the case of the control beam S1-B, with the advent of the inclined cracks crossing the stirrups, the compressive strains in the stirrups suddenly shifted to tensile strain, as shown in Figure 4.23. The figure shows large strain readings, reaching 50% to 60% of the yielding strain of steel, especially by gauges that were either crossed by or were proximate to diagonal cracks within the shear span.

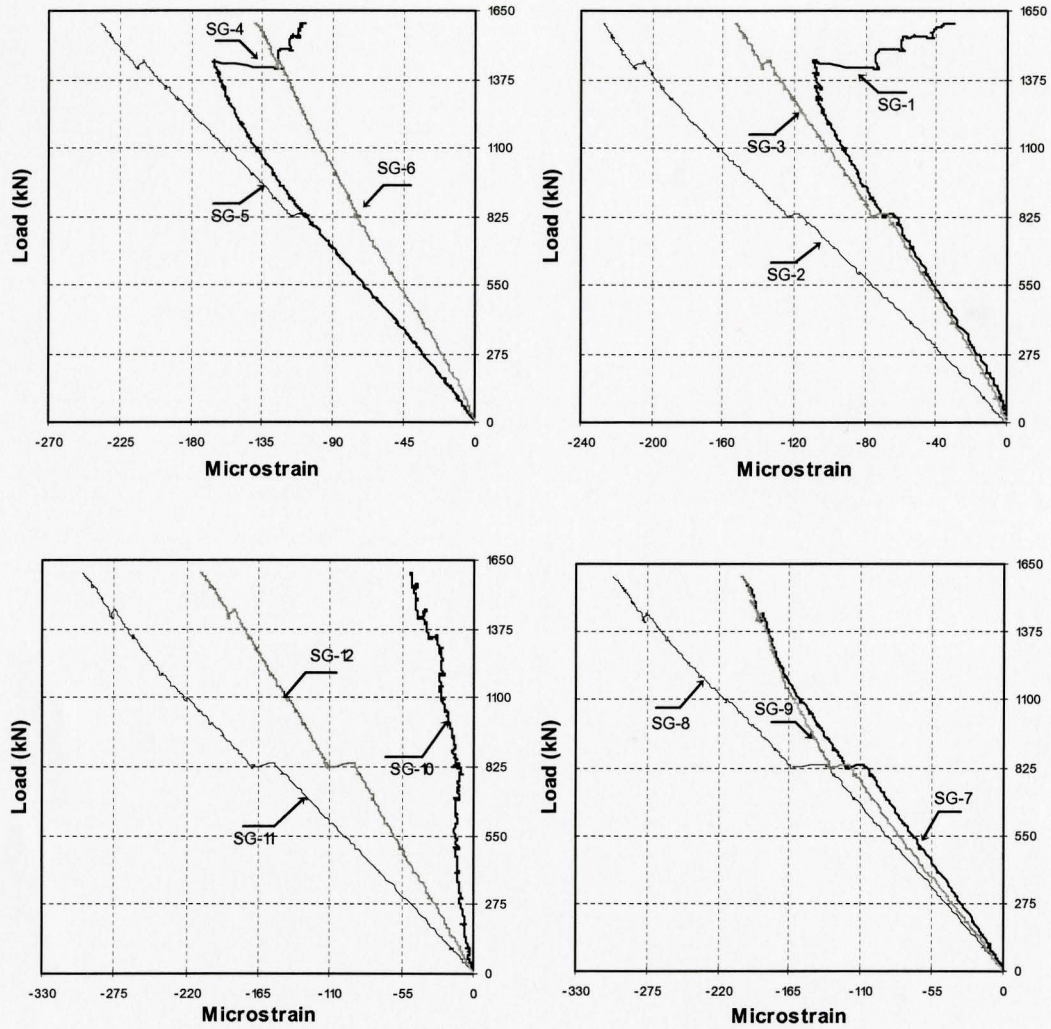


Figure 4.21 Load-strain relationships in the stirrups of F1-A beam

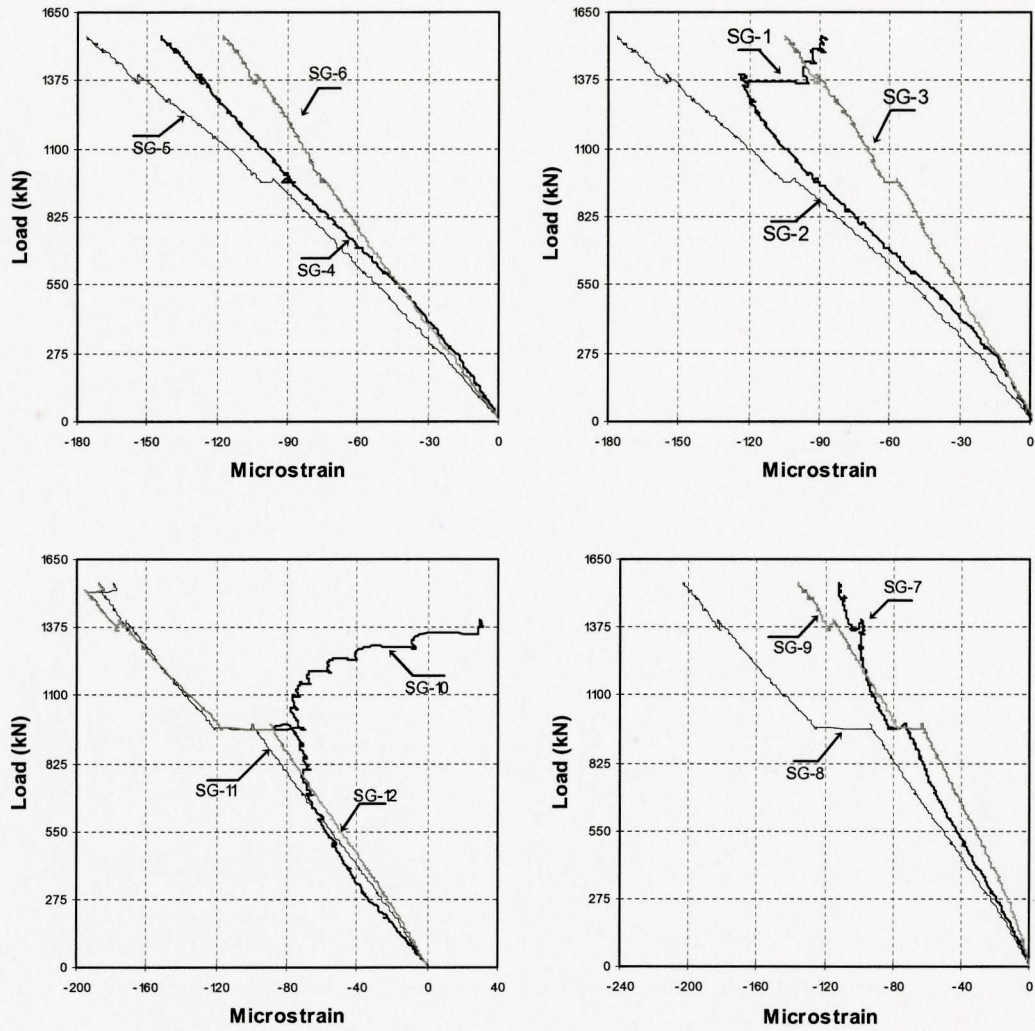


Figure 4.22. Load-strain relationships in the stirrups of F1-B beam

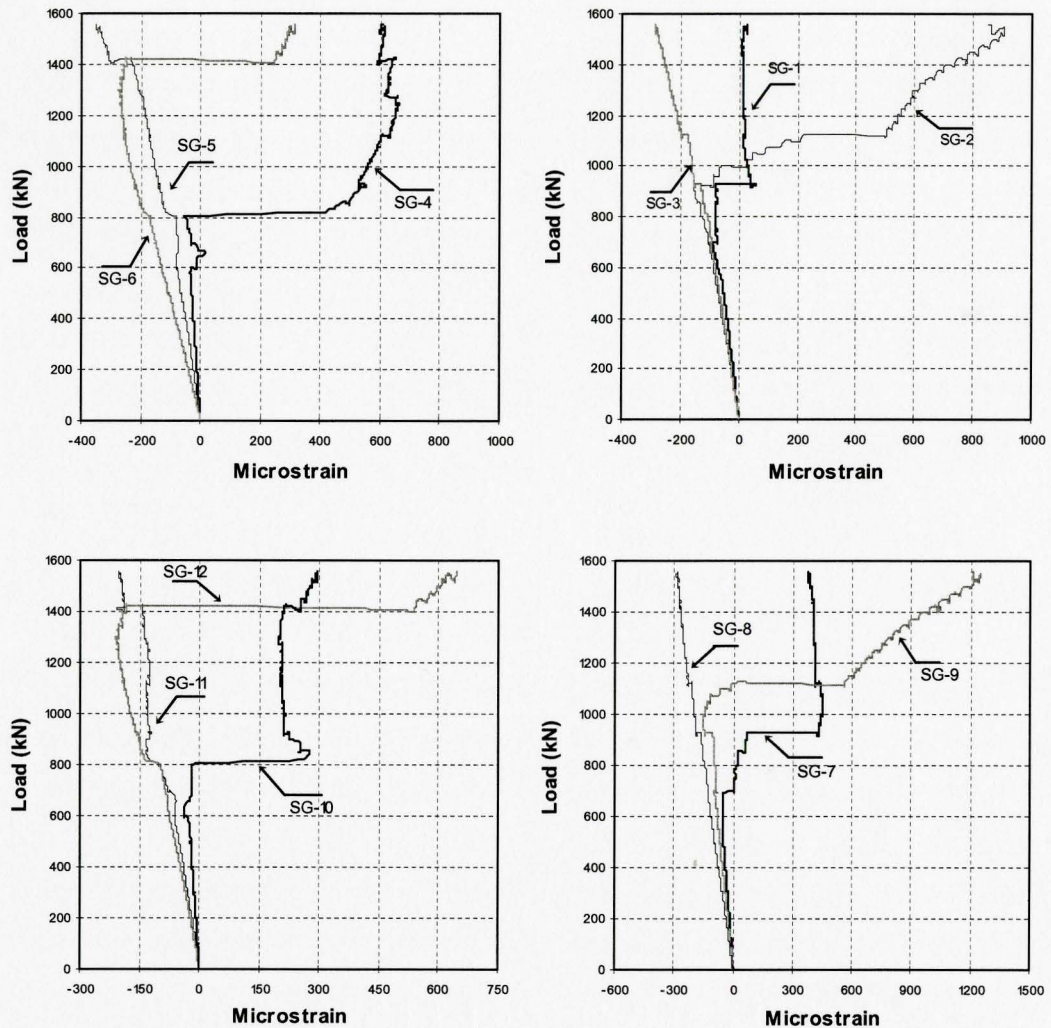


Figure 4.23 Load-strain relationships in the stirrups of S1-B beam

It is clear that the shear reinforcement actively contributes to crack control and shear resistance when diagonal cracks are formed. It is not evident why diagonal cracks did not form in the CFRP reinforced beams despite the fact that the ultimate shear forces carried by these beams were practically equal to that carried by the control beam. It is, however, well known that the rigidity of the

longitudinal reinforcement plays a role with regard to the shear resistance of shallow beams. If it yields, then it reduces the shear resistance of the beam and increases the shear reinforcement contribution to the total shear resistance of the beam. However, for such shift to occur, shear cracks must form. The lack of shear cracks in the CFRP reinforced beams may be due to the smaller restraining effect of the CFRP on concrete shrinkage and consequently smaller shrinkage induced stresses.

Finally, in the light of the relatively high stresses in the steel stirrups, it is not clear why the CSA standard A23.3 does not require stirrups in deep beams. It would be informative if nominally identical deep beams with and without stirrups were tested to find out the degree of contribution of the stirrups to the resistance of such beams.

4.4 Beams with Span-to-Depth Ratio of 2

Similar to the beams tested in the first group, in the second group one specimen was reinforced with steel and the other two were reinforced with CFRP. The beams in this group were designated as S2, F2-A and F2-B. These beams were loaded monotonically up to failure and their response was studied.

Beams S2, F2-A and F2-B were tested at the age of 163, 170 and 178 days after casting, respectively. The results of the standard cylinder tests at these ages are provided in Appendix C, Tables and Figures C.2 and C.3.

The following sections present the experimental results for the beams with span-to-depth ratio of 2, with some important data listed in Table 4.2. Additional record of the beams' behaviour can be found in Appendix B, Figures B.7 to B.12.

Table 4.2. Test results for the beams with span-to-depth ratio of 2

Beam	Ultimate load (kN)	Ultimate shear V_{uexp} (kN)	Flexural cracking load (kN)	Shear cracking load V_{crexp} (kN)	Mid-span deflection (mm)		Failure mode
					After flexural cracking	at the ultimate load	
F2-A	1236	618	300	375	0.8	10.65	F/S
F2-B	1300	650	225	375	0.81	10.9	F/S
S2	1206	603	250	400	0.76	8.5	F

Note:

F = Flexural failure

F/S = combination of flexural and shear failure

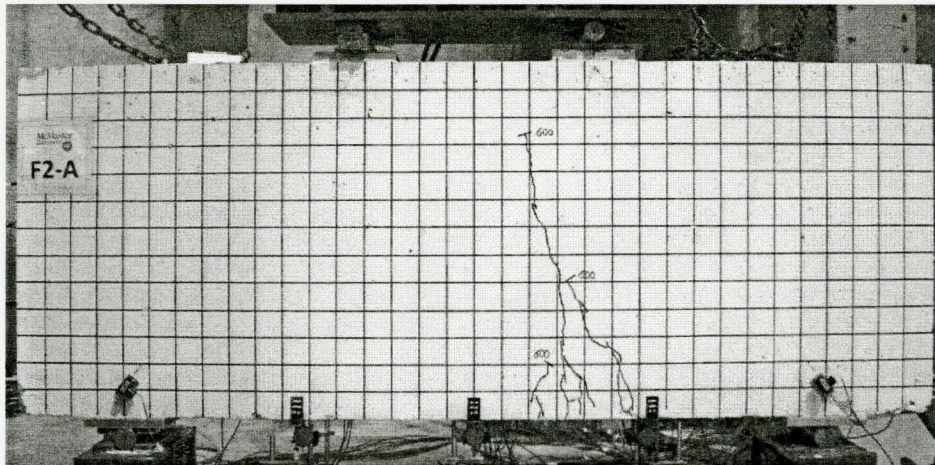
Shear span=600 mm

4.4.1 Observed behaviour of tested beams

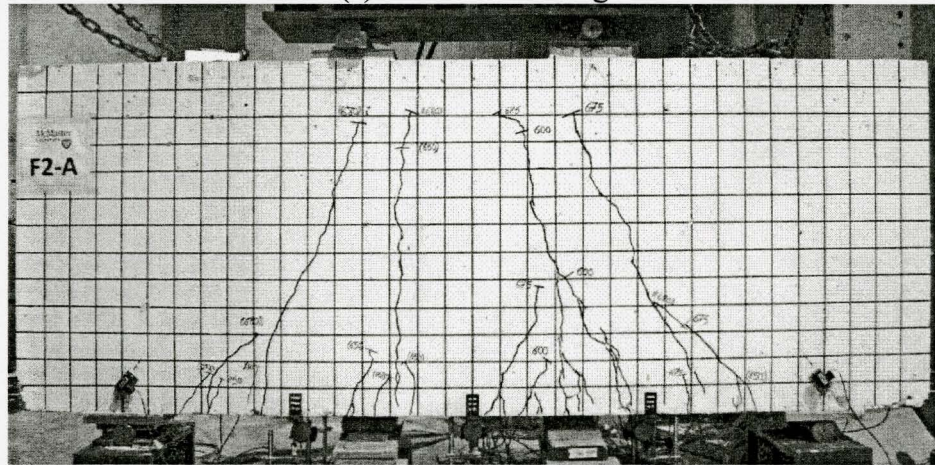
Figures 4.24, 4.25 and 4.26 show the development of cracks in beams F2-A, F2-B and S2, respectively, at three different stages of loading. The crack pattern just before failure of the beams tested in this group is illustrated schematically in Figure 4.27

Table 4.2 presents a summary of the overall behaviour of these beams, including their ultimate capacities and failure modes. In the S2 beam the crushing of concrete was primarily due to the formation of the flexural cracks, while in the corresponding CFRP beams the presence of both flexural and shear cracks led to crushing of the concrete near one of the loading plates.

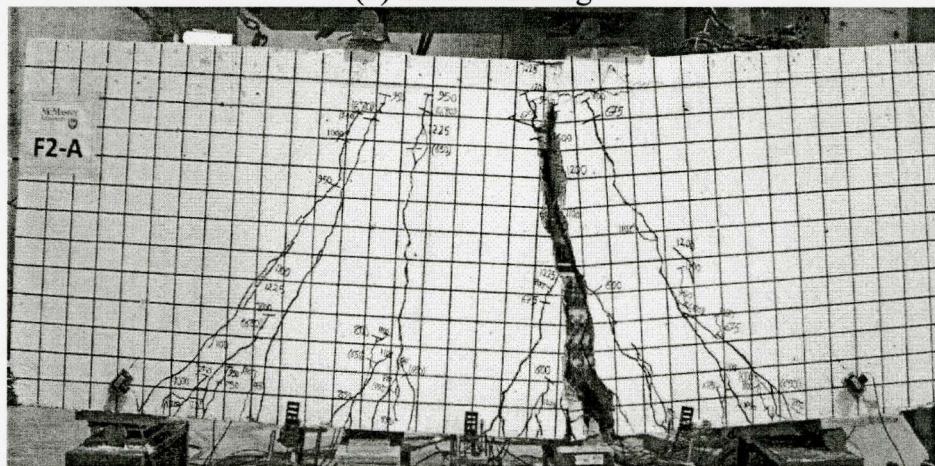
Beams F2-A and F2-B experienced the first crack at a shear force of 300 kN and 225 kN, which correspond to 49% and 35% of the ultimate shear capacity of the beams, respectively. The initial crack in both beams was deemed to be a flexural crack as it appeared at mid-span of the beam within the region of pure bending. Similar to the F1 beams in the first group, the initial cracks in the CFRP reinforced beams were relatively long, resulting in a considerable energy release. The first shear crack in F2-A and F2-B was detected at the shear force of 375 kN, corresponding to 60% and 58% of their respective ultimate shear capacities. These shear cracks initiated from the inner edge of the east support plate and propagated diagonally towards the east loading plate.



(a) Flexural cracking

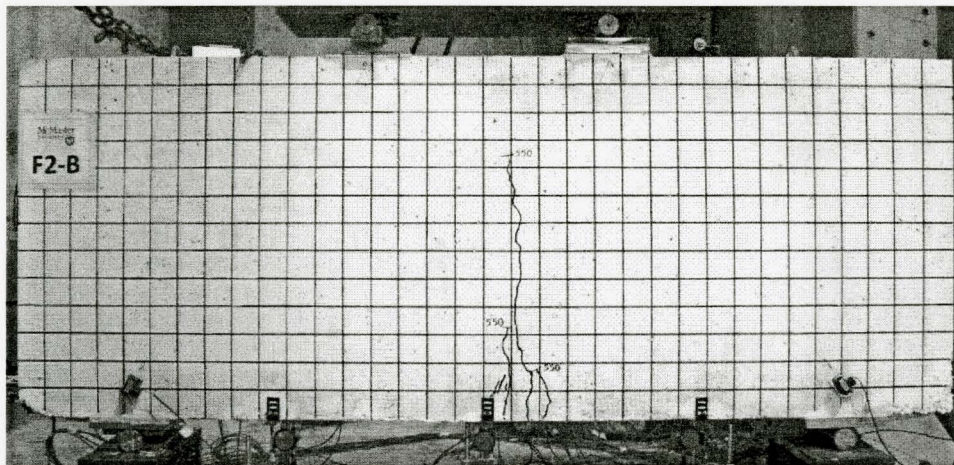


(b) Shear cracking

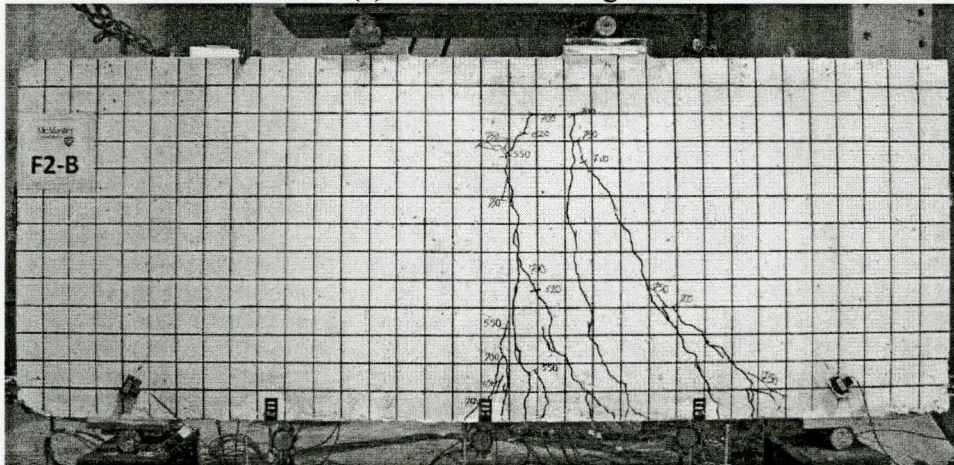


(c) At failure

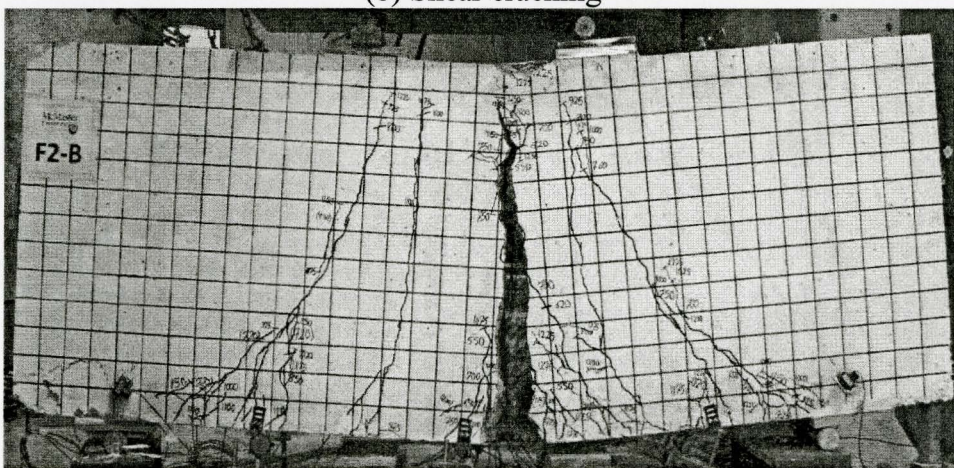
Figure 4.24: Cracking development in the F2-A beam



(a) Flexural cracking

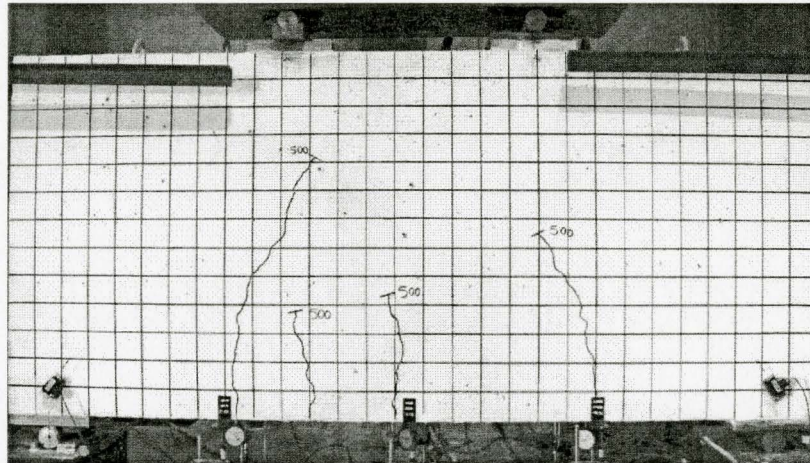


(b) Shear cracking

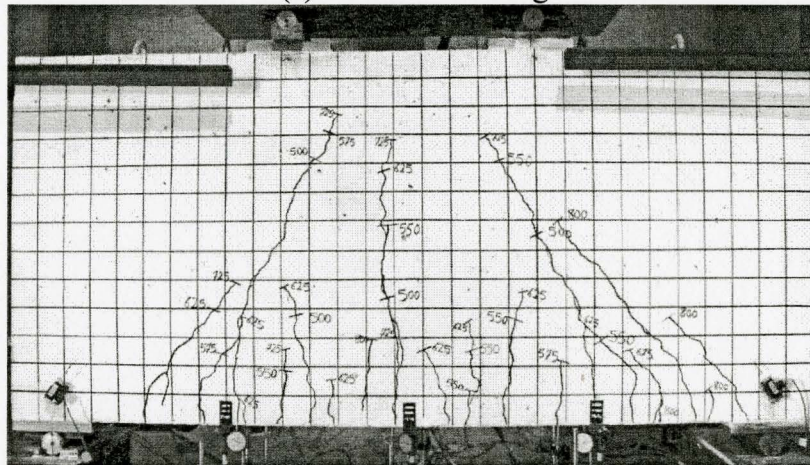


(c) At failure

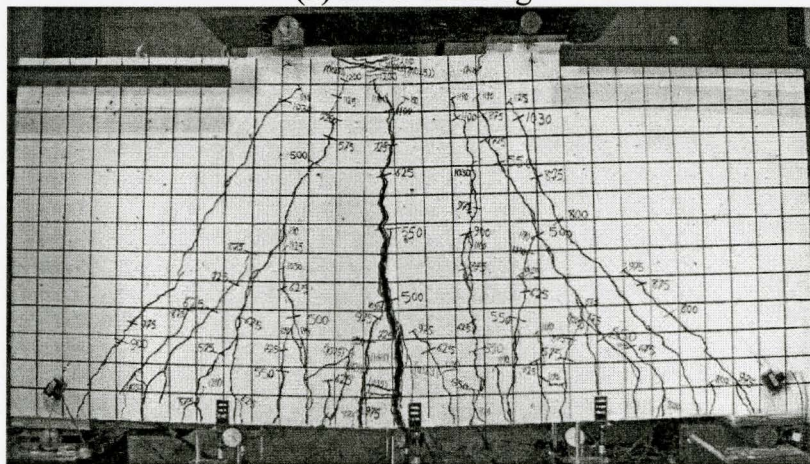
Figure 4.25 Cracking development in the F2-B beam



(a) Flexural cracking



(b) Shear cracking



(c) At failure

Figure 4.26: Cracking development in the S2 beam

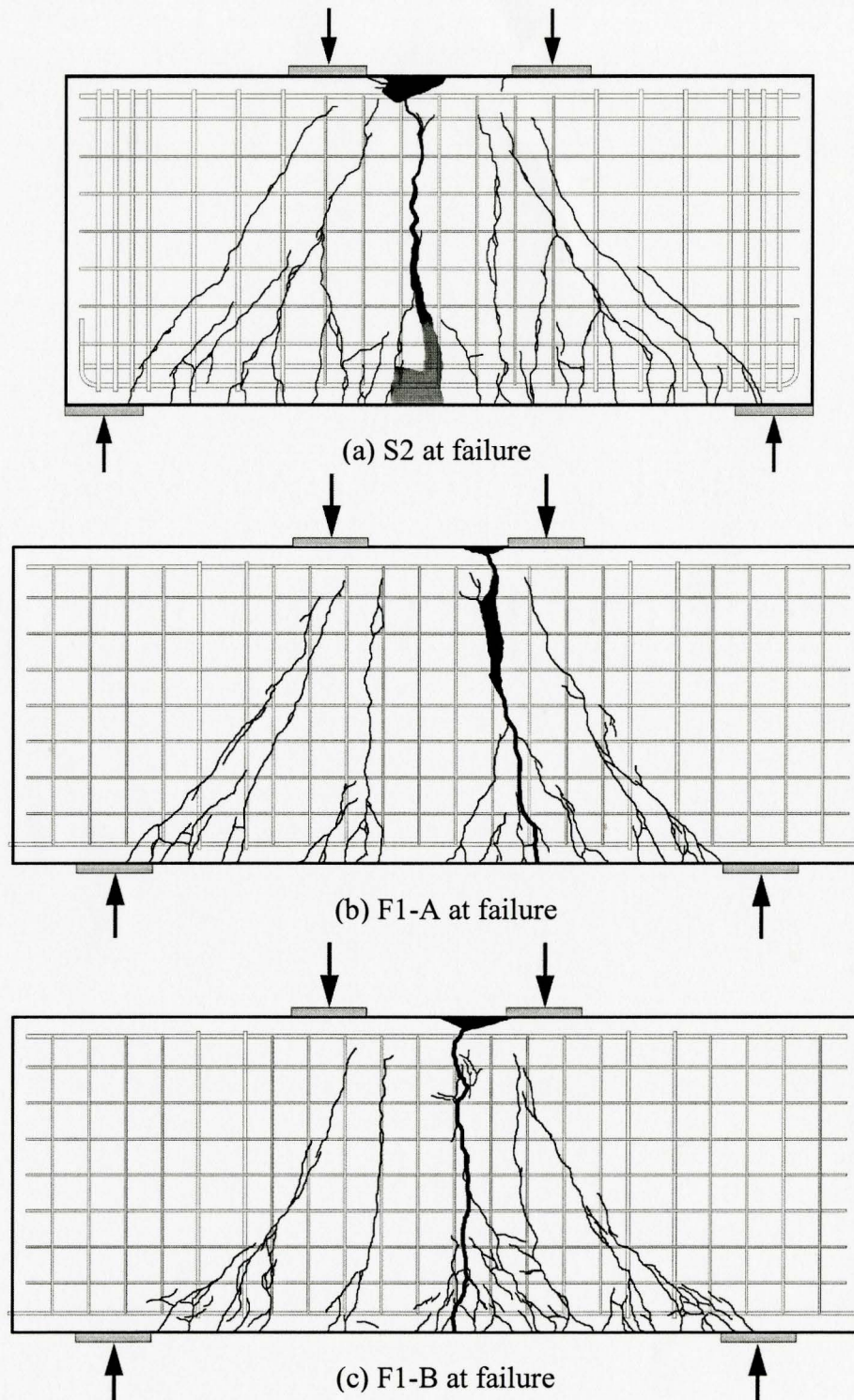


Figure 4.27 Schematic view of the crack pattern for the beams with $l/d=2$

With reference to Figure 4.26a, the control specimen S2 experienced four cracks simultaneously as the shear force reached 250 kN, which corresponds to 41% of the ultimate shear capacity of the beam. Two of these cracks started in the pure bending region and therefore were considered as flexural cracks, while the two outer cracks were considered as shear-flexural cracks, due to their vertical-diagonal orientation. As the load increased, the foregoing shear-flexural cracks turned to shear cracks and propagated diagonally towards the mid-span of the beam. The first shear crack appeared at a shear force of 400 kN or 66% of the ultimate shear capacity of the beam. The first shear crack for this beam, similar to the CFRP reinforced beams, started at the inner edge of the east support plate.

It can be noticed that the cracking loads of the F2-B beam is approximately 10% lower than that of the companion control beam, while in the first group all the CFRP reinforced beams exhibit higher cracking loads than the counterpart steel reinforced beam. This may indicate that in addition to the type of reinforcement, the span-to-depth ratio could also affect the flexural and shear cracking load of deep beams. Of course due to the higher rigidity of the steel reinforcement, the moment of inertia of beam S2 is expected to be a little higher than those of F2-A and F2-B. Hence, the CFRP reinforced beams will experience somewhat higher flexural stresses than the steel reinforced beam, and this could lead to earlier cracking. On the other hand, the restrained shrinkage stresses may induce earlier cracking in the steel reinforced beam. It is not always easy to

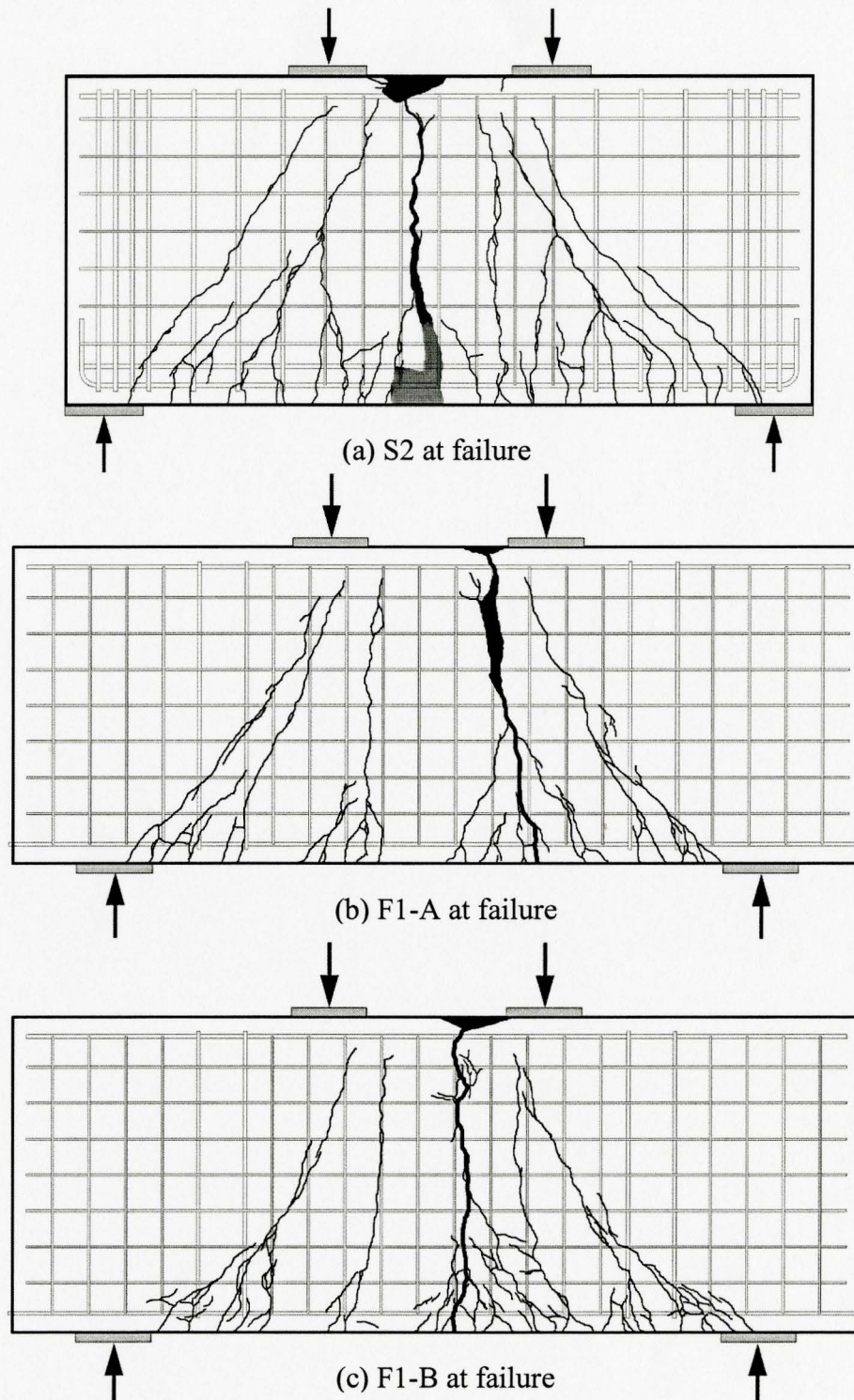


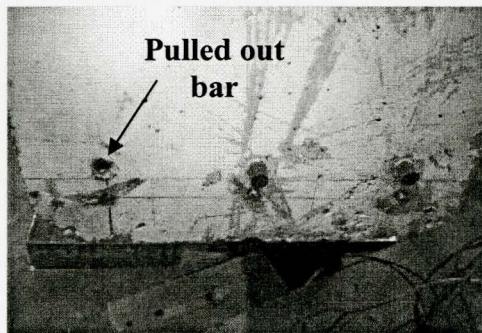
Figure 4.27 Schematic view of the crack pattern for the beams with $l/d=2$

With reference to Figure 4.26a, the control specimen S2 experienced four cracks simultaneously as the shear force reached 250 kN, which corresponds to 41% of the ultimate shear capacity of the beam. Two of these cracks started in the pure bending region and therefore were considered as flexural cracks, while the two outer cracks were considered as shear-flexural cracks, due to their vertical-diagonal orientation. As the load increased, the foregoing shear-flexural cracks turned to shear cracks and propagated diagonally towards the mid-span of the beam. The first shear crack appeared at a shear force of 400 kN or 66% of the ultimate shear capacity of the beam. The first shear crack for this beam, similar to the CFRP reinforced beams, started at the inner edge of the east support plate.

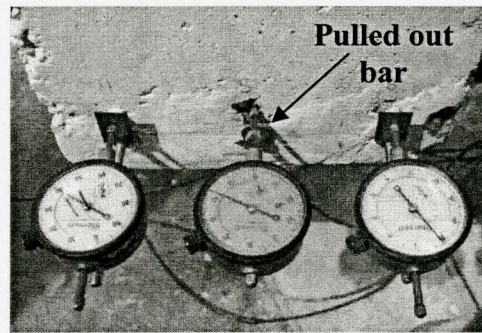
It can be noticed that the cracking loads of the F2-B beam is approximately 10% lower than that of the companion control beam, while in the first group all the CFRP reinforced beams exhibit higher cracking loads than the counterpart steel reinforced beam. This may indicate that in addition to the type of reinforcement, the span-to-depth ratio could also affect the flexural and shear cracking load of deep beams. Of course due to the higher rigidity of the steel reinforcement, the moment of inertia of beam S2 is expected to be a little higher than those of F2-A and F2-B. Hence, the CFRP reinforced beams will experience somewhat higher flexural stresses than the steel reinforced beam, and this could lead to earlier cracking. On the other hand, the restrained shrinkage stresses may induce earlier cracking in the steel reinforced beam. It is not always easy to

precisely qualify the latter stresses due to the many factors which govern shrinkage of concrete.

Figures 4.27b and c, show that the crack pattern and the failure mode of beams F2-A and F2-B are similar. The initial flexural crack in these beams propagated vertically upward and continued to reduce the cross-sectional area of the top, or horizontal, strut until it caused crushing of the concrete at 1225 kN. For both specimens the crushing of the top strut was followed by the anchorage failure of the longitudinal reinforcement at the east end of the beam. It should be noted that in both beams only one rebar was found to be pulled inside the beam. Similar to the anchorage failure observed in F1 beams, the loss of bond occurred between the cover and the core of the Isorod bar due to interlaminar shear failure of the reinforcement, as shown in Figure 4.28. Unfortunately, the end dial gauges were not able to measure any gradual slippage during the test as the anchorage failure occurred suddenly



(a) F2-A reinforcement slippage



(a) F2-B reinforcement slippage

Figure 4.28 Anchorage failure of the CFRP reinforced beams with $l_e/h=2$

The failure of the S2 beam is shown schematically in the Figure 4.27a. It is evident that the critical flexural crack in the pure bending region propagated vertically upward and ultimately caused flexural failure through crushing of the top strut, at a maximum load of 1200 kN. Similar to S1-B beam, the full response of the S2 beam was captured by loading the beam up to the point of rupture of the longitudinal reinforcement. Finally, the number of cracks forming in the CFRP reinforced beams was comparable to those in the control beam, which indicates that the CFRP and steel reinforced beams tested in this group behaved very similarly.

4.4.2 Load-deflection response

The load-deflection response of the beams was obtained by utilizing the same type of instrumentation as that for the first group of beams. Figure 4.29 illustrates the complete load versus mid-span deflection curves for the tested beams in this group. Figure 4.30 shows a partial view of the load-deformation profile of these beams for better comparison. As indicated in Table 4.2, the beams in this group had approximately the same failure load, with a maximum difference of less than 8% among them.

Notice in Figure 4.30 that the cracking loads of S2 and F2-B beams are very close while that of F2-A beam is higher. The pre-cracked stiffness of all three beams is essentially equal; however, after the formation of the first major

crack, the steel reinforced member exhibits much higher stiffness. Furthermore, while beam S2 exhibit a nonlinear response after cracking, beams F2-A and F2-B show a roughly linear response up to failure. This essentially bilinear load-deflection response is typical for slender beams reinforced with FRP. This means that the behaviour of the beams with span-to-depth ratio of 2 appears to be dominated by flexure in contrast to the behaviour of the beams with the span-to-depth ratio of 1, which were dominated by shear deformation.

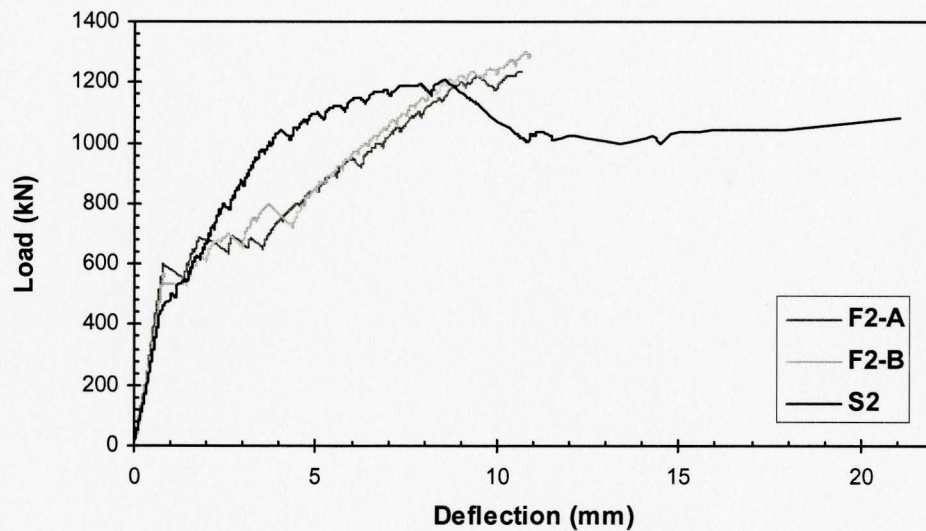


Figure 4.29: Complete load-deflection curves for the beams with $l_e/h=2$

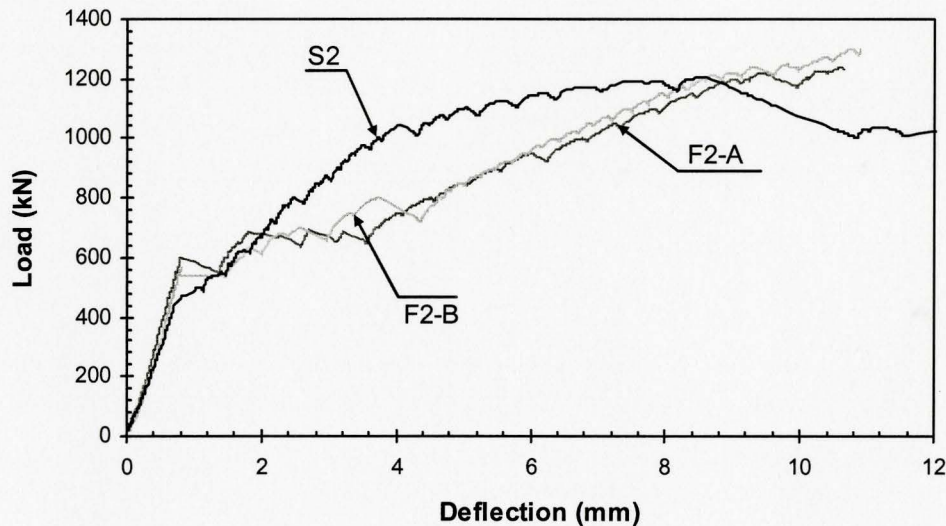


Figure 4.30: Load vs. mid-span deflection curves for the beams with $l_e/h=2$

The bilinear load deflection for the CFRP reinforced beams is indicative of the relatively small change in the neutral axis position caused by increased load. The constancy of the neutral axis position, irrespective of the load level, is indicative of elastic behaviour. Thus the CFRP reinforced beams tend to act similar to elastic members despite the nonlinearity of concrete. This indicates the dominant role of the properties of the longitudinal reinforcing bars on flexural response of the beams.

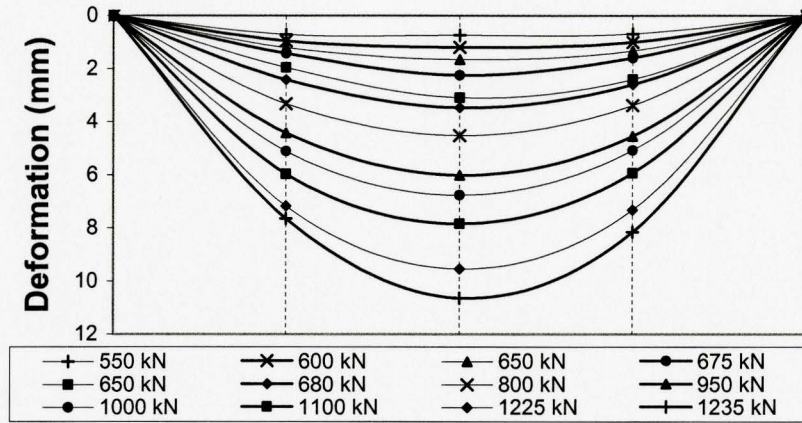
With reference to Figure 4.29, one can again see the large plastic deformations experienced by beam S2 versus the essentially elastic deformations of beams F2-A and F2-B. Notice that although the CFRP reinforced beams have lower stiffness after cracking than the steel reinforced beam, the service load deflections of these beams are not significantly different from the companion

steel reinforced beam. If the service load is assumed to be 50% of the ultimate load, then the corresponding deflections of the three beams are essentially equal. Thus, the lower stiffness of the CFRP reinforced beams may not have negative consequences on their serviceability or ultimate strength.

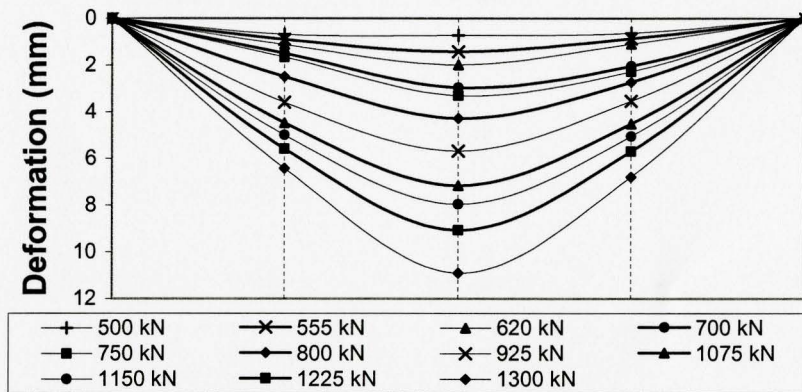
4.4.3 Deflected shape

The deflected shape of each beam tested in this group was obtained similarly to those for the first group of beams. Figures 4.31a, b and c illustrate the deformed shape of F2-A, F2-B and S2, respectively.

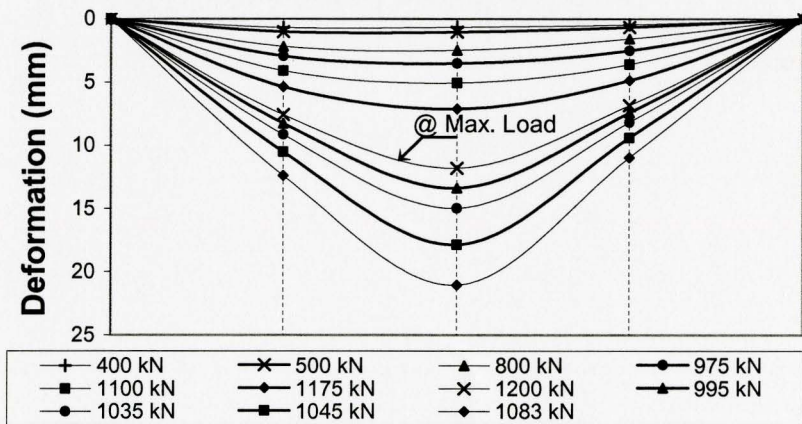
Similar to the beams tested in the first group, prior to cracking, the instrumented points along the span of each beam exhibit equal deformation. This implies that prior to cracking the shear deformations dominated the deflection of the beams. After cracking, at relatively low load levels the beams begin to exhibit flexural deformation by developing curvature. As the load is increased, the flexural stiffness of the beams decrease and the bending deformations become more noticeable. The deflected shapes show that after cracking, the deep beams in this group exhibit a deflected shape similar to that of the slender beams under flexure.



(a) Span deformation of F2-A beam



(b) Span deformation of F2-B beam



(c) Span deformation of S2 beam

Figure 4.31 Deformed shape of the beams with $l_e/h=2$

Notice the increase in deflection and the loss in stiffness of beam S2 after reaching its ultimate shear capacity, (between 1200 kN and 1083 kN), which was accompanied by extensive widening of the critical flexural crack. For the F2 beams, the crushing of concrete in the top compression zone prior to anchorage failure allowed for widening of the critical flexural crack and led to considerable bending deformations prior to failure. Similar to the beams tested in the first group, the control beam S2 experienced more deflection with a long descending branch, whereas the companion FRP reinforced beams failed once their maximum capacity was reached.

4.4.4 Strain in concrete

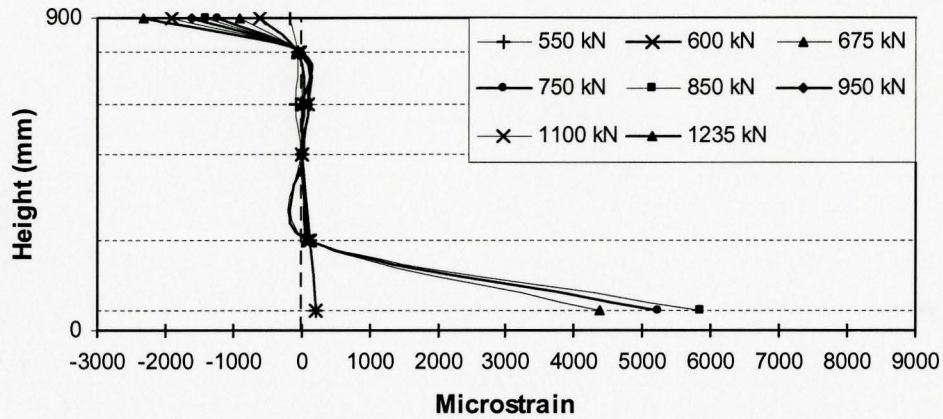
The strain distribution on the surface of beams was measured following the same approach as in the first group of beams. The strain gauge rosette numbering system used in the analysis of the strains along the diagonal struts is shown in Figure 4.13. Draw wire sensors were also used to monitor the average compression strain along the axis of the diagonal struts. Additional details about the instrumentation used to measure the concrete strains are given in Section 3.3.3.1 and presented in Figures 3.23 and 3.24.

4.4.4.1 Mid-span strain profile

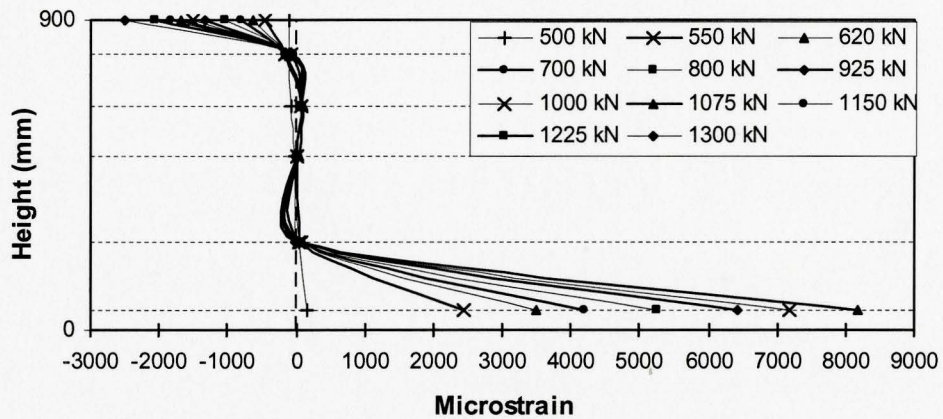
Figures 4.32a, b and c show the strain distribution along the height of the specimens at the mid-span of beams F2-A, F2-B and S2, respectively. The non-linear strain distribution along the depth of the beams indicates that even though their span to depth ratio is twice that of the beams tested in the first group, their strain distribution is similar. This implies that plane section remains plane theory does not apply to the deep beams tested in this group. Additional records of the mid-span strain distribution for the beams in this group could be found in Appendix B, Figure B.8.

As shown in Figure 4.32 all three beams exhibit very similar strain profiles while the neutral points along the height of the beams essentially remain stationary, similar to the beams tested in the first group.

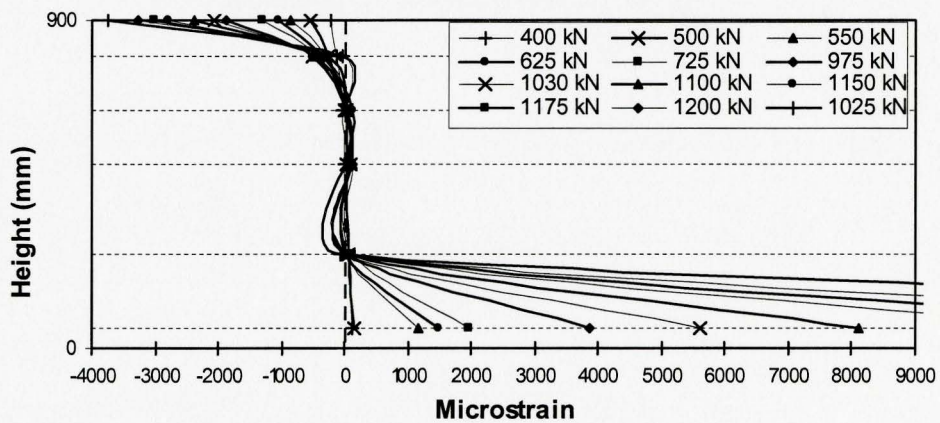
The internal moment arm for the S2 beam was calculated following the same procedure as that applied for the S1-B beam (see Section 4.3.4.1). The calculated internal moment arm for the control beam in this group is approximately $0.71h$, which is below the $0.8h$ recommended by the European code (1964).



(a) Strain along the depth of the F2-A



(b) Strain along the depth of F2-B



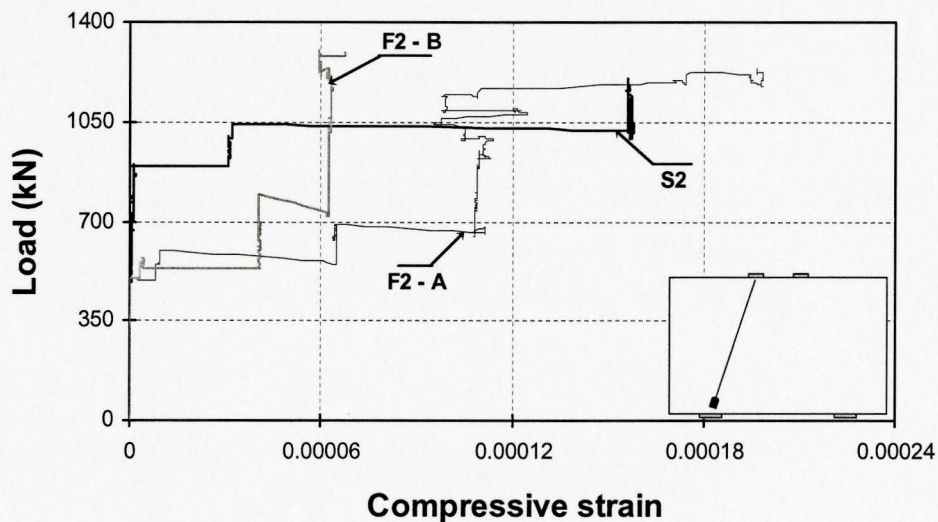
(c) Strain along the depth of the S2

Figure 4.32. Strain distribution along the depth of the beams with span-to-depth ratio of 2

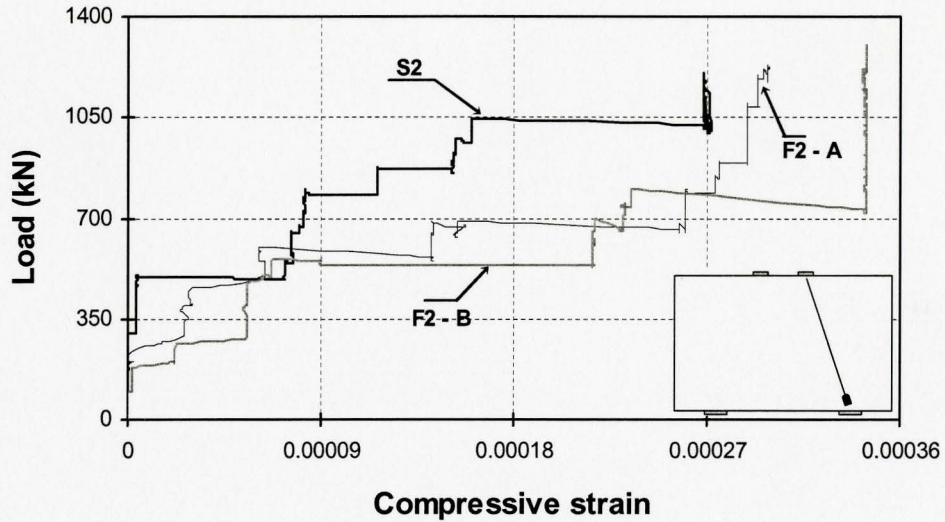
4.4.4.2 Strain along the compression struts

Figures 4.33a and b illustrate the variation of average strains along the axis of the diagonal struts with applied load for the beams in this group. The sudden increases in the strain values indicate the formation of diagonal cracks at that load level. Notice that despite the formation of various shear cracks along the east and west diagonal struts, the average strains did not exceed 0.00036.

The maximum average compressive strain for both CFRP reinforced beams was observed in the east diagonal strut, and ranged from 299 to 344 micro-strain, which is 14% to 16% of the maximum cylinder compressive strain. For the control beam S2, a maximum average compressive strain of 272 micro-strain was recorded along the east diagonal strut, corresponding to 12% of the maximum concrete compressive strain measured in the standard cylinder test.



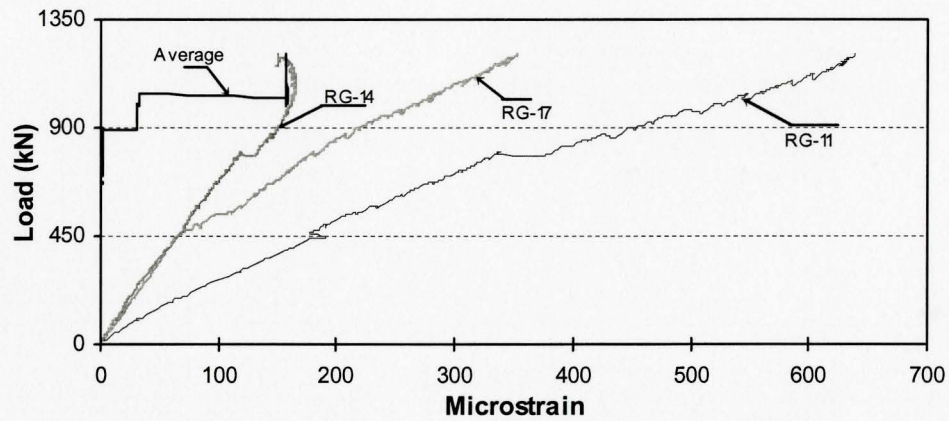
(a) West compression strut



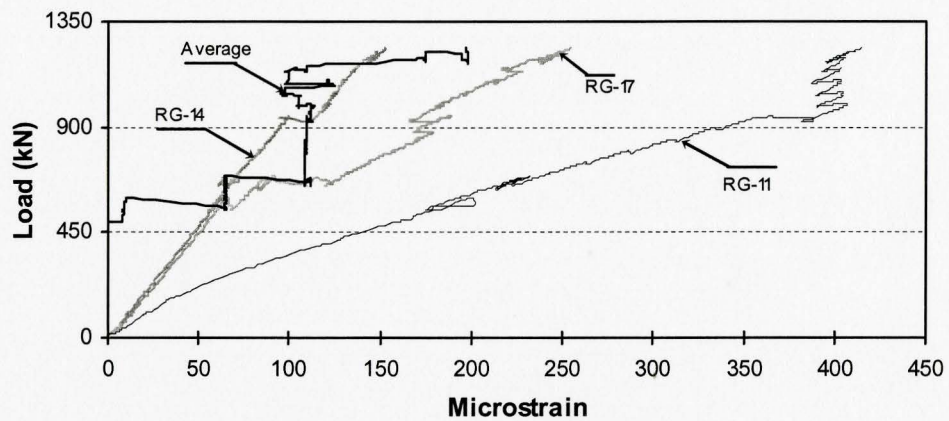
(b) East compression strut

Figure 4.33 Average compression strain in the struts of the beams with span-to-depth ratio of 2

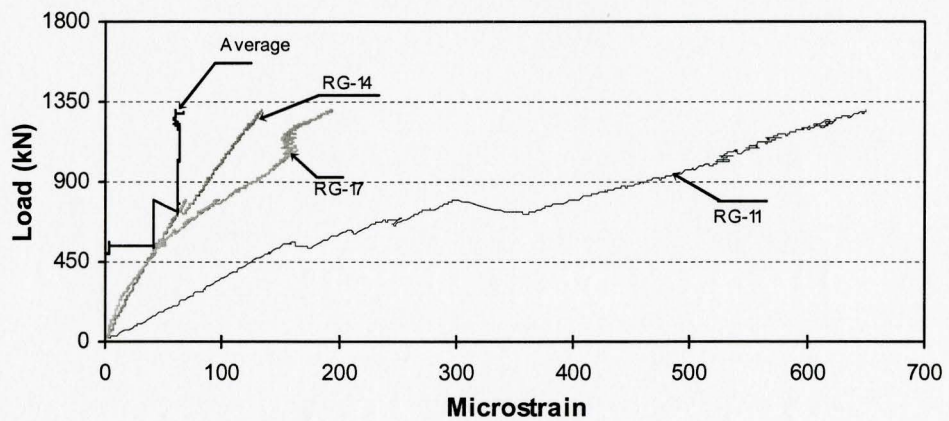
Figures 4.34 and Figure 4.35 show the difference between the average compressive strain measurements by the draw-wire sensors and the three local compressive strains measured by the strain gauge rosettes along the west and the east diagonal struts, respectively. Figure 4.34 illustrates that, similar to the beams tested in the first group, the average compressive strain measured along the west diagonal strut is close to the local strains at the mid-length of the strut and therefore underestimates the diagonal strain near the top and bottom of the strut. However, this was not the case in the east diagonal strut, as shown in Figure 4.35.



(a) S2 beam

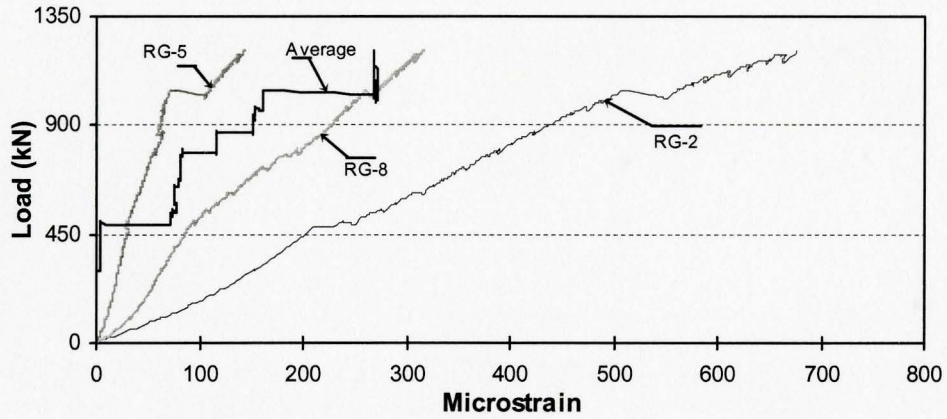


(b) F2-A beam

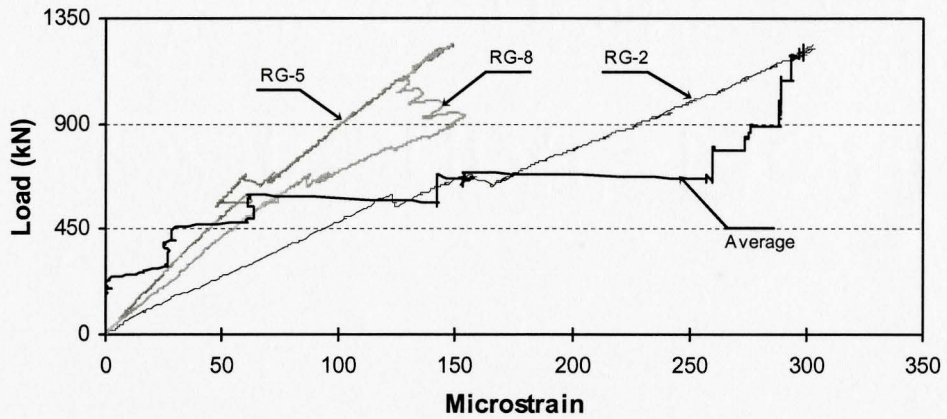


(c) F2-B beam

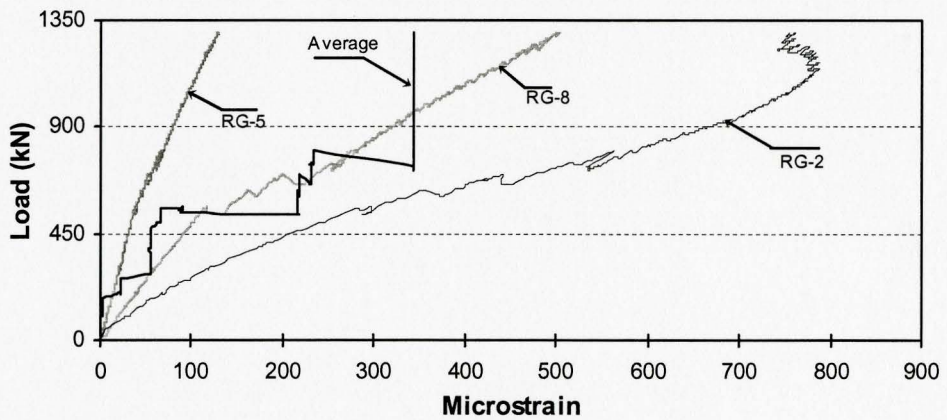
Figure 4.34: Compression strain comparison in the web strut for beams with span-to-depth ratio of 2



(a) S2 beam



(b) F2-A beam



(c) F2-B beam

Figure 4.35 Compression strain comparison in the east strut for beams with span-to-depth ratio of 2

It is clear from the latter figure that the average diagonal strut strain and the local strains along its length cannot be easily related to each other. In the light of this observation, it is difficult to ascertain the validity of the suggested method by CSA A23.3 for calculating the strength of the diagonal struts based on the average strain.

The high compressive strains obtained from the top strain gauges RG-11 and RG-2 indicate the likelihood of shear-compression failure near the CCC nodal zone. On the other hand, the least compressive strains measured by the middle strain gauges RG-14 and RG-15 signify the formation of bottle-shaped diagonal struts.

The strain readings from the strain gauge rosettes were used to calculate the principal tensile and compressive strains at three locations in the diagonal struts. The maximum principal compressive strain for the beams F2-A and F2-B were 685 and 1072 micro-strain, respectively. The maximum principal compressive strain in the F2-A beam was detected at the bottom of the west diagonal strut, while for the specimen F2-B it was measured at the bottom of the east strut. The maximum principal compressive strain for the control specimen was 742 micro-strain which was measured at the top of the east diagonal strut.

The maximum measured principal tensile strain for beams F2-A, F2-B and S2 were 308, 302 and 145 micro-strain, respectively. Notice that the measured

principal tensile strain in the control specimen is very close to the expected cracking strain of 133 micro-strain.

Figure 4.36 illustrates the plot of the local strains normal to the axis of the east and the west diagonal struts. Similar to the beams tested in the first group, the strains normal to the axis of the struts do not exhibit a consistent trend in all the beams or consistency between the east and west struts in the same beam. In general, it seems that at the mid-length of the struts the strain normal to the axis of the strut is tensile, while at the top and bottom of the strut it may be tensile or compressive.

More study and further analysis are required in order to relate either average or local strains to the observed behaviour and failure mode of deep beams. The current CSA procedures for calculating the compressive strength of the concrete struts in deep beams are not directly based on results of tests on deep beams and the present results indicate that relating the average strain to the failure mode may be challenging.

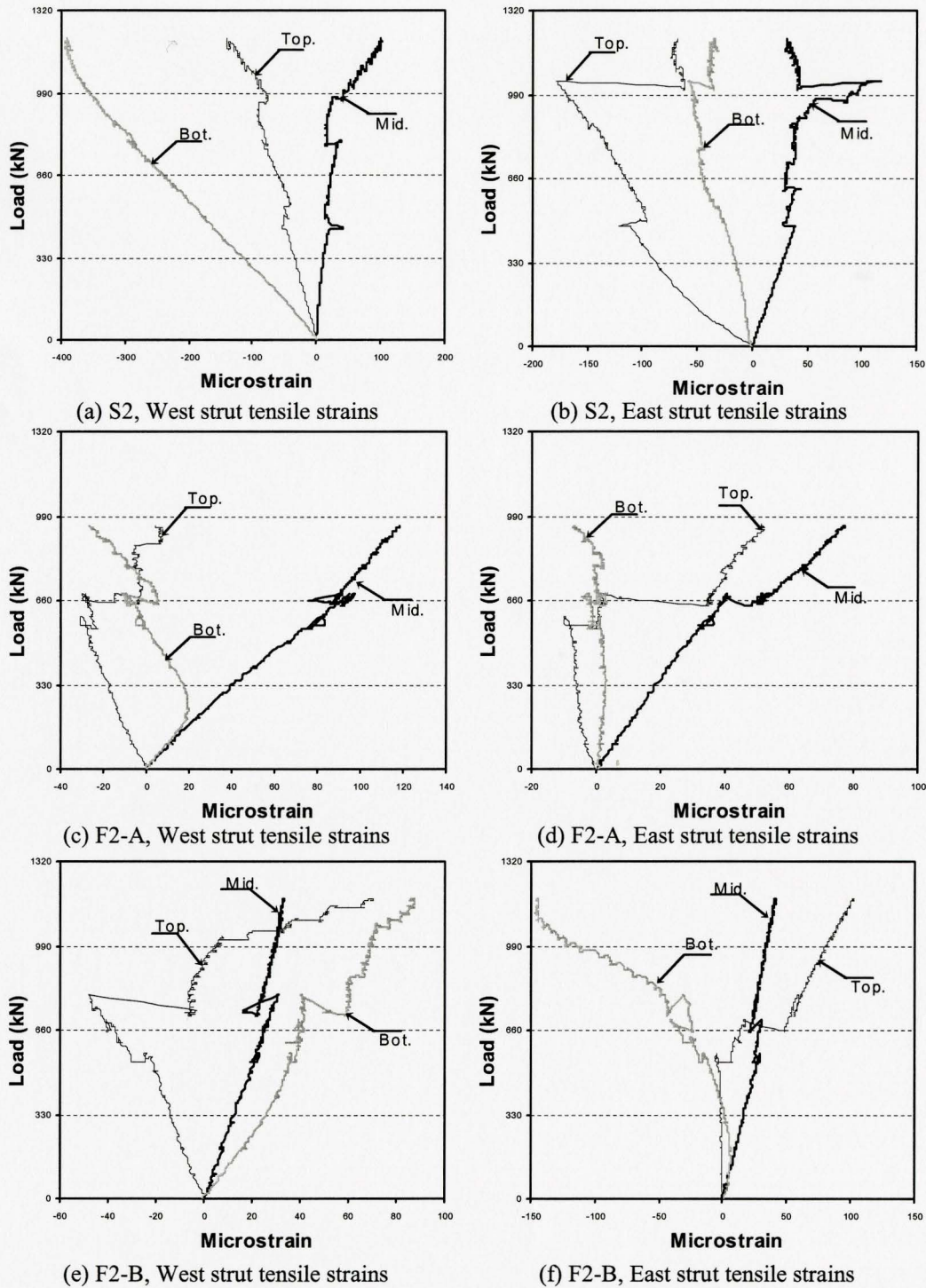


Figure 4.36: Strain measurements normal to the axis of the diagonal struts in the beams with span-to-depth ratio of 2

4.4.5 Strain in reinforcement

Similar to the CFRP reinforced beams tested in the first group, for the beams F2-A and F2-B a total of 17 strain gauges were used to monitor the strains in the reinforcement, with 12 gauges attached to four stirrups and 5 affixed to the longitudinal reinforcement. Figure 4.19 indicates the numbering system of the strain gauges that was used in the analysis of the strains in the stirrups of the CFRP reinforced beams.

For the control specimen, on the other hand, 21 strain gauges were used to measure the strains in the reinforcement, 16 of which were attached to eight stirrups and the remaining 5 to the longitudinal bars. The location and the numbering system of the strain gauges attached to the stirrups of the S2 beam are shown in Figure 4.37

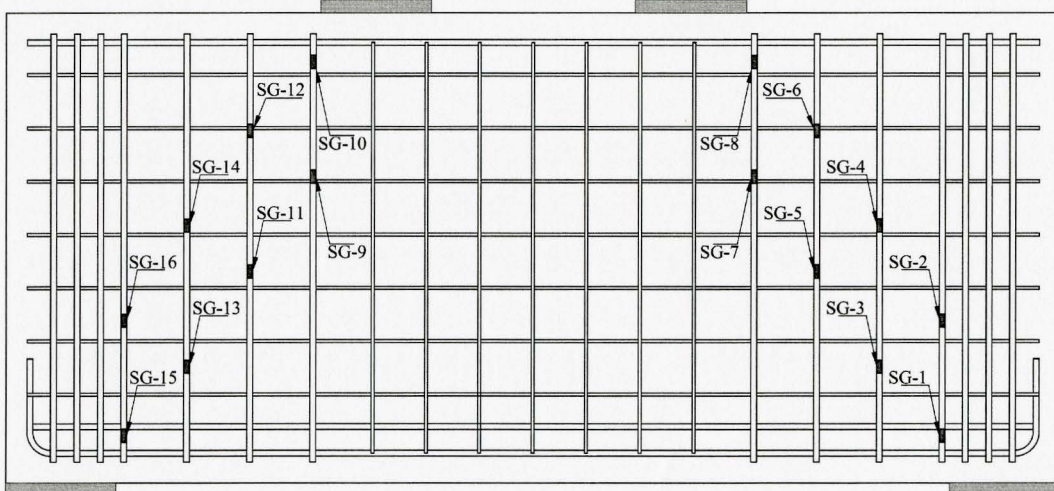


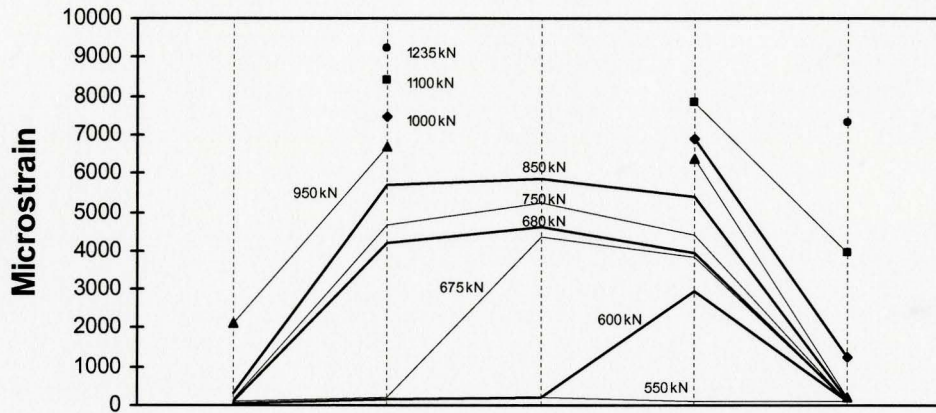
Figure 4.37 Strain gauge numbering and position in the stirrups of S2 beam

4.4.5.1 Strain in longitudinal reinforcement

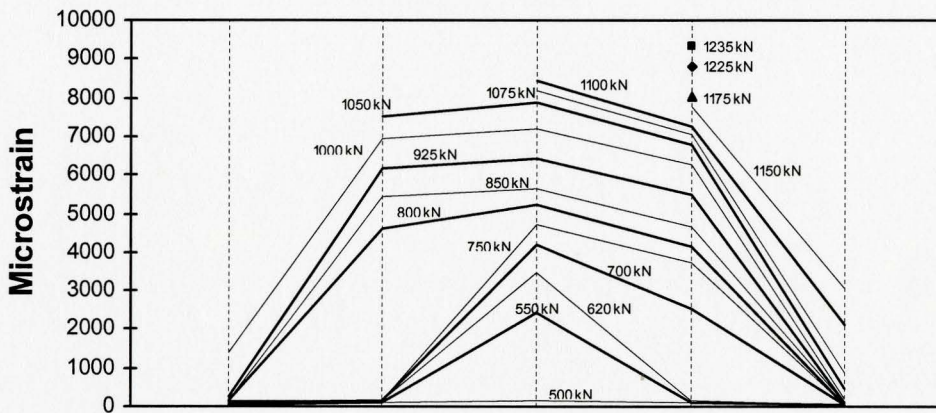
Figures 4.38a, b and c show the strain distribution along the length of the longitudinal rebar in beams F2-A, F2-B and S2, respectively. The discontinuity of the strain profiles in these figures is due to malfunctioning of strain gauges during the test. Notice that the strain distribution in the longitudinal reinforcement essentially exhibits the profile of the bending moment as the beams reach failure, indicating that the longitudinal reinforcement was mainly resisting flexure. This is to be expected since all the beams exhibited predominantly flexural deformation as earlier discussed in Section 4.4.3.

Figures 4.38a and b illustrate that the strain distributions in the CFRP reinforced beams were very similar with an essentially uniform strain distribution within the constant moment region and a gradual decrease of strains towards the supports. For the S2 beam, the strain in the reinforcement near the mid-span increased substantially as the beam approached failure. Note that unlike S1-B, in beam S2, the strain in the longitudinal reinforcement remains negligible near the supports even after the formation of inclined shear cracks.

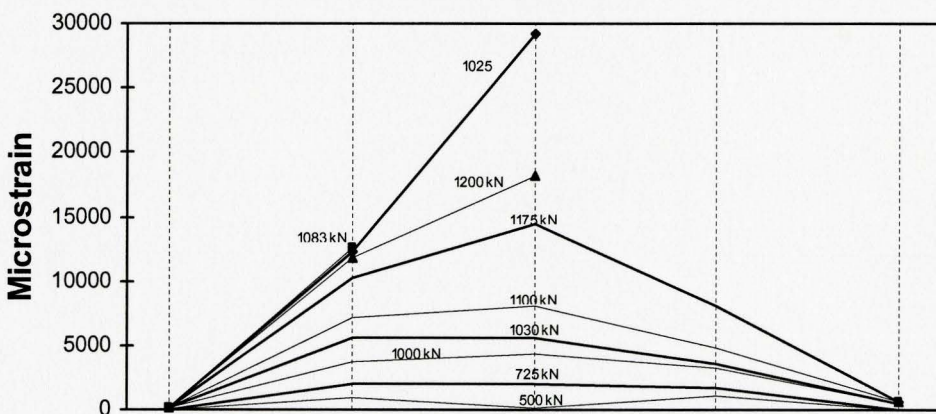
The maximum measured tensile strains in the CFRP longitudinal bars at failure ranged between 9099 and 9316 micro-strain, corresponding to 75% of the ultimate value suggested by the manufacturer. The maximum measured tensile strain in the steel longitudinal rebar at failure was 12576 micro-strain, which is 14% of the measured rupture strain and six times the yield strain.



(a) F2-A beam



(b) F2-B beam



(c) S2 beam

Figure 4.38 Strain distribution along the longitudinal reinforcement of the beams with span-to-depth ratio of 2

The maximum tensile stress in the Isorod reinforcement reached 1165 MPa and 1192 MPa, in beams F2-A and F2-B, respectively, while the maximum tensile stress near the supports was almost 80% of the maximum stress in the span. The average bond stress in the Isorod reinforcement could be calculated by substituting the appropriate strain values, shown in Figure 4.38a and b, in to Equation (4.2). Consequently, the average bond stresses in the F2-A and F2-B beams were 2.5 MPa and 3 MPa, respectively, which are well below the bond stresses measured by Benmokran et al. (2002). Note that these values correspond to the average bond stress on the east side of the beams, as the anchorage failure occurred on that side for both CFRP reinforced specimens.

4.4.5.2 Strain in transverse reinforcement

Figures 4.19 and 4.37, respectively, illustrate the position and numbering of the strain gauges affixed to the stirrups in the CFRP reinforced and steel reinforced beams tested in this group. It should be noted that strain gauge SG-10 in the F2-A beam was damaged during the casting procedure. Figures 4.39, 4.40 and 4.41 show the strain distributions in the stirrups of specimens F2-A, F2-B and S2, respectively.

Figures 4.39 and 4.40 indicate that after the formation of inclined shear cracks the stirrups in the CFRP reinforced members were fully engaged in transferring tension within the shear span and they enhanced the shear strength of

the F2 beams, unlike the CFRP reinforced beams tested in the first group. Notice the large tensile strains in the NEFMAC reinforcement, ranging between 3926 and 4362 micro-strain, as the F2 beams approached failure. These strain values correspond to approximately 35% of the specified maximum tensile strain by the manufacturer (Autocon Inc. 1997).

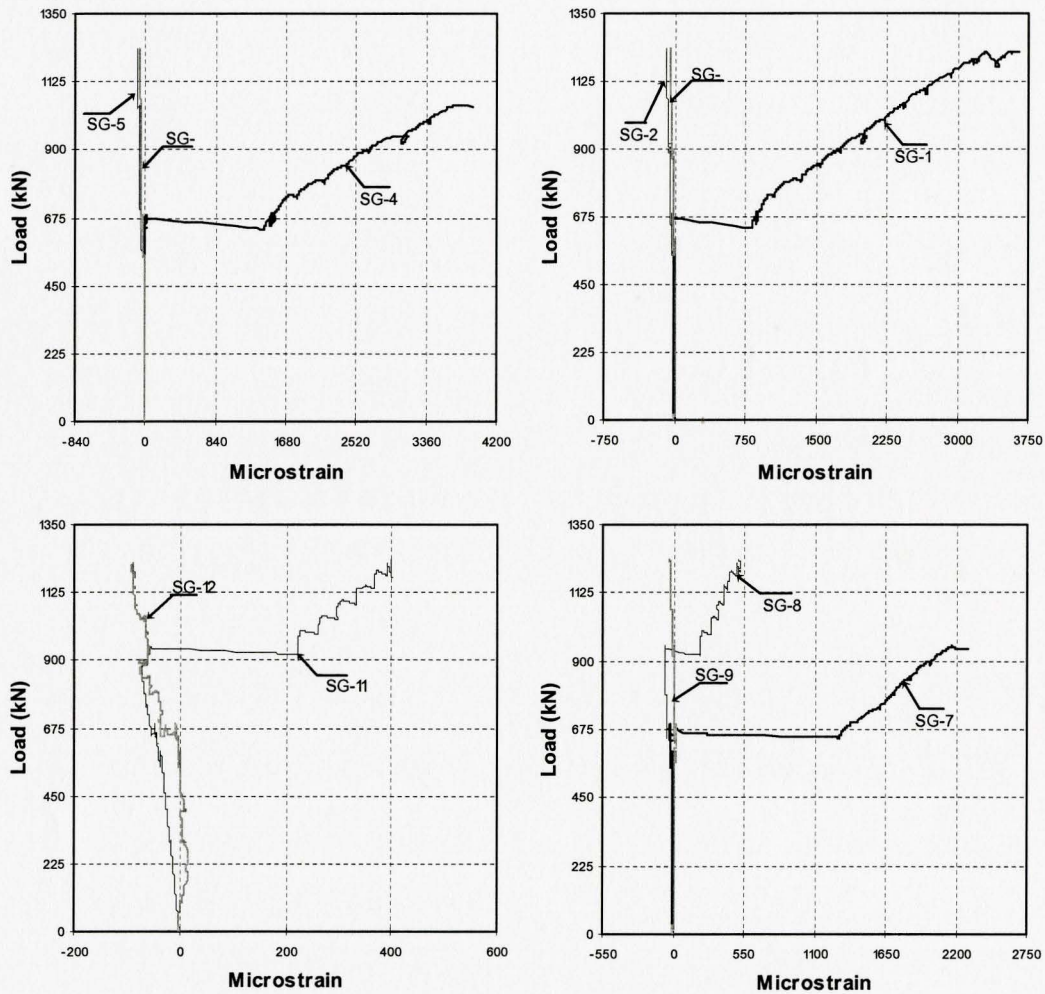


Figure 4.39 Load-strain relationships in the stirrups of F2-A beam

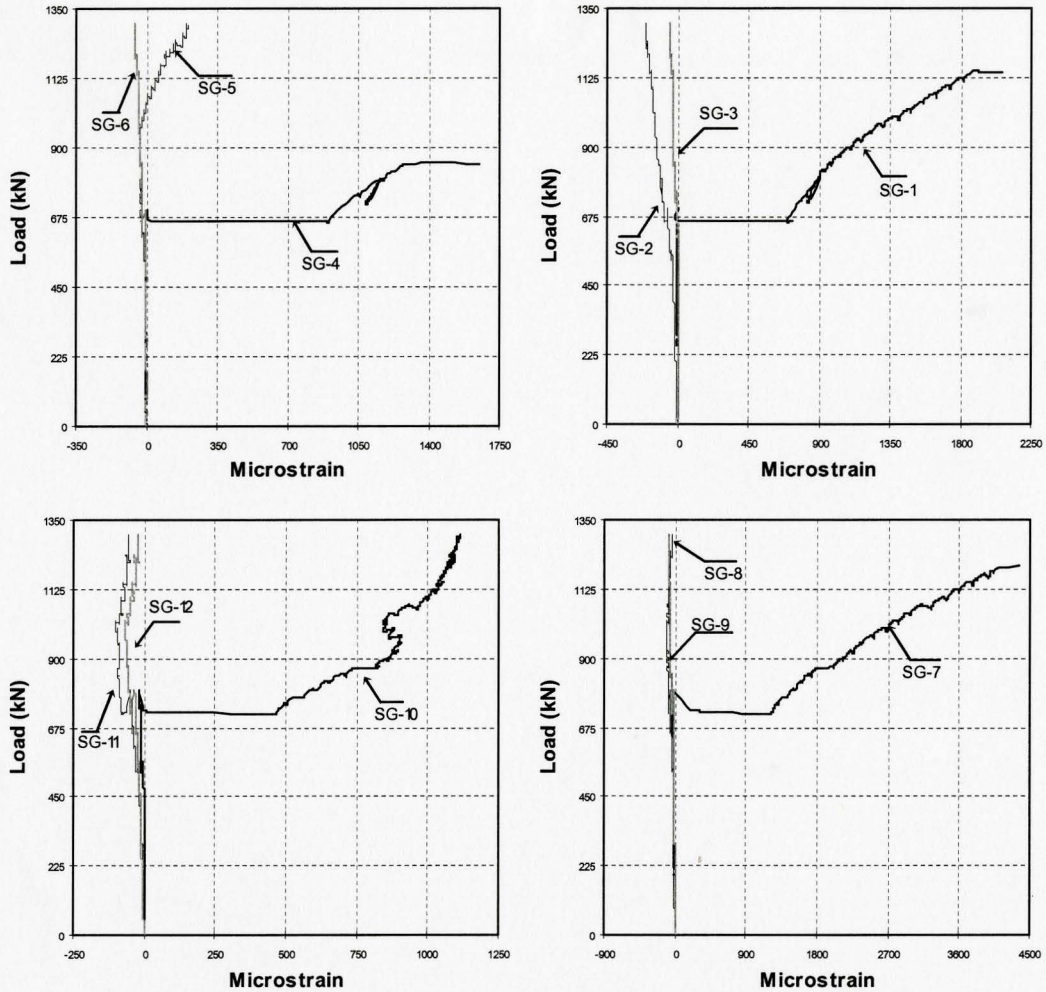


Figure 4.40: Load-strain relationships in the stirrups of F2-B beam

In the case of the control beam S2, the stirrups actively contributed to crack control and to shear resistance of the beam. Figure 4.41 shows large strain readings by the gauges that were either crossed by or were in the vicinity of the inclined cracks. The largest tensile strain was recorded by gauges SG-11, which was 1342 micro-strain or 67% of the yielding strain of steel.

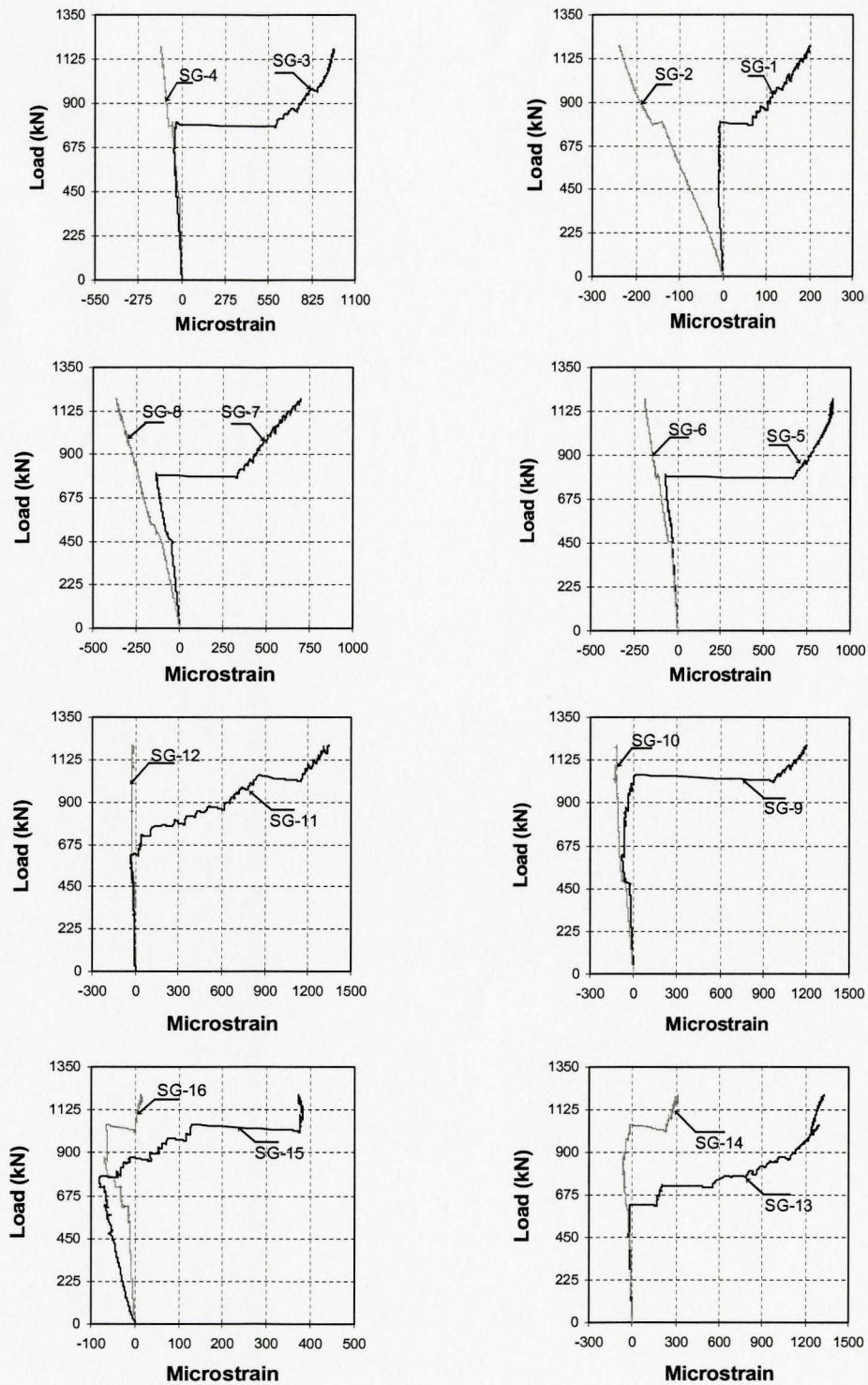


Figure 4.41 Load-strain relationships in the stirrups of S2 beam

CHAPTER 5: ANALYSIS OF RESULTS

5.1 General

One of the objectives of this study is to evaluate the applicability of the current North American design approaches for deep beams reinforced with conventional steel to deep beams reinforced with CFRP. In order to achieve this objective, the strength of the beams tested in this investigation were analyzed using the available design provisions and compared to the corresponding experimental values. Furthermore, the observed mode of failure for each beam was compared with the predicted failure mechanism by the standards.

To further investigate the reason for the difference between the designed and observed strengths of the tested beams and to enquire into the conservative nature of the available design provisions, the strut and the nodal efficiency factors were determined for the beams based on their observed strength and compared with the available stress limits in the code.

5.2 Failure Mechanism

The ultimate shear strengths of the tested beams were calculated based on the provisions of ACI 318-08 and CSA A23.3-04, and the calculated strengths were compared with the corresponding observed shear capacities. The design shear capacity of each beam was determined using both the specified and

measured material properties of the beam. Note that the nominal strength of concrete and steel reinforcement were taken as 30 MPa and 400 MPa, respectively. It should be also pointed out that no strength-reduction factors were used in the design of the beams (refer to Appendix A). Table 5.1 summarizes the ACI and the CSA predicted shear capacity and the observed ultimate shear strength of the tested beams.

Table 5.1 Measured and calculated structural capacities

Beam	Measured ultimate shear V_{uexp} (kN)	Calculated ultimate shear capacities (kN)							
		Specified properties				Measured properties			
		V_{ACI}	V_{CSA}	$\frac{V_{ACI}}{V_{uexp}}$	$\frac{V_{CSA}}{V_{uexp}}$	V_{ACI}	V_{CSA}	$\frac{V_{ACI}}{V_{uexp}}$	$\frac{V_{CSA}}{V_{uexp}}$
S1-B	780	320	319	0.41	0.41	370	375	0.47	0.48
F1-A	800	390	445	0.49	0.56	440	490	0.55	0.61
F1-B	775.5	390	445	0.5	0.57	440	490	0.57	0.63
S2	603	317	295	0.53	0.49	375	340	0.62	0.56
F2-A	618	395	370	0.64	0.6	460	405	0.74	0.66
F2-B	650	395	370	0.61	0.57	460	405	0.71	0.62

Comparing the calculated shear capacities, it is evident that the application of the measured properties for the concrete and steel reinforcement in the design results in larger shear capacity. Comparing the design shear capacities with the experimental results, it is observed that both design standards give conservative predictions of the ultimate load-carrying capacity of the tested deep beams, regardless of the type of reinforcement.

Table 5.1 shows that the CSA strut and tie method (STM) gives relatively better estimation of the ultimate shear strength of the beams having span-to-depth ratio of 1. In the case of the F1 beam series, the CSA standard prediction ranges from 61% to 63% of the observed ultimate shear capacities. On the other hand, for the beams with span-to-depth ratio of 2, the ACI STM method gave better prediction of their ultimate shear strength, ranging from 71% to 74% of the observed ultimate shear strength. The conservative nature of codes provisions may be in part due to the many implicit and explicit assumptions involved in their formulation, e.g., the width of the struts, the angle of inclination of the diagonal strut and the effective strength of concrete in the struts. Although the conservatism of these standards is reassuring in terms of the safety of the design, there is inconsistency among the level of safety of different types of members within the same structure. In other words, shallow beams in the same structure would not be as conservatively designed. Thus, the extra safety of these members may not lead to higher safety of the structure as a whole. Furthermore, over reinforcement may cause other problems such as reinforcement congestion and the shifting of the plastic hinge formation to more critical locations in the structure, for example, to columns.

Based on the ACI and CSA design methods, different failure mechanisms were predicted for the same beam. Table 5.2 compares the observed failure mechanisms with the predicted failure mechanism for each beam tested. The

potential failure mechanisms for deep beams subjected to in-plane shear loading were previously discussed in Section 2.3.3

Table 5.2. Predicted versus actual failure mechanisms for the tested beams

Beam	Observed failure mechanism	Predicted failure mechanism	
		ACI 318-08	CSA-A23.3-04
S1-B	Crushing of the top prismatic strut	Yielding of the transverse tie	Crushing of the top prismatic strut
F1-A	Anchorage failure	Crushing of the CTT nodal zone	Crushing of the top prismatic strut
F1-B	Anchorage failure		
S2	Crushing of the top prismatic strut	Yielding of the longitudinal tie	Crushing of the top prismatic strut
F2-A	Crushing of the top prismatic strut	Crushing of the top prismatic strut	Crushing of the top prismatic strut
F2-B	Crushing of the top prismatic strut		

Table 5.2 indicates that the mode of failure predicted by the CSA standard was very similar to the observed failure mechanism of most of the beams, except the F1 beams, which experienced premature anchorage failure. It is evident that both standards yield satisfactory results for the F2 beam series, as they both predicted the crushing of the top prismatic strut to be the governing failure mechanism for these beams.

Based on the above discussion, the following remarks can be made that even though both design standards significantly underestimated the shear strength of the tested beams, the predicted failure mechanism by the CSA standard was compatible with the actual failure mode observed during the test.

5.3 Efficiency Factors of Concrete Strength

Various researchers have proposed values for the effective concrete strength factor ν , as discussed earlier in Section 2.2.4. Based on the work of these investigators, certain stress limiting factors have been incorporated in the CSA and the ACI standards. The recommended efficiency factors in the two standards are considered to be relatively conservative compared with the unfactored resistance capability of the concrete in the struts and the nodal zones (Su et al., 2001).

It should be pointed out that the recommended efficiency factors in the standards are based on tests conducted on steel reinforced deep beams. Therefore, the applicability of these factors to CFRP reinforced deep beams needs to be investigated. Consequently, in the following sections the concrete compressive stresses in the diagonal struts as well as the nodal zones are calculated based on the observed ultimate shear strength and compared with the efficiency factors suggested in the literature.

5.3.1 Effective compressive strength of the strut

The strut efficiency factor ν , in the current ACI code accounts for the load duration effect through the factor α_l (taken as 0.85) and for the type of strut formation via factor β_s (taken as 1 for the prismatic and 0.75 for the bottle-shaped struts), as stated by Reineck (2002). On the other hand, the CSA standard

recommends that the strength of the compression struts be limited to a maximum value $0.85f'_c$, where f'_c is referred to as the compressive strength of concrete.

Although the CSA standard provides an expression for calculating the maximum strength of the compression strut in the regions crossed by the tension tie, it does not offer a rational approach as to how one can relate the multi-axial state of strains to the concrete compression strength at the top of the diagonal strut proximate to the point of application of the load.

The recommended expressions in the STM provision of the CSA standard, which allow for calculating the maximum compressive strength at the ends of the diagonal struts, proximate to the supports of the beams, are given by Equations (2.30) and (2.31) in Section 2.2.4.3 of this thesis. Note that through Equation (2.31) the principal tensile strain is related to the orientation as well as the strain of both the concrete strut and the longitudinal reinforcement.

For the purpose of this study, the strut efficiency factor at the bottom of the diagonal struts, proximate to the supports, for the present beams is calculated using the following expression given by the CSA standard.

$$v = \frac{1}{(0.8 + 170\varepsilon_1)} \quad (5.1)$$

and

$$\varepsilon_1 = \varepsilon_x + (\varepsilon_x + \varepsilon_2)\cot^2\theta \quad (5.2)$$

where ε_1 and ε_2 are the principal tensile and compressive strains of the concrete, ε_x is the tensile strain of the longitudinal tie, and θ is the angle of the strut relative to the horizontal tie.

It should be noted that when applying Equation (5.2), ν was calculated using three different values for the maximum principal compressive strain, namely ε_2^* , ε_{2ave} and 0.002. The strain ε_2^* was determined from the data captured by the rosette strain gauge near the particular end of the strut, the strain ε_{2ave} was determined from the average compressive strain captured by the draw-wire sensors spanning the diagonal strut (refer to Section 3.3.3), while the strain of 0.002 is suggested by the standard for the CCT nodal zone. Furthermore, Equation (5.1) was solved using either the measured principal tensile strain at the bottom of the diagonal struts, ε_1^* , obtained from the readings of the bottom rosette strain gauges, or the calculated tensile strain, ε_1 , according to Equation (5.2). Consequently, four different values were found for the ν factor. Table 5.3 shows the measured principal strain values and the corresponding calculated efficiency factor for each of the tested beams.

Table 5.3 Measured efficiency factor for the bottom of diagonal struts joining the CCT nodal zone

Beam	Measured strains at CCT node (micro-strain)			Maximum principal tensile strain ε_1^* (micro-strain)	$\varepsilon_1 = \varepsilon_x + (\varepsilon_x + \varepsilon_2) \cot^2 \theta$ (micro-strain)			$v = \frac{1}{0.8 + 170\varepsilon_1}$			
	ε_x	ε_2^*	ε_{2ave}		$\varepsilon_2 = \varepsilon_2^*$	$\varepsilon_2 = \varepsilon_{2ave}$	$\varepsilon_2 = 0.002$	ε_1			ε_1^*
								ε_2^*	ε_{2ave}	ε_2	
S1-B	2600	1700	538	580	2800	2740	2810	0.78	0.79	0.78	1.11
F1-A	4500	1100	180	520	4750	4710	4800	0.62	0.62	0.62	1.13
F1-B	5100	470	249	830	5350	5340	5400	0.58	0.59	0.58	1.06
S2	600	670	272	140	2700	2600	3040	1.04	1.06	0.98	1.21
F2-A	7300	310	299	310	9280	9270	9700	0.42	0.42	0.41	1.17
F2-B	7300	650	344	300	9360	9290	9700	0.42	0.42	0.41	1.18

Note that in the case of the S2 beam, as illustrated in Figure 4.28, at failure the longitudinal reinforcement near the support had a maximum strain of 600 micro-strain, which results in a much higher efficiency factor compared with the other beams (see Table 5.3). Since the strength efficiency factors in the current standards are predicated on the yielding of the longitudinal steel reinforcement, it was decided to recalculate the efficiency factor for this beam by accounting for the yielding of the main steel reinforcement near the supports. The corresponding efficiency factor for the diagonal struts in the S2 beam based on the measured principal and average compression strain and the presumed 0.002 peak compressive strain are 0.8, 0.81 and 0.76, respectively.

It should also be noted that for the specimen F2-B, both strain gauges along the centerline of the supports malfunctioned before failure was reached, but since the longitudinal reinforcement in both F2 beams were strained by almost the same amount at the time of failure, it was decided to apply the F2-A longitudinal tensile strain values when calculating the ε_l for the F2-B beam (taken as 0.0073).

The calculated ν factors in the last column of Table 5.3 are compared with the limiting strength factor of 0.85 recommended by the CSA standard, and 0.64 recommended by the ACI code. Note that the 0.64 efficiency factor as suggested by ACI is computed by multiplying the characteristic factor of the diagonal strut, 0.75, by the load duration factor 0.85.

The ν factors calculated based on the measured local principal tensile strain at the bottom of the strut, ε_1^* , give consistently higher compressive strength than the concrete strength, f'_c , obtained from the standard cylinder test. This was found to be rather odd as the presence of the tie is expected to reduce the strength of the concrete at the bottom of the diagonal struts. Accordingly, it is suggested that the use of Equation (5.1) be restricted only to the calculated principal tensile strain according to Equation (5.2).

The other three columns of Table 5.3 indicate more reasonable stress limit factors. Note that the calculated efficiency factors for the steel reinforced beams are compatible with the CSA predicated value of 0.85. In the case of the CFRP reinforced beams, particularly for the beams with the span-to-depth ratio of 1, the computed factors were closer to the 0.64 factor suggested by the ACI standard. The calculated efficiency factors for the diagonal struts in the F1 beams range from 0.58 to 0.62, whereas for the F2 beams it is 0.42.

It should be pointed out that since the observed failure mechanism was not crushing or splitting of the diagonal struts, it is not possible to establish new efficiency factors based on the current test results. However, the calculated factors could be used as the lower bound of the allowable compressive strength of the struts.

5.3.2 Effective compressive strength of the nodal zones

The literature review on the nodal stress limits (Section 2.2.4) indicated that the efficiency factors suggested by the CSA and ACI codes are mainly empirical and are not quantitatively related to the multi-axial state of stress existing at the nodes. Therefore, further research is required in order to arrive at a more rational approach for finding the stress conditions at the nodal zones. This is particularly important for the bottom nodal zones anchoring the main tie, as the level of strain in the tie reinforcement can significantly affect the strength of the node.

The suggested nodal efficiency factors by the CSA code for the CCC and the CCT nodal zone are 0.85 and 0.75, respectively. The ACI code on the other hand recommends factors of 0.85 and 0.68 for the CCC and the CCT nodes, respectively, by taking in to account the load duration effect. For the purpose of this investigation, it was decided to calculate the principal compressive strength based on the equilibrium of forces in the nodal zones, Figure 5.1, and compare them with the suggested values in the code.

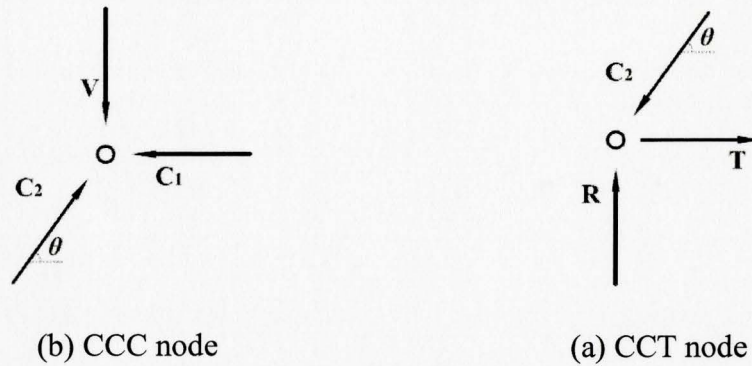


Figure 5.1 Equilibrium of nodal zones in the tested deep beams

The equilibrium equations for either node are not sufficient to calculate the unknown forces and the inclination of the strut at that node. For example, at the CCC node for a known value of V , the unknowns are C_1 , C_2 and θ , and the relevant equilibrium equations are:

$$C_2 = V / \sin\theta \quad (5.3)$$

$$C_1 = V \cot\theta \quad (5.4)$$

Similarly, for CCT node the unknowns are C_2 , T and θ , and the equilibrium equations are:

$$C_2 = R / \sin\theta \quad (5.5)$$

$$T = R \cot\theta \quad (5.6)$$

where C_1 is the force in the top compression strut, C_2 is the force in the diagonal strut, T is the force in the tension tie at the recorded failure load, V , angle θ is the inclination of the diagonal compression strut, and R is the reaction force which is equal to V in the present tests.

In the test at the ultimate load the values of R and V (i.e. the reaction and the applied shear) are known, but the other nodal parameters are not known. Due to three unknowns and two equations of equilibrium, the resisting forces at the nodes do not have unique values. However, if for the steel reinforced beams it is assumed that the tie force has reached its capacity $A_s f_y$ at failure, then from the equilibrium of forces at nodes situated at the support, i.e. Equations (5.5) and (5.6), the values of C_2 and θ can be uniquely determined. For the CFRP reinforced deep beams, on the other hand, due to the high strength of the CFRP longitudinal bars, it is assumed that the compression force in the top prismatic strut C_1 reach its capacity of $0.85 f'_c a b$ before the tension tie reaches its tensile capacity, consequently from the equilibrium of forces at the CCC nodal zone the C_2 and θ can be calculated using Equations (5.3) and (5.4). It should be noted that the values of C_2 calculated by this method would yield the lower bound for the nodal efficiency factor ν , for none of the present beams failed due to diagonal compression failure or crushing of the nodal zones.

In order to find the angle θ and the magnitude of the associated forces at each node, the depth of the compression block as well as the width of the diagonal struts are assumed equal to those suggested by the ACI and CSA standards (refer to Appendix A). Furthermore, the compressive stress in the diagonal struts at failure is assumed equal to the concrete compressive strength f'_c obtained from cylinder tests, and in the top horizontal strut equal to $0.85 f'_c$. The ultimate tensile

stress of the longitudinal reinforcement is assumed equal to f_y for the steel reinforcement and to f_{fu} for the CFRP bars.

The efficiency factor ν is calculated by dividing the computed forces based on nodal equilibrium over the corresponding permissible loads in the nodal zones. The result of this analysis is presented in Table 5.4.

Table 5.4: Calculated effective stress levels at the nodal zones

Beam	Efficiency factors for nodes	
	CCC	CCT
S1-B	0.87	0.53
F1-A	0.94	0.57
F1-B	0.91	0.55
S2	0.36	0.3
F2-A	0.37	0.34
F2-B	0.39	0.35

Based on the results in Table 5.4, the efficiency factor for the CCT nodal zones in all the beams is smaller than the efficiency factor for the CCC nodal zones. This is to be expected because of the higher degree of confinement in the CCC nodal zones, bounded by compressive struts and bearing plates. Furthermore, it is evident that the calculated CCC nodal efficiency factors for the F1 beams are larger than the values suggested by the CSA and ACI standards, which further indicates the conservatism of the current standards when applied to FRP reinforced beams. The existing stress limit factors in the current standards are predicated based on the assumption that the longitudinal reinforcement bars have strained up to the yielding point of steel. In the case of the CFRP reinforced

beams, however, due to the presence of higher strains along the Isorod reinforcements in the vicinity of the CCT nodal zones, the likelihood of failure at the node was much higher.

It should be pointed out that in the case of the CFRP reinforced beams the overall performance of the CCT nodal zone was not affected by the large tensile strains in the Isorod reinforcement, because the beams failed due to anchorage failure and the subsequent crushing of the top prismatic strut. Since the failure did not occur in the nodal zones, the calculated factors represent the lower bound of the strength of the nodes.

The upper limit of these efficiency factors could only be found if beam failure was initiated in the part of the beam with which the factor is associated. This would require extensive testing and the test specimens must be designed such as to ensure desired failure mode. To the writer's knowledge, tests of this kind have never been performed even for steel reinforced deep beams.

It is useful to compare the calculated efficiency factors with the factors recommended by previous researchers, as discussed in Section 2.2.4.2. Table 5.5 gives a list of the recommended stress limit factors and the calculated values for the CFRP reinforced beams obtained in the present investigation. To facilitate the comparison, f'_c is assumed to be 35 MPa.

Table 5.5 Calculated effective stress level for concrete node vs. proposed values

Source	Efficiency factors for nodes	
	CCC	CCT
Collins and Mitchell (1986)	0.85	0.75
Schlaich et al. (1987)	0.85	0.68
MacGregor (1997)	0.71	0.6
Jirsa et al. (1991)	-	0.8
Marti (1985)	0.6	0.6
F1, average factor	0.92	0.56
F2, average factor	0.38	0.34

The efficiency or stress limit factors ν in Table 5.5 suggest that the nodal zone will fail if the concrete stress in that zone reaches $\nu f'_c$. First, we noticed that all other investigations, except Marti (1985), suggested higher ν value for the CCC nodal zone than the CCT nodal zone. On the other hand, the suggested values range from 0.6 to 0.85 for the CCC zone and from 0.6 to 0.8 for the CCT zone. As stated earlier these values have not been derived based on either indepth theoretical analysis or detailed experimental data, and are primarily based on the judgment of these investigators. Some of the values do not appear to be consistent with the observed behaviour of concrete. For instance the $\nu = 0.6$ for CCC nodal zones suggested by Marti indicates that the concrete in a state of biaxial or triaxial compression is weaker than under uniaxial compression. This is clearly counter intuitive and is not supported by experimental observations. The ν values suggested by either Collins and Mitchell (1986) or Schlaich et al. (1987) seem reasonable.

The last two rows of the Table 5.5 show the average values of ν calculated for the F1 and F2 series of beams, however, it is extremely important to point out that these ν values represent lower bounds because they simply indicate the ratio of the actual compressive stress in the concrete at failure of the beam to the compressive strength of concrete. These values do not correspond to the stress causing failure at the particular nodes, since none of the beams failed due to failure of the nodes.

With the preceding explanation in mind, we observe that for the F1 series of beams, the calculated ν values of 0.92 at CCC nodes is higher than any of the suggested values and since the respective node did not fail, it is concluded that all the recommended ν values for the CCC nodal zone are conservative. The CCC column in the Table 5.5 indicates that some ν factors are more conservative than others. Accordingly, it is recommended here that $\nu = 0.85$, as suggested by Collins and Mitchell (1986) and Schlaich et al. (1987), be adopted for CCC nodal zones in FRP reinforced concrete deep beams. For the CCT zones, a value of $\nu = 0.68$, as suggested by Schlaich et al. (1987), may be appropriate. The latter is based on the fact that at $0.56f'_c$ the CCT nodes in F1 beams did not fail, despite the rather large strain values in the CFRP ties anchored in the CCT nodal zones.

CHAPTER 6: SUMMARY, CONCLUSIONS, AND RECOMMENDATIONS

6.1 Summary

The results presented in this thesis were obtained from the in-plane testing of simply supported concrete deep beams reinforced with CFRP reinforcement. The objective of this work was to investigate the influence of using CFRP bars as main tensile reinforcement on the shear and flexural behaviour of deep beams. The findings of the investigation were used to evaluate the applicability of the current design methods for conventional RC deep beams, as contained in the North American concrete standards, to the CFRP reinforced deep beams.

An experimental study was conducted on seven beams tested under four-point bending and monotonically loaded to failure. One of the beams was used as a trial specimen to evaluate the suitability of the test setup while the remaining six beams were used to investigate the behaviour of deep beams, with focus on the effect of the CFRP reinforcement. The main test parameters in the study were the type of reinforcement and the span-to-depth ratio. The span-to-depth ratio of the beams in this study was either one or two, and for each ratio two replicate CFRP reinforced beams and one steel reinforced beam were tested. The responses of the beams were compared by examining their strengths, load-deflection curves, deflected shapes, failure modes, and the strain in their reinforcement and concrete.

The conventional RC deep beams were designed to exhibit flexural failure through the formation of a truss mechanism. To facilitate comparison, the same strut and tie model (STM) used for the steel reinforced beams was applied to the design of the CFRP reinforced beams. In addition, the steel reinforced beams with either span-to-depth ratio exhibited flexure-dominated behaviour, characterized by crushing of the relatively large region of the flexural compression zone between the applied point loads. The four CFRP reinforced beams experienced anchorage failure, triggered by interlaminar shear failure of the Isorod longitudinal bars. The more slender CFRP beams exhibited crushing of the concrete in the flexural compression zone near the loading plate prior to anchorage failure. Despite their different modes of failure, the measured ultimate loads and the corresponding deflections of the specimens with the span to depth ratio of 1 were within 4% and 10% of each other, respectively. On the contrary, for the beams with the span to depth ratio of 2, these quantities were further apart, as their ultimate loads and the corresponding deflections differed by a maximum of 8% and 30%, respectively.

All the tested beams had higher shear capacity than that calculated by the ACI 318-08 (2008) and CSA A23.3-04 (2004) strut and tie model provisions. The level of conservatism of these provisions was not consistent as it varied from one beam to the other (see Table 5.1). The cause of the conservatism was investigated by evaluating the current stress limiting factors for the struts and the nodal zones.

Since the tested beams did not exhibit crushing or splitting of the diagonal struts nor crushing of the nodal zones, the calculated factors based on the current test results give the lower bound of the stress limits at which the struts and the nodes are guaranteed to remain intact. The calculated stress limits were compared with current CSA and ACI provisions and also with the recommendations of the other investigators.

6.2 Conclusion

The following conclusions can be drawn from the results of the current experimental and theoretical investigations:

1. The span-to-depth ratio has a significant influence on the ultimate strength of reinforced concrete deep beams. The beams with the span-to-depth ratio of 1 sustained an average 30% higher ultimate shear than the beams with the span-to-depth ratio of 2.
2. The failure mode of the CFRP reinforced deep beams subjected to in-plane loading was brittle, whereas the steel reinforced beams exhibited a more ductile response via yielding of the longitudinal reinforcement, which ultimately led to flexural compression failure of the latter beams.
3. The CFRP reinforced deep beams resisted slightly higher shear load and experienced larger deformation without significant loss in strength. However, the high strength of the CFRP reinforcement was not fully

- utilized due to premature interlaminar shear failure of the main tension bars.
4. The presence of shear reinforcement in the CFRP reinforced beams with span-to-depth ratio of 1 was found to be ineffective, as the strain measurements showed consistently compression strains in the transverse reinforcement bars. On the other hand, in the companion steel reinforced beam, the stirrups helped to restrain the growth of the inclined cracks and enhanced the shear strength of the member.
 5. The crack pattern in the CFRP reinforced deep beams with span-to-depth ratio of 2 was comparable to that in the counterpart steel reinforced member while in the case of the CFRP beams with the span-to-depth of 1 fewer cracks were detected in comparison with the steel reinforced beams.
 6. The overall load-deflection responses of the CFRP reinforced beams were similar to that of the corresponding conventional steel reinforced specimen up to the maximum load, particularly for the beams with the span-to-depth ratio of 1. However, due to the lower elastic modulus of CFRP material, the stiffness of the CFRP reinforced beams was generally smaller. After the formation of the first crack, the load-deflection curves of the CFRP reinforced beams followed a roughly constant slope up to failure.
 7. The current ACI 318 and CSA A23.3, STM provisions were found to be conservative, regardless of the type of reinforcement. The degree of

- conservatism observed for CFRP reinforced beams is deemed appropriate at this time until further experimental data becomes available.
8. The failure mechanisms of the tested beams were correctly predicted by the CSA A23.3 standard, except for the CFRP reinforced beams having the span-to-depth ratio of 1, which failed due to premature anchorage failure.
 9. The straight bar anchorage provisions in the ACI 440 (2001) were found to be inapplicable to the Isorod bars, since they exhibited interlaminar shear failure before the capacity of the bar could be reached. The experimental evidence suggests that a more refined development length equation must be utilized in order to minimize the occurrence of the anchorage failure instigated by interlaminar shear. For the time being, however, it is suggested that Clause 9.3.3 of the CSA S806 (2002) be used, as the development length based on the CSA requirements is 25% greater than that based on the ACI code requirements.
 10. The compression strut and nodal stress limiting factors suggested by the current CSA and ACI are found to be adequate, but the actual limits for the CFRP reinforced beams could not be determined because they did not exhibit damage in their nodal zones and along their struts. Due to anchorage failure of the CFRP reinforced beams, it was not possible to

draw definitive conclusions about the applicability of the current stress efficiency factors to CFRP reinforced deep beams.

11. Based on the overall evaluation of the experimental results, the CFRP reinforcement can be used in concrete deep beams. However, due to the inadequate interlaminar shear capacity of the Isorod bars, to avoid premature anchorage failure, caution must be exercised when detailing the end development length of these bars.

6.3 Recommendations for future work

The following is recommended for future investigation:

1. Study the behaviour of the same size deep beams involving different types of FRP bars including glass and Aramid.
2. It would be worthwhile to investigate the effectiveness of different types of anchorage on the performance of the FRP longitudinal reinforcement bars, such as 90 (deg) hook and mechanical anchorage.
3. Additional experiments are needed to further investigate the applicability of the current strut and tie models to concrete deep beams reinforced with FRP bars. This could be achieved by testing several similarly reinforced specimens with varying span-to-depth ratio under in-plane loads and monitoring their cracking patterns, crack widths, and deformations.

4. Research is needed to rationally quantify the compressive strength of the nodal zones in the FRP reinforced beams, as the higher strains along the FRP bars in the vicinity of the bottom nodal zones could increase the likelihood of the occurrence of nodal failure.
5. Further research is needed to formulate a more universal development length equation that could safely be applied to all types of FRP reinforcing bars.

REFERENCES

- AASHTO LRFD (1998), “Bridge Design Specifications”, 2nd edition, American Association of State Highway and Transportation Officials, Washington, DC, USA.
- ACI-318-02 (2002), “Building Code Requirement for Structural Concrete and Commentary”, Committee 318, American Concrete Institute, Farmington Hills, Michigan, 433 pp.
- ACI-318-08 (2008), “Building Code Requirements for Structural Concrete and Commentary”, Committee 318, American Concrete Institute, Farmington Hills, Michigan, 465 pp.
- ACI 440.1R-01 (2001), “Guide for the Design and Construction of Concrete Reinforced with FRP Bars”, Committee 440, American Concrete Institute, Farmington Hills, Michigan, 41 pp.
- ASCE-ACI Committee 445 (1998), “Recent Approaches to Shear Design of Structural Concrete”, *Journal of Structural Engineering*, ASCE, 124 (12), December, pp. 1375-1417
- Alshegeir, A., and Ramirez, J. A. (1990), “Analysis of disturbed region with strut-and-tie models”, *Structural Engineering Report*, No. CE-STR-90-1, Purdue University, West Lafayette, Ind.
- Aoyama, H. (1993), “Design Philosophy for Shear in Earthquake Resistance in Japan”, *Earthquake Resistance of Reinforced Concrete Structures-A Volume Honoring Hiroyuki Aoyama*, University of Tokyo, Tokyo, Japan, pp. 407-418.
- Autocon Composites Inc. (1997), “New Fiber Composite Material for Reinforced Concrete (NEFMAC) – Fiber Grid Reinforcement for Concrete”, Product data sheet, Ontario, Canada.
- Benmokran, B., Zhang, B., Laoubi, K., Tighiouart, B., and Lord, I. (2002), “Mechanical and bond properties of new generation of carbon fibre reinforced polymer reinforcing bars for concrete structures”, *Canadian Journal of Civil Engineering*, 29(2), pp. 338-343.

- Bergmeister, K., Breen, J. E., and Jirsa, J. O. (1991), “Dimensioning of the nodes and development of reinforcement”, IABSE Colloquium Structural Concrete, Report Vo. 62, Stuttgart, Germany, pp. 551-556.
- Brown, M. D., and Bayrak, O. (2008), “Design Using Strut-And-Tie Models-Part 1: Evaluating U.S. Provisions”, *ACI Structural Journal*, 105(4), pp. 395-404.
- CAN/CSA-A23.3-04 (2004), “Design of Concrete Structure”, Canadian Standards Association, Rexdale, Ontario, 240 pp.
- CAN/CSA S806-2 (2002), “Design and Construction of Building Components with Fiber Reinforced Polymers”, Canadian Standard Association, Toronto, Ontario, 177 pp.
- CEB-FIB (1978), “Model Code for Concrete Structures: CEB-FIP International recommendation”, 3rd Edition, Comité Euro-International du Béton, Paris, 348 pp.
- Collins, M. P., and Mitchell, D. (1986), “A Rational Approach to Shear Design – The 1984 Canadian Code Provisions”, *ACI Journal*, 83(80), pp. 925-933.
- Collins, M. P., and Mitchell, D. (1991), “Prestressed Concrete Structures”, Prentice Hall Inc., Englewood Cliffs, New Jersey, USA, 766 pp.
- Comité Européen de Béton (1964), “Recommendations for an International Code of Practice for Reinforced Concrete” English Edition, Cement and Concrete Association, London, UK.
- de Paiva, H. A. R., and Siess, C. P. (1965), “Strength and Behaviour of Deep Beams in Shear”, *Journal of the Structural Division, Proceedings of ASCE*, Vo. 91, No. ST5, October, pp. 19-41.
- ENV 1992-1-1: Eurocode 2 (EC2) (1991), “Design of Concrete Structures, Part 1: General Rules and Rules for Buildings”, Thomas Telford, London, UK.
- Jirsa, J. O., Breen, J. E., Bergmeister, K., Barton, D., Anderson, R., and Bouadi, H. (1991), “Experimental studies of nodes in strut-and-tie models”, *Structural Concrete, IABSE Colloquium Structural Concrete*, Stuttgart, pp. 525-532.

- Kani, M.W., Huggins, M.W., and Wittkopp, R.R. (1979), “Kani on Shear in Reinforced Concrete”, Department of Civil Engineering, University of Toronto, Toronto, Ontario, Canada, 225 pp.
- Karbhari, V. M. (1998), “Use of Composite Materials in Civil Infrastructure in Japan”, WTEC Monograph, National Science Foundation, Washington, DC, 191 pp.
- Kong, F. K. (1990), “Reinforced Concrete Deep Beams”, Van Nostrand Reinhold, New York, USA, 288 pp.
- Leonhardt, F., and Walther, R. (1966), “Wandartiger Träger (Deep Beams)”, Deutscher Ausschuss für Stahlbeton, Wilhelm Ernst und Sohn, Bulletin No. 178, 159 pp.
- MacGregor, J. G. (1997), “Reinforced Concrete: Mechanics and Design, 3rd Edition”, Prentice Hall Inc., 939 pp.
- MacGregor, J. G., and Wight, J. K. (2005), “Reinforced Concrete: Mechanics and Design, Fourth edition”, Prentice Hall Inc., New Jersey, USA, 1132 pp.
- Machida, A. (1993), “State-of-the-art Report on Continuous Fiber Reinforcing Materials”, Japan Society of Civil Engineering, Yotsuya 1-chome, Shinjuku-ku, Tokyo, Japan, 164 pp.
- Marti, P. (1985), “Basic Tools of Reinforced Concrete Beam Design”, ACI Journal, 82 (1), pp. 46-56.
- Maruyama, Itoh, and Nishiyama. (1989), “Study on Bond Characteristics of Deformed Fibre Reinforced Plastic Rods”, Proceedings of the Japan Concrete Institute, 11 (1), pp.777-782.
- Mörsch, E. Der Eisenbetonbau, seine Theorie und Anwendung (1912), “Reinforced concrete, theory and application”, Verlag Konrad Wittwer, Stuttgart, Germany.
- Nielsen, M.P. (1984), “Limit Analysis and Concrete Plasticity”, Prentice Hall Inc., Englewood Cliffs, New Jersey, USA, 420 pp.

- Nielsen, M. P. (1971), "On the strength of reinforced concrete discs", Civil Engineering and Building Construction Series, No. 70, Acta Polytechnica Scandinavica, Copenhagen.
- Pultrall Inc. (2007), "Technical Data Sheet Straight Carbon V-ROD", Theford Mines, Quebec, Canada.
- Ramirez, J. A., and Breen, J. E. (1991), "Evaluation of a modified truss model approach for beams in shear", *ACI Structural Journal*, 88(5), pp. 562-571.
- Reineck, K., ed. (2002), "Examples for the Design of Structural Concrete with Strut-and-Tie Models", SP-208, American Concrete Institute, Farmington Hill, Michigan, USA, 242 pp.
- Ritter, W. (1899), "Die Bauweise Hennebique (The Hennebique System)", *Schweizerische Bauzeitung*, Bd. XXXIII, No. 7, January.
- Rogowsky, D. M., and MacGregor, J. G. (1986), "Design of reinforced concrete deep beams" *Concrete International: Design & Construction*, 8 (8), pp. 49-58.
- Rogowsky, D. M., and MacGregor, J. G. (1983), "Shear strength of deep reinforced concrete continuous beams", *Structural Engineering Report*, No. 110, Department of Civil Engineering, University of Alberta, Edmonton, Canada, November, 178 pp.
- Su, R. K. L., and Chandler, A. M. (2001), "Design criteria for unified strut and tie models", *Progress in Structural Engineering and Materials*, 3(3), pp. 288-298.
- Schlaich, J., Weischede, D. (1982), "Detailing of Concrete Structures", *Bulletin d'Information 150*, Comité Euro-International du Béton, Paris, 163 pp.
- Schlaich, J., Schäfer, K., and Jennewein, M. (1987), "Toward a Consistent Design of Structural Concrete", *Journal of the Prestressed Concrete Institute*, 32 (3), pp. 74-150.
- Schlaich, J., Schäfer, K. (1991), "Design and Detailing of Structural Concrete Using Strut-and-Tie Models", *The Structural Engineer*, 69 (6), 13 pp.
- Tennyson, R. C., Mufti, A. A., Rizkalla, S., Tadros, G., Benmokrane, B. (2001), "Structural health monitoring of innovative bridges in Canada with fiber optic sensors", *Smart Materials and Structures*, 10(3), pp. 560-573.

- Vecchio, F.J., and Collins, M. P (1986), “The Modified Compression Field Theory for Reinforced Concrete Elements Subjected to Shear”, *ACI Journal*, 83(2), pp. 219-231
- Vecchio, F J., and Collins, M. P (1982), “The Response of Reinforced Concrete to In-Plane Shear and Normal Stresses” The Department of Civil Engineering, University of Toronto, Toronto, Ontario, Canada.
- Walraven, Joost C. (1981), “Fundamental Analysis of Aggregate Interlock”, *Journal of the Structural Division, Proceedings of ASCE*, Vo. 107, No. ST11, November, pp. 2245-2270.
- Zhang, B., Masmoudi, R., Benmokran, B. (2004), “Behaviour of one-way concrete slabs reinforced with CFRP grid reinforcements”, *Construction and Building Materials*, 18 (8), pp. 625-635.

APPENDIX A: SAMPLE CALCULATION

The procedures used to design the deep beams are outlined in this section. In order to facilitate the design calculations of these beams, it was decided to program the design process in the Mathcad 4.0 notebook. By using the constructed design notebook, it was possible to locate and monitor the governing design parameters as the magnitude of the applied load was adjusted. The magnitude of the load was increased until the strength in at least one of the STM components reached its maximum allowable value. The latter load was treated as the maximum load that the beam could carry and was used to compare with the actual load carrying capacity of the beams measured during the test. The design was only conducted for one-half of the beam due to the symmetry of the geometric and loading conditions.

It must be noted that for the design, the nominal tensile strength of the steel reinforcement (400 MPa) and compressive strength of normal-strength concrete (30 MPa) were used. Consequently, the ultimate strength of each beam was calculated using the nominal properties of the materials. The design procedure was repeated for the same beam, using the measured yield strength of steel and compressive strength of concrete, to achieve a more reasonable comparison between the calculated ultimate load and the observed ultimate load. The full sample calculation for the F1 and the S1 beams are provided in this

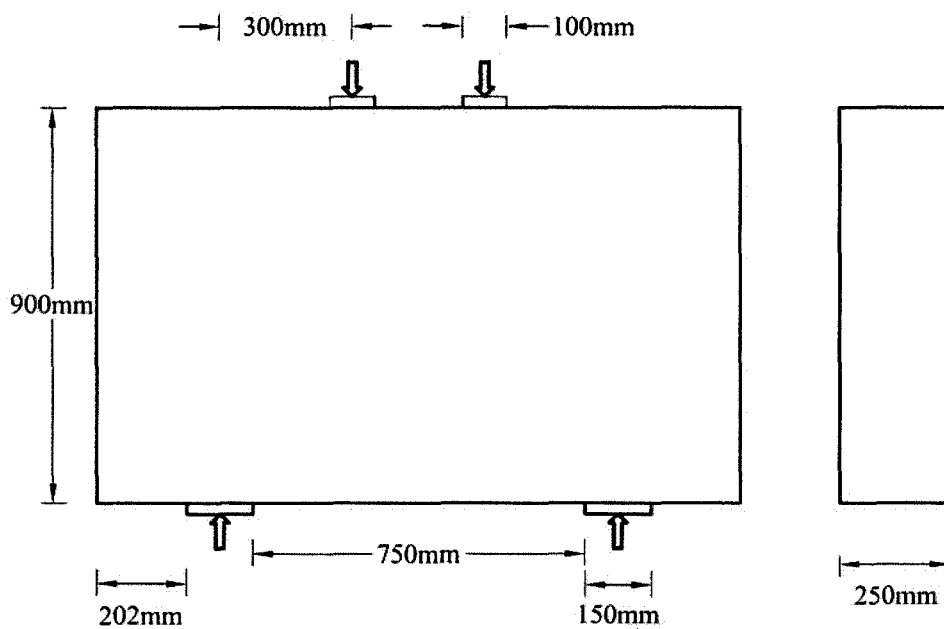
section whereas for the other beams, the results of the calculation and the strength checks for the nodes and struts are provided in a series of tables.

The deep beams were design in accordance with ACI 318 (2008) and ACI 440.1 (2001) provisions. The selected strut and tie model is based on the truss models illustrated by the ACI subcommittee 445-1 (Reineck, 2002).

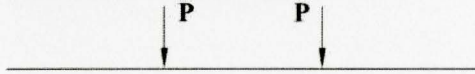
A.1: Design calculations for F1 deep beams

Design calculation for CFRP reinforced deep beam with span-to-depth ratio of 1:

$f'_c := 30$	$\phi_f := 1$	
$L_{shear} := 300$	$\phi_c := 1$	
$L_o := 100$	$P := 390000$	
$L_r := 150$	$o := 202$	
$d_b := 9.5$	$\phi_{flexure} := 1$	(9.3.2.1)
$A_b := 71$	$\phi_{shear} := 1$	(9.3.2.6)
$h := 900$	$f_y := 400$	
$b := 250$	$f_{fu} := 1596$	Pultrall Inc. (2008)



Moment & shear diagram:

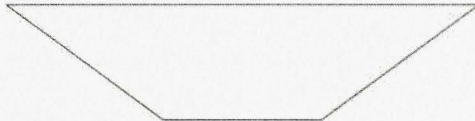


Shear diagram:



$$v := P = 390000$$

Bending moment diagram:



$$M_u := \phi_{flexure} \cdot P \cdot L_{shear} = 117000000$$

Note:

1. The depth of the compression zone is limited to **a**.
2. The tie force is being distributed vertically over the depth **ha**.
3. Ultimate strength in the STM components due to the applied load, **P**, is accounted as a fraction of the nominal strength.
4. **β** value is taken with accordance to the Appendix A.

Strut geometry:

- (A.3.2)
- $\beta_{s1} := 1$ The cross sectional width of the strut is constant across it's length (prismatic).
 - $\beta_{s2} := 0.75$ The cross sectional width of the strut is not constant along its length (bottle-shaped).

Nodal type:

- (A.5.2)
- $\beta_{n1} := 1$ Nodal zones bounded by struts, or bearing areas or both (CCC)
 - $\beta_{n2} := 0.8$ Nodal zones anchoring a tie in one direction only (CCT)
 - $\beta_{n3} := 0.6$ Nodal zones anchoring tie in more than one direction (CTT)

Dimensions of the truss model:

Calculation of the depth of the compression block, **a**, based on the flexural design approach:

Assuming 1 layers of longitudinal reinforcement is provided

$$\begin{aligned} \rightarrow S_{bar} &:= 30 & \rightarrow Cover_{min} &:= 43 \\ d &:= h - Cover_{min} - d_b - \frac{d_b}{2} = 843 \\ M_u &= 1.17 \times 10^8 & M_u &< \phi_{flexure} \cdot M_n & R9.1 \\ \nu &:= 0.85\beta & f_{cu} &:= \nu f'_c \end{aligned}$$

Area of the tie reinforcement:

Knowing that C=T

$$\begin{aligned} \beta &:= \beta_{sl} = 1 & \text{Assuming that the strut has a prismatic geometry} \\ C &:= f_{cu} \cdot b \cdot a \rightarrow 6375.0 \cdot a \cdot \beta & T &:= A_{tie} \cdot f_{fu} \rightarrow 1536 \cdot A_{tie} \\ \frac{C}{T} &= 1 \left| \begin{array}{l} \text{solve, } a \\ \text{float, } 3 \end{array} \right. \rightarrow 0.241 \cdot A_{tie} & a &:= \frac{A_{tie} \cdot f_{fu}}{b \cdot f_{cu}} \text{ float, } 3 \rightarrow \frac{0.241 \cdot A_{tie}}{\beta} \\ M_n &:= \frac{M_u}{\phi_{flexure}} = 117000000 \\ T \cdot \left(d - \frac{a}{2} \right) &= M_n \left| \begin{array}{l} \text{solve, } A_{tie} \\ \text{float, } 3 \end{array} \right. \rightarrow \left(\begin{array}{l} 6902.0 \\ 91.6 \end{array} \right) & ; & \rightarrow A_{tie} := 91.6 \\ a &\rightarrow 0.241 \cdot A_{tie} = 22 & ; & \rightarrow a := 25 \\ jd &:= d - \frac{a}{2} \text{ float, } 5 \rightarrow 830.25 & & jd = 830 \\ h_a &:= 2 \left[h - \left(\frac{a}{2} + jd \right) \right] = 115 \end{aligned}$$

Knowing that the vertical tie is located in the middle of the shear span.

$$\theta := \text{atan} \left[\frac{jd}{\left(\frac{L_{shear}}{2} \right)} \right] = 79.76 \text{ deg}$$

Results:

The depth of compression zone is 25mm, the depth of tie zone is 115mm & the compression struts are portiented 79.8° from the horizontal.

Bearing strength @ the loading points:

Satisfying the Bearing stress < Allowable stress condition

$$\text{Bearing stress @ loading points} = \frac{P}{(L_o \cdot b) \cdot \phi_{shear}} = 15.6$$

Allowable stresses:

$$\nu_{CCC} := \phi_{shear} \cdot 0.85 \cdot \beta_{n1} = 0.85$$

$$\rightarrow \text{Allowable bearing stress} = \nu_{CCC} \cdot f'_c = 25.5 > 15.6 \text{MPa} \checkmark$$

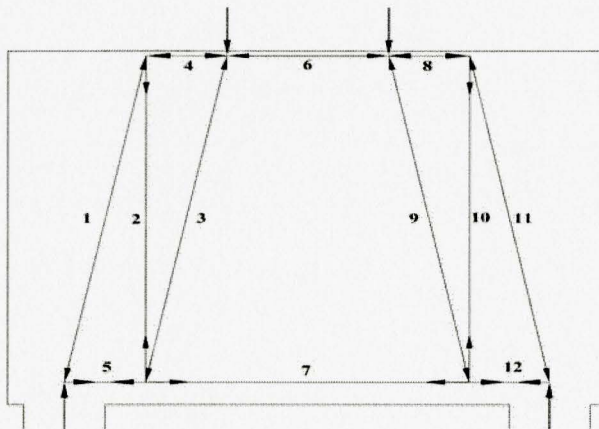
$$\text{Bearing stress @ reaction points} = \frac{P}{(L_r \cdot b) \cdot \phi_{shear}} = 10.4$$

Allowable stresses:

$$\nu_{CCT} := \phi_{shear} \cdot 0.85 \cdot \beta_{n2} = 0.68$$

$$\rightarrow \text{Allowable bearing stress} = \nu_{CCT} \cdot f'_c = 20.4 > 10.4 \text{MPa} \checkmark$$

Internal loads with in the truss model:



Member forces:

$$F_2 := P = 390000 \quad F_{10} := F_2$$

$$F_1 := \frac{F_2}{\sin(\theta)} = 396314 \quad F_{11} := F_1$$

$$F_3 := F_1 = 396314 \quad F_9 := F_3$$

$$F_4 := \frac{F_2}{\tan(\theta)} = 70461 \quad F_8 := F_4$$

$$F_5 := F_4 = 70461 \quad F_{12} := F_8$$

$$F_6 := 2 \cdot F_5 = 140921$$

$$F_7 := F_6 = 140921$$

Check the available width of the strut and nodal zone:

Calculating the available width & compare it with the required width, Satisfying the strength condition outlined in section R9.1 $F_u \leq \phi F_n$

Available width base on the purposed STM:

Node 1:

$$\text{Opposite}_1 := h_a = 115$$

$$\alpha_1 := \text{atan} \left(\frac{L_r}{h_a} \right) = 52.64 \cdot \text{deg}$$

$$\text{Adjacent}_1 := L_r = 150$$

$$\text{Hypotemuse}_1 := \sqrt{h_a^2 + L_r^2} = 189$$

$$\xi_1 := 1.5707963 - \alpha_1 - (1.5707963 - \theta) = 27.11 \cdot \text{deg}$$

$$\text{Width}_{\text{strut}.1} := \text{Hypotemuse}_1 \cdot \cos(\xi_1) = 168$$

Node 2:

$$\text{Opposite}_2 := a = 25$$

$$\text{Adjacent}_2 := \frac{\text{Width}_{\text{strut}.1}}{\sin(\theta)} - \frac{a}{\tan(\theta)} = 166$$

$$\text{Hypotemuse}_2 := \sqrt{\text{Opposite}_2^2 + \text{Adjacent}_2^2} = 168$$

Node 4:

$$\text{Opposite}_4 := a = 25$$

$$\alpha_4 := \text{atan} \left(\frac{a}{L_o} \right) = 14 \cdot \text{deg}$$

$$\text{Adjacent}_4 := L_o = 100$$

$$\text{Hypotemuse}_4 := \sqrt{a^2 + L_o^2} = 103 \quad \rightarrow \xi_4 := 1.5707963 - (\theta + \alpha_4) = -3.8 \cdot \text{deg}$$

$$\text{Width}_{\text{strut}.3} := \text{Hypotemuse}_4 \cdot \cos(\xi_4) = 103$$

Node 3:

→ This nodal zone is not necessarily right angle triangle. It was assumed that that the **B** length was limited by the extension of the width of the strut around nodal zone 3.

$$A := \frac{h_a}{\sin(\theta)} = 116$$

$$B_1 := \frac{h_a}{\tan(\theta)} = 21$$

$$B'_2 := \text{Width}_{\text{strut}.3} \cdot \cos(1.5707963 - \theta) = 101$$

$$B''_2 := (h_a - \text{Width}_{\text{strut}.3} \cdot \sin(1.5707963 - \theta)) \cdot \tan(1.5707963 - \theta) = 17.38$$

$$B_2 := B'_2 - B''_2 = 83.83$$

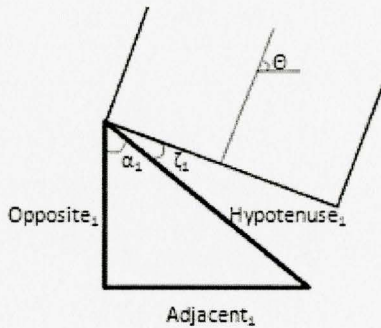
$$B := B_1 + B_2 = 105$$

$$\theta_{N3.1} := \text{atan}\left(\frac{h_a}{B_2}\right) = 53.79 \cdot \text{deg} \quad \theta_{N3.2} := \theta = 79.8 \cdot \text{deg}$$

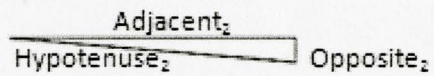
$$\theta_{N3.3} := 3.1415927 - \theta_{N3.1} - \theta_{N3.2} = 46.45 \cdot \text{deg}$$

$$C := \sqrt{h_a^2 + B_2^2} = 142$$

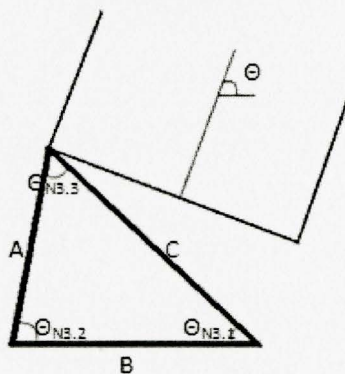
Node 1 dimensions:



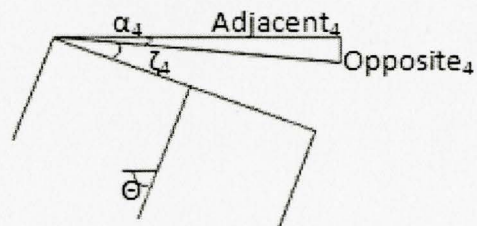
Node 2 dimension.



Node 3 dimension.



Node 4 dimension.



Required width:

Strut width:

β_{s1} is used for horizontal struts and β_{s2} is used for the diagonal struts for the purpose of calculating the nominal compressive strength.

satisfying the strength condition $F_u \leq \phi F_n$

Strut 4:

$$F_{u.4} := F_4 = 70461$$

$$\nu := 0.85\beta_{s1} = 0.85$$

$$f_{cu} := \nu f'_c = 25.5$$

$$F_n := b \cdot f_{cu} \cdot W_{required} \rightarrow 6375.0 \cdot W_{required}$$

$$\rightarrow \frac{F_{u.4}}{\phi_{shear} \cdot F_n} = 1 \left| \begin{array}{l} \text{solve, } W_{required} \\ \text{float, 1} \end{array} \right. \rightarrow 11.0 < a = 25 \quad \checkmark$$

Strut 6:

$$F_{u.6} := F_6 = 140921$$

$$\rightarrow \frac{F_{u.6}}{\phi_{shear} \cdot F_n} = 1 \left| \begin{array}{l} \text{solve, } W_{required} \\ \text{float, 1} \end{array} \right. \rightarrow 22.0 < a = 25 \quad \checkmark$$

Strut 1:

$$F_{u.1} := F_1 = 396314$$

$$\nu := 0.85\beta_{s2} = 0.64$$

$$f_{cu} := \nu f'_c = 19.13$$

$$F_n := b \cdot f_{cu} \cdot W_{required..} \rightarrow 4781.25 \cdot W_{required..}$$

$$\rightarrow \frac{F_{u.1}}{\phi_{shear} \cdot F_n} = 1 \left| \begin{array}{l} \text{solve, } W_{required..} \\ \text{float, 1} \end{array} \right. \rightarrow 82.0 < Width_{strut.1} = 168 \quad \checkmark$$

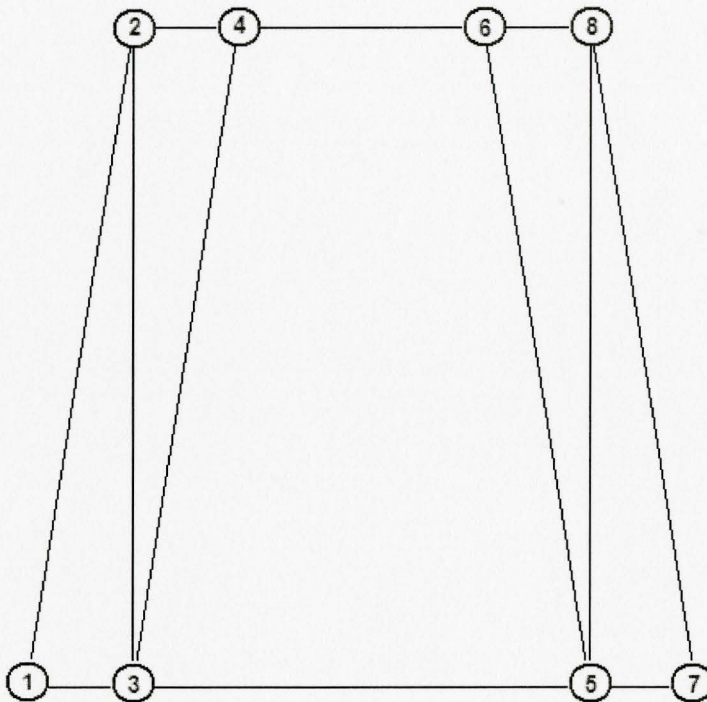
Strut 3.

$$F_{u.3} := F_3 = 396314$$

$$\rightarrow \frac{F_{u.3}}{\phi_{shear} \cdot F_n} = 1 \left| \begin{array}{l} \text{solve, } W_{required..} \\ \text{float, 1} \end{array} \right. \rightarrow 82.0 < Width_{strut.3} = 103 \quad \checkmark$$

Due to symmetry we expect the same results for the struts in the right half of the beam.

Nodal zone perimeter:



Node 1 (CCT):

$$F_1 = 396314 \quad \rightarrow \quad W_{strut.1} := 82$$

$$\rightarrow W_{required} := W_{strut.1} \cdot \frac{\beta_{s2}}{\beta_{n2}} = 77 < Width_{strut.1} = 168 \quad \checkmark$$

$$P = 390000$$

$$\rightarrow W_{required} := \frac{P}{\nu_{CCT} \cdot b \cdot f_c} = 76 < L_r = 150 \quad \checkmark$$

$$F_{u.5} := F_5 = 70461$$

$$\frac{F_{u.5}}{\phi_{shear} \cdot F_n} = 1 \quad \left| \begin{array}{l} \text{solve, } W_{required} \\ \text{float, 1} \end{array} \right. \rightarrow 11.0$$

$$\rightarrow W_{strut.5} := 11$$

$$\rightarrow W_{required..} := W_{strut.5} \cdot \frac{\beta_{s1}}{\beta_{n2}} = 14 < h_a = 115 \quad \checkmark$$

Node 2 (CCT):

$$F_1 = 396314$$

$$\rightarrow W_{required...} := W_{strut.1} \cdot \frac{\beta_{s2}}{\beta_{n2}} = 77 < Width_{strut.1} = 168 \quad \checkmark$$

$$F_{u.4} = 70461 \quad \rightarrow W_{strut.4} := 11$$

$$\rightarrow W_{required....} := W_{strut.4} \cdot \frac{\beta_{s1}}{\beta_{n2}} = 14 < a = 25 \quad \checkmark$$

$$F_2 = 390000$$

$$\rightarrow W_{required.....} := \frac{P}{\nu_{CCT} \cdot b \cdot f_c} = 76 < L_{shear} = 300 \quad \checkmark$$

Node 3 (CTT):

$$F_{u.3} = 396314 \quad \rightarrow W_{strut.3} := 82$$

$$\rightarrow W_{required.....} := W_{strut.3} \cdot \frac{\beta_{s2}}{\beta_{n3}} = 103 < Width_{strut.3} = 103 \quad \checkmark$$

$$F_{u.5} = 70461$$

$$\rightarrow W_{required.....} := W_{strut.5} \cdot \frac{\beta_{s1}}{\beta_{n3}} = 18 < h_a = 115 \quad \checkmark$$

$$F_2 = 390000$$

$$\nu_{CTT} := \phi_{shear} \cdot 0.85 \cdot \beta_{n3} = 0.51$$

$$\rightarrow W_{required.....} := \frac{P}{\nu_{CTT} \cdot b \cdot f_c} = 102 < L_{shear} = 300 \checkmark$$

$$F_{u.7} := F_7 = 140921$$

$$\frac{F_{u.7}}{\phi_{shear} \cdot F_n} = 1 \left| \begin{array}{l} \text{solve, } W_{required} \\ \text{float, 1} \end{array} \right. \rightarrow 22.0$$

$$\rightarrow W_{strut.7} := 22$$

$$\rightarrow W_{required.....} := W_{strut.7} \cdot \frac{\beta_{s1}}{\beta_{n3}} = 37 < h_a = 115 \checkmark$$

Node 4 (CCC):

$$P = 390000$$

$$\rightarrow W_{required...} := \frac{P}{\nu_{CCC} \cdot b \cdot f_c} = 61 < L_o = 100 \checkmark$$

$$F_{u.4} = 70461$$

$$\rightarrow W_{required...} := W_{strut.4} \cdot \frac{\beta_{s1}}{\beta_{n1}} = 11 < a = 25 \checkmark$$

$$F_{u.6} = 140921 \quad \rightarrow W_{strut.6} := W_{strut.7} = 22$$

$$\rightarrow W_{required} := W_{strut.6} \cdot \frac{\beta_{s1}}{\beta_{n1}} = 22 < a = 25 \checkmark$$

$$F_{u.3} = 396314$$

$$\rightarrow W_{required...} := W_{strut.3} \cdot \frac{\beta_{s2}}{\beta_{n1}} = 62 < Width_{strut.3} = 103 \checkmark$$

Main steel requirement in tie zones:

Tie 2 (B/t nodes 2 & 3):

$$F_2 = 390000 \quad A_v := 100 \quad f_{fu,v} := 1180 \quad (\text{Autocon Inc. 1997})$$

$$A_{s2.required} := \frac{F_2}{f_{fu,v}} = 331$$

Tie 2 is a vertical tie so 2 leg stirrups must be used.

$$\text{Required amount of reinforcement} = \frac{A_{s2.required}}{2 \cdot A_v} = 1.65 \quad \rightarrow \quad NEFMAC_{2.required} := 2$$

Tie 5 (B/t nodes 1&3):

$$F_5 = 70461$$

$$A_{s5.required} := \frac{F_5}{f_{fu}} = 44$$

$$\text{Required amount of Reinforcement} = \frac{A_{s5.required}}{A_b} = 0.62$$

At least 2 tie is need to be used in order to hold the stirrups. Also because we don't want the bars to reach their ultimate strength. It appears that the reinforcement for tie 7 would have to be developed over the span of tie 2. Thus, it is safe to assume 2 bars.

$$\rightarrow \quad \text{Isorod}_{5.required} := 2$$

Tie 7 (B/t nodes 3&5):

$$F_7 = 140921$$

$$A_{s7.required} := \frac{F_7}{f_{fu}} = 88$$

$$\text{Required amount of steel} = \frac{A_{s7.required}}{A_b} = 1.24$$

$$\rightarrow \quad \text{Isorod}_{7.required} := 2$$

Placement of reinforcements (vertically):

Node 3 & 5:

$$F_7 = 140921$$

$$\nu_{..} := 0.85\beta_{n3} = 0.51 \quad (\text{CTT})$$

$$f_{cu..} := \nu_{..} \cdot f'_c = 15.3$$

Spread the reinforcement vertically over an area of concrete at least equal to the tension force in the tie.

$$\text{Spread vertically over} = \frac{F_7}{f_{cu..} \cdot b} = 37$$

Allowable Upper & Lower bound for rebar distribution:

$$\frac{h_a}{2} + \frac{F_7}{f_{cu..} \cdot b \cdot 2} = 76$$

$$\frac{h_a}{2} - \frac{F_7}{f_{cu..} \cdot b \cdot 2} = 39$$

Since tie reinforcement is placed in a single layer, place them at 57mm from the extreme tension fibre.

Modified value for the effective depth:

$$d := h - 57 = 843$$

Anchorage of the bottom main reinforcements:

Tie 5:

The development length is being calculated with accordance to the ACI 440.1R-01. The development length is being formulated to minimize the chance of bar-pullout failure and it has been know to be a conservative estimate of the development length for a straight FRP bar.

$$F_5 = 70461$$

$$f_{FRP} := \frac{F_5}{Isorod_{5,required} A_b} = 496$$

$$\phi_{strength.ratio} := \frac{f_{FRP}}{f_{fu}} = 0.31$$

$$L_{d.required} := \frac{d_b \cdot f_{fu}}{18.5} \cdot \phi_{strength.ratio} = 255 \quad (11.1)$$

$$\leftarrow L_{d.available} := L_r + \frac{h_a}{2 \cdot \tan(\theta)} + o = 362 \quad \checkmark$$

Tie 7:

Extend the bar in the tie 5 & 12 zone by:

$$T_2 := F_7 = 1.41 \times 10^5$$

$$f_{FRP} := \frac{T_2}{Isorod_{7,required} A_b} = 992 \quad \phi_{strength.ratio} := \frac{f_{FRP}}{f_{fu}} = 0.62$$

$$L_{d.required} := \frac{d_b \cdot f_{fu}}{18.5} \cdot \phi_{strength.ratio} = 510 \quad (11.1)$$

$$\leftarrow L_{d.available} := \frac{L_{shear}}{2} + \frac{L_r}{2} + \frac{h_a}{2 \cdot \tan(\theta)} + o + \left(\frac{Width_{strut.3}}{2 \cdot \sin(\theta)} - \frac{h_a}{2 \cdot \tan(\theta)} \right) = 479 \quad \checkmark$$

Tie 2:

Spacing of the stirrups:

$$(11.7.4) \quad \rightarrow \quad S \leq \frac{d}{5} = 169 \quad ; \quad S := \frac{L_{shear} - \frac{(L_o + L_r)}{2}}{(NEFMAC_{2,required} + 1)} = 58$$

$$305$$

S=60mm is within the acceptable range. \checkmark

Results:

1. **Extend the beam span by 202 mm from the outer face of the support, on each side.**
2. **Tie 5,12:**
2, 9.5mm diameter Isorod bars is required to transfer the tension at the longitudinal tie element.
Locate the bars horizontally @ 57mm from the extreme tension fibre.
Extend the bars 277mm from nodes 1 & 7.
3. **Tie 7:**
No additional reinforcement is necessary as long as the longitudinal reinforcement provided for the tie 5 & 12 is extended to resist the tension in tie 7.
4. **Tie 2, 10:**
Evenly distribute 2, NEFMAC closed stirrup over the clear shear span.
space the stirrups 60 mm apart (center-to-center).

Crack control reinforcement:

Since the F'_c is less than 41MPa, with accordance to the Appendix A, section A.3.3.1, the axis of the strut must be crossed by layers of reinforcement that satisfy:

$$\Sigma \rho_{vi} \sin \theta \geq 0.003$$

$$d_s := 5.74 \qquad A_s := \pi \frac{d_s^2}{4} = 26$$

$$\rho_{vi} := \frac{2A_{si}}{b \cdot s_i} = \frac{0.003}{\sin(\theta)} \left| \begin{array}{l} \text{solve, } A_{si} \\ \text{float, } 4 \end{array} \right. \rightarrow 0.3811 \cdot s_i$$

$$\rightarrow A_{si} := 0.3808s_i = 26 \left| \begin{array}{l} \text{solve, } s_i \\ \text{float, } 3 \end{array} \right. \rightarrow 68.3$$

Spacing of the stirrups:

$$(11.7.4) \quad \rightarrow s_i \leq \frac{d}{5} = 169 \qquad \text{Use S=102mm spacing.}$$

305

Selection of the welded wire based on the required density of steel, A_s (mm²/m), per 1m:

$$\rightarrow L := 1000$$

$$n := \frac{L}{102} \qquad A_s := n \cdot (A_s) \rightarrow 253.6959267485663333$$

Thus use MW 25.8 grade for the web reinforcement

Results:

1. Apply a layer of MW25.8 X MW25.8 welded-wire mesh as a skin reinforcement to both faces of the deep beams.
2. The size of the mesh must be 102mm X 102mm center to center spacing.

A.2: Design calculations for F2 deep beams**Input parameters:**

$f'_c := 30$	$\phi_f := 1$	
$L_{shear} := 600$	$\phi_c := 1$	
$L_o := 210$	$P := 395000$	
$L_r := 210$	$o := 180$	
$d_b := 9.5$	$\phi_{flexure} := 1$	(9.3.2.1)
$A_b := 71$	$\phi_{shear} := 1$	(9.3.2.6)
$h := 900$	$f_y := 400$	
$b := 250$	$f_{fu} := 1596$	Pultrall Inc. (2008)

Maximum shear and bending moment values:

$$v := P = 395000$$

$$M_u := \phi_{flexure} \cdot P \cdot L_{shear} = 237000000$$

The corresponding depth of compression zone, a , is 50mm, the depth of tie zone, h_a , is 115mm & the compression struts are oriented at an angle, θ , of 69.9° from the longitudinal reinforcements.

The existing forces in the strut and tie elements of the selected STM:

$$F_2 := P = 395000 \quad F_{10} := F_2$$

$$F_1 := \frac{F_2}{\sin(\theta)} = 420590 \quad F_{11} := F_1$$

$$F_3 := F_1 = 420590 \quad F_9 := F_3$$

$$F_4 := \frac{F_2}{\tan(\theta)} = 144468 \quad F_8 := F_4$$

$$F_5 := F_4 = 144468 \quad F_{12} := F_8$$

$$F_6 := 2 \cdot F_5 = 288936$$

$$F_7 := F_6 = 288936$$

Bearing strength @ the loading points:

Satisfying the Bearing stress < Allowable stress condition

$$\text{Bearing stress @ loading points} = \frac{P}{(L_o \cdot b) \cdot \phi_{shear}} = 7.5$$

Allowable stresses:

$$\nu_{CCC} := \phi_{shear} \cdot 0.85 \cdot \beta_{n1} = 0.85$$

$$\rightarrow \text{Allowable bearing stress} = \nu_{CCC} f_c = 25.5 > 7.5 \text{MPa} \quad \checkmark$$

$$\text{Bearing stress @ reaction points} = \frac{P}{(L_r \cdot b) \cdot \phi_{shear}} = 7.5$$

Allowable stresses:

$$\nu_{CCT} := \phi_{shear} \cdot 0.85 \cdot \beta_{n2} = 0.68$$

$$\rightarrow \text{Allowable bearing stress} = \nu_{CCT} f_c = 20.4 > 7.5 \text{MPa} \quad \checkmark$$

Geometric dimensions of the nodal zones:

Node #1:

Opposite₁=115

Adjacent₁=210

Hypotenuse₁=239

Node #2:

Opposite₂=45

Adjacent₂=235

Hypotenuse₂=240

Node #4:

Opposite₄=45

Adjacent₄=210

Hypotenuse₄=215

Node #3:

A=122

B=226

C=217

Verification of strength of Struts:

Strut #	End nodes	β_s	θ (°)	Force (kN)	Width (mm)		Adequacy
					Required	Provided	
4	2-4	1	0	144468	22	45	OK
6	4-6	1	0	288936	45	45	NOT OK
1	1-2	0.75	70	420590	87	237	OK
3	3-4	0.75	70	420590	87	214	OK

Verification of strength of nodal zones:

Node #	Type	B _n	Force (kN)		Width (mm)		Adequacy
			Identity	Magnitude	Required	Provided	
1	CCT	0.8	F ₁	420590	82	237	OK
			P	395000	77	210	OK
			F ₅	144468	28	115	OK
2	CCT	0.8	F ₁	420590	82	237	OK
			F ₄	144468	28	45	OK
			F ₂	395000	77	600	OK
3	CTTT	0.6	F ₃	420590	109	213	OK
			F ₅	144468	37	115	OK
			F ₂	395000	103	600	OK
			F ₇	288936	75	115	OK
4	CCCC	1	P	395000	62	210	OK
			F ₄	144468	22	45	OK
			F ₆	288936	45	45	OK
			F ₃	420590	65	213	OK

Reinforcement requirement:

Tie #	End nodes	θ (°)	Force (kN)	Reinforcement (mm ²)			Adequacy
				Type	Required	Provided	
2	2-3	90	395000	NEFMAC	335	400	OK
5	1-3	0	144468	Isorod	91	213	OK
7	3-5	0	288936	Isorod	181	213	OK

Results:

1. *Extend the beam span by 180 mm from the outer face of the support, on each side.*
2. *Tie 5 and 12:*
 - *3, 9.5 mm diameter Isorod bars is required to transfer the tension at the longitudinal tie element.*
 - *Locate the bars horizontally @ 57mm from the extreme tension fibre.*
 - *Extend the bars 255mm from nodes 1 & 7.*
3. *Tie 7: No additional reinforcement is necessary as long as the longitudinal reinforcement provided for the tie 5 & 12 is extended to resist the tension in tie 7.*
4. *Tie 2 and 10: Evenly distribute 2, NEFMAC closed stirrup over the clear shear span. Space the stirrups 130 mm apart (center-to-center).*
5. *Place a layer of MW25.8 X MW25.8 welded-wire mesh as skin reinforcement to each face of the beam.*
6. *The mesh bars must have a 102mm X 102mm, center to center, spacing.*

A.3: Design calculations for S1-B deep beam

Design calculation for steel reinforced deep beam with span-to-depth ratio of 1:

$$\begin{aligned}
 f'_c &:= 30 & b &:= 250 \\
 L_{shear} &:= 300 & \phi_s &:= 1 \\
 L_o &:= 100 & \phi_c &:= 1 \\
 L_r &:= 150 & P &:= 320000 \\
 d_{b.10} &:= 113 & o &:= 30 \\
 A_{b.10} &:= 100 & \phi_{flexure} &:= 1 & (9.3.2.1) \\
 d_{b.15} &:= 16 & \phi_{shear} &:= 1 & (9.3.2.6) \\
 A_{b.15} &:= 200 & f_{y.10} &:= 400 \\
 h &:= 900 & f_{y.15} &:= 400
 \end{aligned}$$

Maximum shear and bending moment values:

$$v := P = 320000$$

$$M_u := \phi_{flexure} \cdot P \cdot L_{shear} = 96000000$$

Dimensions of the truss model:

Calculation of the depth of the compression block, a , based on the flexural design approach:

Assuming 1 layers of longitudinal reinforcement is provided

$$\rightarrow S_{bar} := 30 \qquad \rightarrow Cover_{min} := 40$$

$$d := h - Cover_{min} - d_{b.15} - \frac{d_{b.10}}{2} = 838$$

$$M_u = 9.6 \times 10^7$$

$$M_u < \phi_{flexure} \cdot M_n \qquad R9.1$$

$$\nu := 0.85\beta$$

$$f_{cu} := \nu f'_c$$

Area of the tie reinforcement:

Knowing that C=T

$$\beta := \beta_{s1} = 1 \quad \text{Assuming that the strut has a prismatic geometry}$$

$$C := f_{cu} \cdot b \cdot a \rightarrow 6375.0 \cdot a \cdot \beta \quad T := A_{tie} \cdot f_y \cdot 10 \rightarrow 400 \cdot A_{tie}$$

$$\frac{C}{T} = 1 \quad \left[\begin{array}{l} \text{solve, } a \\ \text{float, } 3 \end{array} \right] \rightarrow 0.0627 \cdot A_{tie} \quad a := \frac{A_{tie} \cdot f_y \cdot 10}{b \cdot f_{cu}} \text{ float, } 3 \rightarrow \frac{0.0627 \cdot A_{tie}}{\beta}$$

$$M_n := \frac{M_u}{\phi_{flexure}} = 96000000$$

$$T \cdot \left(d - \frac{a}{2} \right) = M_n \quad \left[\begin{array}{l} \text{solve, } A_{tie} \\ \text{float, } 3 \end{array} \right] \rightarrow \left(\begin{array}{l} 26452.0 \\ 289.0 \end{array} \right) \quad ; \quad \rightarrow A_{tie} := 289$$

$$a \rightarrow 0.0627 \cdot A_{tie} = 18 \quad ; \quad \rightarrow a := 25$$

$$jd := d - \frac{a}{2} \text{ float, } 5 \rightarrow 825.85 \quad jd = 826$$

$$h_a := 2 \left[h - \left(\frac{a}{2} + jd \right) \right] = 123$$

Knowing that the vertical tie is located in the middle of the shear span.

$$\theta := \text{atan} \left[\frac{jd}{\left(\frac{L_{shear}}{2} \right)} \right] = 79.71 \cdot \text{deg}$$

Results:

The depth of compression zone is 25mm, the depth of tie zone is 123mm & the compression struts are poriented 79.7° from the horizontal.

Bearing strength @ the loading points:

Satisfying the Bearing stress < Allowable stress condition

$$\text{Bearing stress @ loading points} = \frac{P}{(L_o \cdot b) \cdot \phi_{shear}} = 12.8$$

Allowable stresses:

$$\nu_{CCC} := \phi_{shear} \cdot 0.85 \beta_{n1} = 0.85$$

$$\rightarrow \text{Allowable bearing stress} = \nu_{CCC} f'_c = 25.5 > 12.8 \text{ MPa} \checkmark$$

$$\text{Bearing stress @ reaction points} = \frac{P}{(L_r \cdot b) \cdot \phi_{shear}} = 8.5$$

Allowable stresses:

$$\nu_{CCT} := \phi_{shear} \cdot 0.85 \beta_{n2} = 0.68$$

$$\rightarrow \text{Allowable bearing stress} = \nu_{CCT} f'_c = 20.4 > 8.5 \text{ MPa} \checkmark$$

The existing forces in the strut and tie elements of the selected STM:

$$F_2 := P = 320000 \quad F_{10} := F_2$$

$$F_1 := \frac{F_2}{\sin(\theta)} = 325236 \quad F_{11} := F_1$$

$$F_3 := F_1 = 325236 \quad F_9 := F_3$$

$$F_4 := \frac{F_2}{\tan(\theta)} = 58122 \quad F_8 := F_4$$

$$F_5 := F_4 = 58122 \quad F_{12} := F_8$$

$$F_6 := 2 \cdot F_5 = 116244$$

$$F_7 := F_6 = 116244$$

Check the available width of the strut and nodal zone:

Calculating the available width & compare it with the required width, Satisfying the strength condition outlined in section R9.1 $F_u \leq \phi F_r$

Available width base on the purposed STM.

Node 1.

$$\text{Opposite}_1 := h_a = 123$$

$$\alpha_1 := \text{atan} \left(\frac{L_r}{h_a} \right) = 50.58 \cdot \text{deg}$$

$$\text{Adjacent}_1 := L_r = 150$$

$$\text{Hypotenuse}_1 := \sqrt{h_a^2 + L_r^2} = 194$$

$$\xi_1 := 1.5707963 - \alpha_1 - (1.5707963 - \theta) = 29.13 \cdot \text{deg}$$

$$\text{Width}_{\text{strut.1}} := \text{Hypotenuse}_1 \cdot \cos(\xi_1) = 170$$

Node 2:

$$\text{Opposite}_2 := a = 25$$

$$\text{Adjacent}_2 := \frac{\text{Width}_{\text{strut.1}}}{\sin(\theta)} - \frac{a}{\tan(\theta)} = 168$$

$$\text{Hypotenuse}_2 := \sqrt{\text{Opposite}_2^2 + \text{Adjacent}_2^2} = 170$$

Node 4:

$$\text{Opposite}_4 := a = 25$$

$$\alpha_4 := \text{atan} \left(\frac{a}{L_o} \right) = 14 \cdot \text{deg}$$

$$\text{Adjacent}_4 := L_o = 100$$

$$\text{Hypotenuse}_4 := \sqrt{a^2 + L_o^2} = 103 \quad \rightarrow \quad \xi_4 := 1.5707963 - (\theta + \alpha_4) = -3.7 \cdot \text{deg}$$

$$\text{Width}_{\text{strut.3}} := \text{Hypotenuse}_4 \cdot \cos(\xi_4) = 103$$

Node 3.

→ This nodal zone is not necessarily right angle triangle. It was assumed that that the **B** length was limited by the extension of the width of the strut around nodal zone 3.

$$A := \frac{h_a}{\sin(\theta)} = 125$$

$$B_1 := \frac{h_a}{\tan(\theta)} = 22$$

$$B'_2 := Width_{strut.3} \cdot \cos(1.5707963 - \theta) = 101$$

$$B''_2 := (h_a - Width_{strut.3} \cdot \sin(1.5707963 - \theta)) \cdot \tan(1.5707963 - \theta) = 19.06$$

$$B_2 := B'_2 - B''_2 = 82.15$$

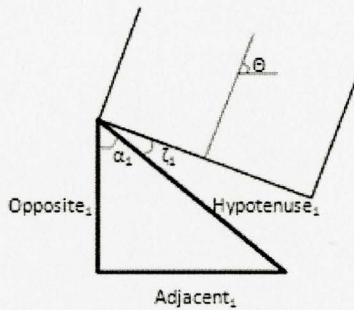
$$B := B_1 + B_2 = 105$$

$$\theta_{N3.1} := \operatorname{atan} \left(\frac{h_a}{B_2} \right) = 56.33 \cdot \text{deg} \quad \theta_{N3.2} := \theta = 79.7 \cdot \text{deg}$$

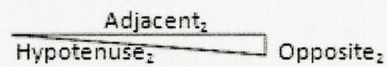
$$\theta_{N3.3} := 3.1415927 - \theta_{N3.1} - \theta_{N3.2} = 43.97 \cdot \text{deg}$$

$$C := \sqrt{h_a^2 + B_2^2} = 148$$

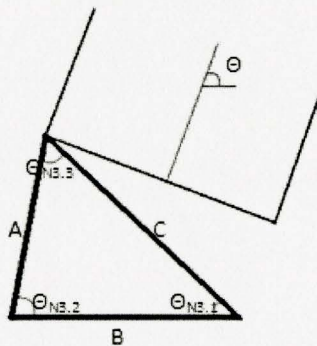
Node 1 dimensions:



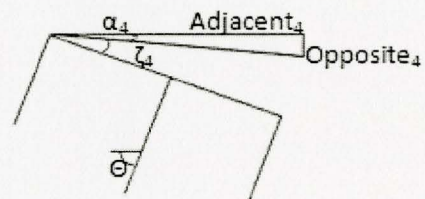
Node 2 dimension.



Node 3 dimension.



Node 4 dimension.



Required width:

Strut width:

β_{s1} is used to for horizontal struts and β_{s2} is used for the diagonal struts for the purpose of calculating the nominal compressive strength.

satisfying the strength condition $F_u \leq \phi F_n$

Strut 4:

$$F_{u.4} := F_4 = 58122$$

$$\nu := 0.85\beta_{s1} = 0.85$$

$$f_{cu} := \nu f'_c = 25.5$$

$$F_n := b \cdot f_{cu} \cdot W_{required} \rightarrow 6375.0 \cdot W_{required}$$

$$\rightarrow \frac{F_{u.4}}{\phi_{shear} \cdot F_n} = 1 \left| \begin{array}{l} \text{solve, } W_{required} \\ \text{float, 1} \end{array} \right. \rightarrow 9.0 < a = 25 \quad \checkmark$$

Strut 6:

$$F_{u.6} := F_6 = 116244$$

$$\rightarrow \frac{F_{u.6}}{\phi_{shear} \cdot F_n} = 1 \left| \begin{array}{l} \text{solve, } W_{required} \\ \text{float, 1} \end{array} \right. \rightarrow 18.0 < a = 25 \quad \checkmark$$

Strut 1:

$$F_{u.1} := F_1 = 325236$$

$$\nu := 0.85\beta_{s2} = 0.64$$

$$f_{cu} := \nu f'_c = 19.13$$

$$F_n := b \cdot f_{cu} \cdot W_{required..} \rightarrow 4781.25 \cdot W_{required..}$$

$$\rightarrow \frac{F_{u.1}}{\phi_{shear} \cdot F_n} = 1 \left| \begin{array}{l} \text{solve, } W_{required..} \\ \text{float, 1} \end{array} \right. \rightarrow 68.0 < Width_{strut.1} = 170 \quad \checkmark$$

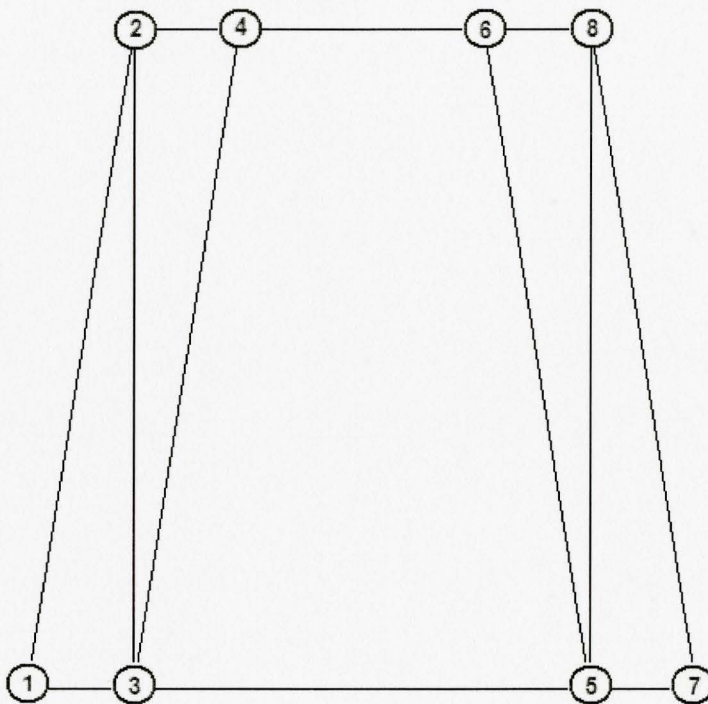
Strut 3.

$$F_{u,3} := F_3 = 325236$$

$$\rightarrow \frac{F_{u,3}}{\phi_{shear} \cdot F_n} = 1 \left| \begin{array}{l} \text{solve, } W_{required} \\ \text{float, 1} \end{array} \right. \rightarrow 68.0 < Width_{strut.3} = 103 \quad \checkmark$$

Due to symmetry we expect the same results for the struts in the right half of the beam.

Nodal zone perimeter:



Node 1 (CCT):

$$F_1 = 325236 \quad \rightarrow \quad W_{strut.1} := 68$$

$$\rightarrow W_{required} := W_{strut.1} \cdot \frac{\beta_{s2}}{\beta_{n2}} = 64 < Width_{strut.1} = 170 \quad \checkmark$$

$$P = 320000$$

$$\rightarrow W_{required} := \frac{P}{\nu_{CCT} \cdot b \cdot f_c} = 63 < L_r = 150 \quad \checkmark$$

$$F_{u.5} := F_5 = 58122$$

$$\frac{F_{u.5}}{\phi_{shear} \cdot F_n} = 1 \quad \left| \begin{array}{l} \text{solve, } W_{required} \\ \text{float, 1} \end{array} \right. \rightarrow 9.0$$

$$\rightarrow W_{strut.5} := 9$$

$$\rightarrow W_{required..} := W_{strut.5} \cdot \frac{\beta_{s1}}{\beta_{n2}} = 11 < h_a = 123 \quad \checkmark$$

Node 2 (CCT):

$$F_1 = 325236$$

$$\rightarrow W_{required...} := W_{strut.1} \cdot \frac{\beta_{s2}}{\beta_{n2}} = 64 < Width_{strut.1} = 170 \quad \checkmark$$

$$F_{u.4} = 58122 \quad \rightarrow W_{strut.4} := 9$$

$$\rightarrow W_{required....} := W_{strut.4} \cdot \frac{\beta_{s1}}{\beta_{n2}} = 11 < a = 25 \quad \checkmark$$

$$F_2 = 320000$$

$$\rightarrow W_{required.....} := \frac{P}{\nu_{CCT} \cdot b \cdot f_c} = 63 < L_{shear} = 300 \quad \checkmark$$

Node 3 (CTT):

$$F_{u.3} = 325236 \quad \rightarrow W_{strut.3} := 68$$

$$\rightarrow W_{required.....} := W_{strut.3} \cdot \frac{\beta_{s2}}{\beta_{n3}} = 85 < Width_{strut.3} = 103 \quad \checkmark$$

$$F_{u.5} = 58122$$

$$\rightarrow W_{required.....} := W_{strut.5} \cdot \frac{\beta_{s1}}{\beta_{n3}} = 15 < h_a = 123 \quad \checkmark$$

$$F_2 = 320000$$

$$\nu_{CTT} := \phi_{shear} \cdot 0.85 \cdot \beta_{n3} = 0.51$$

$$\rightarrow W_{required.....} := \frac{P}{\nu_{CTT} \cdot b \cdot f_c} = 84 < L_{shear} = 300 \checkmark$$

$$F_{u.7} := F_7 = 116244$$

$$\frac{F_{u.7}}{\phi_{shear} \cdot F_n} = 1 \left| \begin{array}{l} \text{solve, } W_{required} \\ \text{float, 1} \end{array} \right. \rightarrow 18.0$$

$$\rightarrow W_{strut.7} := 18$$

$$\rightarrow W_{required.....} := W_{strut.7} \cdot \frac{\beta_{s1}}{\beta_{n3}} = 30 < h_a = 123 \checkmark$$

Node 4 (CCC):

$$P = 320000$$

$$\rightarrow W_{required,..} := \frac{P}{\nu_{CCC} \cdot b \cdot f_c} = 50 < L_o = 100 \checkmark$$

$$F_{u.4} = 58122$$

$$\rightarrow W_{required,..} := W_{strut.4} \cdot \frac{\beta_{s1}}{\beta_{n1}} = 9 < a = 25 \checkmark$$

$$F_{u.6} = 116244 \quad \rightarrow W_{strut.6} := W_{strut.7} = 18$$

$$\rightarrow W_{required} := W_{strut.6} \cdot \frac{\beta_{s1}}{\beta_{n1}} = 18 < a = 25 \checkmark$$

$$F_{u.3} = 325236$$

$$\rightarrow W_{required,..} := W_{strut.3} \cdot \frac{\beta_{s2}}{\beta_{n1}} = 51 < Width_{strut.3} = 103 \checkmark$$

Main steel requirement in tie zones:

Tie 2 (B/t nodes 2 & 3):

$$F_2 = 320000 \qquad f_{y.15} = 400 \qquad A_{b.15} = 200$$

$$A_{s2.required} := \frac{F_2}{f_{y.15}} = 800$$

Tie 2 is a **vertical tie** so 2 leg **stirrups** must be used.

$$\text{Required amount of reinforcement} = \frac{A_{s2.required}}{2 \cdot A_{b.15}} = 2 \qquad \rightarrow \text{No15bar}_{2.required} := 2$$

Tie 5 (B/t nodes 1&3):

$$F_5 = 58122 \qquad f_{y.10} = 400 \qquad A_{b.10} = 100$$

$$A_{s5.required} := \frac{F_5}{f_{y.10}} = 145$$

$$\text{Required amount of Reinforcement} = \frac{A_{s5.required}}{A_{b.10}} = 1.45$$

$$\rightarrow \text{No10bar}_{5.required} := 2$$

Tie 7 (B/t nodes 3&5):

$$F_7 = 116244$$

$$A_{s7.required} := \frac{F_7}{f_{y.10}} = 291$$

$$\text{Required amount of steel} = \frac{A_{s7.required}}{A_{b.10}} = 2.91$$

$$\rightarrow \text{No10bar}_{7.required} := 3$$

Placement of reinforcements (vertically):

Node 3 & 5:

$$F_7 = 116244$$

$$\nu_{..} := 0.85\beta_{n3} = 0.51 \qquad \text{(CTT)}$$

$$f_{cu..} := \nu_{..} f'_c = 15.3$$

Spread the reinforcement vertically over an area of concrete at least equal to the tension force in the tie.

$$\text{Spread vertically over} = \frac{F_7}{f_{cu.} \cdot b} = 30$$

Allowable Upper & Lower bound for rebar distribution:

$$\frac{h_a}{2} + \frac{F_7}{f_{cu.} \cdot b \cdot 2} = 77$$

$$\frac{h_a}{2} - \frac{F_7}{f_{cu.} \cdot b \cdot 2} = 46$$

Since tie reinforcement is placed in a single layer, place them at 57mm from the extreme tension fibre.

Modified value for the effective depth:

$$d := h - 57 = 843$$

Anchorage of the bottom main reinforcements:

Tie 5:

The development length is being calculated with accordance to the ACI 318 (2008). The development length is being formulated to minimize the chance of bar-pullout failure. The development calculations in ACI are based on the SI units system, therefore further adjustment was applied to convert the quantities in to Metric units.

$$f_{y.10.SI} := f_y \cdot 10 \cdot 145.037738007 = 58015$$

$$d_{b.10} = 11.3 \quad \text{Cover is less than 2-1/2 in.}$$

$$d_{b.10.SI} := d_{b.10} \cdot 0.03937 = 0.44$$

$$f_{c.SI} := f_c \cdot 145.037738007 = 4351$$

$$\psi_e := 1 \quad \text{Assuming lightweight aggregate concrete and epoxy-coated reinforcement is not used.}$$

$$\lambda := 1$$

$$\psi_t := 1 \quad \text{Since less than 12 in. of fresh concrete is present below the longitudinal bars.}$$

Check if there is enough length for the straight bars to develop their full strength:

$$L_{d.SI} := \left(\frac{f_{y.10.SI} \cdot \psi_t \cdot \psi_e}{25 \cdot \lambda \cdot \sqrt{f_{c.SI}}} \right) \cdot d_{b.10.SI} = 16 \quad 12.2.2$$

$$\rightarrow L_{d.required} := L_{d.SI} \cdot 25.4 = 398 \quad > \quad L_r = 150 \quad \text{Not Ok}$$

Try 90° hook in order to provide the required development length:

$$\rightarrow L_{dh.SI} := 0.8 \cdot \frac{(0.02 \cdot \psi_e \cdot f_y \cdot 10.SI)}{\lambda \cdot \sqrt{f'_c.SI}} \cdot d_{b.10.SI} = 6 \geq 6in \checkmark \quad 12.5.1$$

$$\rightarrow L_{dh.required} := L_{dh.SI} 25.4 = 159$$

$$< L_{dh.available} := L_r - (Cover_{min} + d_{b.10} - o) + \frac{h_a}{2 \tan(\theta)} \quad \checkmark$$

$$\rightarrow L_{dh} := 160 \quad \rightarrow D_{hook} := 70$$

$$\rightarrow G := 12 \cdot d_{b.10} + 4 \cdot d_{b.10} = 181$$

Confinement of hookes in accordance with the Figure R12.5.3(a), clause 12.5:

Maximum Allowable dimensions:

Provide:

$$S_{outer.stirrup} := 2 \cdot d_{b.10} = 23 \leq 30mm \text{ clear spacing} \quad \rightarrow S_{out} := 45$$

$$S_{inner.stirrup} := 3 \cdot d_{b.10} = 34 \leq 30mm \text{ clear spacing} \quad \rightarrow S_{in} := 45$$

$$No_{conf.stirrup} := \frac{(L_{dh} - S_{out})}{S_{in}} = 3$$

Tie 7:

Check if there is enough length for the straight bars to develop their full strength:

$$\rightarrow L_{d.required} = 398$$

$$> L_{d.available} := \frac{L_{shear}}{2} + \frac{L_r}{2} + \frac{h_a}{2 \cdot \tan(\theta)} + o + \left(\frac{Width_{strut.3}}{2 \cdot \sin(\theta)} - \frac{h_a}{2 \cdot \tan(\theta)} \right) = 307$$

Therefore, 90° hook is used to provide the required development length:

$$\rightarrow L_{dh.SI} = 6 ; L_{dh.required} := L_{dh.SI} 25.4 = 159$$

$$< L_{dh.available} := L_{d.available} - d_{b.10} = 296$$

Tie 2:

Spacing of the stirrups:

$$(11.7.4) \quad \rightarrow \quad S \leq \frac{d}{5} = 169 \quad ; \quad S := \frac{L_{shear} - \frac{(L_o + L_r)}{2}}{(No15bar_{2.required} + 1)} = 58$$

$$305$$

S=60mm is within the acceptable range. ✓

Results:

1. **Extend the beam span by 30 mm from the outer face of the support, on each side.**
2. **Tie 5,12:**
3, No.10 steel bars is required to transfer the tension in the longitudinal tie element.
Locate the bars horizontally @ 57mm from the extreme tension fibre.
The bars are needed to be bented upwards 90°, with $L_{dh}=160\text{mm}$ and 181mm vertical tail.
The closest confinning stirrup from the outer edge of the vertical tail of the hook is to be placed at 45mm.
The other two confinning stirrups are positioned at a spacing of 45mm from each other (center-to-center)
3. **Tie 7:**
No additional reinforcement is necessary as long as the longitudinal reinforcement provided for the tie 5 & 12 is extended to resist the tension in tie 7.
4. **Tie 2, 10:**
Evenly distribute 2, No.15 closed steel stirrups over the clear shear span. space the stirrups 60 mm apart (center-to-center).

Crack control reinforcement:

Since the F'_c is less than 41MPa, with accordance to the Appendix A, section A.3.3.1, the axis of the strut must be crossed by layers of reinforcement that satisfy:

$$\Sigma \rho_{vi} \sin \theta \geq 0.003$$

$$d_s := 5.74 \qquad A_s := \pi \frac{d_s^2}{4} = 26$$

$$\rho_{vi} := \frac{2A_{si}}{b \cdot s_i} = \frac{0.003}{\sin(\theta)} \left| \begin{array}{l} \text{solve, } A_{si} \\ \text{float, } 4 \end{array} \right. \rightarrow 0.3811 \cdot s_i$$

$$\rightarrow A_{si} := 0.3808s_i = 26 \left| \begin{array}{l} \text{solve, } s_i \\ \text{float, } 3 \end{array} \right. \rightarrow 68.3$$

Spacing of the stirrups:

$$(11.7.4) \quad \rightarrow s_i \leq \frac{d}{5} = 169 \qquad \text{Use S=102mm spacing.}$$

305

Selection of the welded wire based on the required density of steel, A_s (mm²/m), per 1m:

$$\rightarrow L := 1000$$

$$n := \frac{L}{102} \qquad A_s := n \cdot (A_s) \rightarrow 253.6959267485663333$$

Thus use **MW 25.8** grade for the web reinforcement

Results:

1. **Apply a layer of MW25.8 X MW25.8 welded-wire mesh as a skin reinforcement to both faces of the deep beams.**
2. **The size of the mesh must be 102mm X 102mm center to center spacing.**

A.4: Design calculations for S2 deep beam**Input parameters:**

$$\begin{aligned}
 f_c &:= 30 & \phi_s &:= 1 \\
 L_{shear} &:= 600 & \phi_c &:= 1 \\
 L_o &:= 210 & P &:= 317000 \\
 L_r &:= 210 & o &:= 0 \\
 d_{b.10} &:= 11.3 & \phi_{flexure} &:= 1 & (9.3.2.1) \\
 A_{b.10} &:= 100 & \phi_{shear} &:= 1 & (9.3.2.6) \\
 f_{y.10} &:= 400 & b &:= 250 \\
 & & h &:= 900
 \end{aligned}$$

Maximum shear and bending moment values:

$$v := P = 317000$$

$$M_u := \phi_{flexure} \cdot P \cdot L_{shear} = 190200000$$

The corresponding depth of compression zone, a , is 50mm, the depth of tie zone, h_a , is 165mm & the compression struts are oriented at an angle, θ , of 69.3° from the longitudinal reinforcements.

The existing forces in the strut and tie elements of the selected STM:

$$F_2 := P = 317000 \quad F_{10} := F_2$$

$$F_1 := \frac{F_2}{\sin(\theta)} = 338825 \quad F_{11} := F_1$$

$$F_3 := F_1 = 338825 \quad F_9 := F_3$$

$$F_4 := \frac{F_2}{\tan(\theta)} = 119638 \quad F_8 := F_4$$

$$F_5 := F_4 = 119638 \quad F_{12} := F_8$$

$$F_6 := 2 \cdot F_5 = 239275$$

$$F_7 := F_6 = 239275$$

Bearing strength @ the loading points:

Satisfying the Bearing stress < Allowable stress condition

$$\text{Bearing stress @ loading points} = \frac{P}{(L_o \cdot b) \cdot \phi_{shear}} = 6$$

Allowable stresses:

$$\nu_{CCC} := \phi_{shear} \cdot 0.85 \cdot \beta_{n1} = 0.85$$

$$\rightarrow \text{Allowable bearing stress} = \nu_{CCC} \cdot f'_c = 25.5 > 6 \text{ MPa} \quad \checkmark$$

$$\text{Bearing stress @ reaction points} = \frac{P}{(L_r \cdot b) \cdot \phi_{shear}} = 6$$

Allowable stresses:

$$\nu_{CCT} := \phi_{shear} \cdot 0.85 \cdot \beta_{n2} = 0.68$$

$$\rightarrow \text{Allowable bearing stress} = \nu_{CCT} \cdot f'_c = 20.4 > 6 \text{ MPa} \quad \checkmark$$

Geometric dimensions of the nodal zones:

Node #1:

*Opposite*₁=165

*Adjacent*₁=210

*Hypotenuse*₁=267

Node #2:

*Opposite*₂=45

*Adjacent*₂=255

*Hypotenuse*₂=259

Node #4:

*Opposite*₄=45

*Adjacent*₄=210

*Hypotenuse*₄=215

Node #3:

A=177

B=227

C=233

Verification of strength of Struts:

Strut #	End nodes	β_s	θ (°)	Force (kN)	Width (mm)		Adequacy
					Required	Provided	
4	2-4	1	0	119638	18	45	OK
6	4-6	1	0	239275	37	45	OK
1	1-2	0.75	70	338825	70	255	OK
3	3-4	0.75	70	338825	70	212	OK

Verification of strength of nodal zones:

Node #	Type	B _n	Force (kN)		Width (mm)		Adequacy
			Identity	Magnitude	Required	Provided	
1	CCT	0.8	F ₁	338825	66	255	OK
			P	317000	62	210	OK
			F ₅	119638	23	165	OK
2	CCT	0.8	F ₁	338825	66	255	OK
			F ₄	119638	23	45	OK
			F ₂	317000	62	600	OK
3	CTTT	0.6	F ₃	338825	88	212	OK
			F ₅	119638	30	165	OK
			F ₂	317000	83	600	OK
			F ₇	239275	62	165	OK
4	CCCC	1	P	317000	50	210	OK
			F ₄	119638	18	45	OK
			F ₆	239275	37	45	OK
			F ₃	338825	53	212	OK

Reinforcement requirement:

Tie #	End nodes	θ (°)	Force (kN)	Reinforcement (mm ²)			Adequacy
				Type	Required	Provided	
2	2-3	90	317000	No.10	793	800	OK
5	1-3	0	119638	No.10	300	600	OK
7	3-5	0	239275	No.10	600	600	NOT OK

Results:

1. Tie 5,12:

- 6, No.10 steel bars is required to transfer the tension in the longitudinal tie element.
- Locate the first layer of longitudinal reinforcements at 57mm and the second layer at 108mm from the extreme tension fibre.
- The bottom layer longitudinal bars are bended upwards 90°, with $L_{dh}=160\text{mm}$ and 181mm vertical tail.
- The closest confining stirrup from the outer edge of the vertical tail of the hook is to be placed at 45mm, while the other two confining stirrups are positioned at a spacing of 45mm from each other (center-to-center)

2. Tie 7:

No additional reinforcement is necessary as long as the longitudinal

reinforcement provided for the tie 5 & 12 is extended to resist the tension in tie 7.

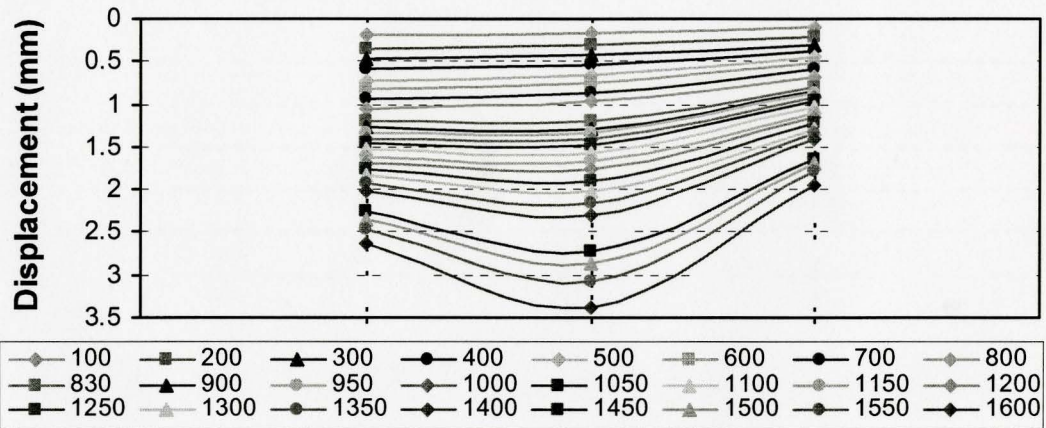
3. ***Tie 2, 10:***
Evenly distribute 4, No.10 closed steel stirrups over the clear shear span. Place the stirrups 120 mm apart (center-to-center).
4. ***Place a layer of MW25.8 × MW25.8 welded-wire mesh as skin reinforcement to each face of the beam.***
5. ***The mesh bars must have a 102mm × 102mm, center to center, spacing.***

APPENDIX B: ADDITIONAL EXPERIMENTAL DATA

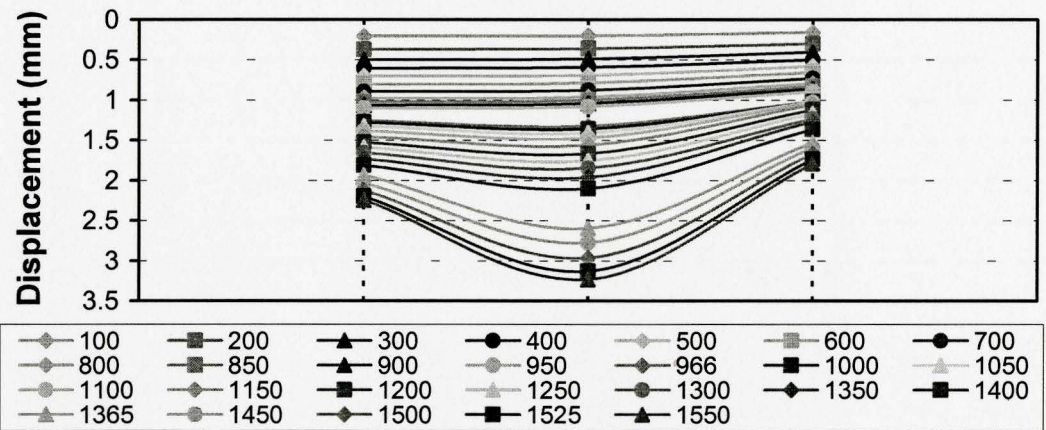
Additional records of the behaviour of each tested beam is provided in this Appendix.

The figures below represent the deformed shape, mid-span strain distribution along the depth of the beams and the longitudinal reinforcement strain distribution in each beam every time the test was stopped and the cracks were marked.

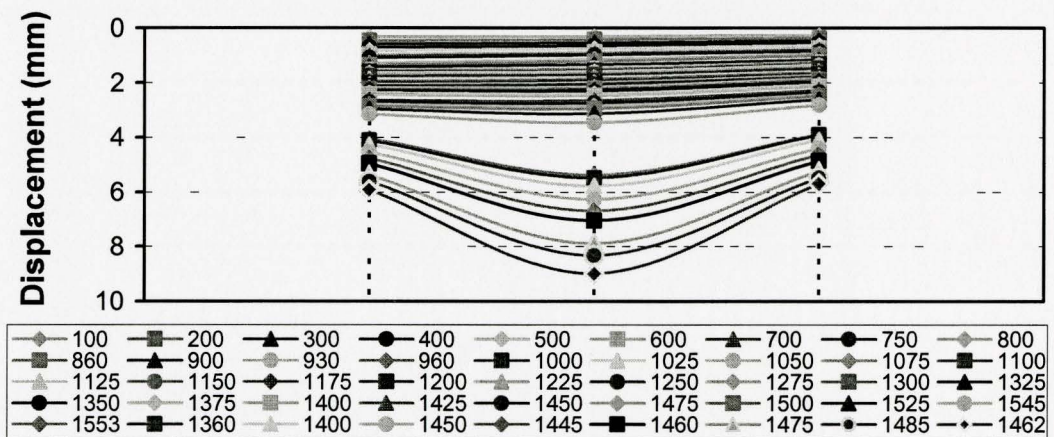
The complete plot of the rosette strain measurements are also provided in this Appendix.



(a) Span deformation of the F1-A

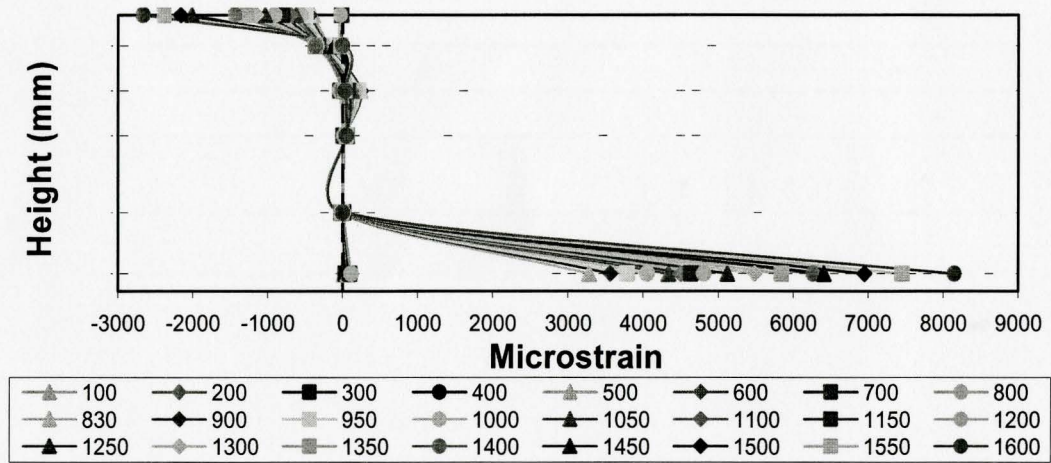


(b) Span deformation of the F1-B

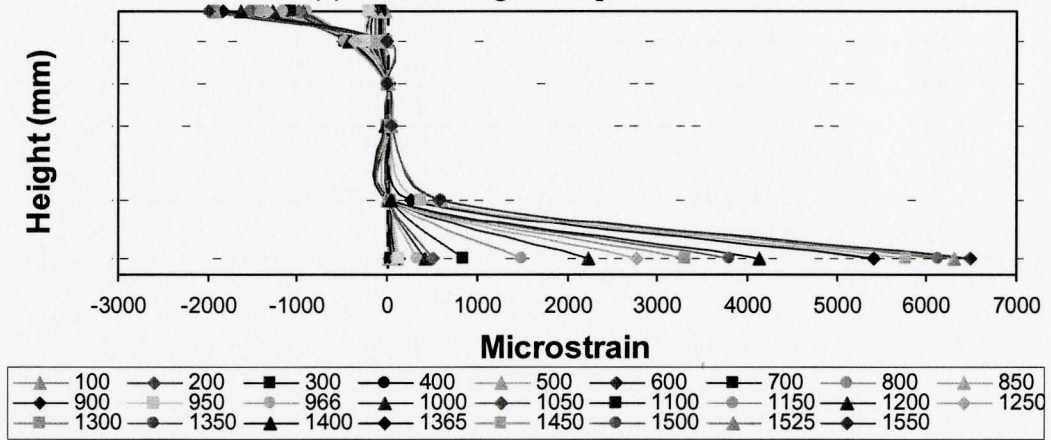


(c) Span deformation of the S1-B

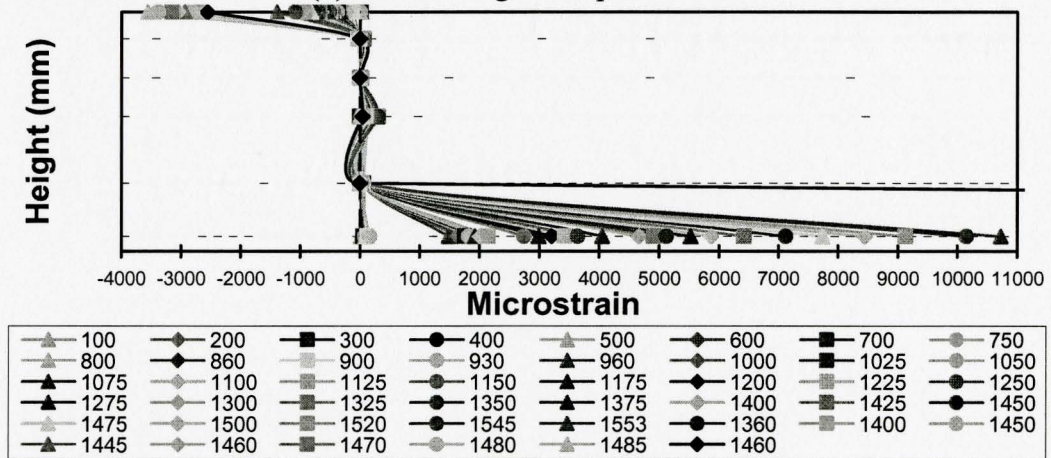
Figure B.0.1 Deformed shape of the beams with $l_e/h=1$



(a) Strain along the depth of F1-A

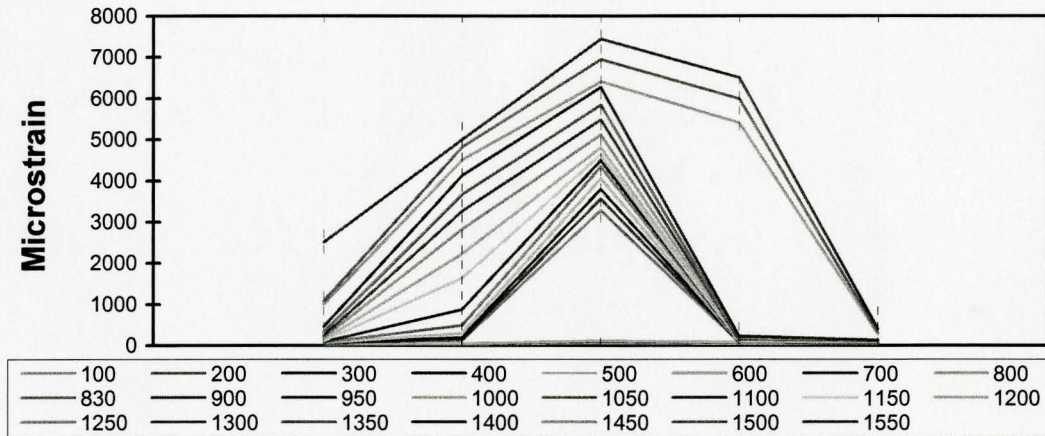


(b) Strain along the depth of F1-B

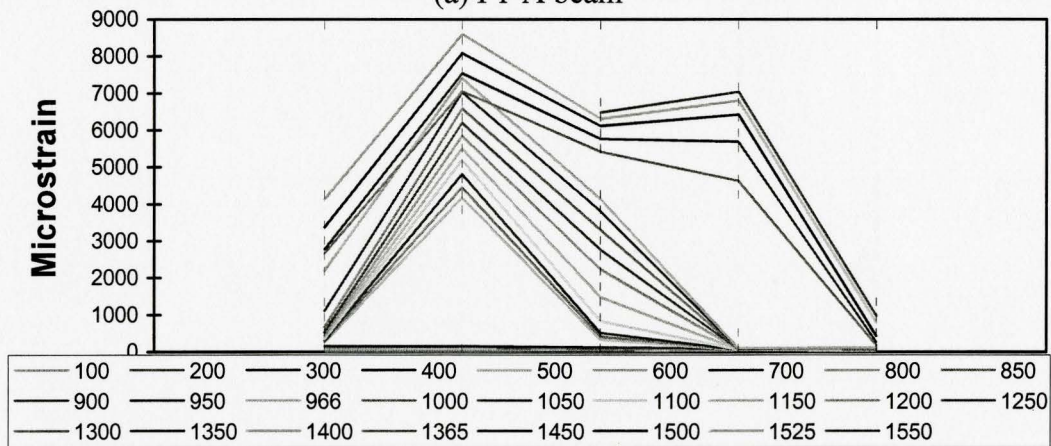


(c) Strain along the depth of S1-B

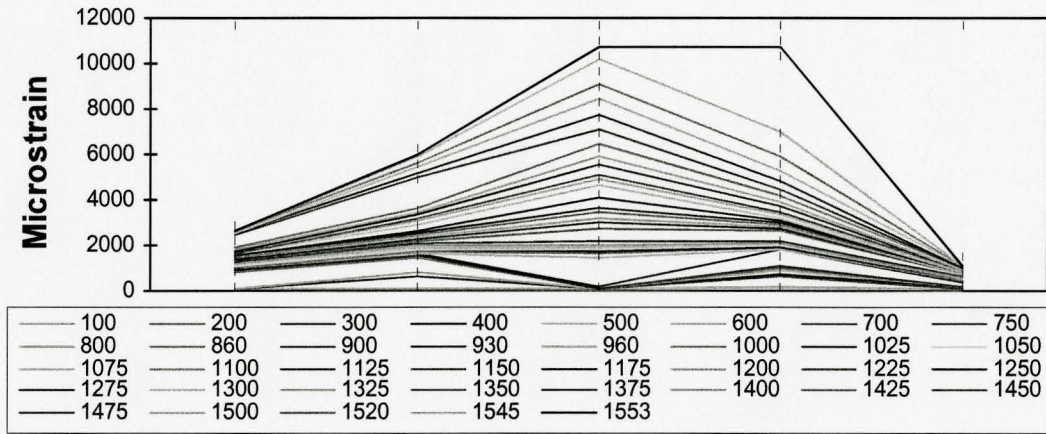
Figure B.1.2. Strain distribution along the depth of the beams with $l_e/h=1$



(a) F1-A beam

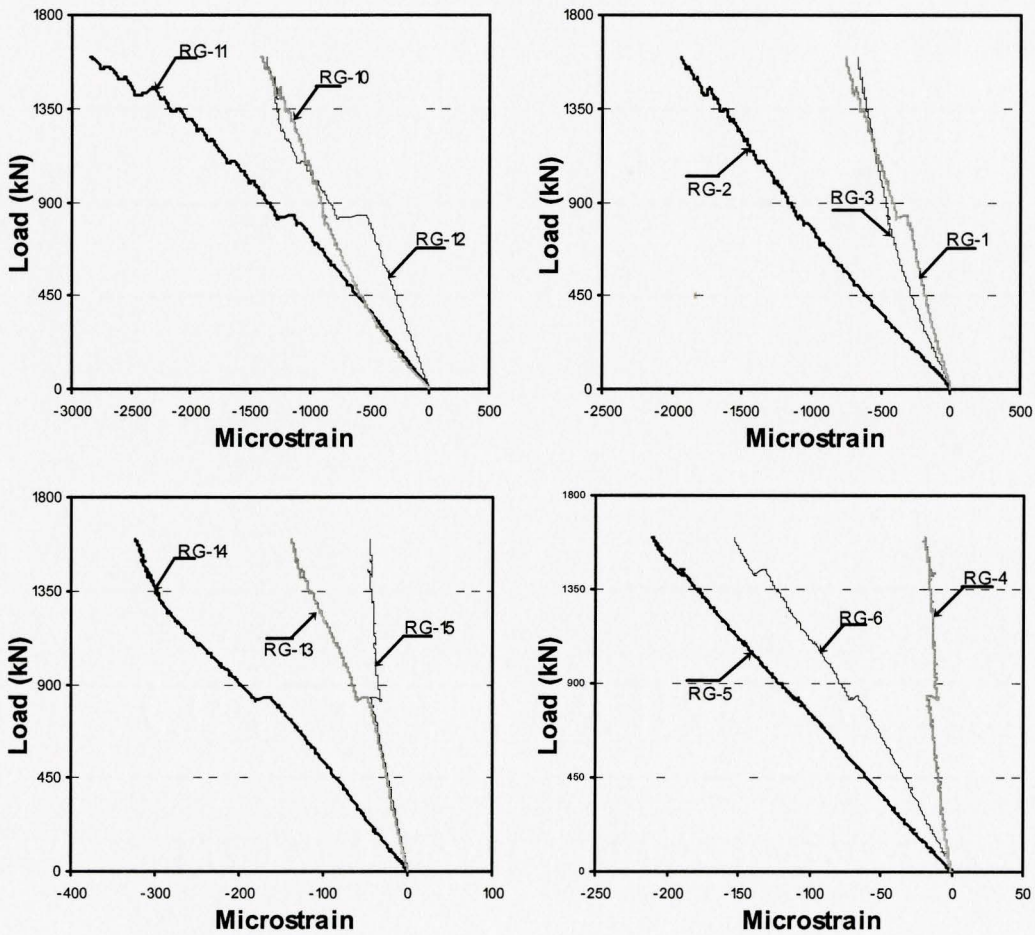


(b) F1-B beam



(c) S1-B beam

Figure B.1.3 Strain distribution along the longitudinal bar of the beams with $l_e/h=1$



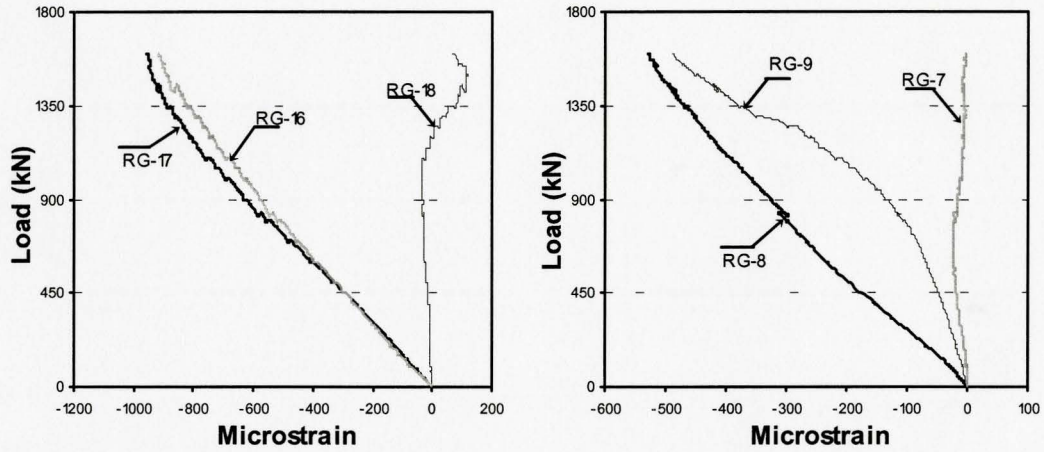
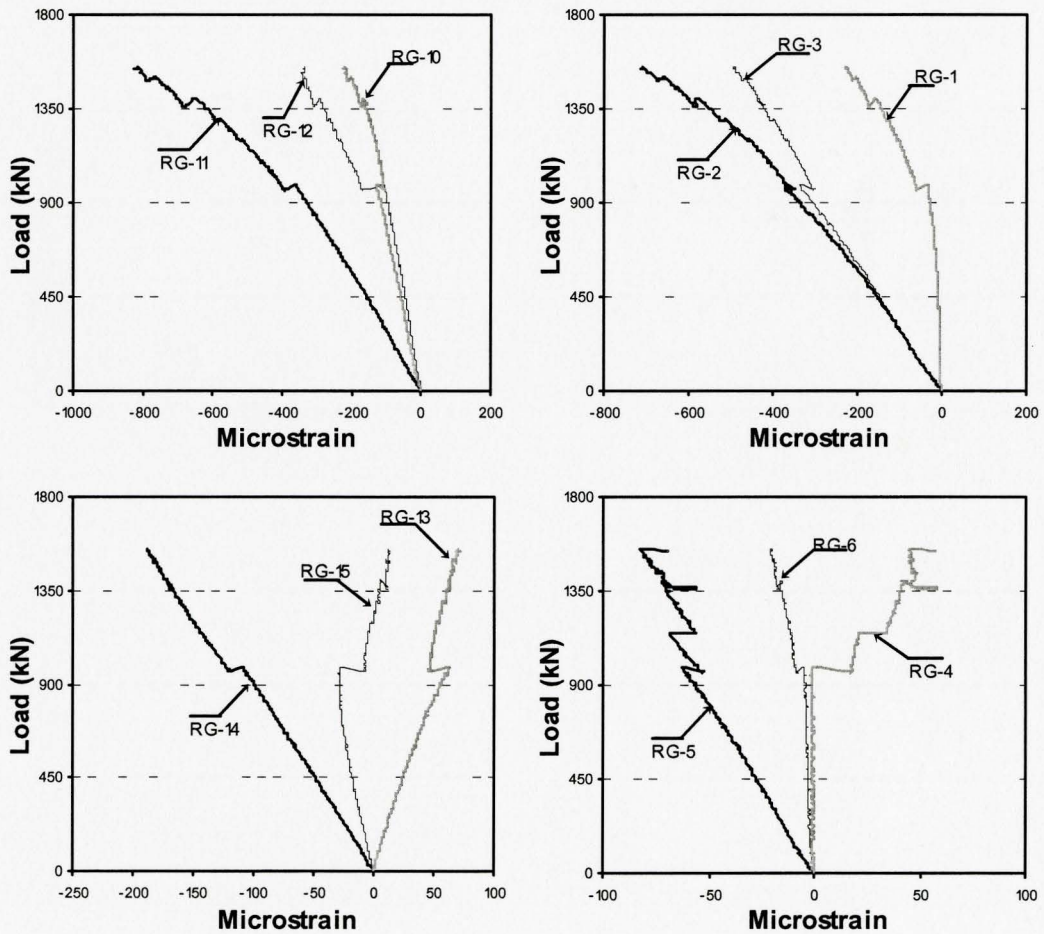


Figure B.1.4: Strain measurements from the rosette gauges in the F1-A beam



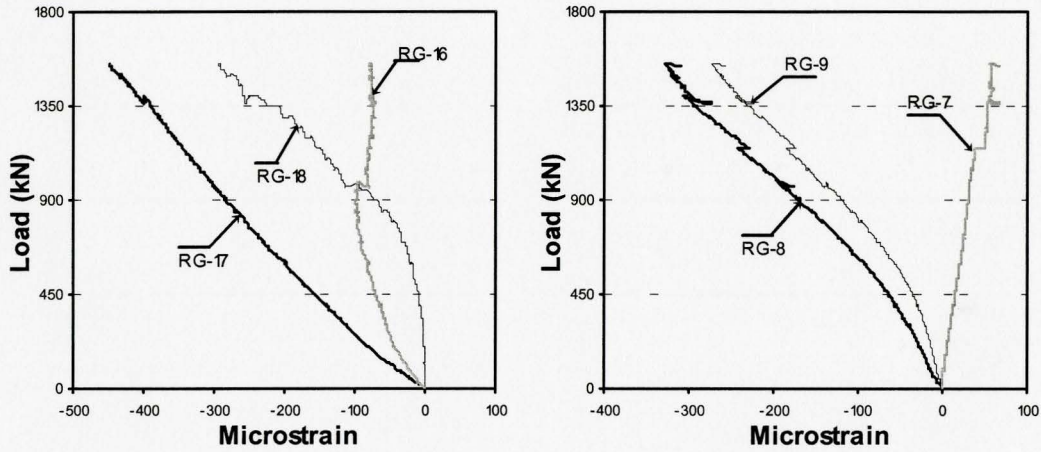
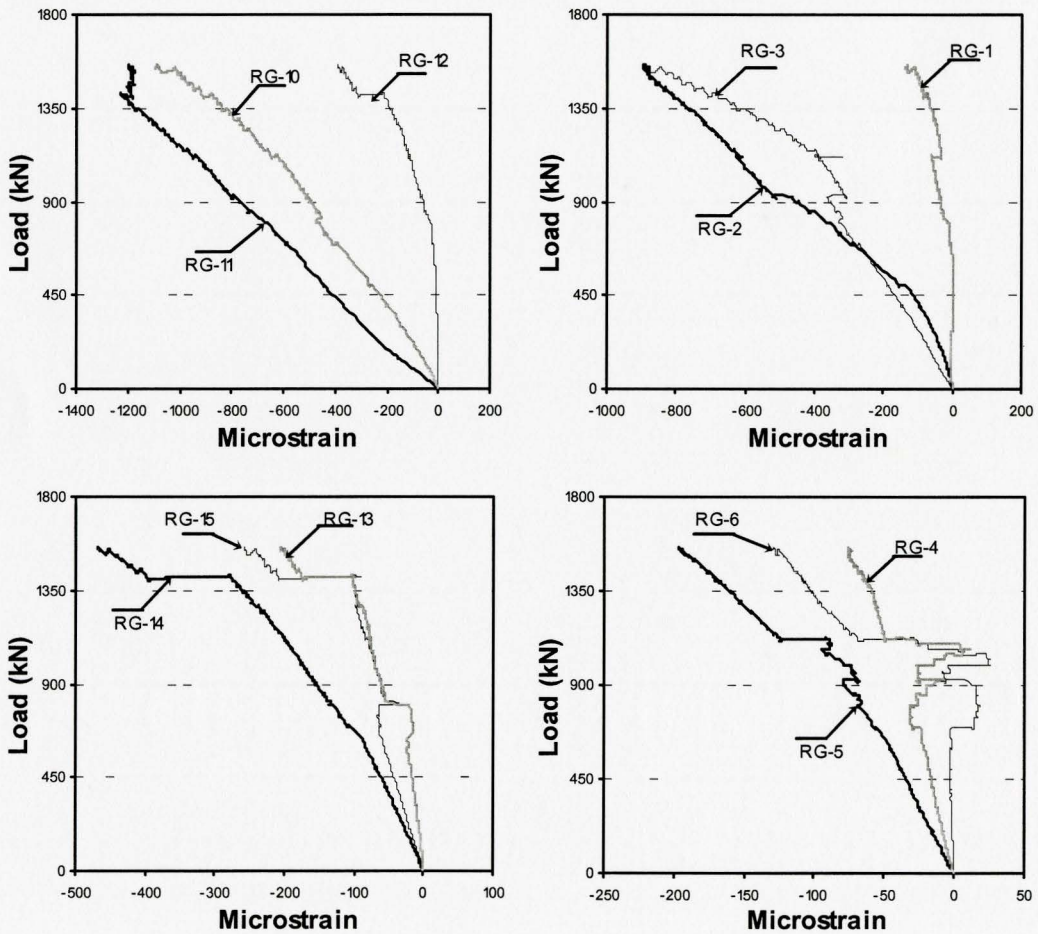


Figure B.1.5 Strain measurements from the rosette gauges in the F1-B beam



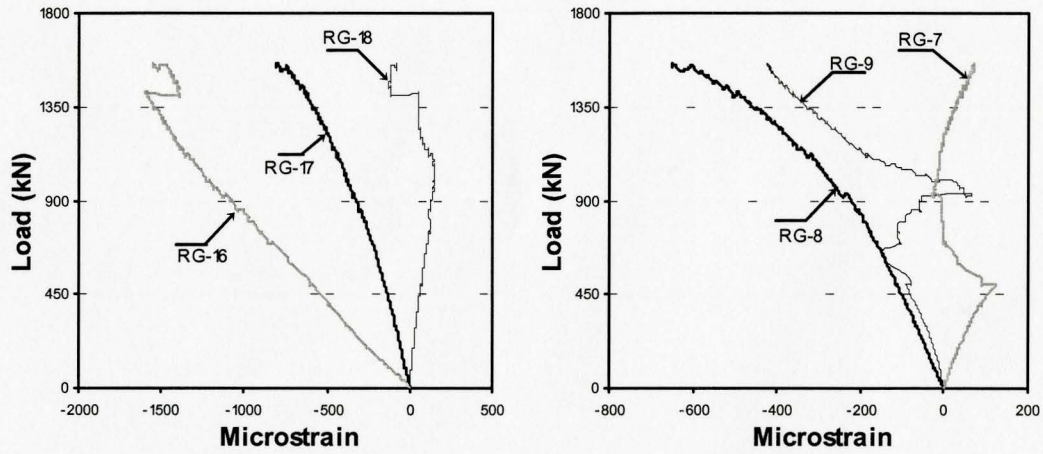
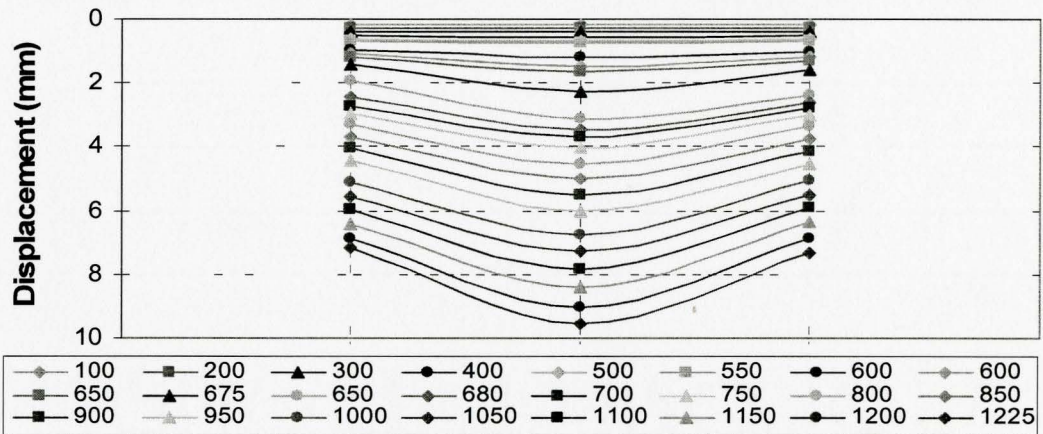
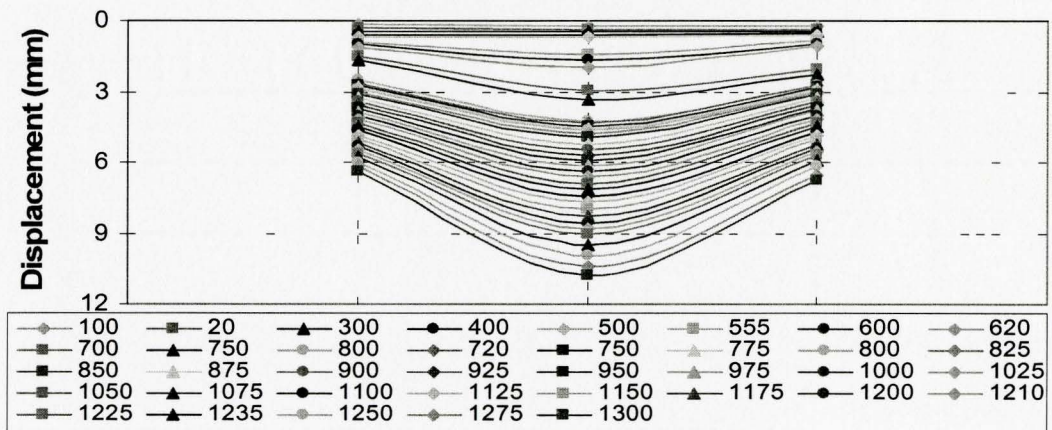


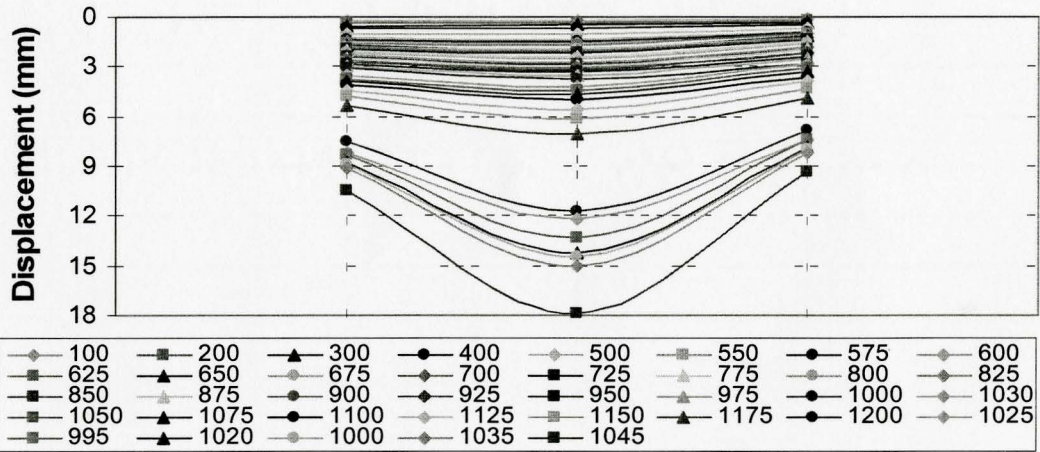
Figure B.1.6: Strain measurements from the rosette gauges in the S1-B beam



(a) Span deformation of the F2-A

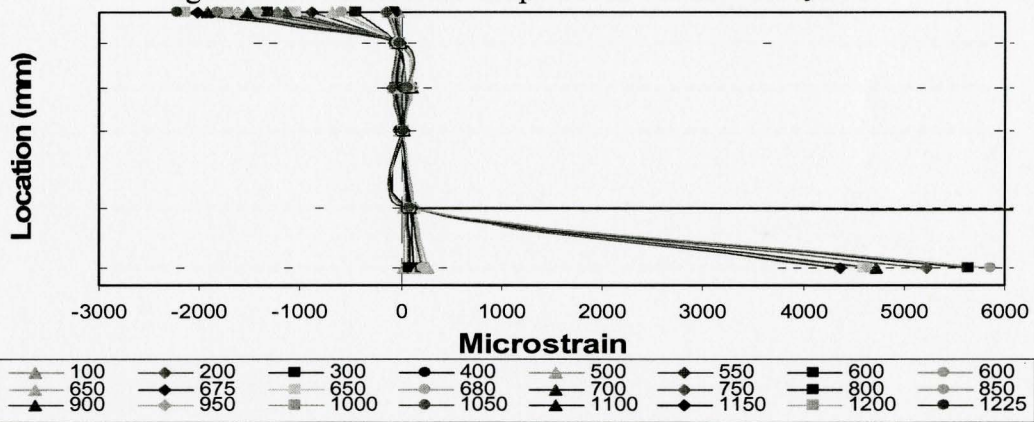


(b) Span deformation of the F2-B

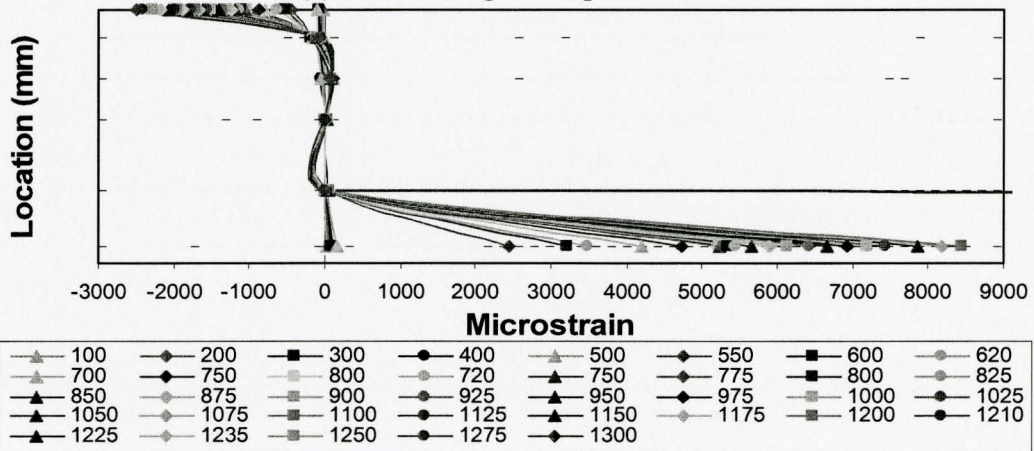


(c) Span deformation of the S2

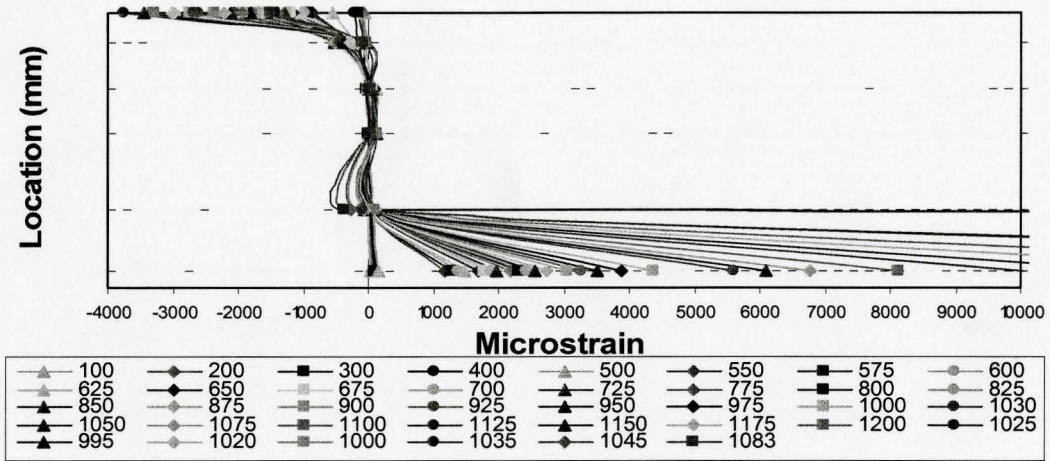
Figure B.1 7 Deformed shape of the beams with $l_e/h=2$



(a) Strain along the depth of F2-A

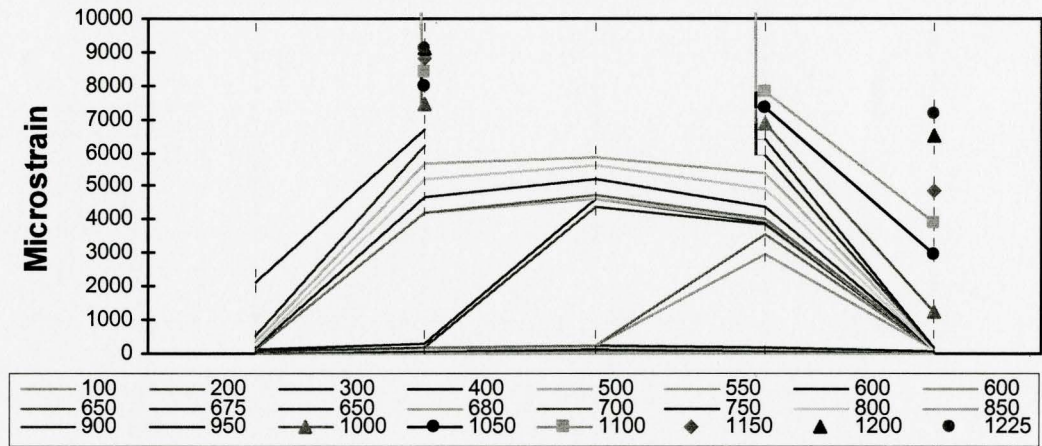


(b) Strain along the depth of F2-B

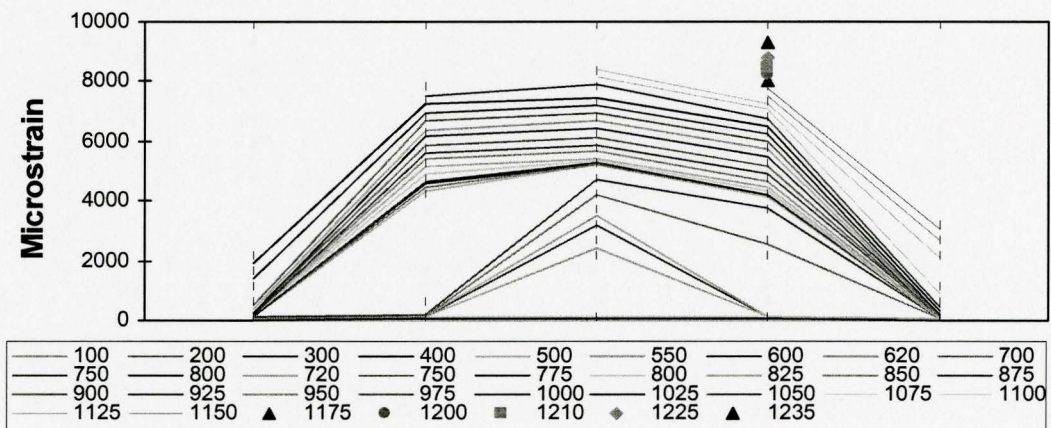


(c) Strain along the depth of S2

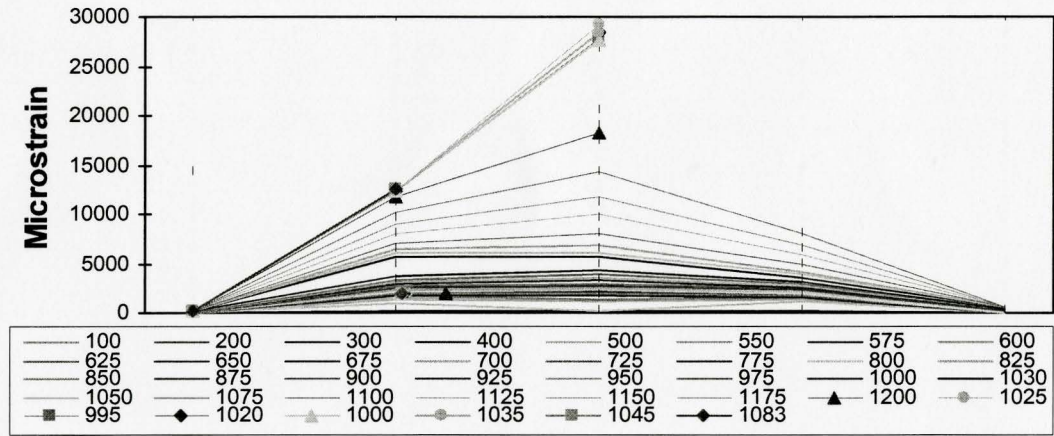
Figure B.1.8. Strain distribution along the depth of the beams with $l_e/h=2$



(a) F2-A beam

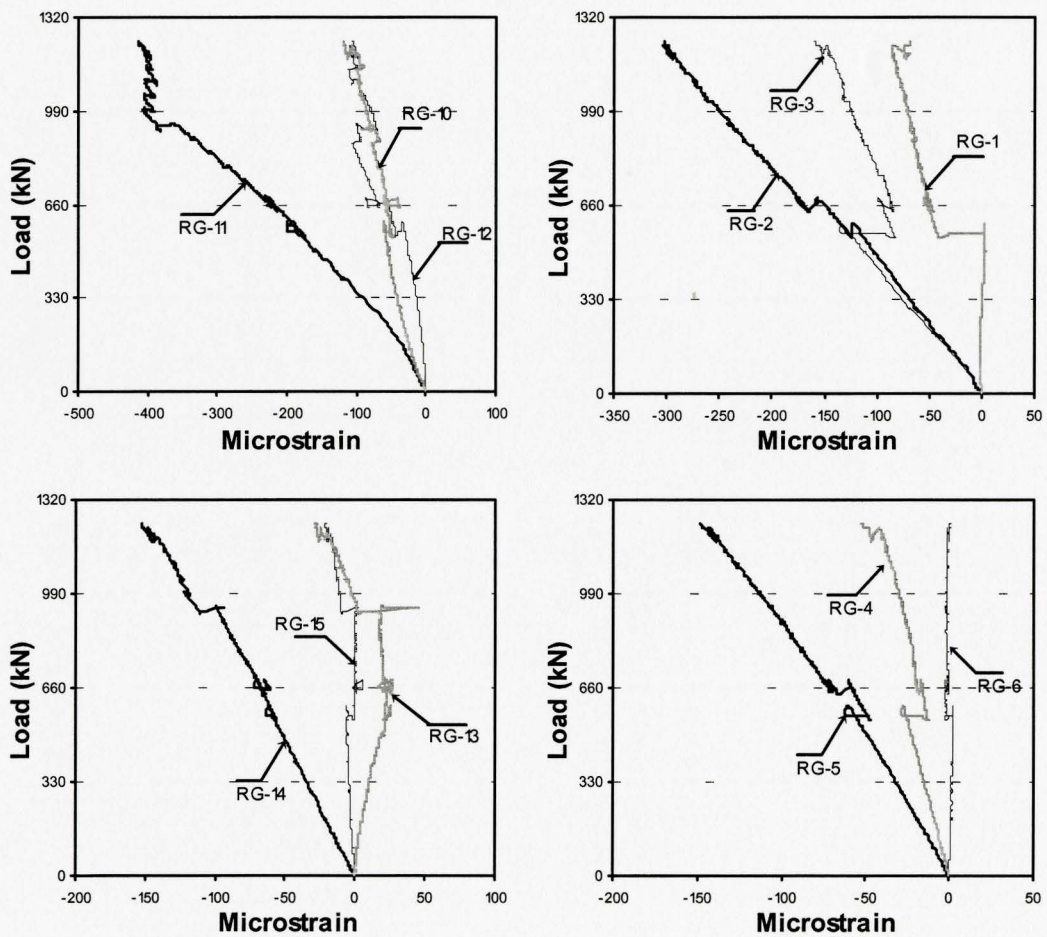


(b) F2-B beam



(c) S2 beam

Figure B.1.9: Strain distribution along the longitudinal bar of the beams with $l_e/h=2$



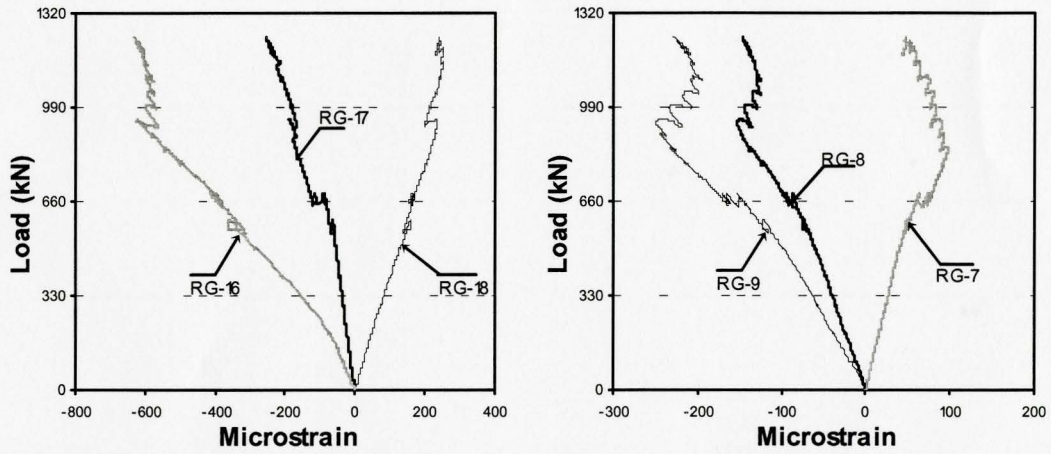
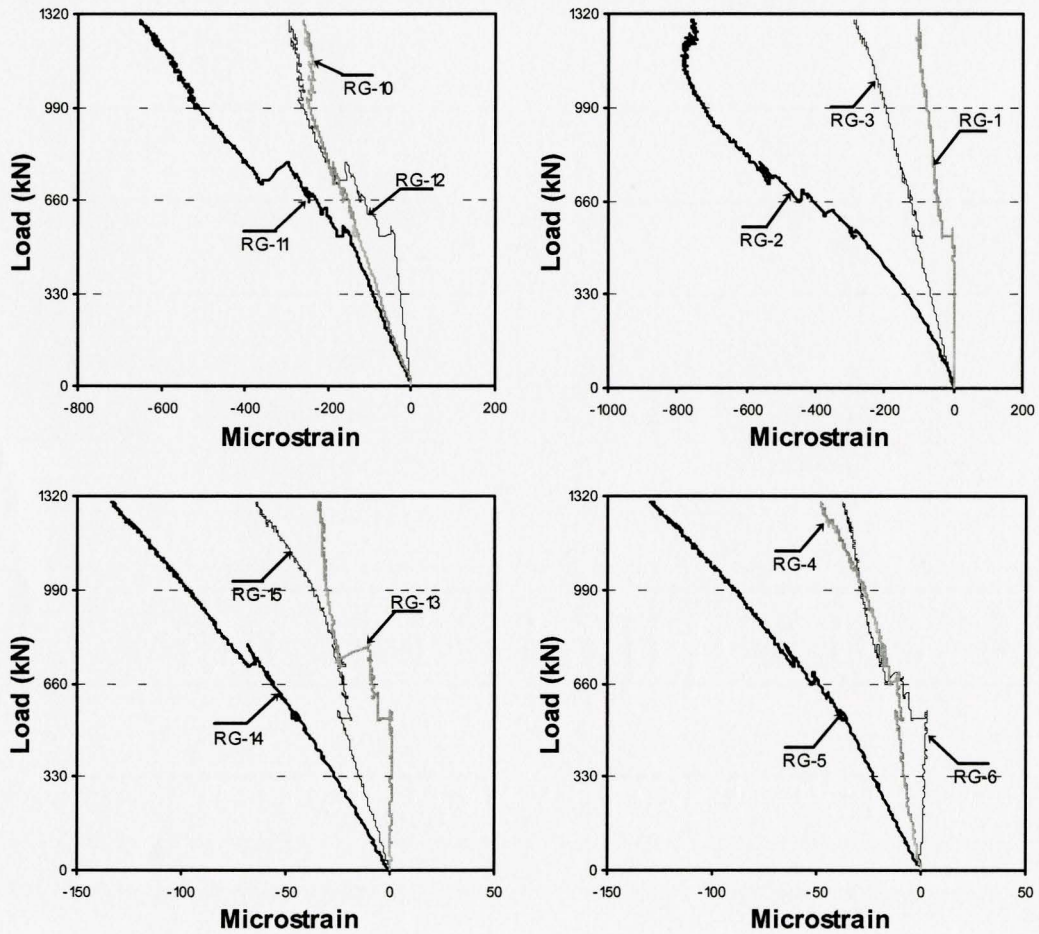


Figure B.1 10: Strain measurements from the rosette gauges in the F2-A beam



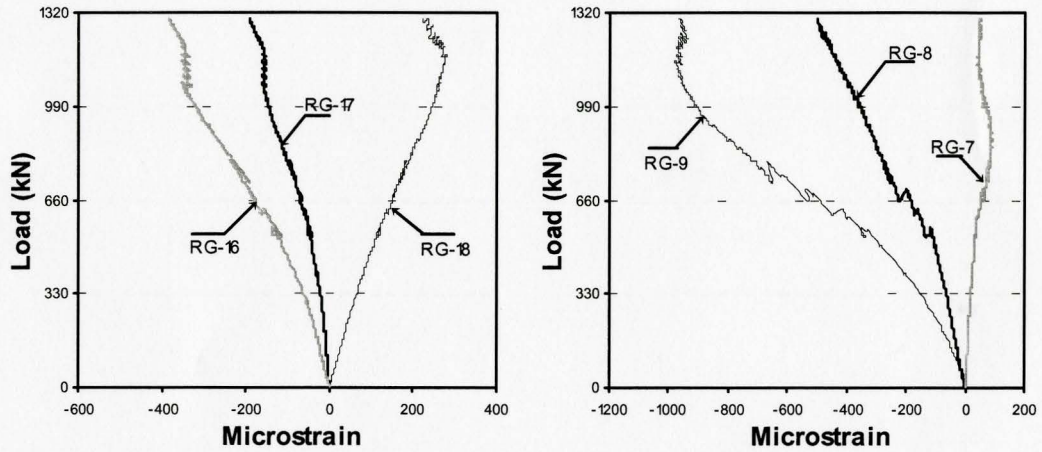
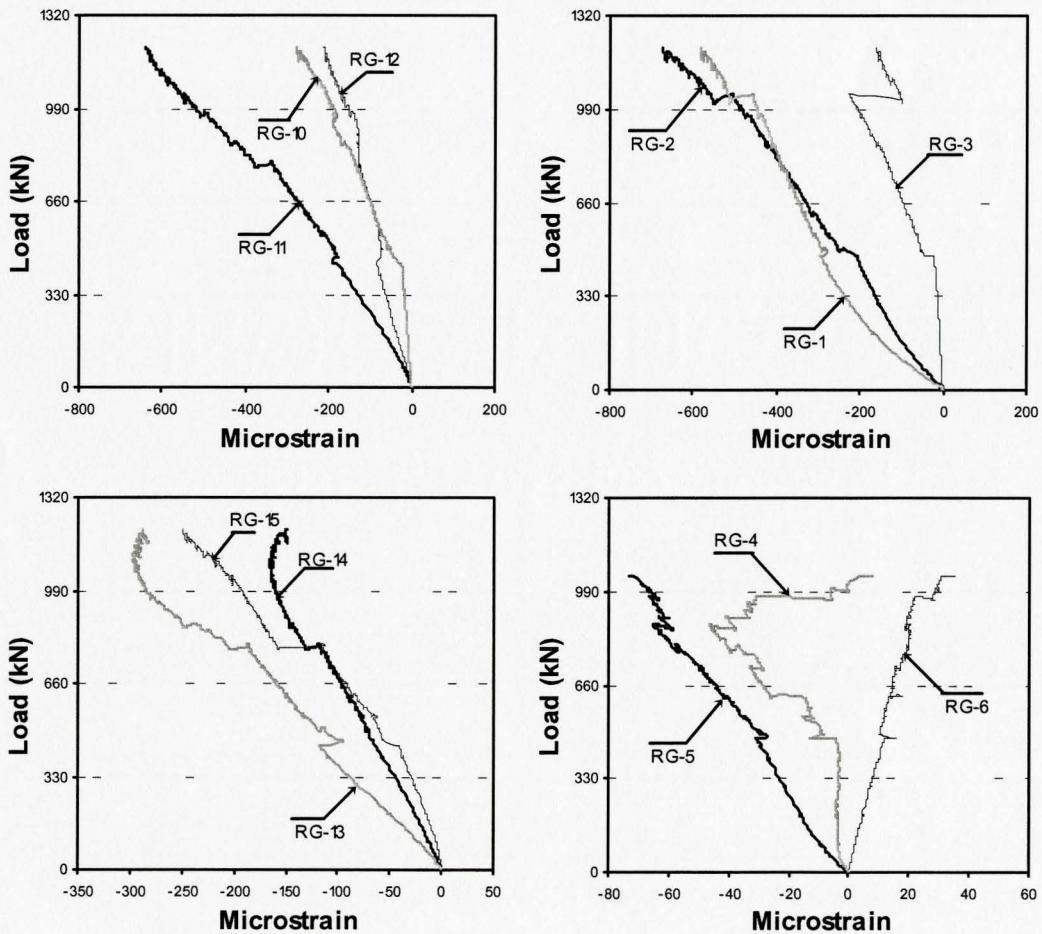


Figure B.1 11 Strain measurements from the rosette gauges in the F2-B beam



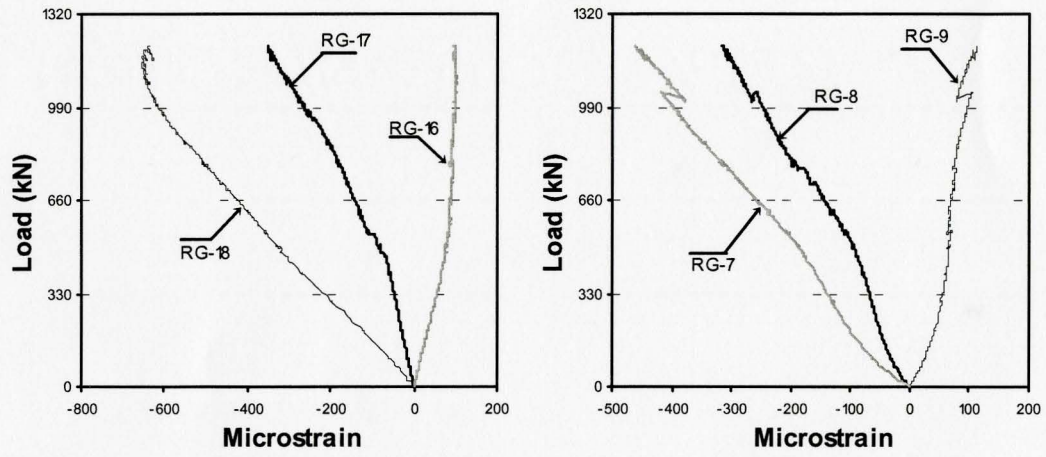


Figure B.1 12. Strain measurements from the rosette gauges used in the S2 beam

APPENDIX C: MATERIAL TESTING

The properties of the materials used in fabrication of the beams are listed in the tables below.

Table C.1 Compressive cylinder strength of concrete, for specimens F1-A/B (151 days after casting)

Cylinder Number	Test type	Test results (MPa)	Average strength (MPa)
Cylinder 1	Compressive Strength	33.61	33.71
Cylinder 2	Compressive Strength	34.08	
Cylinder 3	Compressive Strength	33.43	

Table C.2. Compressive cylinder strength of concrete, for specimen S2 (163 days after casting)

Cylinder Number	Test type	Test results (MPa)	Average strength (MPa)
Cylinder 1	Compressive Strength	34.62	34.37
Cylinder 2	Compressive Strength	34.83	
Cylinder 3	Compressive Strength	33.66	

Table C.3 Compressive cylinder strength of concrete, for specimens F2-A/B (176 days after casting)

Cylinder Number	Test type	Test results (MPa)	Average strength (MPa)
Cylinder 1	Compressive Strength	35.39	34.95
Cylinder 2	Compressive Strength	33.88	
Cylinder 3	Compressive Strength	35.58	

Table C.4: Compressive cylinder strength of concrete, for specimen S1-B (182 days after casting)

Cylinder Number	Test type	Test results (MPa)	Average strength (MPa)
Cylinder 1	Compressive Strength	36.10	35.38
Cylinder 2	Compressive Strength	36.27	
Cylinder 3	Compressive Strength	33.77	

Table C.5 Tensile properties of No.10 steel reinforcing bar

Rebar trial	Elastic modulus (GPa)	Average E (GPa)	Yielding strength (Mpa)	Average σ_y (MPa)
Trial 1	184.72	194.2	470	473
Trial 2	194.32		475	
Trial 3	203.55		475	

Table C.6: Tensile properties of No.15 steel reinforcing bar

Rebar trial	Elastic modulus (GPa)	Average E (GPa)	Yielding strength (Mpa)	Average σ_y (MPa)
Trial 1	210.08	204.68	473	464
Trial 2	198.73		460	
Trial 3	205.22		460	

The corresponding stress-strain relationships for concrete are shown in the figures bellow.

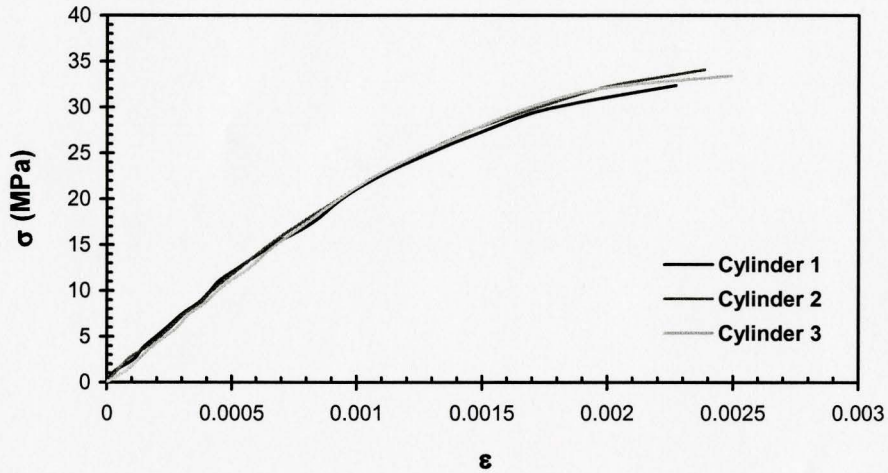


Figure C.1 Stress-strain relationship of the concrete for F1 beams (151 days after casting)

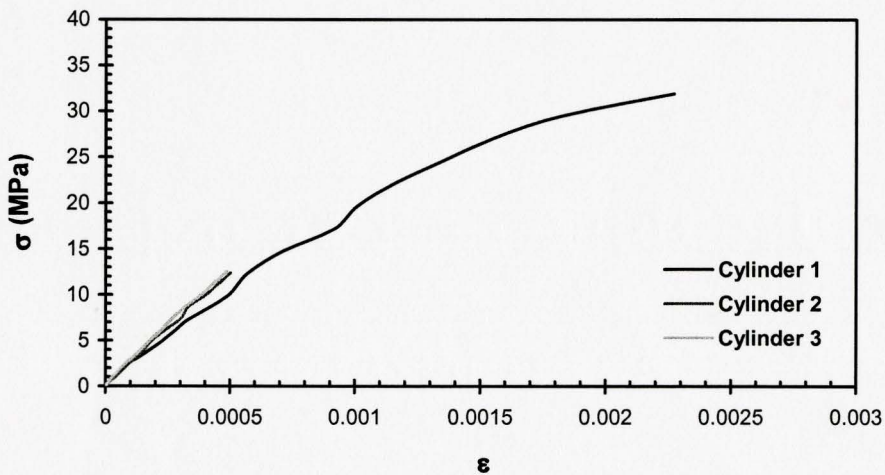


Figure C.2. Stress-strain relationship of the concrete for S2 beams (165 days after casting)

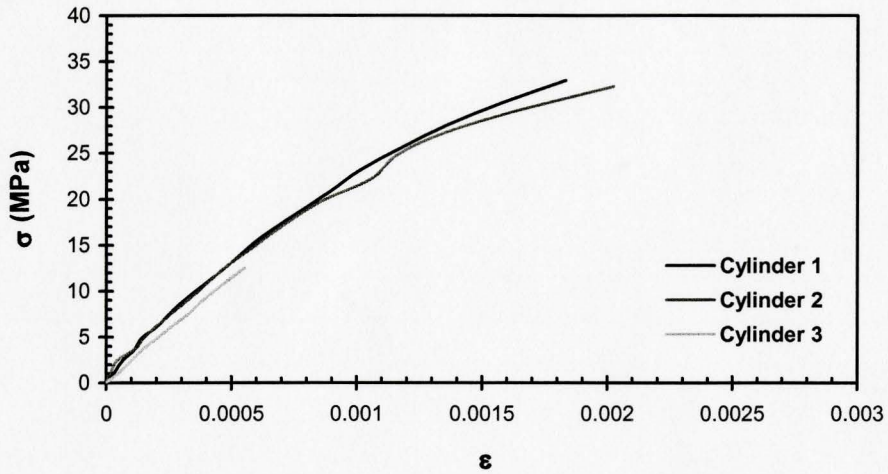


Figure C.3 Stress-strain relationship of the concrete for S2 beams (176 days after casting)

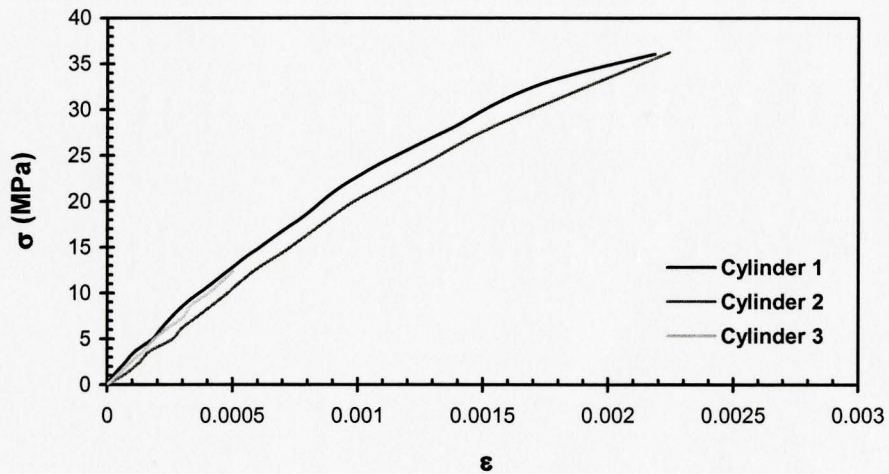


Figure C.4: Stress-strain relationship of the concrete for S1-B beam (182 days after casting)